Multiscale Modeling of Phase-Transformation-Mediated Deformation Twinning in Metastable Titanium Alloys

by

Ganlin Chen

A dissertation submitted in partial fulfillment
of the requirements for the degree of
Doctor of Philosophy
(Materials Science and Engineering)
in The University of Michigan
2026

Doctoral Committee:

Associate Professor Liang Qi, Chair
Assistant Professor Ashley Bucsek
Associate Professor Yue Fan
Professor Amit Misra



A solo journey along the Dalton Highway to the Arctic in the closing days of 2022 — a quiet adventure that has continued to inspire my Ph.D. path and the road beyond.

Ganlin Chen

gavincgl@umich.edu

ORCID iD: 0000-0002-0275-0855

© Ganlin Chen 2026

DEDICATION

To my prefrontal cortex.

ACKNOWLEDGEMENTS

First and foremost, I would like to express my deepest and most sincere gratitude to my advisor, Prof. Liang Qi, whose guidance and mentorship have been the foundation of my doctoral journey. I still remember our very first conversation, when you asked me what motivated me to pursue a Ph.D. I answered that it was the philosophy of asking a question and then dedicating oneself to answering it. Looking back, I feel extraordinarily fortunate that the training I received from you was precisely that — a rigorous, principled, and deeply thoughtful approach to scientific inquiry that matched exactly what I had hoped to find. These are gifts that cannot be taught in a classroom, and I am deeply grateful that you gave them to me so generously. Your uncompromising standards in research and your quiet humility in life and in your relationships with others have become a role model that I carry with me far beyond the research. What I have learned from you is not only how to do good science, but how to be a good scientist — and a good person. Your dedication to research and your spirit for life have profoundly shaped who I am and will continue to inspire me throughout my future career.

I would like to express my sincere gratitude to my committee members, Professor Ashley Bucsek, Professor Yue Fan, and Professor Amit Misra, for their invaluable suggestions during my data meetings and for the inspiring discussions that shaped the final part of this thesis. I would like to extend a special thank you to Professor Amit Misra, your prompt and reliable responses to every request I made left a lasting impression on me. Your dependability and professionalism have shown me what it means to be someone that others can truly count on, and that is a standard of character I try to carry with me throughout my career.

I sincerely acknowledge all the financial support during my PhD, including the National Science Foundation under award #CMMI-2121866, and Engineering Graduate Student Fellowship.

I am deeply fortunate to have shared this tough Ph.D. journey with my warm and kind colleagues in the Qi Research Group. First I would like to show my great thankfulness to Dr. Aditya Sundar, who is the my mentor and bring me into the world of computational materials science, opening a door that has defined the entire trajectory of my doctoral research. I am grateful to Prof. Yong-jie Hu, Dr. Aditya Sundar, Dr. Zhucong Xi, Dr. Vaidehi Menon, Dr. Amir Zahiri, Jierui Zhao, Dr. Subhendu Chakraborty, Pravendra Patel, Amanda Boahemaa,

and Yijie Sun for their unwavering friendship, the countless hours of discussion on research questions and for always being willing to think through a problem together at a moment's notice. I carry the memory of our time together with great fondness.

I would like to thank my great friends in MSE department: Dr.Zhucong Xi, Dr.Jiadong Chen, Dr.Chao Huang, Dr.Zhixiong Yin, Dr.Yuchen Wu, Fenghe Fu, and Dr.Bokai Zhang, whose presence in my life has been one of the greatest gifts of my time at the University of Michigan. We got to know with each other since 2019, and together we navigated the uncertainty and isolation of the Covid-19 pandemic — a chapter of life that was hard for everyone, yet somehow made lighter by the fact that we faced it side by side. The joy, laughter, and warmth we shared over these seven years in Ann Arbor have colored my doctoral journey.

I would also like to express my heartfelt gratitude to my long-time friends, whose companionship has enriched my life both inside and outside of the University of Michigan. I would first show thank you to Wei Hu: It is a remarkable fortune that two classmates from those early years found themselves reunited as alumni of the same university, and an even greater one that we became neighbors here in Ann Arbor. Your friendship has been a constant source of brightness in my life. More than that, the deep, thoughtful, and unhurried conversations we have shared have a rare quality that I treasure deeply. I then would thank Dr.Xiaoyu Guo, it is a great fortune to have a friendship with you in Ann Arbor. Your sincerity and generosity of spirit have time and again washed away my anxieties and restored a sense of calm and courage that carried me through the most demanding stretches of doctoral life. The long weekend tea talks we shared were an indispensable part of my life here. Wandering freely across topics of life, dreams, and research, those conversations did more than pass the time; they nourished my spirit, sharpened my thinking, and reminded me again and again of what truly matters. I would also like to thank Yifan Wang, a friend whose roots in my life stretch all the way back to primary school. Though the demands of life mean that our conversations are infrequent, there is something extraordinary about the ones we do have — each one, however occasional, carries the quiet power of reminding me who I am and where I come from. I would also like to thank Yiran Liu, Dr. Gangbin Yan, ChenHaoyue Wang, whose trust in me has meant more than words can easily express. Our random, unplanned conversations have a wonderful dual gift for my Ph.D life.

I would also like to extend my most profound gratitude to my parents for their unconditional love, unwavering support, and constant encouragement, which have been the quiet backbone of everything I have accomplished in this journey.

I reserve a special place in these acknowledgements for my grandfather, whose passing in the first week of 2023 left a shadow over my heart that lingers still. Losing you cast a

grief over my life like an overcast sky that has never quite lifted — a presence that is felt most in the moments of achievement I wish I could share with you. Your meticulous care in everything you did and the quiet resilience of your character have woven themselves so deeply into the fabric of my daily life that living by those same values has become my way of remembering you.

I am also deeply grateful to the swing by Silver Park in Northwood, where I sat and watched the clouds drift through spring, the Milky Way unfold in summer, the maples burn in autumn, the snow fall in winter, and countless sunsets pass over Ann Arbor in every season. In moments of pressure, it offered me quiet relief; in moments of happiness, it became a gentle witness. It held my wandering thoughts, my solitude, and my small joys, and became one of the most peaceful companions of my Ph.D. journey.

Last but not least, I would like to thank myself. Through the long and often solitary stretch of doctoral life, I carried self-doubt, failed simulations, and weeks without visible progress with quiet resolve, reason, and gentleness. Even when the end felt impossibly far away, I kept showing up, maintained the small disciplines that held everything together, and refused to let stillness become surrender. I stayed true to myself, persevered through invisible struggles, and continued to try honestly even when confidence wavered. I am proud of what I have achieved.

PREFACE

We live in a complex world. When I began this doctoral research in materials science, I found myself asking a question that would guide the entire study: is there a simple underlying physical picture hiding beneath all of complexity of materials? Metastable β-titanium alloys is one of most complex systems in physical metallurgy. So many interesting events to investigate. This is an ideal system for Ph.D. study.

This thesis represents my attempt to answer that question. The study of deformation mechanisms in metastable β-titanium alloys has long been rich in experimental observations, yet individual findings often remain as isolated case studies and difficult to connect into a coherent and predictive picture. Rather than adding further observations to this collection, I have tried to take a different approach: starting from the most fundamental level of individual phenomena and building upward, step by step, until these pieces assemble into a framework broad enough to predict, rather than merely describe, the deformation behavior of these alloys.

In this sense, the four parts of this thesis trace a journey from careful observation of specific phenomena toward a generalized, physically transparent framework that I hope captures something essential about how these alloys deform. I do not claim that this framework is complete. It is a tiny step that connects atomic-scale mechanisms to macroscopic mechanical behavior in a way that is predictive, testable, and, I hope, useful to the broader community studying metastable β-titanium alloys.

It is my sincere hope that the reader — whether a student encountering these alloys for the first time or an experienced researcher in the field — finds something of value or simply little hints here, and perhaps shares in the conviction that even the most complex physical

systems yield, eventually, to patient and systematic inquiry.

TABLE OF CONTENTS

DEDICATION ii

ACKNOWLEDGEMENTS iii

PREFACE vi

LIST OF FIGURES xi

LIST OF TABLES xxviii

LIST OF APPENDICES xxix

LIST OF ACRONYMS xxx

ABSTRACT xxxiii

CHAPTER

1 Introduction 1

1.1 Motivation 1
1.2 Outline 3
1.3 Fundamental Theories 6
1.3.1 Diffusionless (Martensite) Phase Transformation 6
1.3.2 Metastability 11
1.3.3 Deformation Twinning 13
1.3.4 Couplings of Diffusionless Transformation-Deformation Twinning . 17
1.3.5 Heterogeneous Nucleation in Solids 18
1.3.6 Twin Boundary Migration 22
1.4 Computational methods 26
1.4.1 Density Functional Theory (DFT) Calculations 26
1.4.2 Molecular Dynamics (MD) Simulations 27
1.4.3 Phase Field (PF) Modeling 32

2 Stability and Growth Kinetics of {112} Twin 34

2.1 Introduction 35
2.2 Methods 40
2.2.1 DFT Calculations 40

2.2.2 Choices of Alloy Compositions Based on Phase Stability 42
2.2.3 ω Phase Identification in Twinned Supercells 47
2.2.4 MD Calculations 48
2.2.5 Calculations of Twinning Pathway 48
2.2.6 Experimental Characterizations of Twin Boundary Structures . . . 51
2.3 Results 52
2.3.1 Structures and Stability of {112} Twin Embryos at 0 K 52
2.3.2 Stability of {112} Twin Embryos at Room Temperature 57
2.3.3 Growth of {112} Twin Embryos 64
2.3.4 Controlling {112} Twin Growth by Tuning β Phase stability 73
2.4 Discussions 76
2.5 Conclusions 82
3 Interfacial Structure Evolution and Growth Kinetics of {332} Twin . . . 84
3.1 Introduction 85
3.2 Methods 87
3.2.1 Supercell Setup 87
3.2.2 MD Simulations 87
3.3 Results 88
3.3.1 {332} Twin Stability 88
3.3.2 {332} Twin Growth 92
3.3.3 Composition-dependent {332} Twin Growth Mechanisms 95
3.4 Discussion 98
3.5 Conclusion 100
4 Energetic Model for Nucleation of Deformation Modes 103
4.1 Introduction 104
4.2 Materials and Methods 108
4.2.1 MD Simulations on Nucleation of Defects 108
4.2.2 Metadynamics for Phase Transformation Barriers 110
4.2.3 Calculations of Lattice Constants and Elastic Constants 111
4.2.4 Misfit Strain along Interfaces between Phase Boundaries 112
4.3 Results 113
4.3.1 MD Simulations on Deformation Modes 113
4.3.2 Experimental Observations of Deformation Modes 119
4.3.3 β Phase Stability and $\beta - \alpha$" Transformation Reversibility 122
4.3.4 Evaluations of Misfit Strain Energies during β-α" Transformation . 124
4.3.5 Twin Nucleation Metric 131
4.4 Discussion 136
4.5 Conclusion 142
5 Theoretical Prediction on Twin Nucleation Strength 144
5.1 Introduction 145
5.2 Methods 147
5.3 Results 147

5.3.1 Heterogeneous Nucleation Framework . . . 147
5.3.2 Metastability of Ti-Nb-Mo Ternary Alloys . . . 149
5.3.3 Macroscopic Yield Stress Prediction via Twin Nucleation Metric . . . 152
5.4 Discussion . . . 158
5.5 Conclusion . . . 162

6 Summary . . . 164

6.1 Remark . . . 164
6.1.1 Bridging Fundamental Mechanisms and Alloy Design . . . 164
6.1.2 Toward Physics-Based Alloy Design . . . 166
6.2 Conclusion . . . 169
6.3 Future Work . . . 171

Appendix A General Mathematical Solution for Invariant Plane Strain . . . 176

A.1 Deformation Gradient and Invariant Plane Condition . . . 176
A.2 Hermitian Form and Eigenvalue Decomposition . . . 176
A.3 Necessary Condition for IPS . . . 177
A.4 Recovery of the Shear Vector . . . 178
A.5 Rotation Correction and Physical Solutions . . . 178

Appendix B Stability and Growth Kinetics of {112} Twin . . . 180

B.1 DFT Relaxation . . . 180
B.2 $d_{[111]}$ Histogram for DFT Relaxed Supercells . . . 192
B.3 Thickness Measurement . . . 194
B.4 Shear Stress-Strain Curves for Twin Growth . . . 196
B.5 Twin Nucleation at Twist Grain Boundaries . . . 197
B.5.1 Grain boundary Set Up . . . 197
B.5.2 Shear Stress-Strain Curves for Twin Nucleation . . . 199
B.5.3 Twin Nucleation at Twist Grain Boundary . . . 200

Appendix C Energetic Model for Nucleation of Deformation Modes . . . 201

C.1 Structural Analysis on Metastable Phases during Deformations . . . 201
C.2 Misorientation Calculation of β Phases During Deformations . . . 202
C.3 Identifications on Barriers of β-α" Phase Transformations . . . 203
C.4 Calculations of Directional Elastic Moduli, Poisson's Ratio and Misfit Strain Energy Density . . . 204
C.5 Misfit Strain between β and α" Phase at Deformed State . . . 206
C.6 Atomic Structure of {112} and {332} Twin Boundary. . . . 212
C.7 β Grains Misorientation Plots under Loading. . . . 213
C.8 Atomic Structure of Deformation Modes and Structural Evolution . . . 215
C.9 Free Energy Landscape of Phase Space in Ti-Mo and Ti-Nb Systems . . . 223
C.10 Shear Components of β and α" Grains during Shear Loading. . . . 224
C.11 Elastic Constants and Elastic Moduli of Ti Alloys at 0 K. . . . 232
C.12 Competition of Δg_{twin} under Loading Conditions . . . 234

BIBLIOGRAPHY . . . 235

LIST OF FIGURES

FIGURE

1.1 Classification scheme of diffusionless(displacive) phase transformations in broad materials science. This diagram is adapted from [47]. Main phase transformation behaviors we investigated in this study are marked in red. 9

1.2 Illustrations of atomistic structures of metastable phases and possible diffusionless phase transformation behaviors in metastable Ti alloys. (a) Schematic draw for crystal structures of β (BCC like), α" (HCP-like in Orthorhombic) phases and the corresponding diffusionless transformation pathways. Red and Blue atoms are at A and B stacking of $\{011\}$ layers in BCC lattice, respectively. β can transfer to α" phase via shuffling between A and B layers along $[01\bar{1}]$ direction (accompanied by an essential deviatoric strain). (b) The schematic draw for β to ω phase diffusionless transformation. Pink, green, and yellow atoms are at A, B, and C stacking of $\{112\}$ layers in BCC lattice, respectively. β can transfer to ω phase via atomic shuffling two out of every three $\{112\}$ layers in opposite $\langle 111\rangle$ directions. 10

1.3 Schematic illustration of twinning elements in crystals. Adapted from [88]. . . 15

1.4 Simulation snapshots of early-stage twin nucleation and growth near a grain boundary. Grey atoms are at grain boundary while red atoms are in twin phase. 23

1.5 Schematic draw on the layer-by-layer growth mechanism of $\{112\}$ twin in conventional BCC alloys. In BCC lattice, atoms in $\{112\}$ planes follow ABCABC... stacking sequence along $\langle 112\rangle$ directions, different colors of atoms indicate different stacking planes. Balck dased lines indicate stacking fault created by dislocation dissociation on successive $\{112\}$ planes. Purple lines indicate the location of twin boundary while gray region redicates twin phase. 25

1.6 Schematic illustration of Free energy landscape exploration via Metadynamics. . 31

2.1 Illustrations of atomistic structures related to possible diffusionless phase transformation and twinning in BCC lattice. (a) Schematic draw for crystal structures of β (BCC), α' (HCP), α" (Orthorhombic) phases and the corresponding diffusionless transformation pathways. Brown and purple atoms are at A and B stacking of $\{01\bar{1}\}$ layers in BCC lattice, respectively. (b) The schematic draw for β to ω phase diffusionless transformation. Blue, orange, and magenta atoms are at A, B, and C stacking of $\{01\bar{1}\}$ layers in BCC lattice, respectively. Blue and rose atoms are at A and B stacking of (0001) layers in ω phase, respectively. (c) $\{112\}$ twin formation through a layer-by-layer twin dislocation slip mechanism. Grey shape indicates the $\{112\}$ twin region. Green and red atoms are in BCC lattice and at $\{112\}$ twin boundaries, respectively. Here a is the lattice constant and $b_{\text{tw}} = \frac{1}{6}\langle 111\rangle$ is the $\{112\}$ twin Burgers vector. 36

2.2 Schematic draw for 3-step construction of 3-layer $\{112\}$ twin embryo structures in 108-atom Ti_3Nb supercells. In the example, blue color represents Ti atoms and green color represents Nb atoms. The first step is to shift one atomic $(11\bar{2})$ plane along the $[11\bar{2}]$ direction periodically to generate a "new" supercell with the same SQS-optimized lattice occupations but different layer index numbers (an original Layer n becomes a new Layer $n+1$ (or Layer $n-17$ due to the periodic condition), where n is an integer from 1 to 18). Then we obtain 18 different twinned supercells. The second step is to generate an n-layer $\{112\}$ twin embryo in the middle of the supercell based on a layer-by-layer mechanism [198]. After the twin embryo generated, there is still one twin growth fault between the top and bottom layers on the boundary of the supercell along $[11\bar{2}]$ direction. So the third step is to change the supercell by tilting its $[11\bar{2}]$ axis along [111] direction by n twin Burgers vector (b_{tw}) to avoid the mismatch at the supercell boundary. 43

2.3 Illustrations of $\{112\}$ twin embryo structures in a 108-atom Ti_3Nb supercell ((a)-(h)) and quantitative analyses for β (BCC) to ω (hexagonal) phase transformation in DFT-relaxed supercell based on values of a structural descriptor((i)). (a), (c), (d), and (e) show a perfect 18-layer BCC matrix, 3-layer twin embryo, 6-layer twin embryo, and 9-layer twin embryo in unrelaxed structures, respectively; (b) and (f)-(h) are the corresponding DFT-relaxed structures. The coordination system is the same as Figure 2.1 (c). Numbers at the left side of (a) are the layer indexes for the atomic layer along the $[11\bar{2}]_\beta$ direction. Red lines in (c), (d), and (e) indicate the crystal orientations. Grey shapes in (c) to (h) indicate the $\{112\}$ twin embryo region. Blue and green atoms are Ti and Nb, respectively. (i) Explanations of the definition of a structural descriptor $d_{[111]}$ to distinguish between individual atoms in β phase and those in ω phase quantitatively. $d_{[111]}$ is the shortest distance projection along $[111]_\beta$ direction between one atom and its first-nearest neighbors of all the atoms in the supercell defined in (a). 44

2.4 Structural descriptor for ω phase identification. (a) is the scatter plot of P_1-P_2 vs VEC for Ti-Nb alloy. Here we employed method from Ikeda's work [95] to identify local athermal ω phases in bulk BCC supercell. P_1 and P_2 is the largest, and second largest projection along $\langle\ 111\ \rangle$ group directions, respectively. Statistically, when P_1-P_2 is less than 0.04, the supercells are in BCC phase while they are in ω phase when P_1-P_2 is greater than 0.04. (b) is the snapshot for a configuration of a 144-atom supercell used for investigating the composition region where β is thermodynamically (meta)stable. Here the supercell with basis vectors of $4[100]\times3[01\bar{1}]\times3[011]$ in the unit of conventional BCC lattice vectors. Blue atoms are Ti and green atoms are Nb. 46

2.5 Schematic illustration for a twin pathway through homogeneous displacement mechanism near an existing {112} twin boundary in a bicrystal structure. (a) is the bicrystal structure that contains a $(11\bar{2})$ twin boundary in the middle, viewing along $[\ 1\bar{1}0]$ direction. Atoms in green color have the same orientation as BCC twin in Figure 2.3 while atoms in light brown color have the same orientation as BCC matrix in Figure 2.3. The twin boundary between two $(11\bar{2})$ atomic planes is indicated by a red dashed line. White color atoms are on $(11\bar{2})$ atomic planes adjacent to the twin boundary. (b) is the bicrystal structure under a twinning pathway created by homogeneous displacements between different parts of the upper crystal. Atoms in the first $(11\bar{2})$ atomic layer adjacent to the twin boundary shift together by $\lambda \times \frac{1}{2}[111]]$ relative to the lower crystal. Atoms above the first $(11\bar{2})$ atomic layer adjacent to the twin boundary shift together by $2\lambda \times \frac{1}{2}[111]$ relative to the lower crystal. $\frac{1}{2}[111]$ is the full Burgers vector and λ ranges from 0 to 1 at the interval of 0.01. Atoms in grey shade regions are fixed during the energy minimization and the atoms out of the grey regions are only allowed to be relaxed in the Z direction normal to $(11\bar{2})$. 51

2.6 Twin boundary energy γ_{TB} defined in Equation 2.2 vs. the number of $(11\bar{2})$ layers of twin embryos for alloys with different VEC values. All cases were calculated by DFT using a supercell of 108 atoms plotted in Figure 2.3 (a). For each type of twin embryo structure at a given alloy composition, there are 18 possible cases to locate the twin embryo with different $(11\bar{2})$ layer indexes plotted in Figure 2.3 (a). So the "violin" plots of these 18 data points are used to illustrate the distribution and the mean value of γ_{TB} for each twin embryo structure at a given alloy composition. The detailed alloy compositions and the corresponding VEC values are shown at the top of each subfigure. 55

2.7 Histograms of $d_{[111]}$ values (normalized in the unit of the length of $\frac{1}{2}[111]_\beta$) for DFT-relaxed supercells of different alloy compositions and twin embryo structures. From left to right the subfigures in each row are for the perfect BCC matrix, 3-layer twin, 6-layer twin, and 9-layer twin embryo structure for a specific composition, respectively. (a)-(d) are for Ti_3Nb (VEC=4.25); (e)-(h) are for Ti_3Mo (VEC=4.5). 57

2.8 Configurations of {112} twin embryos in Ti-Nb alloys after MD simulations (200 ps and the NPT ensemble ($P = 0$ and $T = 300$ K)). Subfigures of each column from left to right are supercells that initially (before MD relaxations) have the perfect BCC lattice, 3-layer twin embryo, 6-layer twin embryo, and 9-layer twin embryo, respectively, in different alloys. Subfigures of each row are supercells for different alloys. (a)-(d): Unrelaxed supercells of all alloy cases before MD relaxations. (e)-(h): Relaxed Ti_3Nb supercells. (i)-(l): Relaxed Ti_2Nb supercells. (m)-(p): Relaxed TiNb supercells. (q)-(t): Relaxed pure Nb supercells. The light brown color represents the BCC matrix while the green color represents the BCC twin. Phase identification is conducted by Polyhedral template matching (PTM) [117]and phase variants identification (BCC matrix and BCC twin) is conducted by Grain segmentation method [19] in the current version of OVITO [183] 59

2.9 Atomistic structures of {112} twin boundaries from MD simulations and experiments. (a)–(c) Relaxed supercells containing stable twin embryos with the minimum number of atomic layers: (a) 9 layers for Ti_3Nb (VEC = 4.25), (b) 6 layers for Ti_2Nb (VEC = 4.33), and (c) 6 layers for TiNb (VEC = 4.5); brown and green atoms represent the BCC matrix and BCC twin, respectively.(d)–(f) Corresponding phase-identified snapshots of (a)–(c), where white and black atoms represent the β (BCC) and ω phases, respectively; red dashed lines mark twin boundaries aligned with the twinning plane and green dashed lines mark twin boundary steps, with thick boundary regions in (d) highlighted by both colors indicating ω phase formation.(g)–(h) Aberration-corrected HAADF-STEM images of the ω phase at a {112} twin boundary in 20% cold-rolled Ti-24Nb-4Zr-8Sn: (g) nanoscale ω layer at the twin boundary; (h) unit cells of hexagonal ω and BCC β phases.(i) Distribution of ω phase thicknesses at twin boundaries across different VEC values compiled from published data [132, 60, 111, 239, 215, 37, 205]; solid points indicate the length-weighted average thickness and error bars represent the weighted standard deviation. 62

2.10 Stress-strain curves and atomistic structure changes when constant shear loading is applied to supercells that contain stable twin embryos with the minimum {112}-layer thickness for different Ti alloys. Inserted graphs in each subfigure are the snapshots at the initial state and the final state of the shear process. (a) Ti_3Nb starting from a relaxed 9-layer twin embryo. (b) Ti_2Nb starting from a relaxed 6-layer twin embryo. (c) TiNb starting from a relaxed 6-layer twin embryo. (d) Pure Nb starting from a relaxed 3-layer twin embryo. Atoms marked in light brown color in the inserted figures are in the BCC matrix while atoms marked in green color in the inserted figures are in the BCC twin. The orange solid lines in the inserted figures indicate the crystal orientations of the BCC phase. 65

2.11 Evolution of atomistic structures during the shrinkage of the twin embryo in Ti_3Nb under the increasing shear strain along the twinning direction. (a) shows the snapshots of the twin region (green color) at/near some critical points of this detwinning process during the MD simulations. (b)-(f) are schematic illustrations for the whole process of the initial twinning from a perfect single crystal and the later detwinning process in Ti_3Nb assisted by reversible β (BCC twin variant) to α'/α" phase to β (BCC matrix variant) phase transformation. Here BCC matrix is in light brown color, α'/α" phase is in purple color, and BCC twin is in green color. During the twinning and detwinning process, atomic displacements by slip are marked in dark brown arrows, while atomic displacements by shuffle are marked in blue arrows. The magnitudes of atomic displacements shown in (c)-(f) are calculated in reference to the initial state of the perfect crystal in (b). The label index of each atomic layer along $[11\bar{2}]$ direction is shown on the left side of (b) and the right side of (f). Here one twin Burgers vector $b_{\text{tw}} = \frac{1}{6}[111]$. . 67

2.12 The energy profiles of 2-layer twin growth faults induced by $\lambda \times \frac{1}{2}[111]$ homogeneous displacements (described by Section 2.2.5) in Ti-Nb alloys and pure Nb. (a) shows the structure snapshots at some critical stages during the 2-layer stacking twin growth faults generation process in pure Nb. Stage A is the initial state before twin growth faults generation (λ=0). Stage B, C, and D are at the transition state of the first energy barrier, the local energy minimum, and the transition state of the second energy barrier of the twin growth fault energy profile, respectively. Stage E is the state when the displacement fault magnitude equals one full Burgers vector (λ=1). (b) shows the plots of the energy profile of 2-layer twin growth faults for different Ti-Nb alloys and pure Nb as a function of $\lambda \times \frac{1}{2}[111]$ displacements. The star symbols in the plots mark the Stage D location of energy barriers for anti-twinning ($\gamma^{\text{AT}}_{\text{TGF}}$), while the hexagon symbols indicate the Stage B location of energy barriers for twinning ($\gamma^{\text{TW}}_{\text{TGF}}$). The inserted table shows the value of $\gamma^{\text{AT}}_{\text{TGF}}/\gamma^{\text{TW}}_{\text{TGF}}$ in metal/alloys with different compositions. 72

2.13 Shear stress-strain curves for 9-layer twin embryo for different compositions under different temperatures. (a)-(d) are all for Ti_3Nb but at different temperatures. (d)-(h) are all at 300K but at different compositions. (i)-(l) are the snapshots for $Ti_{0.74}Nb_{0.26}$ during deformation viewed from the shear direction [111]. The red rectangle in the (i)-(l) represents the twin boundary of the stable twin embryo before applying the shear loading. Light brown color in (i)-(l) represents BCC matrix, purple color represents α'/α" phase, and green color is for BCC twin. The phase identification is completed by Polyhedral template matching (PTM) [117]and Grain segmentation method [19]. 74

2.14 Schematic draw of the free energy landscape variations for the homogeneous diffusionless transformations to indicate the variation of twin boundary migration kinetics. In each subfigure, solid curves represent the BCC matrix and BCC twin (left and right), respectively; the dashed curve in the middle is for the ω phase. The color bar for the free energy landscape curves is shown on the right of the figure. Darker red is for lower VEC Ti alloys while lighter red is for higher VEC Ti alloys. ΔG_a in the plots represents the energy barrier of BCC matrix $\rightarrow \omega$ phase transformation and ΔG_b represents the energy barrier of ω phase $\rightarrow$ BCC twin transformation. Since ΔG_b in (a) is very small, we do not mark it there. . 77

3.1 Stability analysis of pre-inserted {332} twin embryos in Ti–Nb alloys at 300 K. The columns show initial twin thicknesses of 5, 11, 17, and 22 atomic layers. The first row shows the unrelaxed configurations, in which the BCC twin embryo is embedded in the BCC matrix. The following rows show the relaxed structures for Ti_3Nb, Ti_2Nb, and TiNb, corresponding to VEC values of 4.25, 4.33, and 4.50, respectively. Beige atoms indicate the BCC matrix, green atoms indicate the BCC twin, and purple atoms indicate the spontaneous transferred α'/α'' phase. The relaxation results reveal a strong dependence of {332} twin stability on composition and embryo thickness. Thin twin embryos are unstable and tend to disappear during relaxation, whereas thicker embryos can be retained and are accompanied by local α'/α'' transformation near the twin interface. This behavior suggests that the stability of {332} twins in metastable Ti–Nb alloys is closely coupled to local martensitic transformation and depends on both alloy composition and twin embryo size. 89

3.2 Stability analysis of pre-inserted {332} twin embryos in Ti–Mo alloys at 300 K. The columns show initial twin thicknesses of 11, 17, and 22 atomic layers. The first row shows the unrelaxed configurations, in which the BCC twin embryo is embedded in the BCC matrix. The following rows show the relaxed structures for Ti–12Mo (wt.%), Ti–66.7Mo (wt.%), and Pure Mo, corresponding to VEC values of 4.13, 5, and 6, respectively. Beige atoms indicate the BCC matrix, green atoms indicate the BCC twin, and purple atoms indicate the spontaneous transferred α'/α'' phase. 91

3.3 Shear stress–strain curves for {332} twin-boundary migration in Ti–Nb bicrystal models under engineering strain rate of 1×10^7 s^{-1}. The columns correspond to Nb contents of 25, 33, and 50 at.%, respectively. The rows correspond to temperatures of 600, 300, and 20 K, respectively. Orange, olive, and purple curves denote simulations at 600, 300, and 20 K, respectively. The vertical axis shows the shear stress in MPa, and the horizontal axis shows the imposed shear strain γ. 92

3.4 Shear stress–strain curves for {332} twin-boundary migration in Ti–Mo bicrystal models under engineering strain rate of 1×10^8 s^{-1}. The columns correspond to Mo contents of 10, 12, 15, 25 wt.% and pure Mo, respectively. The rows correspond to temperatures of 500, 400, 300, and 200 K, respectively. Orange, blue, olive, and purple curves denote simulations at 500, 400, 300, and 200 K, respectively. The vertical axis shows the shear stress in MPa, and the horizontal axis shows the imposed shear strain γ. 93

3.5 Atomic displacement analysis during {332} twin growth in Ti–Nb alloys at 300 K. Panels (A)–(C) show the Ti_3Nb system, and panels (D)–(F) show the TiNb system. Panels (B) and (E) show atomic configurations before and after shear deformation, with the initial states at $\gamma = 0$ and the deformed states at $\gamma = 0.0077$ for Ti_3Nb and $\gamma = 0.00726$ for TiNb. The viewing directions are indicated by the in-plane axes $X = [113]$ and $Z = [\bar{3}\bar{3}2]$. Blue horizontal lines mark the analyzed twin region. Panels (A) and (D) plot the displacement magnitude along the X direction as a function of atomic coordinate along the Z direction. Panels (C) and (F) plot the displacement magnitude along the Z direction as a function of atomic coordinate along the Z direction. Layer labels L1–L12 for Ti_3Nb and L1–L10 for TiNb identify the atomic layers within the analyzed twin region. The displacement is normalized by the average atomic layer distance along each direction. 97

4.1 **Coexistence of {112} twin and {332} twin in 5% cold-rolled Ti2448 (Ti-24Nb-4Zr-8Sn) sample. A** is the TEM figure illustrating morphology of {112} twin and {332} twin, red circle mark the boundary of {332} twin, and orange circle mark the boundary of secondary {112} twin located inside the {332} twin region. **B-C** are the diffraction patterns at the boundary of{112} twin and {332} twin. **D-E** are schematic draws for the {112} twin boundary and {332} twin boundary.**F** show an example of formation of BCC twin phase via reversible β-α" phase transformations. 106

4.2 **Atomistic structural evolution and deformation modes of Ti-Nb alloys under varying temperature, composition, and stress/strain conditions by MD simulations. In all cases, the shear loading is along [311] direction on ($\bar{2}$33) planes.** Temperature, composition and stress/strain conditions are fixed in each row: **(A-C)** is Ti_5Nb under 77 K, non-confined simple shear condition; **(D-F)** is Ti_5Nb under 77 K, confined simple shear condition; **(G-I)** is Ti_4Nb under 300 K, non-confined simple shear condition; **(J-L)** is Ti_2Nb under 300 K, non-confined simple shear condition. From top to down, **(A,D,G,J)** are snapshots of atomistic structures before loading applied; **(B,E,H,K)** are snapshots of atomistic structures when applied shear strain is 0.12 and different deformation modes produced; **(C,F,I,L)** illustrate nucleation of different metastable phases during shear loading and dynamic volume fraction change. Color interpretation of atoms in the MD snapshots locating at the top of the figure. dominant deformation mode of each row is different: **(A-C)** is α" martensite; **(D-F)** is {332} twin; **(G-I)** is {112} twin and **(J-L)** is dislocation slip. 115

4.3 **Schematic illustration of temperature- and composition-dependent deformation mechanisms in metastable β Ti alloys.** The background color qualitatively represents the stability of the β phase, increasing from lower left (sand color) to upper right (sea blue color). The corresponding deformation modes are consistent with Table 4.1. Colors of data points represent different dominate deformation modes: red is TRIP; orange is {112} twin; light green is {332} twin and bright green is dislocation. Shape of data points represent different loading condition: circle is NSS and rectangle is CSS. The transition between mechanisms is strongly temperature, chemical composition and loading condition-dependent, highlighting the competition between nucleation-controlled deformation modes in metastable alloys. 118

4.4 **Temperature and composition conditions for {332} twin nucleation for Ti-Nb alloys in experiments [83, 82, 220, 226, 177, 38, 125, 231, 77, 219, 75, 227, 12].** In **A**, data points marked in pink rectangle (Nb concentration is less than 24 wt%) indicates that dominant deformation mode is α" martensite and {332} twin. {332} twin (and small volume of {112} twin) can form insensitive to temperature and loading condition when Nb concentration is between 25 wt% and 36 wt% (data points in light green circle). {332} twin can form by carefully controlling loading condition under cryogenic temperatures (Nb concentration is between 36 wt% and 47 wt%). Within this region, {112} twin and slip can also form and compete with {332} twin nucleation. When Nb concentration is larger than 47 wt%, shown in purple region, {332} twin can not form in any condition and dislocation slip is the dominant deformation mode. As for alloys that marked with "*", Nb is the dominant β stabilizer element in the composition but the alloy is not binary, they also include small amount of neutral elements and oxygen in addition. In **B**, we also present the predicted deformation modes of samples in **A** by $\overline{\text{Bo}} - \overline{\text{Md}}$ diagram. The definition of colors of data points in **B** are consistently based on the deformation modes observed in experiments in **A**.The experimental-fitted boundaries for different deformation modes are from Morinaga [146]. Clearly, compared to experimental observations of deformation modes in the samples shown in **A**, there are large deviation compared to $\overline{\text{Bo}} - \overline{\text{Md}}$ prediction, especially those marked in red rectangles. 120

4.5 β-α" **energy landscape for Ti alloys, including unstable BCC Ti-alloy (α-Ti alloys), metastable BCC Ti-alloys and stable BCC Ti-alloy.** Here we choose two collective variables: shuffle magnitude between (011) planes along $[0\bar{1}1]$ directions and "b/a" ratios ("b" is the length of $\langle 0\bar{1}1\rangle$ in BCC and "a" is the length of $\langle 100\rangle$ in BCC phase). Positions of BCC and α"/α phase are marked in the figure. **A** is for Ti_5Nb at 77 K. **B** is Ti_5Nb at 300 K and **C** is Ti_4Nb at 300 K. **D** is the case of stable BCC Ti-alloys, which we can only observe one global minima at BCC phase and no local minima for α" phase. The corresponding transformation barriers and $P_{\text{chem}}^{\beta\leftrightarrow\alpha''}$ are label in the sub figures. . 123

4.6 **Facted interfaces of BCC and nucleated α" phase before nucleation of different deformation modes. (A)** is illustration on the all conventional coherent $\beta\|\alpha$" interfaces (marked in orange and blue) consistent with the BOR and defined by {211} planes with in-plane $\langle\bar{1}11\rangle$ directions, lying in the [311]–[$\bar{2}$33] zone. We also mark the ($\bar{2}$33) plane along [311] direction (green line) that closely align to the {332} twin boundary formed under shear loading. The coordinate system in **(A)** is consistent with that of initial state of simulation box in **(B-H)**. **(B)** is the snapshot when the system close to the stage of α" phase nucleation saturation. Corresponding setting is consistent with the case in Figure 4.2 (A-D). **(C-D)** are snapshots of critical stage of {112} twin nucleation in the case of Figure 4.2 (I-L). **(E-H)** are the snapshots of {332} twin nucleation process in the case of Figure 4.2 (E-H). Here we want to present how the interfaces of $\beta\|\alpha$" (bottom of the figures) tilt from blue lines to green lines that closely align with {332} twinning plane. Definitions on the colors of atoms are consistent with the definition in Figure 4.2. Lines in **(B-H)** mark some facted interfaces between BCC and nucleated α" phase. Lines with the same color as **A)** correspond to closely related orientation. 126

4.7 **Schematic draw on BCC-to-α" phase transformation and two BCC-α" interphase boundary align with twinning plane. A** illustrate BCC-α" phase transformation pathway by shuffling ($0\bar{1}1$) planes along [011] direction. Color of atoms indicating ABAB stacking. In addition to shuffle, the lattice also undergo lateral strain along [100] directions during transformation. To simplify illustration, we do not draw here. α" phase is similar to HCP phase, and the real atomic structure of α" phase varies with different metastable alloys under different temperature, we draw perfect HCP here as an example. **B** and **D** are two theoretical calculated BCC-α" interphase boundaries align with twinning planes during BCC-α" phase transformation. Orange and green arrows indicate the directions that parallel to the interface. **C** and **E** illustrate two types of BCC twin boundary structure after α" phase transfering back to BCC phases under shear along the directions marked in blue arrows. **A-B-C** is the pathway for {112} twin formation by BCC-to-α" phase reversible phase transformation and **A-D-E** is the pathway for {332} twin formation by BCC-to-α" phase reversible phase transformation. In real cases (both in MD and experiments), there are phase transformation behaviors along twin boundaries. Since we here is to illustrate structural relationships of α", twin and matrix, we do not draw the real twin boundary structure. The illustrations and snapshots of twin boundaries are in Section S2.1 of the Appendix C. 129

4.8 **Dynamic change of twin nucleation metric, $\Delta g^*_{\mathbf{twin}}$ under different stress/strain conditions for different alloy systems.** In all cases, the volume of nucleated α" phase saturates when applied shear strain is around 0.1. And twins starts to nucleate right after. The orange curves represent $\Delta g^*_{\{112\}\text{twin}}$ under loading conditions while the green curves correspond to $\Delta g^*_{\{332\}\text{twin}}$ under loading conditions. The alloy composition, temperature and loading type are at top of each subfigure. In each subfigure, we compare the magnitude of $\Delta g^*_{\{112\}\text{twin}}$ and $\Delta g^*_{\{332\}\text{twin}}$ at critical stage (external shear strain is 0.1,marked in light blue lines). Meanwhile, we mark the MD observations on the type of twin about to nucleate. All the snapshots of final deformed simulation box are in Section S2.3 of the Appendix C. 134

4.9 **A step-by-step workflow to calculate energetic parameters to distinguish deformation modes in metastable BCC alloys.** 137

4.10 **A conceptual flowchart for criteria of deformation modes selection in metastable β-Ti alloys.** 139

5.1 **Composition-dependent map of metastability in the Ti-Mo-Nb system at 77 K (A) and 300 K (B).** The color bar represents the difference in misfit strain energy density between twinning modes, $W^{\text{misfit}}_{\{332\}\text{twin}}$ - $W^{\text{misfit}}_{\{112\}\text{twin}}$ (meV/atom), where negative values (blue) indicate preference for {332} twinning and positive values (red) favor {112} twinning. Grey and yellow regions have no metastable phases and only one phase exists. Grey regions correspond to compositions where the β phase is unstable and only α'/α'' exist, while light-yellow regions indicate stable β (BCC) where α'/α'' is unstable. The dashed purple line marks a compositional pathway along which all alloys remain metastable in both temperature with respect to the $\beta \rightarrow \alpha'/\alpha''$ transformation. Compositions along this metastable pathway are selected for subsequent analysis to evaluate the predicted yield stress based on competing twinning modes. 151

5.2 **A conceptual flowchart for criteria of deformation modes selection in metastable β-Ti alloys.** 155

5.3 **Comparison of critical stress for {112} and {332} twinning modes as a function of Nb concentration at 77 K and 300 K for $\mathbf{Ti}_{92-0.6x}$-$\mathbf{Mo}_{8-0.4x}$-$\mathbf{Nb}_x$ alloy system.**Figure 5.3 (A) and (B) shows the predict critical stress for {112} and {332} twinning modes. Orange solid line with circle markers represent $\sigma^{\{112\}\text{Twin}}_{\text{crit}}$ while green solid line with square markers represent $\sigma^{\{332\}\text{Twin}}_{\text{crit}}$. Star markers represent experimental measured yield strength. Dominant twinning mode for green star markers are {332} twin while dominant twinning mode for orange star markers are {112} twin (mix with TRIP). Figure 5.3 (C) and (D) show the decomposition of $\sigma^{\text{Twin}}_{\text{crit}}$. Orange dashed line with circle markers represent $\sigma^{\{112\}\text{Twin}}_{\text{misfit}}$ while green dashed line with square markers represent $\sigma^{\{332\}\text{Twin}}_{\text{misfit}}$. Gray solid line with triangle markers represent $\sigma^{\text{Twin}}_{\text{chem}}$. Nb concentration uniquely defines the alloy composition (with Mo varying linearly and therefore not shown explicitly). [101, 77, 234, 141, 208, 224, 83, 141, 70, 1] 157

5.4 **Schematic framework and validation of the twin nucleation-based yield stress model for TWIP dominant metastable β Ti alloys. The model modified the Equation 5.4 and introduces an effective twinning strain to link the twin nucleation barrier with a measurable stress scale.**(A) is a schematic illustration of the twin nucleation pathway in terms of critical stress as a function of shear strain. The process evolves from the initial state (IS, β matrix) to the final state (FS, β twin) through a transition state (TS, α" phase). Before TS, α" phase have not formed, essential step for twin nucleation is not satisfied and so it is dashed line. Twin can form only after TS. The effective shear strain at the transition state is approximated as $\gamma_{\text{TS}} \approx \frac{1}{2}\gamma_{\text{twin}}$, while $\gamma_{\text{FS}} = \gamma_{\text{twin}}$, defined in Equation 5.4. (B) is comparison between the calculated effective yield stress obtained from twinning nucleation model and the experimental yield stress for metastable Ti-based alloys. The high coefficient of determination ($R^2 = 0.947$) indicates strong agreement. [101, 77, 234, 141, 208, 224, 83, 141, 70, 1] 158

6.1 Illustrations on overall summary of this thesis. Left part is the main contents for the thesis. Right part is the overall objectives. In brief, it is to make quantitative connections between thermomechanical conditions-deformation modes-mechanical properties. 165

B.1 Snapshots for unrelaxed and DFT fully relaxed atomic structures of 3-layer twin embryo in Ti_3Nb. Blue color is for Ti atoms, green color is for Nb atoms and region between two dark purple lines indicated the initial location of twin boundaries. 180

B.2 Snapshots for unrelaxed and DFT fully relaxed atomic structures of 3-layer twin embryo in Ti_3Nb. Blue color is for Ti atoms, green color is for Nb atoms and region between two dark purple lines indicated the initial location of twin boundaries. 181

B.3 Snapshots for unrelaxed and DFT fully relaxed atomic structures of 6-layer twin embryo in Ti_3Nb. Blue color is for Ti atoms, green color is for Nb atoms and region between two dark purple lines indicated the initial location of twin boundaries. 182

B.4 Snapshots for unrelaxed and DFT fully relaxed atomic structures of 6-layer twin embryo in Ti_3Nb. Blue color is for Ti atoms, green color is for Nb atoms and region between two dark purple lines indicated the initial location of twin boundaries. 183

B.5 Snapshots for unrelaxed and DFT fully relaxed atomic structures of 9-layer twin embryo in Ti_3Nb. Blue color is for Ti atoms, green color is for Nb atoms and region between two dark purple lines indicated the initial location of twin boundaries. 184

B.6 Snapshots for unrelaxed and DFT fully relaxed atomic structures of 9-layer twin embryo in Ti_3Nb. Blue color is for Ti atoms, green color is for Nb atoms and region between two dark purple lines indicated the initial location of twin boundaries. 185

B.7 Snapshots for unrelaxed and DFT fully relaxed atomic structures of 3-layer twin embryo in Ti_3Mo. Blue color is for Ti atoms, purple color is for Mo atoms and region between two dark purple lines indicated the initial location of twin boundaries. 186
B.8 Snapshots for unrelaxed and DFT fully relaxed atomic structures of 3-layer twin embryo in Ti_3Mo. Blue color is for Ti atoms, purple color is for Mo atoms and region between two dark purple lines indicated the initial location of twin boundaries. 187
B.9 Snapshots for unrelaxed and DFT fully relaxed atomic structures of 6-layer twin embryo in Ti_3Mo. Blue color is for Ti atoms, purple color is for Mo atoms and region between two dark purple lines indicated the initial location of twin boundaries. 188
B.10 Snapshots for unrelaxed and DFT fully relaxed atomic structures of 6-layer twin embryo in Ti_3Mo. Blue color is for Ti atoms, purple color is for Mo atoms and region between two dark purple lines indicated the initial location of twin boundaries. 189
B.11 Snapshots for unrelaxed and DFT fully relaxed atomic structures of 9-layer twin embryo in Ti_3Mo. Blue color is for Ti atoms, purple color is for Mo atoms and region between two dark purple lines indicated the initial location of twin boundaries. 190
B.12 Snapshots for unrelaxed and DFT fully relaxed atomic structures of 9-layer twin embryo in Ti_3Mo. Blue color is for Ti atoms, purple color is for Mo atoms and region between two dark purple lines indicated the initial location of twin boundaries. 191
B.13 Histograms of $d_{[111]}$ values (normalized in the unit of the length of $\frac{1}{2}[111]_\beta$) for DFT-relaxed supercells of different alloy compositions and twin embryo structures. From left to right the subfigures of upper row are for the perfect BCC matrix, 3-layer twin, 6-layer twin, and 9-layer twin embryo structure for Ti_3V (VEC=4.25), respectively. The subfigures at the lower row are histograms of $d_{[111]}$ values for corresponding twin embryo strictures for Ti_2Nb (VEC=4.33). . 192
B.14 Histograms of $d_{[111]}$ values (normalized in the unit of the length of $\frac{1}{2}[111]_\beta$) for DFT-relaxed supercells of different alloy compositions and twin embryo structures. From left to right the subfigures of upper row are for the perfect BCC matrix, 3-layer twin, 6-layer twin, and 9-layer twin embryo structure for Ti_4NbV (VEC=4.33), respectively. The subfigures at the lower row are histograms of $d_{[111]}$ values for corresponding twin embryo strictures for Ti_4NbMo (VEC=4.5). 193
B.15 Illustration of method to measure statistical results of ω phase thickness on $\{112\}$ twin boundaries in β-Ti alloys. The aberration-corrected high-angle annular dark field scanning transmission electron microscopy (HAADF-STEM) imaging showing the hexagonal ω phase formed at $\{112\}$ deformation twin boundary in the 20% cold-rolled Ti-24Nb-4Zr-8Sn alloy. This is also presented in the main text. 194
B.16 Shear stress-strain curves for 9-layer twin embryo for different compositions. Engineering shear strain rate is 4×10^8 s^{-1} along [111] direction on $(11\bar{2})$ planes at 300 K. 196

B.17 Schematic draw of Σ 9 ⟨111⟩ twist grain boundary. Purple and yellow matrix indicate two grains in different orientations. Grain 2 is generated by clockwise rotating Grain 1 along $[1\bar{1}0]$ axis by 38.94°. The corresponding front views along $[1\bar{1}0]$ are shown in the dotted purple and yellow rectangles, respectively. Green planes indicate the location of grain boundaries, and the simulation box is periodic along shared $[1\bar{1}0]$ direction. 198
B.18 Schematic illustration of shear deformation on different cases and the corresponding shear stress-strain curves. (a) and (b) is shear deformation setup for 120000-atoms supercells without grain boundaries, (c) is shear deformation setup for the 120000-atoms supercell containing grain boundaries. Orange arrows indicate the direction of shear stress applied. (d)-(f) shows the shear stress-strain curves for (a), (b) and (c), respectively. The engineering shear strain rate is 10^8/s and the deformation process is operated at constant 300K. 199
B.19 Twin nucleation dynamics in Ti_3Nb (VEC=4.25) containing grain boundaries under uniform shear along anti-twinning direction. (a)-(f) are snapshots of both side views (along [111] direction) of some critical states and cross-section views of twin nucleic, corresponding shear strain γ is 0.0968, 0.0976, 0.0988, 0.1048, 0.1052 and 0.1056, respectively. Color coding for atoms in all subfigures are based on phases of atoms are in, which is identified by Common Neighbor Analysis (CNA)in OVITO [183, 91, 59]. Atoms in blue are in BCC phase, atoms in red are in HCP (α'/α" phase). Atoms in white color is unrecognized in CNA. Since atoms at grain boundaries can not identify the phase and CNA method can not identify ω phase and so those atoms are classfied as "Other" in CNA. Here we treat "Other" atoms as those at grain boundaries and in ω phase. Light blue dashed lines in (a)-(f) mark the location for cross-section cutting. 200

C.1 **Atomic structure of {112} twin and {332} twin boundary**.**A** is snapshot of an example of {332} twin, which is Ti_5Nb at 77 K under "Confined Simple Shear" condition, and the current applied shear strain is 0.12. Shear direction is along [311] direction on $(\bar{2}33)$ planes. **B** is an enlarged figure showing atomic structure of {332} twin boundary. We can observe α" phase at the twin boundary. **C** is snapshot of an example of {112} twin, which is Ti_4Nb at 300 K under "Non-confined Simple Shear" condition, and the current applied shear strain is 0.12. Shear direction is along [311] direction on $(\bar{2}33)$ planes. **C** is an enlarged figure showing atomic structure of {112} twin boundary, more precisely, twin tip. We can observe ω phase surrounding the tip. 212
C.2 **Misorientation of β grains along $[0\bar{1}1]$ directions under loading conditions.** Heatmap on data points is based on corresponding volume fraction of total β grains at the certatin strain state. **A** is Ti_5Nb at 77 K, under non-confined simple shear condition, dominant deformation mode is α" martensite with small amount of {112} twin; **B** is Ti_5Nb at 77 K, under confined simple shear condition, dominant deformation mode is {332} twin; **C** is Ti_4Nb at 300 K, under non-confined simple shear condition, dominant deformation mode is {112} twin; **D** is Ti_2Nb at 300 K, under non-confined simple shear condition, dominant deformation mode is dislocation slip. 214

C.3 **Atomistic structural evolution and deformation modes of Ti_5Nb alloys under 300 K and "Confined simple shear" loading condition by MD simulations. In all cases, the shear loading is along [311] direction on ($\bar{2}$33) planes. (A)** are snapshots of atomistic structures when applied shear strain is 0.12 and dominant deformation mode is {332} twin; **(B)** illustrate how parent β phase evolve during deformation and how new β variants forms and confirm the twin relationship relative to parent phase; **(C)** illustrate nucleation of different metastable phases during shear loading and dynamic volume fraction change. Color interpretation of atoms in the MD snapshots locating at the top of the figure. 215

C.4 **Atomistic structural evolution and deformation modes of Ti_5Nb alloys under 300 K and "Non-confined Simple Shear" loading condition by MD simulations. In all cases, the shear loading is along [311] direction on ($\bar{2}$33) planes. (A)** are snapshots of atomistic structures when applied shear strain is 0.12 and dominant deformation mode is {112} twin and α" martensite; **(B)** illustrate how parent β phase evolve during deformation and how new β variants forms and confirm the twin relationship relative to parent phase; **(C)** illustrate nucleation of different metastable phases during shear loading and dynamic volume fraction change. Color interpretation of atoms in the MD snapshots locating at the top of the figure. 216

C.5 **Atomistic structural evolution and deformation modes of Ti_4Nb alloys under 77 K and "Confined simple shear" loading condition by MD simulations. In all cases, the shear loading is along [311] direction on ($\bar{2}$33) planes. (A)** are snapshots of atomistic structures when applied shear strain is 0.12 and dominant deformation mode is {332} twin; **(B)** illustrate how parent β phase evolve during deformation and how new β variants forms and confirm the twin relationship relative to parent phase; **(C)** illustrate nucleation of different metastable phases during shear loading and dynamic volume fraction change. Color interpretation of atoms in the MD snapshots locating at the top of the figure. 217

C.6 **Atomistic structural evolution and deformation modes of Ti_4Nb alloys under 77 K and "Non-confined Simple Shear" loading condition by MD simulations. In all cases, the shear loading is along [311] direction on ($\bar{2}$33) planes. (A)** are snapshots of atomistic structures when applied shear strain is 0.12 and dominant deformation mode is {112} twin and α" martensite; **(B)** illustrate how parent β phase evolve during deformation and how new β variants forms and confirm the twin relationship relative to parent phase; **(C)** illustrate nucleation of different metastable phases during shear loading and dynamic volume fraction change. Color interpretation of atoms in the MD snapshots locating at the top of the figure. 218

C.7 **Atomistic structural evolution and deformation modes of Ti_4Nb alloys under 300 K and "Confined simple shear" loading condition by MD simulations. In all cases, the shear loading is along [311] direction on ($\bar{2}$33) planes.** **(A)** are snapshots of atomistic structures when applied shear strain is 0.12 and dominant deformation mode is {112} twin; **(B)** illustrate how parent β phase evolve during deformation and how new β variants forms and confirm the twin relationship relative to parent phase; **(C)** illustrate nucleation of different metastable phases during shear loading and dynamic volume fraction change. Color interpretation of atoms in the MD snapshots locating at the top of the figure. 219

C.8 **Atomistic structural evolution and deformation modes of Ti_2Nb alloys under 77 K and "Confined simple shear" loading condition by MD simulations. In all cases, the shear loading is along [311] direction on ($\bar{2}$33) planes.** **(A)** are snapshots of atomistic structures when applied shear strain is 0.12 and dominant deformation mode is dislocation slip; **(B)** illustrate how parent β phase evolve during deformation and how new β variants forms and confirm the twin relationship relative to parent phase; **(C)** illustrate nucleation of different metastable phases during shear loading and dynamic volume fraction change. Color interpretation of atoms in the MD snapshots locating at the top of the figure. 220

C.9 **Atomistic structural evolution and deformation modes of Ti_2Nb alloys under 77 K and "Non-confined Simple Shear" loading condition by MD simulations. In all cases, the shear loading is along [311] direction on ($\bar{2}$33) planes.** **(A)** are snapshots of atomistic structures when applied shear strain is 0.12 and dominant deformation mode is {112} twin and dislocation slip; **(B)** illustrate how parent β phase evolve during deformation and how new β variants forms and confirm the twin relationship relative to parent phase; **(C)** illustrate nucleation of different metastable phases during shear loading and dynamic volume fraction change. Color interpretation of atoms in the MD snapshots locating at the top of the figure. 221

C.10 **Atomistic structural evolution and deformation modes of Ti_2Nb alloys under 300 K and "Confined simple shear" loading condition by MD simulations. In all cases, the shear loading is along [311] direction on ($\bar{2}$33) planes.** **(A)** are snapshots of atomistic structures when applied shear strain is 0.12 and dominant deformation mode is dislocation slip; **(B)** illustrate how parent β phase evolve during deformation and how new β variants forms and confirm the twin relationship relative to parent phase; **(C)** illustrate nucleation of different metastable phases during shear loading and dynamic volume fraction change. Color interpretation of atoms in the MD snapshots locating at the top of the figure. 222

C.11 **β-α" free energy landscape of varies Ti-Nb and Ti-Mo alloy systems at different temperatures. Here we choose two collective variables: shuffle magnitude between (011) planes along $[0\bar{1}1]$ directions and "b/a" ratios ("b" is the length of $\langle 0\bar{1}1\rangle$ in β and "a" is the length of $\langle 100\rangle$ in β phase). Positions of β and α" phase are marked in the figure. (A)** is Ti_4Nb at 77 K. **(B)** is Ti-10Mo (wt.%) at 300 K. 223
C.12 **Shear components of β and α" grains at high shear loading state that close to defects nucleation state.** Here, X is along $[100]_\beta$, Y is along $[011]_\beta$ and Z is along $[0\bar{1}1]_\beta$. **(A)** is β grain in Ti_5Nb at 77 K, under "Confined simple shear" loading condition and **(B)** is α" phase in Ti_5Nb at 77 K, under "Confined simple shear" loading condition. 224
C.13 **Shear components of β and α" grains at high shear loading state that close to defects nucleation state.** Here, X is along $[100]_\beta$, Y is along $[011]_\beta$ and Z is along $[0\bar{1}1]_\beta$. **(A)** is β grain in Ti_5Nb at 77 K, under "Non-confined Simple Shear" loading condition and **(B)** is α" phase in Ti_5Nb at 77 K, under "Non-confined Simple Shear" loading condition. 225
C.14 **Shear components of β and α" grains at high shear loading state that close to defects nucleation state.** Here, X is along $[100]_\beta$, Y is along $[011]_\beta$ and Z is along $[0\bar{1}1]_\beta$. **(A)** is β grain in Ti_5Nb at 300 K, under "Confined simple shear" loading condition and **(B)** is α" phase in Ti_5Nb at 300 K, under "Confined simple shear" loading condition. 226
C.15 **Shear components of β and α" grains at high shear loading state that close to defects nucleation state.** Here, X is along $[100]_\beta$, Y is along $[011]_\beta$ and Z is along $[0\bar{1}1]_\beta$. **(A)** is β grain in Ti_5Nb at 300 K, under "Non-confined Simple Shear" loading condition and **(B)** is α" phase in Ti_5Nb at 300 K, under "Non-confined Simple Shear" loading condition. 227
C.16 **Shear components of β and α" grains at high shear loading state that close to defects nucleation state.** Here, X is along $[100]_\beta$, Y is along $[011]_\beta$ and Z is along $[0\bar{1}1]_\beta$. **(A)** is β grain in Ti_4Nb at 77 K, under "Confined simple shear" loading condition and **(B)** is α" phase in Ti_4Nb at 77 K, under "Confined simple shear" loading condition. 228
C.17 **Shear components of β and α" grains at high shear loading state that close to defects nucleation state.** Here, X is along $[100]_\beta$, Y is along $[011]_\beta$ and Z is along $[0\bar{1}1]_\beta$. **(A)** is β grain in Ti_4Nb at 77 K, under "Non-confined Simple Shear" loading condition and **(B)** is α" phase in Ti_4Nb at 77 K, under "Non-confined Simple Shear" loading condition. 229
C.18 **Shear components of β and α" grains at high shear loading state that close to defects nucleation state.** Here, X is along $[100]_\beta$, Y is along $[011]_\beta$ and Z is along $[0\bar{1}1]_\beta$. **(A)** is β grain in Ti_4Nb at 300 K, under "Confined simple shear" loading condition and **(B)** is α" phase in Ti_4Nb at 300 K, under "Confined simple shear" loading condition. 230

C.19 **Shear components of β and α" grains at high shear loading state that close to defects nucleation state.** Here, X is along $[100]_\beta$, Y is along $[011]_\beta$ and Z is along $[0\bar{1}1]_\beta$. **(A)** is β grain in Ti_4Nb at 300 K, under "Non-confined Simple Shear" loading condition and **(B)** is α" phase in Ti_4Nb at 300 K, under "Non-confined Simple Shear" loading condition. 231
C.20 **Nb concentration dependent elastic constants and shear modulus. A** shows elastic constants of parent β (BCC-like) phase: C_{11} is in blue color; C_{12} is in orange color and C_{44} is in green color. **B** presents directional elastic moduli of parent β phase: G_{111} is in blue color; G_{311} is in orange color, and C' is in green color, which characterize the shear modulus for β to α" phase transformations along Burgers path;E_{100} is in red color;E_{111} is in purple color and E_{311} is in brown color. 233
C.21 **Dynamic change of effective twin nucleation metric, $\Delta g_{\mathbf{twin}}$ under loading conditions for different alloy systems.** 234

LIST OF TABLES

TABLE

4.1 Deformation mechanisms of Ti-Nb alloys at different temperatures. (shear strain rate is $10^8/s$), Here "CSS" in the table is short for "Confined Simple Shear","NSS" in the table is short for "Non-confined Simple Shear". 117
4.2 Elastic parameters and misfit strains for different alloy systems. 131
4.3 Summary on the energetic descriptors for twinning nucleation behaviors and reversibility between β and α" phase. Unit of all energetic parameters is meV/atom. $P_{\text{chem}}^{\beta\leftrightarrow\alpha''}$ is dimensionless. "DM" is short for deformation modes. 132

LIST OF APPENDICES

APPENDIX

A General Mathematical Solution for Invariant Plane Strain 176

B Stability and Growth Kinetics of {112} Twin 180

C Energetic Model for Nucleation of Deformation Modes 201

LIST OF ACRONYMS

ATAT Alloy Theoretic Automated Toolkit

BCC Body-Centered Cubic

BZ Brillouin Zone

CI-NEB Climbing Image Nudged Elastic Band

CG Conjugated Gradient

CNA Common Neighbor Analysis

CNT Classical Nucleation Theory

CV Collective Variable

DB-FIB Dual-Beam Focus Ion Beam

DD Dislocation Dynamics

DFT Density Functional Theory

EBSD Electron BackScatter Diffraction

FCC Face-Centered Cubic

FEA Finite Element Analysis

FEL Free Energy Landscape

GB Grain Boundary

GGA Generalized Gradient Approximation

GSF Generalized Stacking Fault

GSFE Generalized Planar Fault Energy

HAADF High Angle Annular Dark Field-scanning

HEA High Entropy Alloy

HCP Hexagonal Close-Packed

IPF Inverse Pole Figure

IPS Invariant Plane Strain

LAMMPS Large-Scale Atomic/Molecular Massively Parallel Simulator

LDA Local Density Approximation

MD Molecular Dynamics

MEAM Modified Embedded Atom Method

MEP Minimum Energy Path

MLP Machine Learning Potential

MT Martensitic transformation

MTP Moment Tensor Potential

NPH Isoenthalpic–Isobaric Ensemble

NPT Isothermal-Isobaric Ensemble

OVITO Open Visulization Tool

PAW Projector-augmented wave potentials

PBE Perdew-Burke-Ernerhof

PF Phase Field

PFIB Plasma-source Focused Ion Beam

PT Phase Transformation

PTM Polyhedral Template Matching

SQS Special Quasi-random Structure

STEM Scanning Transmission Electron Microscopy

TB Twin Boundary

TEM Transmission Electron Microscopy

TRIP TRansformation-induced Plasticity

TWIP TWinning-induced Plasticity

VASP Vienna *Ab Initio* Simulation Package

VEC Valence Electron Concentration

VTST Vasp Transition State Theory

WQ Water Quenching

ABSTRACT

Titanium alloys occupy a unique position among structural materials, offering low density, high specific strength, excellent corrosion resistance, and remarkable biocompatibility that render them indispensable across various advanced engineering applications. This versatility stems from titanium's sensitivity of phase stability to alloy chemistry: increasing Valence Electron Concentration (VEC) of alloys drives the equilibrium dominant phase constitution from the stable α (Hexagonal Close-Packed (HCP)) phase through dual-phase α+β to the stable β (Body-Centered Cubic (BCC)) phase, defining a spectrum of alloy systems with distinct phase constitutions; the metastable ω phase (hexagonal/trigonal) further appears as a secondary constituent across these systems under quenching, low-temperature aging, or elevated pressure conditions. Beyond these well-studied categories, metastable β alloys represent a special class in which β (BCC-like, parent phase), α" (HCP-like) and ω phases coexist in thermodynamically metastable states, conferring exceptional tunability of mechanical properties. However, this tunability comes at the cost of extraordinary mechanistic complexity. Deformation in metastable β alloys proceeds primarily through two competing mechanisms: diffusionless phase transformations ($\beta \leftrightarrow \alpha$" and $\beta \leftrightarrow \omega$) and deformation twinning (mainly {112} twin and {332} twin). Both mechanisms are crystallographically unique to these alloy systems, and their strong mutual competition and coupling renders their activation and interaction exceedingly difficult to predict or control, presenting a fundamental challenge for linking deformation mechanisms to macroscopic mechanical behavior. A fundamental bottleneck remains the absence of atomistic-level understanding of the thermodynamic and kinetic origins governing these deformation pathways and their mutual couplings. In this thesis, the high-fidelity atomistic simulations are employed to elucidate

phase transformation-mediated deformation twin ({112} twin and {332} twin) nucleation and growth, from which atomistic and continuum-scale models are developed to assess mechanism activity and establish quantitative connections to macroscopic mechanical properties, providing a unified framework for the rational design of metastable β titanium alloys.

This dissertation is therefore organized into four major parts. In the first part, {112} twin stability and growth kinetics in metastable Ti alloys are investigated; although {112} twin is less commonly observed in metastable Ti alloys, it is common in stable BCC metals, and this part reveals how $\beta \leftrightarrow \omega$ phase transformations fundamentally alter {112} twinnability and how this relationship evolves with alloy composition and temperature. In contrast to {112} twin, {332} twin is prevalent and unique to metastable β titanium alloys yet absent in stable BCC metals. In the second part, the stability and growth kinetics of {332} twins are therefore systematically analyzed, elucidating how $\beta \leftrightarrow \alpha''$ phase transformations govern {332} twin growth and how composition and temperature modulate this behavior. Taken together, the findings of these two parts reveal that, in relatively stable Ti alloys, the resolved twin growth stresses of {112} and {332} twins converge to comparable and competitive levels, indicating that competition between {112} twin and {332} twin are governed primarily by nucleation rather than growth kinetics. Motivated by this insight, the third part systematically examines the temperature-, composition-, and loading-condition-dependent nucleation of competing deformation modes, and the predicted deformation mode selection trends show strong consistency with experimental observations and two energetic metrics are proposed to quantitatively capture the competition among these mechanisms. Finally, building upon these mechanistic insights, the fourth part develops a theoretical framework that combines the proposed energetic metrics with heterogeneous nucleation theory to predict the twinning stress of TWinning-induced Plasticity (TWIP) titanium alloys, showing strong agreement with experimental measurements across broad temperature and alloy ranges and demonstrating its potential as a physically informed tool for high-throughput alloy design.

CHAPTER 1

Introduction

1.1 Motivation

On 31 March 1972, the Soviet Union launched Kosmos-482, a spacecraft designed to descend through the extreme atmosphere of Venus and transmit data from its surface [213]. A failure of the upper rocket stage prevented escape from Earth's gravity, leaving the probe stranded in an elliptical orbit for over 53 years until its re-entry on 10 May 2025, when it reportedly splashed down in the Indian Ocean. While the mission failed, the fate of its descent capsule is notable from a materials science perspective. Encased in a titanium shell designed for Venusian entry, the module endured over 50 years in low Earth orbit—exposed to thermal cycling, ultraviolet radiation, and high vacuum—and ultimately survived re-entry under extreme conditions with its body largely intact. This example demonstrates the exceptional durability and environmental resilience of titanium alloys, which offer a combination of properties unmatched by most structural materials. Their high specific strength - among the highest of any metallic material - makes them indispensable wherever mass savings are critical, such as in aerospace structures, gas turbine engine components, and biomedical implants [8]. Their outstanding corrosion resistance, stemming from the spontaneous formation of a stable and adherent oxide layer, renders them suitable for aggressive chemical environments, marine applications, and long-term implantation in the human body [190]. Their broad service temperature range, spanning from cryogenic conditions to several hundred degrees Celsius, further broadens their engineering utility.

Yet, for all their attractive properties, the industrial development of titanium alloys are considerably slower than other structural alloys. Their high chemical reactivity at elevated temperatures, the strong sensitivity of their microstructure to subtle variations in composition and thermomechanical history, and the relatively high cost of raw materials and primary processing all contribute to this inertia. As a result, the alloy palette used in industry today remains narrow, and the optimization of processing parameters for emerging manufacturing routes is still largely empirical [8].

A key reason for this slow progress lies in the complexity of microstructures, particularly within the class of metastable β-titanium alloys. Pure titanium undergoes an allotropic transformation from the high-temperature body-centred cubic (bcc) β-phase to the HCP α-phase upon cooling through the β-transus temperature. By alloying with β-stabilising elements, it is possible to retain the β-phase in a metastable state at room temperature. However, this metastability gives rise to a cascade of intermediate phases including the orthorhombic α''-martensite, the hexagonal ω-phase, and composition-modulated β regions. These metastable phases can form, co-exist, or transform into one another depending sensitively on alloy composition, temperature, and applied mechanical loading [8]. This rich phase landscape makes the metastable β-Ti system one of the most complex among structural metallic alloys.

In addition to phase complexity, metastable Ti alloys can activate a diverse set of deformation mechanisms. Under external loading, metastable β-Ti alloys can deform not only by conventional dislocation slip, but also through stress-induced martensitic transformation ($\beta \rightarrow \alpha$"), reversible phase transformations associated with superelasticity, and a variety of twinning modes, including those on high-index crystallographic planes rarely observed in other metallic systems. [8, 120]. Limited understanding of phase evolution and deformation modes competition under varying conditions remains a major obstacle to the efficient Ti alloy design and reliable processing for desired properties.

At the same time, metastable β-Ti alloys provide a valuable model system for metastable

engineering. The concept of "metastability engineering"—the deliberate use of metastable phases and transformation pathways to achieve properties unattainable in stable systems—has emerged as an important paradigm in modern alloy design [171, 109, 212]. Within this framework, metastable β-Ti alloys are particularly well suited: their phase stability can be tuned through composition, temperature; their transformation pathways are accessible over a wide range of external conditions, and their diverse properties, including high strength, superelasticity, and biocompatibility. Insights gained from understanding structural evolution and deformation in metastable Ti alloy systems can also extend to practical alloy design for other metastable systems, such as steels, cobalt alloys, and recent developed metastable high entropy alloys [212, 94].

This dessertation is situated within this context. By focusing on metastable β-Ti alloys as a model system, combined with atomistic simulations, this dissertation pursues a mechanistic and crystallographically rigorous understanding of the coupled interplay between phase transformation and deformation in this alloy class. These results aim to advance the fundamental science of metastability engineering in metallic alloys and to establish a physically based design methodology that can accelerate the rational development and reliable processing of next-generation titanium alloys and extend insights to other metatsable alloy systems.

1.2 Outline

Specifically, the dessertation addresses three interconnected objectives. First, by combining crystallographic theory with atomic-scale characterisation, the crystallographic coupling between stress-induced phase transformation ($\beta \leftrightarrow \omega$, $\beta \leftrightarrow \alpha$")and deformation twinning (most common {112} twin and {332} twin) are examined in detail, with particular emphasis on the early-stage nucleation of transformation-induced twins and the subsequent kinetics of their growth – processes that remain poorly understood yet critically govern the onset and evolution of plasticity. Second, building on these mechanistic insights, a thermodynamic

framework is developed that explicitly accounts for the kinetic barriers associated with competing deformation modes, providing a physically grounded basis for predicting deformation mechanisms under given set of external conditions in different Ti alloy systems. Third, this framework is extended into a generalised yield strength model for metastable β-Ti alloys, capable of capturing the dependence of macroscopic mechanical response on alloy composition, temperature, and loading conditions.

Following the three main objectives, this dissertation is constructed into six parts shown as follow:

In Chapter 1, we have already introduced the motivation and scope of this study, highlighting the need for a clearer understanding of phase transformation–mediated deformation mode selection and evolution in metastable Ti alloys, as well as the potential for extending these insights to metastability engineering in other alloy systems. In the rest of this chapter, we will review several important fundamental theories required for this study, along with the introduction of key computational methods we employed in this study and required for future study.

In Chapter 2, we investigate the stability and growth kinetics of {112} twins in metastable β Ti-Nb alloys. While {112} twinning is the dominant mode in conventional stable BCC alloys, it exhibits anomalous behavior in metastable β-Ti systems. Using DFT and MD simulations, we identify the critical role of the ω phase in governing the stability of early-stage {112} twin embryos and their growth kinetics under shear loading. We further examine how composition and temperature influence the $\beta \leftrightarrow \omega$ transformation and, consequently, the twinnability of {112} twins. In addition, we shade lights on long time debates regarding the role of the ω phase in the origin of {112} twinning by investigating twin nucleation behaviors from grain boundaries.

In Chapter 3, we investigate the {332} twinning mode, a distinctive deformation mechanism in metastable β Ti-Nb and Ti-Mo alloys. We examine the growth kinetics of {332} twins and characterize the $\beta \leftrightarrow \alpha$" transformation at the twin boundary, confirming that {332}

twin growth proceeds through reversible phase transformations. Because the twinnability of {332} twins depends on β-phase stability, we further study their growth behavior across a range of alloy compositions and temperatures, spanning metastable to stable BCC systems. The results show that, although the growth mechanisms differ significantly between metastable and stable BCC alloys, the twin migration stress does not vary substantially. This indicates that the limited {332} twinnability in stable BCC alloys is governed primarily by nucleation rather than growth.

In Chapter 4, we investigate the early-stage nucleation of deformation modes, including twinning and phase transformations. Molecular dynamics (MD) simulations are used to systematically characterize atomic-scale nucleation behavior in metastable Ti-Nb alloys as a function of temperature, composition, and loading conditions. Through energetic and structural analysis, we show that the dominant deformation mechanisms and preferred twinning-plane orientations are governed by two key parameters: the free energy barrier for homogeneous $\beta \leftrightarrow \alpha$" transformation and the misfit strain energy associated with specific phase boundaries. These quantities vary systematically with thermodynamic and mechanical conditions and account for the deformation-mode transitions observed in both simulations and experiments. Together, they provide a direct link between external conditions and atomistic nucleation behavior.

In Chapter 5, extending the analysis from Ti–Nb and Ti–Mo binary systems to the Ti–Nb–Mo ternary system, we further incorporate the energetic parameters proposed in Chapter 4 into a heterogeneous nucleation framework to predict the yield strength of TWIP Ti alloys. The framework is free of empirical fitting parameters, and all inputs are physically defined quantities, ensuring strong physical fidelity and direct interpretability of the underlying mechanisms. The predicted strengths show great agreement with experimental data, particularly in capturing trends with temperature and composition. Within the metastable regime, compositional tuning effectively alters twinning mode preference by modifying the misfit strain energy associated with twin nucleation, while temperature primarily influences

the overall yield strength through changes in the chemical free energy contribution. Because this framework avoids the need for explicit simulation of complex deformation processes using highly accurate interatomic or machine learning potentials, it can be efficiently extended to other metastable Ti alloy systems for alloy design.

In Chapter 6, we summarize the key findings and conclusions in this dissertation. In brief, this work systematically establishes the thermodynamic and kinetic framework governing phase transformation-induced deformation twinning in metastable β-Ti alloys. The theoretical models derived from a series of atomistic-scale simulations, serve as a physically grounded bridge across time and length scales, enabling efficient prediction of macroscopic yield stress without recourse to empirical fitting. As future work, the mechanistic insights into twin growth behavior and the energetic parameters characterizing twin nucleation can provide well-defined inputs for mesoscale and crystal plasticity models, facilitating the modeling of dynamic microstructure evolution under realistic loading conditions. This developed multi-scale modeling strategy has the good potential to offer a physically informed pathway toward the accelerated design of next-generation metastable titanium alloys.

1.3 Fundamental Theories

1.3.1 Diffusionless (Martensite) Phase Transformation

The term "phase transformation" in materials science is rooted in the concept of "phase transition" in statistical mechanics. In statistical mechanics, a phase transition is defined by the singular behavior of the free energy of a system as a control variable (such as temperature, pressure, or an applied field) is varied through a critical value. The system undergoes an abrupt, qualitative change in its macroscopic state, and this change is not specific to materials: analogous transitions occur in traffic flow, social networks, and biological systems, wherever collective behavior emerges from many interacting degrees of freedom. In condensed matter physics, phase transitions are classified according to the continuity of the free energy

and its derivatives at the transition point – first-order transitions involve a discontinuous jump in the order parameter and latent heat, while continuous (second-order) transitions exhibit a divergence in susceptibility and no latent heat – and they are characterized by symmetry breaking, scaling laws, and universality [116, 68].

The materials science concept of "phase transformation" inherits this thermodynamic foundation but adds an essential dimension: the physical process by which the transition is achieved. Whereas a phase transition is defined purely by the thermodynamic state change in a mathematical abstract way, a phase transformation addresses the how: the atomic mechanisms, transformation pathways, and microstructural changes through which the system evolves from one phase to another. Consequently, phase transformations are governed not only by thermodynamic driving forces, captured by the free energy difference between parent and product phases in high dimension space, but also by kinetic factors including nucleation barriers, atomic mobility, and the availability of accessible transformation pathways. A critical implication of this duality is that a thermodynamically favorable phase transition does not guarantee that the corresponding transformation will actually occur on any practical timescale: when kinetic barriers are sufficiently large, the system may remain trapped in a metastable state indefinitely, as is the case for the metastable β-Ti alloys that are the central subject of this thesis. Understanding phase transformation therefore demands a framework that unifies thermodynamic driving forces with kinetic accessibility, whcih is a challenge that bridges statistical mechanics, crystallography, and materials engineering.

Phase transformations in crystalline solids are broadly classified by the atomic mechanism through which one crystal structure converts to another. In thermally activated diffusional transformations, such as precipitation or eutectoid decomposition, atoms migrate individually over distances far exceeding one interatomic spacing, driven by chemical potential gradients, and the product phase generally carries a composition different from the parent. In contrast, diffusionless (or displacive) transformations proceed by the cooperative, quasi-military displacement of atoms over sub-interatomic distances, without long-range atomic

diffusion and without any change of chemical composition [45, 68]. Because all atoms move in a correlated manner, these transformations can proceed at speeds approaching the speed of sound and remain, in principle, operative even at cryogenic temperatures where thermally activated processes are negligible.

Martensitic transformation (MT) is the prototypical and most technologically significant member of diffusionless phase transformation though its classification is a long time debates in history. Historically, the hardened phase produced in quenched steels was first characterized by Adolf Martens in the late nineteenth century, and the underlying transformation mechanism was not fully rationalized until the mid-twentieth century [161, 129, 182]. Meanwhile, martensite transformation behavior is not unique in steels but also found in other alloy systems, such as β Ti alloys. Therefore, the definition of MT is a controversial issues in history. Cohen, Olson, and Clapp at the 1979's International Conference of Martensitic Transformation [161] classified MT as a type of diffusionless phase transformation for the first time, as shown in Figure 1.1. In brief, from structural and energetic point of view, MT share three characteristic with disffusionless phase transformation (compositionally invariant is also a hidden characteristic) :

(1) lattice-distortive displacement (affine transformation mainly);

(2) deviatoric dominate (invariant plane strain);

(3) strain energy dominate;

Later, from a crystallographic and physical perspective, a unified and widely accepted modern definition—integrating thermodynamic, kinetic, mechanical, and crystallographic considerations—was articulated by Hsu (Xu) at the 1995 International Conference on Martensitic Transformations [93]. According to this definition, MT is:

(1) a first-order structural phase transformation proceeding by diffusionless atomic displacement,

(2) encompassing both uniform lattice deformation and non-uniform atomic shuffle,

(3) characterized by macroscopic shape change, surface relief, and satisfaction of an

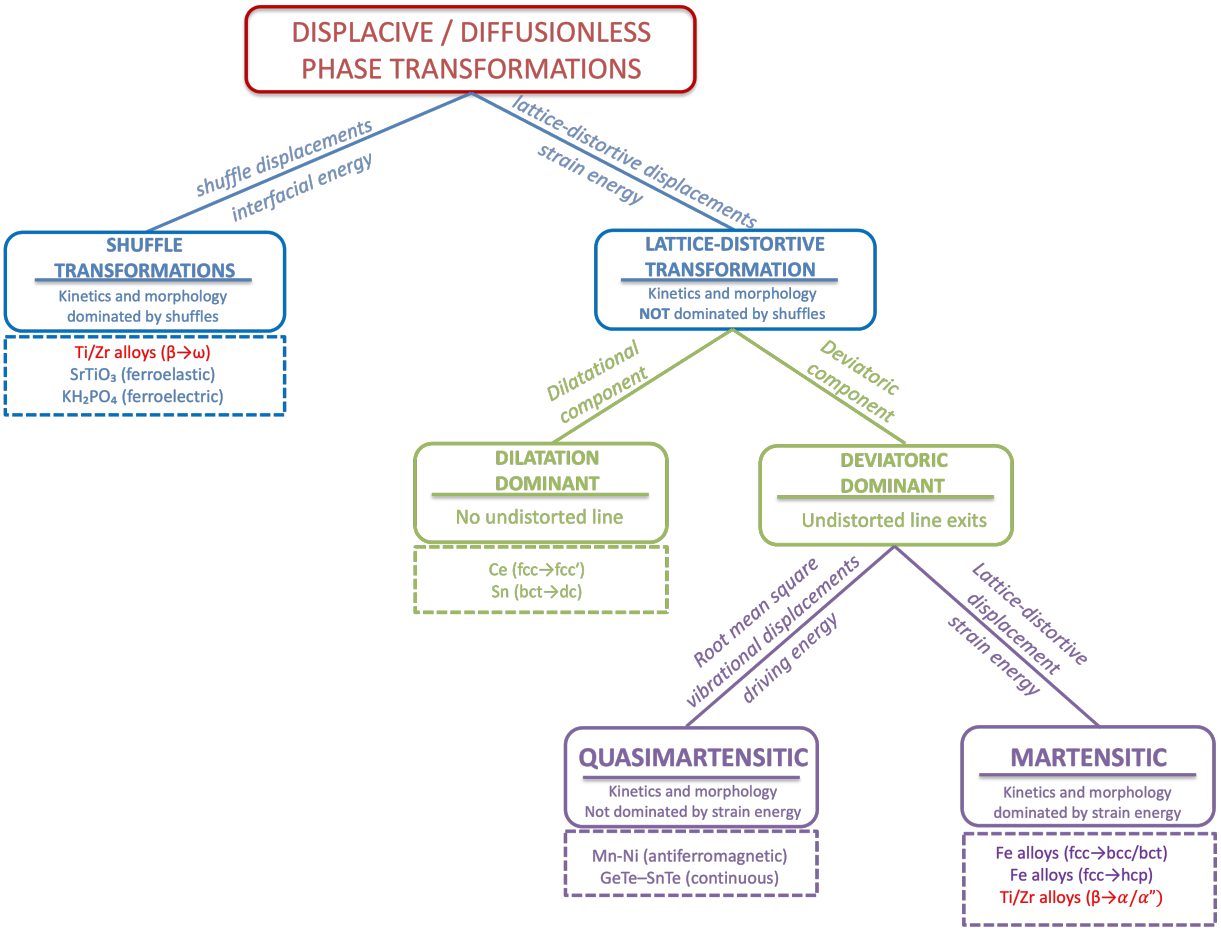


Figure 1.1: Classification scheme of diffusionless(displacive) phase transformations in broad materials science. This diagram is adapted from [47]. Main phase transformation behaviors we investigated in this study are marked in red.

invariant-plane strain condition.

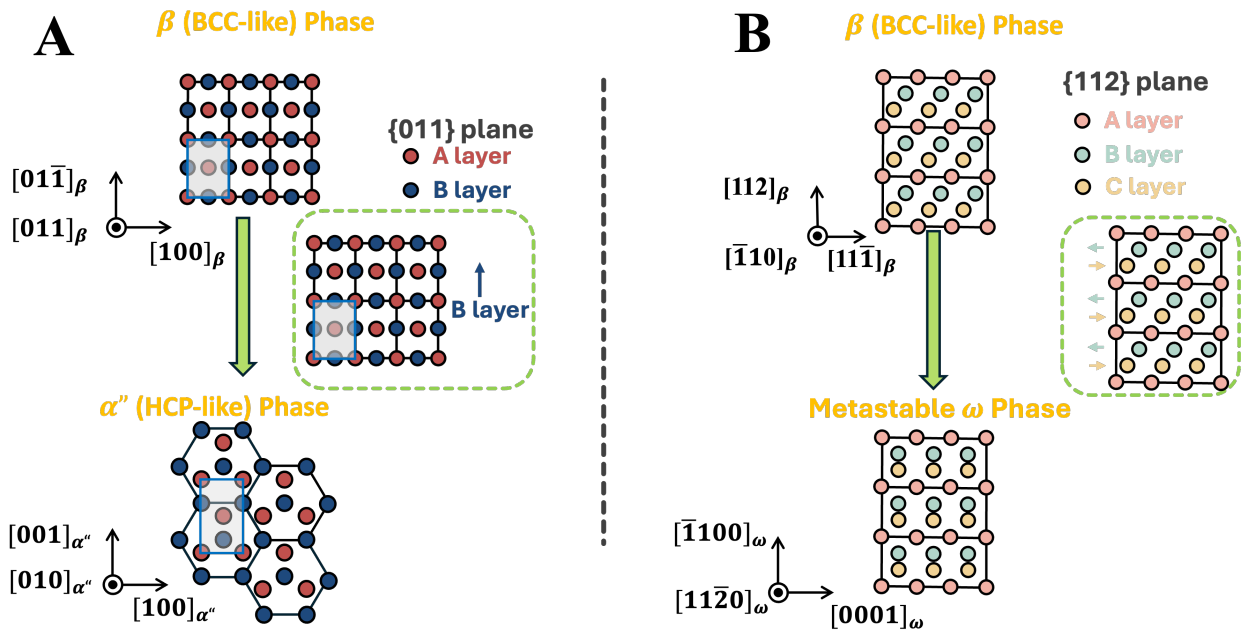


Figure 1.2: Illustrations of atomistic structures of metastable phases and possible diffusionless phase transformation behaviors in metastable Ti alloys. (a) Schematic draw for crystal structures of β (BCC like), α" (HCP-like in Orthorhombic) phases and the corresponding diffusionless transformation pathways. Red and Blue atoms are at A and B stacking of $\{011\}$ layers in BCC lattice, respectively. β can transfer to α" phase via shuffling between A and B layers along $[01\bar{1}]$ direction (accompanied by an essential deviatoric strain). (b) The schematic draw for β to ω phase diffusionless transformation. Pink, green, and yellow atoms are at A, B, and C stacking of $\{112\}$ layers in BCC lattice, respectively. β can transfer to ω phase via atomic shuffling two out of every three $\{112\}$ layers in opposite $\langle 111 \rangle$ directions.

In this study, metastable Ti alloys exhibit two phase transformation behaviors: $\beta \leftrightarrow \alpha$" phase transformation belonging to this type of MT and $\beta \leftrightarrow \omega$ phase transformation belonging to shuffle-dominant disffusionless phase transformation (refer to Figure 1.1). In Figure 1.2, we illustrate corresponding phase transformation pathways. Viewed from a condensed matter physics standpoint, both MT-like $\beta \leftrightarrow \alpha$" phase transformation and shuffle-dominate $\beta \leftrightarrow \omega$ phase transformation are classified as first-order structural phase transformation and undergo spontaneous symmetry breaking process. The β phase adopts a body-centered cubic (BCC) structure with space group $Im\bar{3}m$, characterized by high symmetry (containing four-fold rotational symmetry). In metastable Ti alloys, this phase can transform into

several lower-symmetry structures, including the hexagonal close-packed α' phase (containing three-fold rotational symmetry), the orthorhombic α'' phase with space group $Cmcm$ ((containing two-fold rotational symmetry)), and the hexagonal ω phase with space group $P6/mmm$ (containing three-fold rotational symmetry) [73, 74]. Among these, the α'' phase can be regarded as an intermediate state between the β and α' phases, sharing a similar underlying transformation pathway. In particular, the $\beta \rightarrow \alpha''$ transformation follows a lattice correspondence analogous to the Burgers pathway for BCC-to-HCP transformation, but to an incomplete extent. This transformation is associated with a reduction in symmetry from the parent BCC phase to the orthorhombic product phase, giving rise to multiple crystallographically equivalent transformation pathways.Crystallographically equivalent transformation pathways provide potential to form compositionally invariant twin phase, we will discuss in the later sections.

1.3.2 Metastability

The preceding section we introduce the definition, classification and physical process of diffusionless phase transformation. Thermodynamically, occurrence of diffusionless phase transformations line in an important energetic condition: multiple phases exists and free energy of the product phase lies below or close to that of the parent phase at the same composition, and kinetically accessible whenever the nucleation barrier can easily be overcame thermally, mechanically, or through heterogeneous sites. In other words, this essential condition for diffusionless transformation can be defined as "metastability" of the parent phase. [161, 47, 193]

Metastability is not a peculiarity of metallic alloys: it is a ubiquitous feature of complex systems wherever multiple competing free-energy minima exist separated by finite barriers. In condensed matter physics, it arises in spin glasses, supercooled liquids, ferroelectrics, and structural glasses [116]. In structural geology, it governs the persistence of high-pressure mineral phases (such as diamond and coesite) at the Earth's surface long after the pressure

that stabilized them has been removed. Even in everyday contexts, metastability determines the crystal form of confectionery fats, the shelf life of pharmaceutical polymorphs, and taste of chocolate sold in markets [98].

In all of these systems, the common underlying physics is identical: the free energy landscape possesses multiple local minima, and the observable state of the system reflects not only thermodynamic stability but also the kinetic history : the path by which the system arrived at its current configuration and the barriers it has or has not been able to cross.

In the context of metallic alloys, the concept of metastability acquires additional concreteness through the lattice-dynamic and thermodynamic frameworks established in the preceding section. The free energy landscape of a metallic crystal is not a smooth, featureless surface but is structured by the discrete crystallographic symmetries of competing phases, the phonon spectra of each phase, and the elastic interactions between coexisting structural domains [99]. The competing local free-energy minima correspond to distinct crystal structures and the barriers between them correspond to the structural distortion along minimum energy path.

As for metastability engineering in metallic alloys, it is through two primary levers. The first is compositional control: by alloying with elements that differentially stabilize one phase relative to another, the relative depths of the free-energy minima are adjusted, and the temperature at which a given phase becomes thermodynamically unfavorable (e.g., the β-transus, or the martensite start temperature M_s) is systematically shifted [97]. The second is thermal processing: by cooling rapidly through a temperature range where diffusional transformation would normally occur, the high-temperature phase is kinetically frozen into a metastable state at lower temperatures, preserving a microstructure that is far from equilibrium but thermodynamically trapped [97]. Once metastability achieved in the alloy system with multiple metastable phases coexists, by mechanical loading , it provides an active design space in which properties inaccessible in thermodynamically stable systems such as superelasticity, TRansformation-induced Plasticity (TRIP), Invar or Elinvar anomalies.

As for state-of-art metastable β-Ti alloy engineering approaches, pure titanium undergoes an allotropic transformation from the BCC-like β-phase (stable above $\sim$882 °C) to the HCP-like α-phase at lower temperatures. By alloying with β-stabilizer elements such as Mo, V, Nb, Ta, and Cr, the β-transus temperature is progressively suppressed and M_s is driven below room temperature, retaining the β-phase in a metastable state at ambient conditions [8]. The degree of β-phase metastability, or the relative stability between different metastable phases, can be parameterized through the VEC or the empirical molybdenum equivalent $[\mathrm{Mo}]_{\mathrm{eq}}$. [160].

However, these current metastable Ti alloy design strategies remain largely confined to compositional space and carry no information on how the relative stability between competing phases evolves with temperature or responds to mechanical loading. In practice, thermomechanical processing subjects the alloy to continuously varying temperature and strain/stress fields, yet no established framework explicitly maps how temperature change the metastability boundaries in composition space, or how an applied stress couples to the phase stability landscape to govern which deformation mode is activated and at what conditions the competition between them shifts. Consequently, the optimization of microstructures remain largely empirical, guided by trial-and-error rather than physical understanding. A theoretical framework that integrates compositional metastability with its temperature and mechanical-loading dependence is therefore a prerequisite for the rational metastability engineering. In this thesis, we primarily focus on developing theoretical framework for alloy design including temperature and mechanical loading.

1.3.3 Deformation Twinning

In crystallography theory, twins are defined as two crystals, or two regions within a single crystal, that share a common plane (the twin boundary) and are related to one another by a specific symmetry operation, either a reflection in that plane or a rotation of 180° about an axis [46, 123]. Twins are not a product of deformation alone: according to their formation

mechanism, crystallographic twins are broadly classified into three categories: growth twin, annealing twin and deformation twin. Growth twins form during crystal growth from the vapor or liquid phase under conditions far from thermodynamic equilibrium. Annealing twins (or transformation twins) arise during solid-state phase transformation, recrystallization, or other thermal treatments. Deformation twins, which are the subject of the present section and investigated in this thesis, are triggered by the application of mechanical loading and constitute one of the most important modes of plastic deformation in crystalline solids. More specifically, following the definition proposed by Bilby, A deformation twin is a region of a crystalline body which has undergone a homogeneous shape deformation in such a way that the resulting product structure is identical with that of the parent, but oriented differently. [46, 14].

The crystallographic description of a deformation twin is completely specified by six elements, illustrated schematically in Figure 1.3 [88]

- K_1 - **invariant twinning plane** (the habit plane or composition plane), which is undistorted and unrotated by the twinning shear. This plane constitutes the twin boundary in the classical (rational) case.
- η_1 - **twinning direction**, lying in K_1, along which the simple shear is applied.
- K_2 - **conjugate (reciprocal) undistorted plane**, which is distorted by the shear but left undistorted in length (though rotated). Together with K_1, it defines the shape of the homogeneous strain ellipsoid.
- η_2 - **conjugate twinning direction**, lying in K_2 and in the plane of shear P.
- P - **plane of shear**, perpendicular to both K_1 and K_2 and containing η_1 and η_2.
- s - **magnitude of the twinning shear**, defined as the displacement per unit length perpendicular to K_1, which together with K_1 and η_1 fully specifies the affine deformation tensor of the twinning operation.

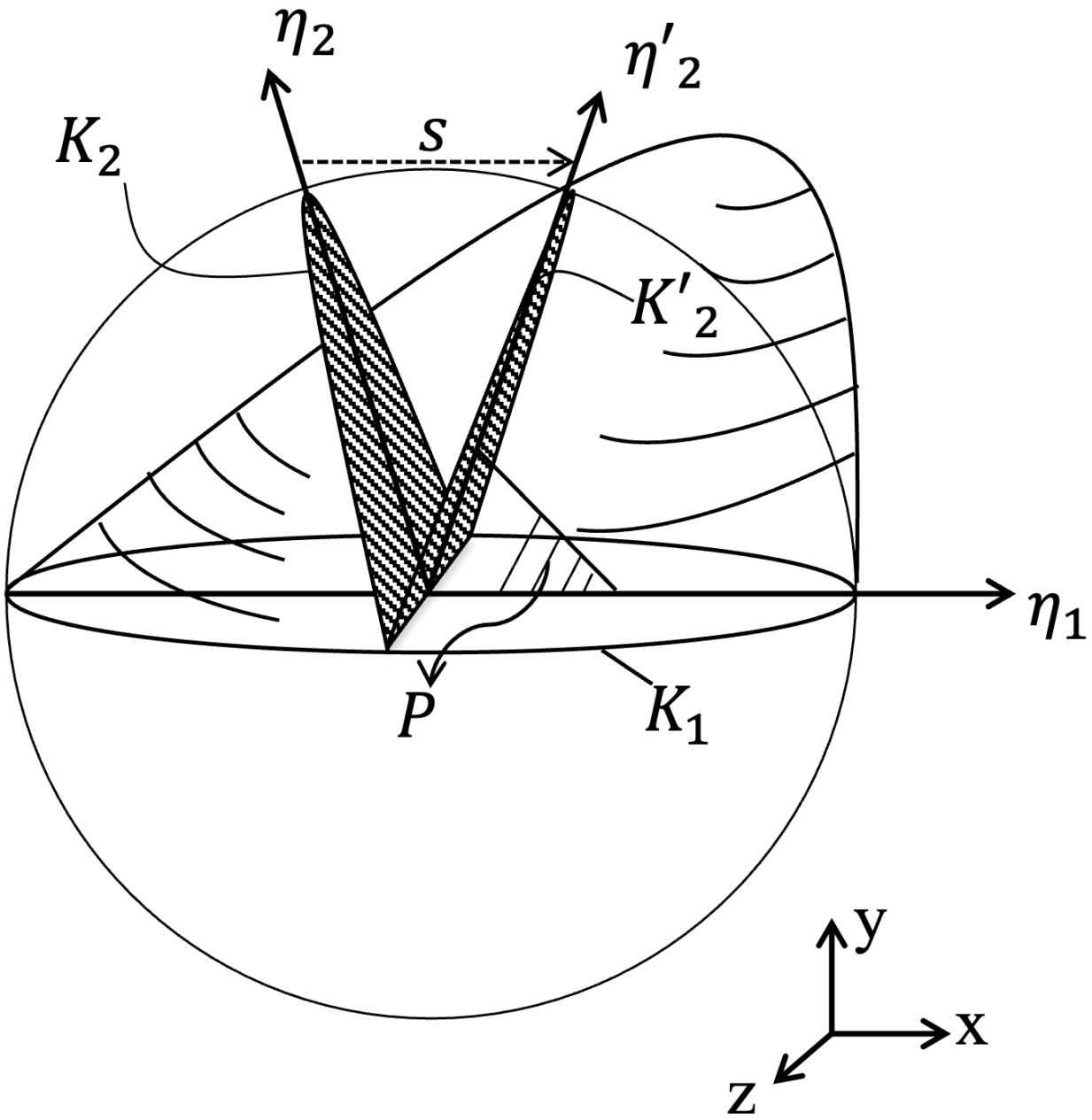


Figure 1.3: Schematic illustration of twinning elements in crystals. Adapted from [88].

In practice, since P and s are uniquely determined once the other four elements are known, a twinning mode is conventionally specified by the quartet $(K_1, \eta_1, K_2, \eta_2)$ [46]. Based on the rationality of these elements, twins are classified as: type I twins, in which K_1 and η_2 are rational (defined by integer Miller indices) while K_2 and η_1 may be irrational; type II twins, in which K_2 and η_1 are rational while K_1 and η_2 may be irrational; and compound twins, in which all four elements are rational [46]. In type I twins, the crystallographic orientation relationship between twin and parent is a reflection in K_1; in type II twins, it is a rotation of 180° about η_1. When the plane of shear P is a mirror plane of the crystal, type I and type II orientations become equivalent and the twin is compound. Most observed deformation twins in metastable Ti alloys – including the $\{112\}\langle 11\bar{1}\rangle$ twin in bcc metals and the $\{332\}\langle 11\bar{3}\rangle$ twin in metastable bcc alloys – are compound twins [46].

In stable metallic systems, deformation twinning assumes particular importance as a plastic carrier in two distinct regimes. First, in crystals of low crystallographic symmetry(HCP or orthorhombic phase), the number of independent slip systems available for homogeneous plastic deformation is few. In such structures, twinning supplements slip to provide the additional independent strain components necessary for grain-scale compatibility, and its suppression leads directly to premature intergranular fracture [46]. Second, in higher-symmetry structures (BCC and Face-Centered Cubic (FCC)), twinning becomes a dominant mechanism under conditions of low temperature, high strain rate, or shock loading, where the flow stress rises to a level at which twinning is preferred over continued dislocation glide [123]. Under these conditions, the onset of twinning is often manifested as a sharp load drop (in BCC metals) or a sustained plateau (in FCC alloys) in the stress–strain curve, reflecting the sudden cooperative reorientation of large volumes of crystal.

However, in metastable alloys, such as β Ti alloys in this study, the role of deformation twinning in titanium alloys is unusually complex. Depending on alloy composition and hence the degree of β-phase metastability, twinning may operate on the conventional $\{112\}\langle 11\bar{1}\rangle$ system (characteristic of stable bcc metals), or on the high-index $\{332\}\langle 11\bar{3}\rangle$ (and recently

observed $\{5\ 8\ 11\}\langle 51\bar{3}\rangle$, $\{10\ 9\ 3\}\langle\bar{3}11\rangle$ [229, 4]) system involving a combination of shear and shuffle. The activation of these highly indexed twinning are closely coupled to the proximity of the $\beta \rightarrow \alpha''$ martensitic instability [123, 8]. Unlike classical slip-assisted twin nucleation and migration mechanism in conventional stable metallic system, the mechanism of twinnability in β Ti alloys is closely correlated with diffusionless phase transformations, in both deformation atoms follow a collective motion rather than random diffusion.

1.3.4 Couplings of Diffusionless Transformation-Deformation Twinning

Following the concepts illustrated in preceding sections, deformation twinning and diffusionless phase transformation share a profound crystallographic kinship that goes beyond their superficial resemblance as cooperative, diffusionless shear processes. Both are fundamentally symmetry-breaking events: twinning reduces the point group symmetry of the parent crystal by breaking certain rotational symmetries and producing a reoriented domain, while martensitic transformation reduces the space group symmetry of the parent phase and generates a set of crystallographically equivalent product variants whose number and type are dictated by the lost symmetry operations [72, 74]. In both cases, the boundary between the parent and product domains, twin boundary or phase boundary, must satisfy the condition of mechanical compatibility, expressed by the kinematic compatibility condition (or Hadamard jump condition). For a planar interface between two domains with deformation gradients $\mathbf{F}_1$ and $\mathbf{F}_2$ referenced to a common undeformed state, this condition requires [99]:

$$\mathbf{F}_2 - \mathbf{F}_1 = \mathbf{a} \otimes \mathbf{n}, \tag{1.1}$$

where $\mathbf{a}$ is the shear (shape-change) vector and $\mathbf{n}$ is the unit normal to the interface plane [99]. Equation (1.1) embodies the classical Invariant Plane Strain (IPS) condition: the existence of an interface plane $\mathbf{n}$ within which macroscopically undistorted and unrotated. IPS con-

strains simultaneously the habit plane orientation and the magnitude and direction of the shape strain. Because a rotation matrix $\mathbf{Q}$ must also be incorporated to account for the crystallographic misorientation between the two domains, the full twin boundary condition is written:

$$\mathbf{Q}\mathbf{F}_j - \mathbf{F}_i = \mathbf{a} \otimes \mathbf{n}, \tag{1.2}$$

where $\mathbf{F}_i$ and $\mathbf{F}_j$ are the deformation gradient matrices of the two contacting structural domains (inputs), and $\mathbf{Q}$, $\mathbf{a}$, and $\mathbf{n}$ are the misorientation matrix, twinning shear vector, and twin plane normal (outputs) [74]. If Eq. (1.2) admits two conjugate solutions, they correspond to the type I (rational plane, irrational direction) and type II (rational direction, irrational plane) twins of classical crystallographic theory; if all four twinning elements are rational, the twin is compound. The critical insight is that Eq. (1.2) is equally applicable to boundaries between two variants of the same phase (deformation twins), between a parent phase and a transformed product (phase boundaries). It is this generality that makes the IPS formalism the natural unifying language for describing the coupling between twinning and transformation. Meanwhile, this underlying couplings between martensite phase transformation and deformation twinning in metastable β Ti alloys is a center assumption in this study. In the appendix A, we also provide a step-by-step calculation on solving the {112} and {332} twinning mode via Hadamard jump condition.

1.3.5 Heterogeneous Nucleation in Solids

Classical Nucleation Theory (CNT) is widely employed in condensation of vapours, solidification of liquids, diffusional participation in solids, providing the foundational framework for understanding how a new phase embryo forms within a parent phase. In its homogeneous limit, the theory treats the formation of a spherical nucleus entirely within a defect-free parent as a competition between the volumetric free energy gain and the surface penalty of

creating a new interface. For a coherent spherical nucleus of radius r, the total free energy change is:

$$\Delta G(r) = \frac{4}{3}\pi r^3 \left(\Delta G_{\text{chem}} + \Delta G_{\text{strain}}\right) + 4\pi r^2 \gamma, \tag{1.3}$$

where $\Delta G_{\text{chem}} < 0$ is the chemical driving force per unit volume, $\Delta G_{\text{strain}} > 0$ is the elastic strain energy density arising from the misfit between nucleus and matrix, and $\gamma > 0$ is the interfacial energy per unit area [173]. Maximising Eq. (1.3) with respect to r gives the critical nucleus radius r^* and the associated activation barrier ΔG^*:

$$r^* = \frac{-2\gamma}{\Delta G_{\text{chem}} + \Delta G_{\text{strain}}}, \qquad \Delta G^* = \frac{16\pi\gamma^3}{3\left(\Delta G_{\text{chem}} + \Delta G_{\text{strain}}\right)^2}. \tag{1.4}$$

In condensed matter, and in metallic alloys in particular, the homogeneous limit is rarely if ever realized. The fundamental reason is the unavoidable presence of several factors that conspire to make the homogeneous activation barrier prohibitively large [173]. First, solid-solid interfaces are highly anisotropic, with energies that depend sensitively on the crystallographic orientation relationship between parent and nucleus; unlike liquid-vapour interfaces, they cannot be treated as isotropic or structureless. Second, and most importantly in the context of diffusionless transformation, any nucleus of a product phase with a different crystal structure or lattice parameter than the parent must accommodate a transformation strain : either elastically (for a coherent nucleus) or by introducing misfit dislocations (for a semi-coherent or incoherent nucleus). This strain energy ΔG_{strain} enters the barrier with the same sign as γ and thus raise ΔG, often catastrophically: for coherent martensitic nuclei, estimates of ΔG^* under homogeneous conditions are tens to hundreds of $k_{\text{B}}T$, making the homogeneous nucleation rate effectively zero [173]. Third, the crystalline solids contain abundant defects: dislocations, grain boundaries, stacking faults. These defects do not merely play roles of catalysts for nucleation; they interact specifically and quantitatively with the transformation strain and interface energy of the nucleus, reducing ΔG^* in a manner that depends on the coherency character of the nucleus and the type of singularity. The

overwhelming conclusion from both theoretical analysis and experimental observation is that nucleation in solids is always effectively heterogeneous, with the operational nucleation sites determined by the geometry and energy of the available defect population [173].

In the context of martensite transformation and deformation twinning, based on the density of defects, there are two types of heterogeneous nucleation theory: (defects-assisted) local nucleation model and lattice instability model.

As for defects-assisted local nucleation model, mainly dislocation-mediated, a pre-existing elastic strain field of the dislocation extends over a region of radius $\sim b/\varepsilon$ (where b is the Burgers vector magnitude and ε is the transformation strain), and which can interact favorably with the eigenstrain of the nucleus. For a nucleus with a dilatational transformation strain (volume change), the tensile strain field on the tension side of an edge/screw dislocation provides a local driving force that partially offsets ΔG_{strain} in Eq. (1.3). Meanwhile,the dislocation core region, which is heavily distorted and represents the highest-energy part of the dislocation, can be replaced partially or wholly by the incoherent or semi-coherent interface of the nucleus, thereby eliminating a substantial amount of core energy without the need to create additional interface area. Cahn's analysis [34] of incoherent nucleation on dislocations parameterised this reduction through a factor $f(\alpha) \in [0, 1]$, where α is a dimensionless measure of the dislocation-nucleus interaction energy relative to the interfacial energy, so that the effective barrier becomes:

$$\Delta G^*_{\text{het}} = f(\alpha)\, \Delta G^*_{\text{hom}}, \tag{1.5}$$

with $f(\alpha) \to 0$ as the interaction becomes dominant and $f(\alpha) \to 1$ in the absence of interaction (recovering the homogeneous limit) [173].

As for lattice instability nucleation model, it states that restoring force against a structural distortion vanishes and the transformation barrier disappears entirely, which represents the opposite extreme from classical nucleation and is physically distinct from both homogeneous and defect-assisted heterogeneous mechanisms. The thermodynamic condition for lattice

instability is the vanishing of one or more elastic stiffness constants, or more precisely of their appropriate combination for a given deformation mode. Zener [225] first noted that BCC crystals with a small value of the elastic anisotropy parameter(called Zener ratio):

$$S = \frac{2C_{44}}{C_{11} - C_{12}} \tag{1.6}$$

are susceptible to shear instabilities toward close-packed structures, and that S decreases systematically toward the martensitic transformation temperature in many alloy systems [173]. More generally, the soft-mode or phonon-instability picture of martensitic nucleation, developed by Zener, Clapp, Cook [173], treats the structural fluctuations giving rise to the new phase as elastic waves whose free energy cost is proportional to the relevant soft elastic constant. As that constant softens toward zero, the free energy barrier for fluctuations in the transformation direction vanishes, and the parent phase becomes absolutely unstable against the transformation – the strain spinodal limit. In this non-classical picture, the activation barrier $\Delta G^{\ddagger}$ diminishes continuously as the instability is approached [161].

It is important to emphasize that in real metallic alloys, especially metastable Ti alloys we investigated in this thesis, the lattice instability mechanism does not operate in isolation from structural defects. Rather, dislocations, stacking faults, and grain boundaries interact with the soft elastic modes of the parent lattice in a synergistic fashion: pre-existing defects concentrate local strain and shift the local composition or stress state in a manner that drives the local value of the relevant elastic constant toward zero before the bulk average does so [173]. The coupling between dislocation structures and phonon instability provides a physically consistent explanation for martensitic nucleation in metallic systems. In most cases, martensitic nucleation is heterogeneous because it starts from pre-existing defects. However, it also shows features of a collective lattice instability, such as the strong sensitivity of M_{s} to composition and the sharp onset of transformation. This behavior cannot be fully described as a purely thermally activated, site-by-site nucleation process. Instead,

heterogeneous nucleation in solids should be viewed as a spectrum. At one limit, defects assist classical barrier crossing. At the other limit, defects enhance a lattice instability that is already close to occurring. Which regime dominates depends on alloy composition, temperature, and the character of the available defect population. This perspective provides the theoretical foundation for the nucleation models developed in the present thesis.

1.3.6 Twin Boundary Migration

The preceding section, we introduce the heterogeneous nucleation models that describe the early stage nucleation of phase transformation and deformation twinning. From macroscopic view, the nucleation of these defects strongly correlated with elastic limit and yield strength of alloys. Once nucleates, a following step is dynamic growth. Investigation of twin growth is both scientifically interest and engineering important. From scientific point of view, in metatstable Ti alloy systems, growth of deformation twinning is abnormal compared to conventional BCC alloys since experiments always observe unusual phase transformation at twin boundary [215, 114, 113]. From engineering point of view, growth of deformation twinning exerts a profound indirect influence on mechanical behavior through two effects. First, each newly formed twin boundary acts as a planar obstacle to dislocation glide and thereby increasing the effective Hall–Petch-type strengthening as the twin density increases during deformation. This is the mechanism underpinning the remarkable strength–ductility synergy achieved in twinning-induced plasticity (TWIP) steels and alloys, where sustained twinning throughout deformation maintains a high strain hardening rate and delays plastic instability [123]. Second, twin boundaries can serve as preferential sites for crack initiation, particularly when twin–twin or twin–grain boundary intersections produce high local stress concentrations, which is a significant consideration in the fatigue and fracture behavior of twinning-prone alloys [123].

The theoretical framework for twin growth distinguishes two physically distinct processes: lateral propagation of the twin boundary in the twinning plane, and thickening of the twin

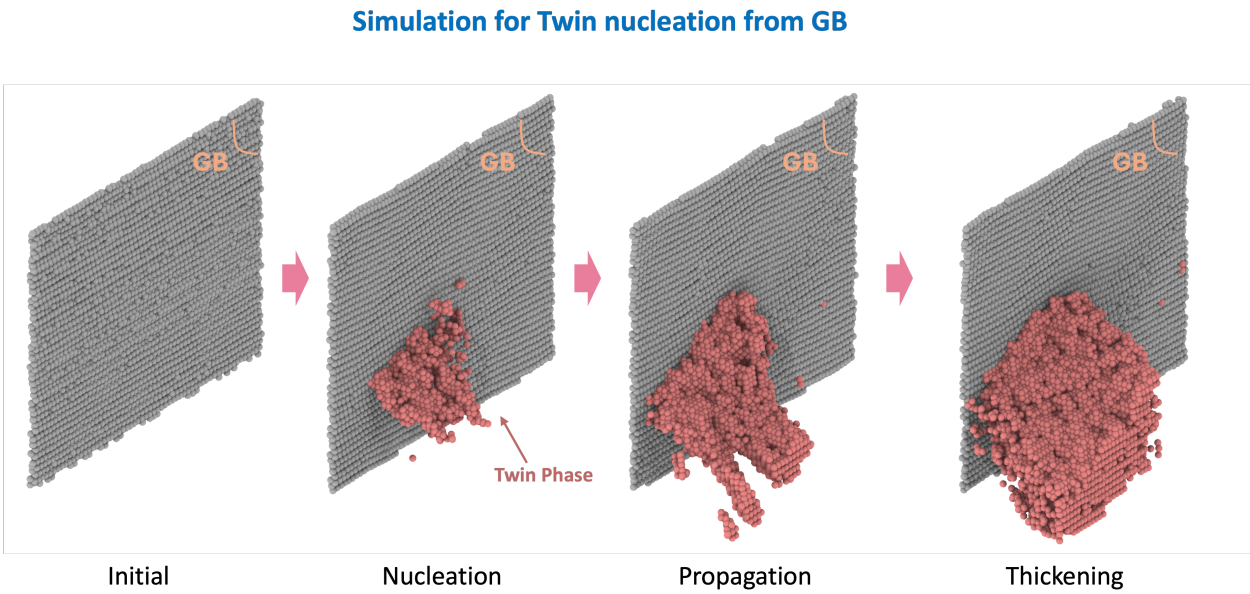


Figure 1.4: Simulation snapshots of early-stage twin nucleation and growth near a grain boundary. Grey atoms are at grain boundary while red atoms are in twin phase.

normal to K_1. As shown in Figure 1.4, lateral propagation is generally rapid and governed by the glide mobility of twinning partial dislocations along K_1, carrying a shape-change analogous to a dislocation sweeping its slip plane. Twin thickening, by contrast, requires the successive addition of new twinning layers and constitutes the kinetically limiting step.

Following classical twin growth theory, thickening proceeds by the thermally-assisted nucleation of closed twinning dislocation loops on the existing twin boundary, with an activation energy [46]:

$$W_c = \frac{\pi \mu b_t^2}{2} \ln\left(\frac{R_c}{r_i}\right) - \pi R_c^2 \tau b_t, \tag{1.7}$$

where μ is the shear modulus, b_t is the twinning partial Burgers vector, R_c is the critical loop radius, r_i is the dislocation core radius, and τ is the resolved shear stress on K_1 [46]. The critical radius and associated activation energy are set by $\partial W/\partial R = 0$, yielding $R_c = \mu b_t/(2\tau)$ and $W_c \propto \mu b_t^2/\tau$. In practice, for twinning dislocations in cubic metals where $b_t \sim a/6\langle 111\rangle$ is of the order of one-third of the interatomic spacing, the spontaneous thermal nucleation rate is negligibly small, and alternative growth mechanisms -pole mechanisms,

cross-slip sources, and grain boundary emission are required to sustain thickening [46, 123]. This can be summarized by the well-known layer-by-layer twin growth mechanism, as shown in Figure 1.5. From energetic aspects, Vitek modifies the well-known layer-by-layer growth mechniasm and suggested that [199] the non-planar core structure of the $1/2\langle 111\rangle$ screw dislocation in many stable BCC materials imposes an additional constraint: a single $b_t = 1/6\langle 111\rangle$ twinning partial is intrinsically unstable (its stacking fault energy is 1.6–9.4 times that of a full dislocation), so twin thickening in BCC proceeds in a discrete fashion, advancing $3n$ atomic layers ($n = 1, 2, \ldots$) at a time through the cooperative glide of dislocation: a stable bundle of three $1/6\langle 111\rangle$ twinning partials on adjacent $\{112\}$ planes [123].

In metastable β Ti alloys, though twin growth dynamics also follow propagation within twinning plane and thickening along twinning normal plane, it is not simply dislocation and kink-pair mediated. Instead, reversible phase transformations plays important roles. For example, experimental evidence has confirmed that the $\{112\}\langle 111\rangle$ twin boundary in metastable β-Ti alloys is not a sharp crystallographic interface but rather carries a transitional ω-phase layer whose thickness varies with local stress and composition [123, 39]. In this picture, twin thickening proceeds not by twinning-partial glide but by a sequential interfacial atomic shuffle: a cooperative $\beta_M \rightarrow \omega_T \rightarrow \beta_T$ structural transformation. The β matrix (β_M) first shuffles to a transient ω-like configuration, then reverses to the twin orientation β_T [39]. Because the shuffle involves no macroscopic shear and no dislocation translation, its kinetics are governed by the energy barriers along the shuffle pathway, rather than by the Peierls resistance of twinning partials. This regime can be directly studied using atomistic calculations, for example through the Generalized Planar Fault Energy (GSFE) surface. However, it is difficult to describe using classical continuum theories of twin growth. Therefore, a central question in this thesis is how phase transformation couples with twin growth kinetics in metastable β-Ti alloys. Another key question is which energetic parameters control the competition between shear-based growth and shuffle-mediated growth pathways.

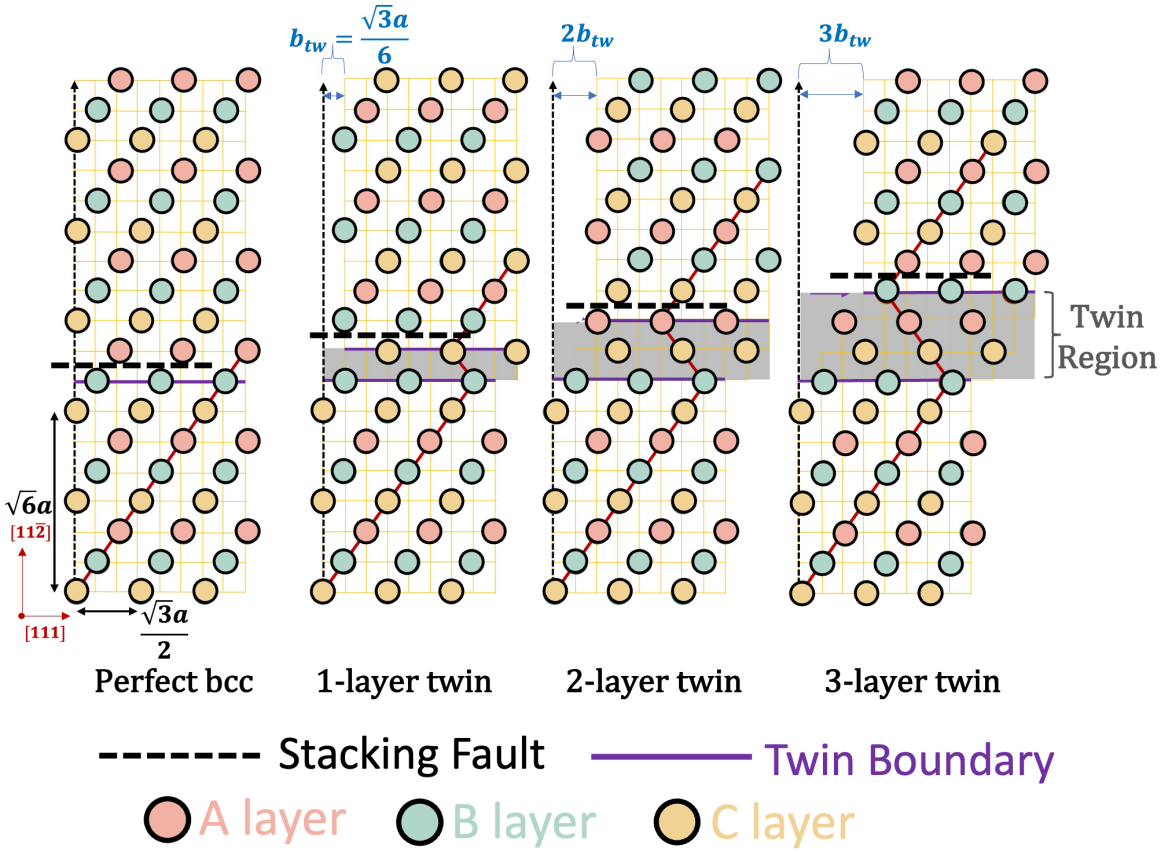


Figure 1.5: Schematic draw on the layer-by-layer growth mechanism of {112} twin in conventional BCC alloys. In BCC lattice, atoms in {112} planes follow ABCABC... stacking sequence along ⟨112⟩ directions, different colors of atoms indicate different stacking planes. Balck dased lines indicate stacking fault created by dislocation dissociation on successive {112} planes. Purple lines indicate the location of twin boundary while gray region redicates twin phase.

1.4 Computational methods

1.4.1 DFT Calculations

Density functional theory (DFT) is a quantum mechanical framework for computing the ground-state electronic structure and total energy of a many-body system from first principles, without reliance on empirical parameters. Its theoretical foundation rests on the two Hohenberg–Kohn theorems [90]: the first establishes that the ground-state total energy E of an interacting electron system in an external potential $v(\mathbf{r})$ is a unique functional of the ground-state electron density $n(\mathbf{r})$ alone; the second guarantees that the true ground-state density minimizes this functional. The computationally tractable form of DFT is provided by the Kohn–Sham scheme [104], which maps the interacting many-electron problem onto an equivalent system of non-interacting electrons moving in an effective potential, yielding a set of self-consistent single-particle equations:

$$\left[-\frac{\hbar^2}{2m}\nabla^2 + v_{\text{ext}}(\mathbf{r}) + v_{\text{H}}(\mathbf{r}) + v_{\text{xc}}(\mathbf{r})\right]\psi_i(\mathbf{r}) = \varepsilon_i\,\psi_i(\mathbf{r}), \tag{1.8}$$

where v_{ext} is the external (ionic) potential, v_{H} is the classical Hartree electrostatic potential of the electron density, and $v_{\text{xc}} = \delta E_{\text{xc}}[n]/\delta n$ is the exchange-correlation potential, which is the only term requiring approximation. The electron density is reconstructed self-consistently from the occupied Kohn–Sham orbitals: $n(\mathbf{r}) = \sum_i |\psi_i(\mathbf{r})|^2$, and the total energy is:

$$E[n] = T_s[n] + \int v_{\text{ext}}(\mathbf{r})\, n(\mathbf{r})\, \mathrm{d}^3r + E_{\text{H}}[n] + E_{\text{xc}}[n], \tag{1.9}$$

where T_s is the kinetic energy of the non-interacting reference system and E_{H} is the Hartree energy [104]. In practice, the exchange-correlation energy $E_{\text{xc}}[n]$ is approximated using the generalised gradient approximation (GGA), most commonly in the Perdew–Burke–Ernzerhof (PBE) parameterisation [167], which captures both local and gradient-dependent contributions to exchange and correlation with a computational cost that scales favorably

with system size.

In the context of the present thesis, DFT calculations are employed to investigate the intrinsic phase transformation at twin boundary, and coupling of twin stability with phase transformation at the atomistic scale in metastable β-Ti alloys.

1.4.2 MD Simulations

1.4.2.1 MD Methods

Molecular dynamics (MD) simulation is a computational method that resolves the classical time evolution of a many-body system by numerically integrating Newton's equations of motion for each atom:

$$m_i \ddot{\mathbf{r}}_i = \mathbf{F}_i = -\frac{\partial \mathcal{U}(\{\mathbf{r}_j\})}{\partial \mathbf{r}_i}, \tag{1.10}$$

where $\mathbf{m}_i$ and $\mathbf{r}_i$ are the mass and position of atom i, and $\mathbf{F}_i$ is the force derived from the interatomic potential energy $\mathcal{U}(\{\mathbf{r}_j\})$: a function of the instantaneous positions of all atoms in the system [2]. Given an initial configuration and velocity distribution (drawn from a Maxwell-Boltzmann distribution at the desired temperature), Equation (1.10) is integrated forward in time using a symplectic algorithm with a time step $\Delta t \sim 1$–$2\,\mathrm{fs}$, which is short enough to resolve the fastest atomic vibrations while conserving the total energy to acceptable precision.

The physical justification for treating atomic motion classically rests on the Born-Oppenheimer approximation [21, 22]: because the electron mass is three to four orders of magnitude smaller than any nuclear mass, electrons respond to nuclear displacements quasi-instantaneously and can be assumed to remain in their ground state at all times. The nuclear dynamics therefore unfold on a single potential energy surface $\mathcal{U}(\{\mathbf{r}_j\})$ – the ground-state electronic energy as a function of nuclear coordinates – and the full electron–nuclear problem is decoupled into a quantum-mechanical electronic problem (solved once, yielding $\mathcal{U}$) and a classical nuclear dynamics problem (solved by integrating Eq. (1.10)) [21]. This

separation is the theoretical foundation that makes both DFT total-energy calculations and MD force-field simulations physically consistent: DFT provides the Born–Oppenheimer surface from first principles, while MD explores its topology at finite temperature and stress through classical trajectories.

The accuracy of any MD simulation rests critically on the quality of the interatomic potential $\mathcal{U}$: for metallic systems, the embedded-atom method (EAM) and its extensions provide the most widely used functional form [54]:

$$\mathcal{U} = \sum_i F_i(\rho_i) + \frac{1}{2}\sum_{i\neq j} \phi_{ij}(r_{ij}), \tag{1.11}$$

where $\phi_{ij}(r_{ij})$ is a pairwise repulsion between atoms i and j at separation r_{ij}, $\rho_i = \sum_{j\neq i} f_j(r_{ij})$ is the local electron density at site i contributed by its neighbors, and $F_i(\rho_i)$ is the embedding energy representing the quantum-mechanical cost of placing atom i into that electron density [54]. By construction, the EAM captures the many-body character of metallic bonding: the environment-dependent bond weakening that pair potentials cannot reproduced. By this way, EAM potential has been shown to describe elastic constants, phonon dispersions, stacking fault energies, and surface energies of transition metals in good quantitative agreement with DFT calculations when the potential is carefully fitted to a suitable training set. For multi-component alloy systems such as metastable β-Ti alloys, specialized bond-order or machine-learning interatomic potentials trained against DFT energy landscapes offer further improvement, particularly for capturing the energy differences between competing structural phases (β, α'', ω) whose relative stability are sensitive to small changes in composition and local configuration [188].

The central strength of MD as a tool for studying phase transformations, twin nucleation, and twin growth kinetics is its ability to access atomistic mechanisms at finite temperature under controlled mechanical loading, in a way that neither DFT nor continuum models can. Temperature enters MD naturally through the initial velocity distribution and is maintained during the simulation by a thermostat, typically the Nosé-Hoover scheme, which augments

the equations of motion with a fictitious heat-bath degree of freedom to enforce canonical (NVT) sampling with minimal perturbation to the dynamics [92]. Pressure and stress state are controlled through the Parrinello–Rahman or related barostat, which allows both the atomic positions and the simulation cell shape to evolve, enabling the system to accommodate the volumetric and deviatoric strains associated with a martensitic transformation or the passage of a twinning front without artificial constraint [165]. The composition dependence of phase stability and transformation kinetics is straightforwardly explored by constructing supercells with varying alloy compositions as random solid solutions and comparing the transformation behavior across the composition series. Mechanical loading is imposed either by applying a homogeneous strain to the simulation box at a controlled strain rate, or by prescribing a stress tensor via the barostat, and the transformation strain to be extracted directly. Together, temperature, composition, and stress state define the three-dimensional external parameter space within which the competition between dislocation slip, stress-induced martensitic transformation, and deformation twinning unfolds in metastable β-Ti alloys, and MD is uniquely positioned to map this competition at the atomic scale.

In the context of the present thesis, MD simulations serve two complementary roles. First, they are used to investigate the temperature- and composition-dependent phase transformation kinetics and twin nucleation processes in metastable β-Ti alloys at the atomic scale. By resolving the structural evolution at transformation fronts and twin boundaries, we capture the α'' or ω transitional structures that mediate twinning as described in the preceding section, and identifying the operative nucleation pathways and their associated energy barriers under conditions inaccessible to static DFT calculations (finite temperature, dynamic loading, large system sizes with realistic defect populations). Second, MD simulations of twin boundary migration under controlled shear loading provide the composition and temperature dependent twin growth stress. Meanwhile, MD can help reveal the interficial structural evolution at twin boundary during migration. In this way, insights from MD simulations help develop the theoretical model for twinnability. The theoretical model further bridges the

gap between atomic behaviors and the continuum-level kinetic and thermodynamic models, completing the multi-scale computational framework of this thesis.

1.4.2.2 Metadynamics

We here introduce metadynamic methods to explore the phase transformation barrier close to minimum energy path. Conventional MD is fundamentally limited by timescale: the femtosecond integration step constrains accessible simulation times to the microsecond regime at most, which means that thermally activated processes with barriers significantly larger than $\sim 10\, k_{\mathrm{B}}T$ are never observed within a tractable simulation. For the study of phase transformation nucleation in metastable β-Ti alloys, this is a critical limitation: the nucleation of the α'' martensite or ω phase from the β matrix involves crossing free energy barriers that are precisely in this thermally inaccessible regime under the temperatures and stresses of experimental interest. Metadynamics [49, 115], an enhanced sampling method developed by Laio and Parrinello, overcomes this limitation by augmenting the physical potential energy surface with a history-dependent bias potential $V_G(\mathbf{s}, t)$ that progressively fills the free energy basins already visited:

$$V_G(\mathbf{s}, t) = \sum_{t'<t} w \exp\left(- \sum_{\alpha} \frac{\left[s_\alpha - s_\alpha(t') \right]^2}{2\delta s_\alpha^2} \right), \tag{1.12}$$

where $\mathbf{s} = \{s_\alpha\}$ is a low-dimensional set of collective variables (CVs) that parameterise the relevant structural degrees of freedom, w is the deposition height of each Gaussian hill, and δs_α is its width along each CV direction [115]. As the simulation proceeds, the accumulating bias discourages the system from revisiting previously explored configurations and drives it over the free energy barriers that would otherwise trap it. In the long-time limit, the bias potential $V_G(\mathbf{s}, t)$ converges to the negative of the true free energy surface (FES) projected onto the CV space:

$$F(\mathbf{s}) = - \lim_{t \to \infty} V_G(\mathbf{s}, t) + \text{const.}, \tag{1.13}$$

thereby yielding the free energy barriers $\Delta F^{\ddagger}$ between the parent and product phases directly, rather than requiring them to be inferred indirectly [115]. Well-tempered metadynamics [10] refines this scheme by gradually reducing the deposition height as $w(t) = w_0 \exp(-V_G/k_B \Delta T)$, where ΔT is a bias temperature parameter, which improves convergence and reduces the statistical error in the recovered free energy surface. A shcematical draw on the enhanced sampling method is shown in Figure 1.6.

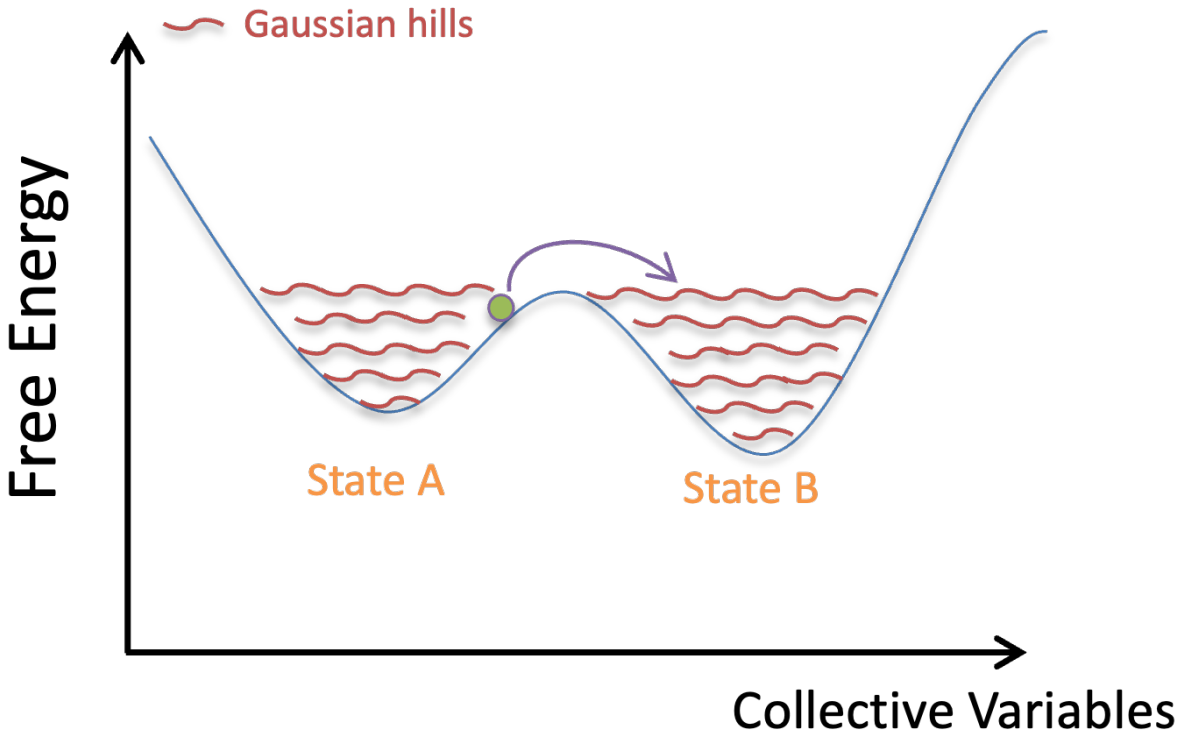


Figure 1.6: Schematic illustration of Free energy landscape exploration via Metadynamics.

The choice of collective variables is the central challenge in applying metadynamics to structural phase transformations. For the $\beta \rightarrow \alpha''$ and $\beta \rightarrow \omega$ transformations in metastable β-Ti alloys, appropriate CVs must capture the essential structural changes: the lattice distortion (such as shear components in phase transformation strain tensor), and the atomic shuffle amplitude that accompanies the transformation. By constructing CVs from combinations of these structural order parameters, metadynamics simulations can reconstruct

the two-dimensional free energy surface as a function of both transformation strain and shuffle coordinate, revealing the height and location of the saddle point that separates the metastable β basin from the α'' or ω product basin at arbitrary temperature and composition. In the present thesis, this approach is employed to extract the temperature- and composition-dependent transformation free energy barriers in metastable β-Ti alloys, providing the kinetic barrier parameters that enter the thermodynamic nucleation model and cannot be accessed by static DFT calculations or conventional MD alone.

1.4.3 PF Modeling

Finally, we brief introduce Phase-field (PF) modeling method, though we do not employ it in this thesis, the insights for twin migration and nucleation model for twin in this thesis can serve as inputs to Phase-field ((PF) modeling to investigate microstructure evolution in mesoscale.

Phase-field (PF) modeling describes the evolution of a microstructure through a set of spatially and temporally continuous order parameter fields $\{\eta_i(\mathbf{r}, t)\}$, each representing the local structural state of the material. For instance, the degree of transformation from the β-phase to a specific α'' or ω variant, or the presence of a particular twin domain [40]. Rather than tracking individual atoms or explicitly resolving interfaces as sharp boundaries, PF regularities all interfaces as diffuse regions of finite width, described by smooth gradients in the order parameter fields. The free energy functional of the system is written as:

$$\mathcal{F}[\{\eta_i\}] = \int_V \left[f_{\text{chem}}(\{\eta_i\}) + \sum_i \frac{\kappa_i}{2} |\nabla \eta_i|^2 + f_{\text{elast}}(\{\eta_i\}, \boldsymbol{\varepsilon}) \right] \mathrm{d}V, \tag{1.14}$$

where f_{chem} is the local chemical free energy density (a multi-well Landau polynomial whose minima correspond to the stable or metastable phases), $\kappa_i |\nabla \eta_i|^2/2$ is the gradient energy penalty that assigns a finite energy cost to interfaces and determines their width, and f_{elast} is the elastic strain energy density arising from the transformation eigenstrain

associated with each variant [40, 99]. The temporal evolution of each order parameter field is governed by the time-dependent Ginzburg–Landau (TDGL) equation:

$$\frac{\partial \eta_i(\mathbf{r},t)}{\partial t} = -L_i \frac{\delta \mathcal{F}}{\delta \eta_i(\mathbf{r},t)}, \tag{1.15}$$

where L_i is a kinetic coefficient that governs the rate of order parameter relaxation and is directly related to the interface mobility [40]. Because PF solves Eqs. 1.14–1.15 on a mesoscale computational domain, it can capture the collective dynamics of many interacting twin domains and transformation variants. These dynamics include variant impingement, domain coarsening, and elastic accommodation between neighboring variants. PF can also describe the feedback between transformation strain and the nucleation of subsequent variants. These processes are difficult to access with atomistic simulations because the required domain is too large. They are also difficult to treat with analytical models because the geometry and variant interactions are too complex. Although phase-field modeling is not directly employed in the present thesis, the atomistic and thermodynamic quantities derived herein constitute precisely the set of physically grounded inputs (κ_i, L_i, f_{chem}) that PF requires to simulate dynamic microstructure evolution in metastable β-Ti alloys at the mesoscale. The multiscale framework established in this thesis therefore provides a direct and physically consistent pathway toward predictive phase-field modeling of TRIP- and TWIP-active microstructure evolution under realistic thermomechanical processing conditions. The insights and models derived from this multiscale modeling framework is beneficial to both scientific understanding on complex defects evolutions in Ti alloy systems and industrial Ti alloy processing and design.

CHAPTER 2

Stability and Growth Kinetics of {112} Twin

$\{112\}\langle 11\bar{1}\rangle$ deformation twin, shortened as {112} twin, is usually the dominant twinning mode in transition metal alloys in a body-centered cubic (BCC) lattice except for many BCC β titanium (Ti) alloys. To understand this twin-mode variation, we investigate stability and early-stage growth kinetics of {112} twin embryos with multiple atomic layers in a series of β-Ti alloys by applying density functional theory (DFT) and classical atomistic simulations. Both simulation methods demonstrate that, as average valence electron concentration (VEC measured in a unit of e/a) of Ti alloys decreases, $\beta \rightarrow \omega$ phase transformations at {112} twin boundaries, which are confirmed by our transmission electron microscopy characterizations, increase the critical thickness of {112} layers as stable twin embryos, possibly raising {112} twin nucleation energy barriers. In simulations of twin embryo growths under applied shear stress on {112} planes, when VEC (or temperature) values are low ($\sim$4.25 e/a at 300 K), the applied shear stress results in β twin $\rightarrow$ α'/α" phase $\rightarrow$ β matrix phase transformations through an anti-twinning mechanism inside the existing twin embryos; concurrently, ω phases strongly impede the twin boundary migration; these combined effects result in eliminations of {112} twin embryos. However, when VEC increases slightly ($\sim$4.34 e/a at 300 K), ω phases at twin boundaries reduce the required stress for {112} twin embryo growth compared with the cases with high VEC values (e.g., $\sim$4.50 e/a at 300 K). These changes of ω effects on {112} twin embryo growth kinetics could originate from free energy landscape variations of β matrix $\rightarrow$ ω phase $\rightarrow$ β twin phase transformations.

2.1 Introduction

β titanium (Ti) alloys in body-centered cubic (BCC) lattice are important for many industrial applications [179, 27, 8, 134, 30], such as aerospace, healthcare, and power generations [134, 8, 120, 152]. Depending on thermomechanical processes, phases with different crystal structures can be observed in β-Ti alloys, e.g., β phase in BCC lattice, α' phase in hexagonal close-packed (HCP) structure, α" phase in an orthorhombic lattice, and ω phase in a hexagonal lattice. The diffusionless transformations between β and other phases can induce large plastic strain, which is the underlying mechanism of the shape memory effect and superior plasticity in some β-Ti alloys [53, 229, 103, 102, 174]. There are also multiple types of deformation twinning modes in β-Ti alloys that may play different roles in plastic deformation depending on alloy compositions and deformation conditions [229, 53]. For example, $\{112\}\langle 11\bar{1}\rangle$ twin (shortened as $\{112\}$ twin in the following sections), commonly observed as the major deformation twinning mode in conventional BCC transition metals [238], is not the leading twinning mode in many β-Ti alloys [114, 51, 125, 185, 89]. Meanwhile, twinning modes with highly-indexed (Miller indices larger than 2) twin-boundary planes (so-called highly-indexed twinning), especially $\{332\}\langle 11\bar{3}\rangle$ twin (shortened as $\{332\}$ twin in the following sections), can be activated and act as the dominate twinning mode in many β-Ti alloys [81, 16, 80, 79, 189, 185]. Extensive studies have shown the exceptional performances of highly-indexed twinning in improving mechanical properties of β-Ti alloys [81, 138, 163, 139, 141, 185]. For example, Hanada et al. reported that the $\{332\}$ twin can produce high work hardening rate and further significantly improve the ductility of slip-dominated β-Ti alloys [81]. Min et al. found that $\{332\}$ twin combined with dislocation slip can effectively improve the yield strength and greatly enhance uniform elongation [138].

However, a lack of clear understanding of the origin and the mutual competitions of $\{112\}$, $\{332\}$, and other highly-indexed twins impedes the efforts to improve the mechanical properties of β-Ti alloys. Recently, many studies reported hierarchical twin structures, which

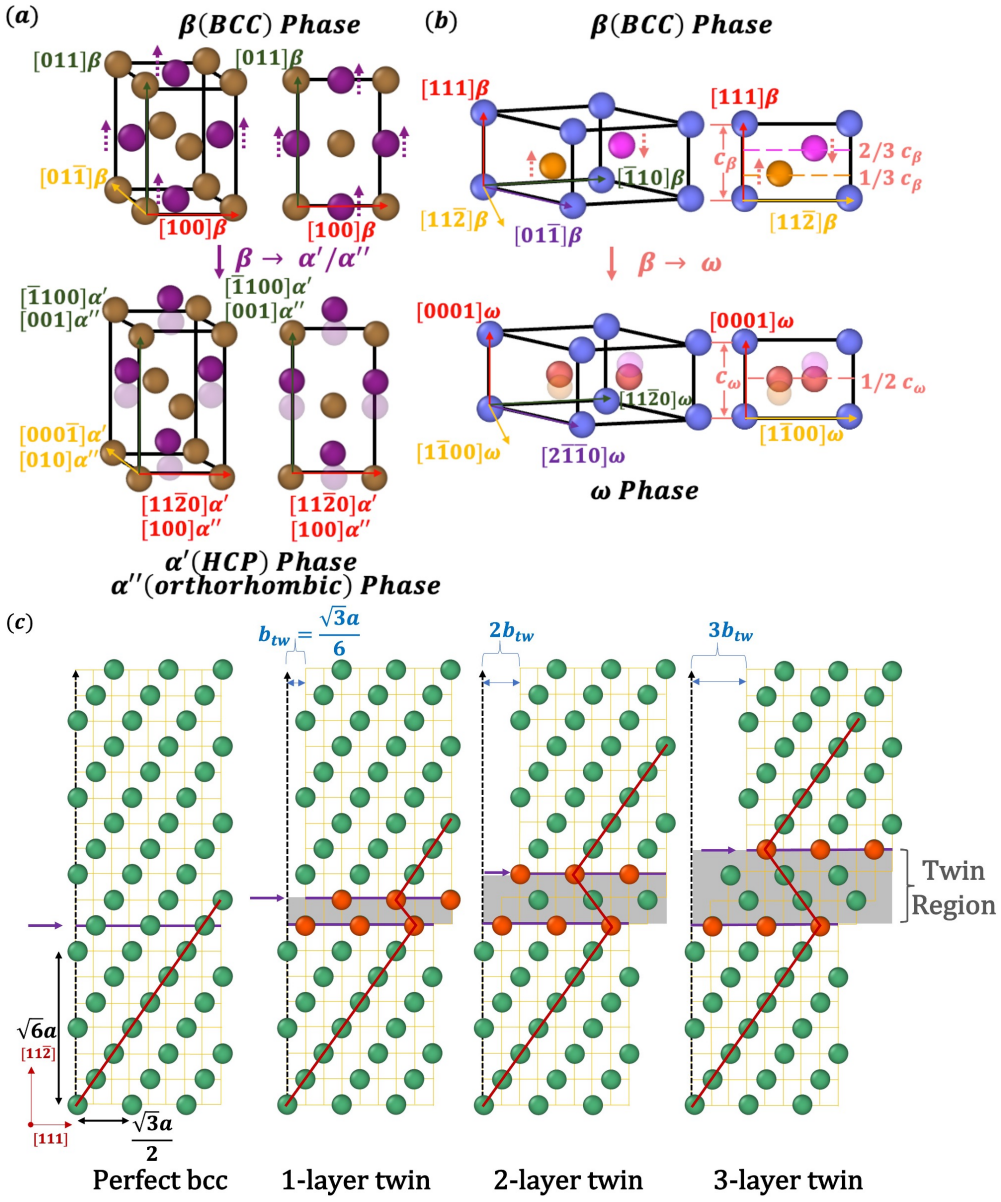


Figure 2.1: Illustrations of atomistic structures related to possible diffusionless phase transformation and twinning in BCC lattice. (a) Schematic draw for crystal structures of β (BCC), α' (HCP), α" (Orthorhombic) phases and the corresponding diffusionless transformation pathways. Brown and purple atoms are at A and B stacking of $\{01\bar{1}\}$ layers in BCC lattice, respectively. (b) The schematic draw for β to ω phase diffusionless transformation. Blue, orange, and magenta atoms are at A, B, and C stacking of $\{01\bar{1}\}$ layers in BCC lattice, respectively. Blue and rose atoms are at A and B stacking of (0001) layers in ω phase, respectively. (c) $\{112\}$ twin formation through a layer-by-layer twin dislocation slip mechanism. Grey shape indicates the $\{112\}$ twin region. Green and red atoms are in BCC lattice and at $\{112\}$ twin boundaries, respectively. Here a is the lattice constant and $b_{\text{tw}} = \frac{1}{6}\langle 111\rangle$ is the $\{112\}$ twin Burgers vector.

are composed of multiple types of twinning modes with different volumetric ratios, at the early stage of {332} twin formation. Mantri et al. observed a secondary {112} twin inside {332} twin by a tensile tested Ti-12 wt.% Mo alloy samples [131]. Sun et al. carried out experiments to show that both {112} and {332} twins are activated simultaneously in Ti–12 wt.% Mo alloy in the early deformation stage (uniaxial tensile loading) [185]. However, how to control the volume fraction of {112} twin and {332} twin in the hierarchical twin structure is still unclear. Current studies agree that twin system selection is controlled by the Schmid factor [53, 229, 11, 113, 71], but it is still unclear how materials properties (e.g., composition) and external conditions (e.g., temperature, engineering strain rate) affect the critical resolved shear stress for a particular twin mode. Meanwhile, there is a lack of quantitative investigations on the role of {112} twin in the formation mechanism of the hierarchical twin structures and how these hierarchical twin structures further affect the mechanical behavior of β-Ti alloys. Thus, to fully understand the variation of deformation twin modes and the related impacts on the mechanical behavior of β-Ti alloys, it is critical to first uncover the physical mechanisms of the {112} twin nucleation and early-stage growth kinetics in β-Ti alloys. These mechanisms may result in the rare appearances of {112} twins and promote the alternative highly-indexed twins in β-Ti alloys depending on alloy compositions and deformation conditions.

In many BCC transition metals and alloys, {112} twin nucleation and growth can be explained by the formation and glide of twin dislocations [50, 46, 65, 201]. The first dislocation model for {112} twin in BCC metals is called the Cottrell–Bilby model [50], which proposed that a stress-assisted dissociation of a sessile $\frac{1}{2}\langle 111\rangle$ screw dislocations on {112} planes results in a $\frac{1}{3}\langle 112\rangle$ sessile and a $\frac{1}{6}\langle 111\rangle$ glissile partial dislocations, and the twin further nucleates from this monolayer fault nucleus. Later, it was realized that the dissociation process in the Cottrell–Bilby model is not energetically favourable [180]. Meanwhile, Mahajan et al. conducted experiments to prove that twins should be nucleated by screw dislocations [130]. Based on this observation, Sleeswy et al. modified the Cottrell–Bilby pole

model and proposed that a {112} twin nucleus can be formed by dissociation of a $\frac{1}{2}\langle 111\rangle$ screw dislocation into three $\frac{1}{6}\langle 111\rangle$ partial dislocations located on {112} planes [180]. This model is widely accepted and the formation of twin embryos can be achieved by the glide of $\frac{1}{6}\langle 111\rangle$ partial dislocations on adjacent {112} planes under applied shear stress to generate {112} atomic layer faults [166, 29]. Furthermore, Vitek confirmed that in order to form a metastable {112} twin embryo, the minimum number of {112} atomic layer faults should be three [198]. Once the twin embryo is stabilized, it can further grow through a layer-by-layer mechanism by slipping more {112} planes along the $\langle 111\rangle$ direction [197]. Ogata et al. used DFT calculations to evaluate {112} twin embryos for BCC Mo metals by calculating the twinning energy landscape, suggesting that Mo twin can grow in a layer-by-layer fashion after the twin embryo reaches five {112} layers [156]. Ojha et al. adopted similar theoretical methods and further provided both computational and experimental results for twin embryos of other metals and alloys, e.g., Fe, V, Nb, Ta, W, Fe-Si alloys, Fe-Ni alloys, and Fe-V alloys, showing the minimum thickness of twin embryos indeed changing with alloy types and compositions [157].

Structures and growth kinetics of {112} twins in β-Ti alloys are more complex than those in other BCC transition metals and alloys. The local stress and strain accumulated at twin boundaries can activate the metastable phase transformations [125], which can play an important role in the nucleation and growth of {112} twins. It is widely acknowledged that β to ω phase transformation is activated at {112} twin boundaries [114, 132, 37, 215, 112, 218, 121, 124, 216, 169, 52, 239, 125]. Recently, many studies indicate that reversible phase transformations between β and ω phases have a close relationship with {112} twin nucleation and growth [114, 215, 124, 132], but they are still in a debate on the detailed mechanisms. Wu et al. proposed that ω phase can promote {112} twin formation and growth in β-Ti alloys. They suggested that switch between β phase and ω phase could be the driving force for {112} twin nucleation and growth [215], since they observed {112} twins nucleate and grow inside the nanoscale ω phase in Ti-30Nb-3Pd (wt.%) (VEC=4.275) alloy. Meanwhile,

they argued that structurally ω phase has an equal probability to transfer back to BCC matrix or BCC twin, indicating that ω phase can serve as an intermediate state for twin growth. However, Chen et al. [37] argued that ω may not promote {112} growth, and the probability of transformation of ω phase to BCC twin is less than 0.5 because distorted ω phase prefers to transform back to the BCC matrix rather than to BCC twin. Moreover, Wu et al. observe a high density of ω phases in Ti-30Nb (wt.%) (VEC=4.18) after quenching from solid-solution treatment condition at 900 °C for 1h but no {112} twins can be found [215], which suggests that ω phase does not promote {112} formation and growth in this alloy.

To reconcile the above debates, the aim of this study is to enhance our understanding of how diffusionless phase transformations affect the stability and growth kinetics of {112} twin embryos in β-Ti alloys. To achieve this goal, we employ both density functional theory (DFT) calculations and atomistic simulations based on classical interatomic potentials to determine the stability of twin configurations in various compositions and elements. Additionally, we investigate the growth kinetics of stable twin embryos under applied shear stress on {112} twin planes in β-Ti alloys at different temperatures using atomistic simulations. Both DFT and atomistic simulation results demonstrate that, as the valence electron concentration (VEC) of Ti alloys decreases with varying alloy compositions, the $\beta \rightarrow \omega$ phase transformations at {112} twin boundaries increase the critical thickness of {112} layers as stable twin embryos, possibly raising energy barriers of {112} twin nucleation events.

In addition, our atomistic simulations show that, as the thermodynamic stability of β phase is reduced as the VEC and/or temperature is below critical values ($\sim$4.25 e/a at 300 K), the applied shear stress that should drive the {112} twin growth can result in β twin $\rightarrow \alpha$'/α" $\rightarrow \beta$ matrix phase transformations inside the existing twin embryo and ω phases at the twin boundaries impede the twin boundary migration simultaneously, leading to the detwinning behavior to eliminate the {112} twin embryos. When the VEC value increases gradually at a constant temperature (300 K), the applied shear stress can drive

the normal {112} twin growth through twin boundary migrations, but ω phases at {112} twin boundaries can first reduce and then increase the required stress for the growth of the existing stable twin embryo; the minimum required stress for {112} twin embryo growth is observed in a Ti-Nb alloy with an intermediate VEC value ($\sim$4.34 e/a at 300 K). We explain the changes of ω effects on {112} twin embryo growth kinetics by using the free energy landscape variations of β matrix $\rightarrow$ ω phase $\rightarrow$ β twin phase transformations. These findings are useful for understanding the thermodynamic and kinetic factors that result in the rare appearances of {112} twins in many β-Ti alloys. These thermodynamic and kinetic factors can provide effective strategies to manipulate the chemical compositions to tune the {112} twin activities. Similar investigations on the correlations between metastable phase stability and highly indexed twinning modes will be conducted in the future. The generated knowledge together will be utilized to tune the types and ratios of deformation twin modes to improve the mechanical properties of β-Ti alloys.

2.2 Methods

2.2.1 DFT Calculations

Three steps were applied to construct the supercells of β-Ti alloys that contain {112} twin embryos with different thicknesses for investigations of their atomistic structures and energetic stability at 0K. In the first step, we constructed 108-atoms supercells in perfect BCC lattice with orthogonal basis vectors, namely $\frac{3}{2}[111]\times2[\bar{1}10]\times3[11\bar{2}]$, based on the conventional BCC lattice vectors. There are 18 atomic layers along $[11\bar{2}]$ direction, so each {112} layer contains 6 atoms. Meanwhile, the special quasi-random structure (SQS) method was employed to generate lattice occupations of different chemical elements at given compositions [240, 194]. This method optimizes the correlation function of lattice occupations in finite periodic supercells for simulations of random solid-solution alloys. Figure 2.3 (a) shows an example of such an SQS supercell for Ti_3Nb alloy in a perfect BCC lattice before struc-

tural relaxation by DFT calculations. For all 18 $(11\bar{2})$ layers in a supercell, we assigned a number from 1 to 18 as its layer index from the bottom to the top of the supercell along $[11\bar{2}]$ direction plotted in Figure 2.3 (a). We can also shift one atomic $(11\bar{2})$ plane along the $[11\bar{2}]$ direction periodically to generate a "new" supercell with the same SQS-optimized lattice occupations but different layer index numbers (an original Layer n becomes a new Layer $n+1$ (or Layer $n-17$ due to the periodic condition), where n is an integer from 1 to 18). For each SQS-optimized lattice configuration, we can generate 18 supercells with different layer indexes. Correspondingly, we can deform all these supercells to generate twin layers at the same locations (between Layer i and Layer j, where i and j are integers between 1 and 18) in the same SQS-optimized supercell but with different local alloy compositions and occupations.

In the second step, we generated an n-layer $\{112\}$ twin embryo in the middle of the supercell based on a layer-by-layer mechanism [198]. Starting from Layer $9-\frac{n}{2}$ (or Layer $9-\frac{n+1}{2}$ if n is an odd integer), we shifted the upper $(11\bar{2})$ planes along the [111] direction by the length of one twin Burgers vector b_{tw}, which is equivalent to $\frac{1}{6}[111]$, then we shifted all the upper $(11\bar{2})$ planes above Layer $10-\frac{n}{2}$ (or Layer $10-\frac{n+1}{2}$ if n is an odd integer) by two b_{tw}. We repeated this layer-by-layer process until all the upper $(11\bar{2})$ planes above Layer $9+\frac{n}{2}$ (or Layer $9+\frac{n-1}{2}$ if n is an odd integer) by n b_{tw}, Thus, a n-layer twin growth fault was created at the middle of the supercell on successive $(11\bar{2})$ planes as the twin embryo region marked in grey color in Figure 2.1 (c). However, there is still one twin growth fault between the top and bottom layers on the boundary of the supercell along $[11\bar{2}]$ direction. So our third step was to change the supercell by tilting its $[11\bar{2}]$ axis along [111] direction by n b_{tw} to avoid the mismatch at the supercell boundary.

In this study, we generate three different types of twinned supercells with 3, 6, and 9 $(11\bar{2})$ layers of twin embryos in the middle of each supercell. We chose these numbers of layers because Vitek suggested that the minimum number of $\{112\}$ layer faults to form a metastable $\{112\}$ twin embryo should be three in pure BCC metals [198]; We also preferred to choose to

tilt $3m$ b_{tw} (m is an integer) of the $[11\bar{2}]$ supercell axis since $3m$ b_{tw} equal to m full Burgers vector in a perfect BCC lattice. The final supercells with these twin embryos are shown in Figure 2.3 (c), (d), and (e) for 3, 6, and 9 $(11\bar{2})$ layers of twin embryos, respectively. We also provide the schematic draw of this three-step supercell construction process in Figure 2.2. In addition, for each SQS-optimized lattice occupation of a given alloy composition, 18 different configurations of n-layer twin embryo were generated by using all 18 supercells with different layer indexes as mentioned in the first step. Thus, each n-layer twin embryo has different local alloy compositions and occupations, and the average concentrations of all 18 n-layer twin embryos are guaranteed to be equal to the alloy composition in its perfect BCC lattice.

All DFT calculations were performed using the Vienna Ab Initio Simulation Package (VASP) software [108, 106]. We performed Brillouin zone (BZ) k-point sampling using the Γ-centered algorithm with 3×3×2 grids, with a first-order Methfessel-Paxton smearing of 0.2 eV for Brillouin zone integration[136]. Pseudopotentials based on the projector augmented wave (PAW) method were employed for the elemental constituents, with the generalized gradient approximation (GGA) of Perdew-Burke-Ernzerhof (PBE) for exchange-correlation energy functional [167, 107, 18, 108]. The electronic configurations of pseudopotentials for Ti, Nb, V, and Mo were Ti_pv, Nb_sv, V_pv, and Mo_pv, respectively. The corresponding electron configuration is $([\text{Ar}])3s^2 3p^6 3d^2$, $([\text{Kr}])4s^2 4p^6 4d^3 5s^2$, $([\text{Ar}])3s^2 3p^6 3d^2$, $([\text{Kr}])4s^6 4d^4 5s^2$, respectively. We set the energy convergence threshold for all calculations at 10^{-5} eV and used a plane-wave cutoff energy of 350 eV. The methods used for data visualization and analyses for DFT results on structures and energies are from Seaborn, a Python data visualization library [211].

2.2.2 Choices of Alloy Compositions Based on Phase Stability

In this study, we investigated how {112} twin boundaries may induce $\beta \rightarrow \omega$ diffusionless phase transformation and how ω phase could further affect the {112} twin embryo stability

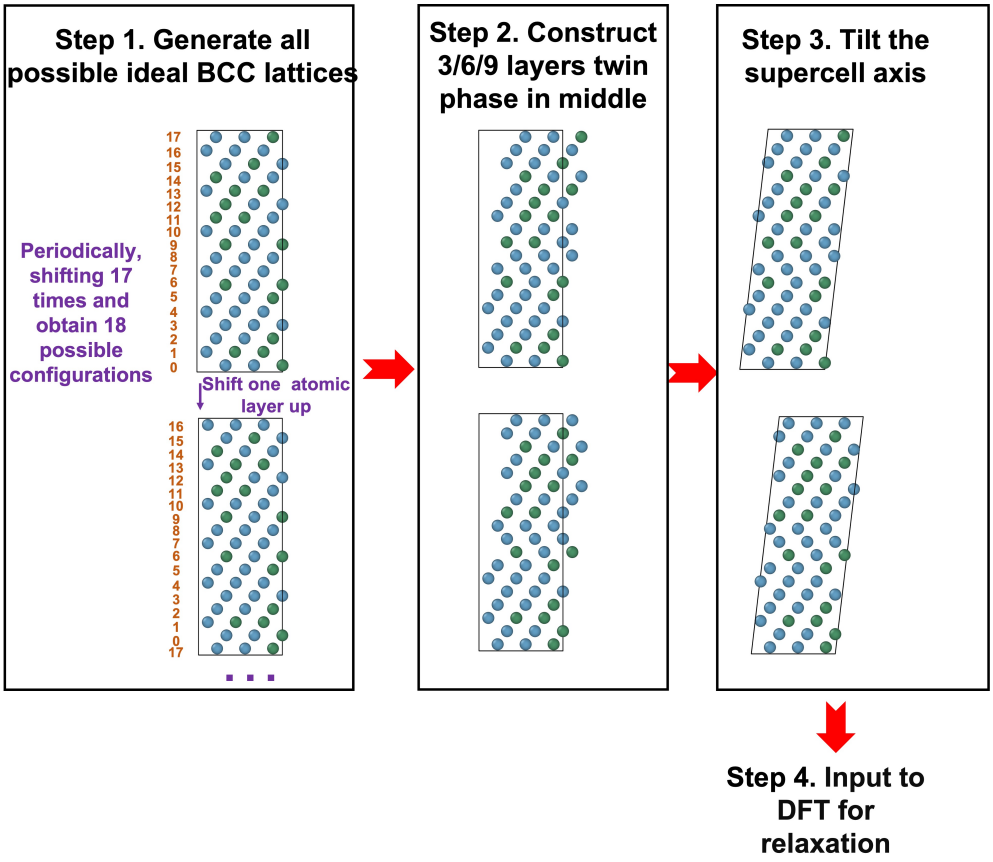


Figure 2.2: Schematic draw for 3-step construction of 3-layer {112} twin embryo structures in 108-atom Ti_3Nb supercells. In the example, blue color represents Ti atoms and green color represents Nb atoms. The first step is to shift one atomic $(11\bar{2})$ plane along the $[11\bar{2}]$ direction periodically to generate a "new" supercell with the same SQS-optimized lattice occupations but different layer index numbers (an original Layer n becomes a new Layer $n+1$ (or Layer $n-17$ due to the periodic condition), where n is an integer from 1 to 18). Then we obtain 18 different twinned supercells. The second step is to generate an n-layer {112} twin embryo in the middle of the supercell based on a layer-by-layer mechanism [198]. After the twin embryo generated, there is still one twin growth fault between the top and bottom layers on the boundary of the supercell along $[11\bar{2}]$ direction. So the third step is to change the supercell by tilting its $[11\bar{2}]$ axis along [111] direction by n twin Burgers vector (b_{tw}) to avoid the mismatch at the supercell boundary.

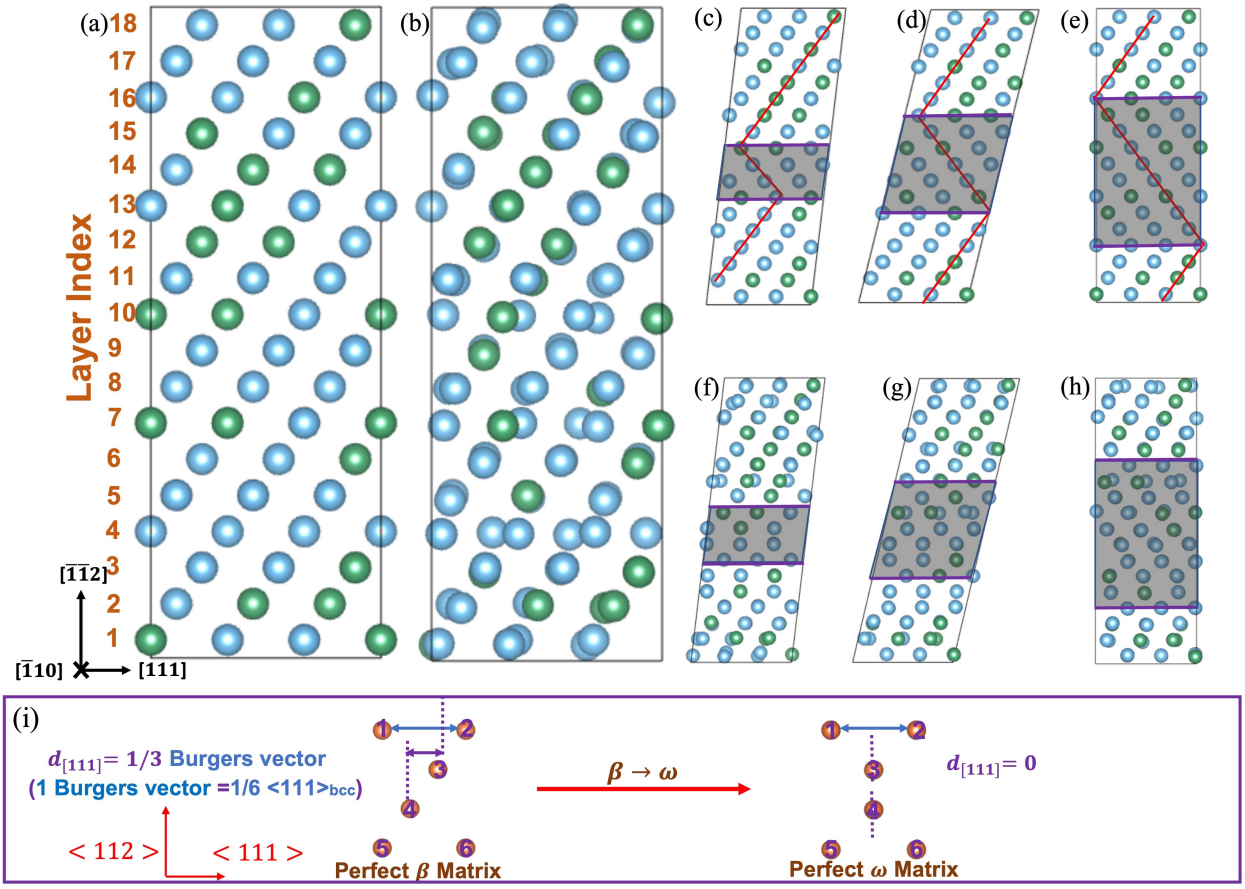


Figure 2.3: Illustrations of {112} twin embryo structures in a 108-atom Ti_3Nb supercell ((a)-(h)) and quantitative analyses for β (BCC) to ω (hexagonal) phase transformation in DFT-relaxed supercell based on values of a structural descriptor((i)). (a), (c), (d), and (e) show a perfect 18-layer BCC matrix, 3-layer twin embryo, 6-layer twin embryo, and 9-layer twin embryo in unrelaxed structures, respectively; (b) and (f)-(h) are the corresponding DFT-relaxed structures. The coordination system is the same as Figure 2.1 (c). Numbers at the left side of (a) are the layer indexes for the atomic layer along the $[11\bar{2}]_\beta$ direction. Red lines in (c), (d), and (e) indicate the crystal orientations. Grey shapes in (c) to (h) indicate the {112} twin embryo region. Blue and green atoms are Ti and Nb, respectively. (i) Explanations of the definition of a structural descriptor $d_{[111]}$ to distinguish between individual atoms in β phase and those in ω phase quantitatively. $d_{[111]}$ is the shortest distance projection along $[111]_\beta$ direction between one atom and its first-nearest neighbors of all the atoms in the supercell defined in (a).

and growth kinetics. Thus, we should investigate the composition region where β is thermodynamically (meta)stable so that the $\beta \rightarrow \omega$ transformation would not spontaneously occur. Meanwhile, phase stability in Ti alloys is highly related to VEC: $\beta \rightarrow \omega$ transformation can be easily induced by local chemical concentration fluctuations and local lattice distortion when the average VEC is low (close to 4.0 e/a, where e/a means electron per atom) [95, 114]. Here we define the VEC for pure Ti, pure Nb, pure V, and pure Mo as 4.0, 5.0, 5.0, and 6.0 e/a, respectively, although some core electrons of these chemical elements are included in their electronic configurations of pseudopotentials. We first generated around 100 supercells in perfect BCC lattice with different VEC values ranging from 4.0625 to 4.5 e/a. As we show in Figure 2.1 (b), β to ω phase transformation is achieved by atomic displacements along one of preferred $\langle 111 \rangle_\beta$ directions. Meanwhile, if no external stress/strain is applied and ω phase forms after DFT relaxations, the preferred $\langle 111 \rangle_\beta$ directions can be random locally. To quantify the displacement direction preference and further evaluate the ratio of ω phase in the DFT-relaxed supercell, we employed the approach developed by Ikeda et al. [95]. In each relaxed supercell, we first calculated and averaged all atomistic displacements from the perfect lattice sites projected along four distinct directions: $[111]_\beta$, $[1\bar{1}\bar{1}]_\beta$,$[\bar{1}\bar{1}1]_\beta$, and $[\bar{1}1\bar{1}]_\beta$, respectively. The averaged displacement magnitudes of four $\langle 111 \rangle_\beta$ directions are normalized by c_ω, which is the distance between the first nearest neighbors in the corresponding BCC lattice. Secondly, the four averaged displacement magnitudes along four $\langle 111 \rangle_\beta$ directions are sorted as P_1 ,P_2, P_3, and P_4 in the order of decreasing magnitudes, respectively. Thirdly, the structural descriptor P_1-P_2 is defined as the value to quantify the ratio of ω phase in the relaxed supercell. If P_1-P_2 of the supercell is smaller than $0.04c_\omega$, this supercell is regarded to stay the in BCC lattice from the statistically average aspect [95]. Otherwise, the relaxed supercell is considered to be transferred into ω phase. The calculated P_1-P_2 for all the supercells are shown in 2.4.

Based on the scatter plot presented in Figure 2.4, when VEC is equal or greater than 4.25 e/a for a series of Ti alloys, the BCC lattice can be preserved and does not spontaneously

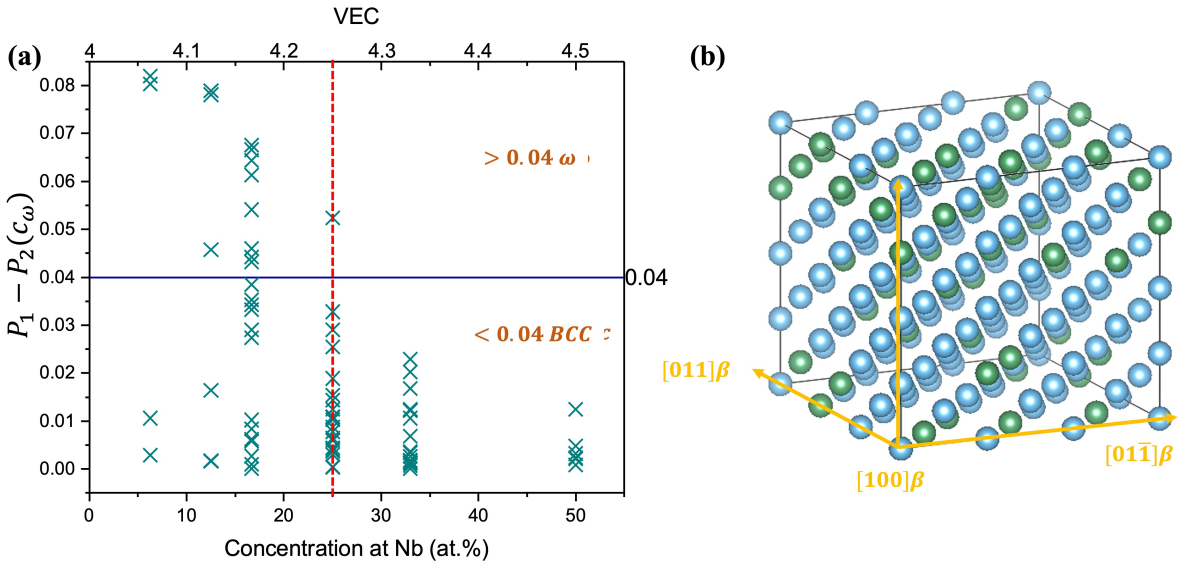


Figure 2.4: Structural descriptor for ω phase identification. (a) is the scatter plot of P_1-P_2 vs VEC for Ti-Nb alloy. Here we employed method from Ikeda's work [95] to identify local athermal ω phases in bulk BCC supercell. P_1 and P_2 is the largest, and second largest projection along $\langle\ 111\ \rangle$ group directions, respectively. Statistically, when P_1-P_2 is less than 0.04, the supercells are in BCC phase while they are in ω phase when P_1-P_2 is greater than 0.04. (b) is the snapshot for a configuration of a 144-atom supercell used for investigating the composition region where β is thermodynamically (meta)stable. Here the supercell with basis vectors of 4[100]×3[01$\bar{1}$]×3[011] in the unit of conventional BCC lattice vectors. Blue atoms are Ti and green atoms are Nb.

transfer to ω phase after DFT relaxations. These results of the critical VEC value (4.25 e/a) are generally consistent with previous Ikeda's results [95]. So we only investigated the supercells with VEC no less than 4.25. We conducted DFT calculations to investigate the atomic configurations and stability of twin embryos without any external stress at zero K. Thus, the supercells for DFT calculations of twin embryo stability in Section 2.2.1 were made up of six different compositions: $Ti_{81}Nb_{27}$ (VEC=4.25 e/a), $Ti_{81}V_{27}$ (VEC=4.25 e/a), $Ti_{72}Nb_{36}$ (VEC = 4.33 e/a), $Ti_{72}Nb_{18}V_{18}$ (VEC = 4.33 e/a), $Ti_{81}Mo_{27}$ (VEC = 4.5 e/a), and $Ti_{72}Nb_{18}Mo_{18}$ (VEC = 4.5 e/a). Hence average VEC values for the alloys we constructed here range from 4.25 to 4.5 e/a. However, it should be emphasized that the critical VEC value for ω phase should depend on both types of chemical elements and temperatures. In the following sections, we ignore the unit of e/a for VEC values for convenience.

2.2.3 ω Phase Identification in Twinned Supercells

To quantitatively identify the ω phase formed after the DFT relaxation in the twinned supercells, we propose a structural descriptor $d_{[111]}$ to distinguish the phases (ω and β) for different twinned supercells. Here we do not employ P_1-P_2 illustrated in the previous section to identify the ω phase for the following reasons [95]. β to ω phase transformation has the preference of atomic displacement direction in twinned supercells constructed following the orientations plotted in Figure 2.3. On the other hand, the descriptor of P_1-P_2 is only suitable for the bulk β phase and it fails to work for those twinned supercells. Based on the orientations of supercells defined in Figure 2.3, the smallest distance projected along $[111]_\beta$ between one atom and its nearest-neighbor atoms on the adjacent $(11\bar{2})$ layers is $\frac{1}{3}$ of $\frac{1}{2}[111]_\beta$ in β phase. However, this projection distance is 0 in a perfect ω phase. The detailed illustration is shown in Figure 2.3 (i).

2.2.4 MD Calculations

Molecular dynamics (MD) simulations were performed by Large-scale Atomic/Molecular Massively Parallel Simulator (LAMMPS) [170]to investigate Ti-Nb binary alloys using modified embedded atom method (MEAM) potential developed by Ehemann et al. [57]. As for the simulation box setting, 32400 atoms were included in a supercell with basis vectors of $15[111]\times20[\bar{1}10]\times9[11\bar{2}]$ in the unit of conventional BCC lattice vectors. For examinations of twin embryo stability at room temperature, MD simulations were performed on the supercells at a constant temperature of 300K under the isothermal-isobaric (NPT) ensemble ($P = 0$) for 200 ps. The time step was set to be 1 fs. The energy and structure of the system were calculated every 1 ps. For chemical compositions of Ti alloys, we chose five different compositions: Ti_3Nb (VEC = 4.25), Ti_2Nb (VEC =4.33), TiNb (VEC = 4.5), $TiNb_3$ (VEC = 4.75), and pure Nb (VEC =5). Besides, each composition was applied to generate 4 different structures: perfect BCC, 3-layer twin embryo, 6-layer twin embryo, and 9-layer twin embryo, which are all consistent with the structures setting of DFT calculations plotted in Figure 2.3. Furthermore, we deformed the supercells that contain the stable twin embryos by applying shear stress with a constant engineering shear strain rate of 4 $\times10^8$ s^{-1} along [111] direction on $(11\bar{2})$ plane at 300 K. The time step for the deformation simulation was also 1 fs. An MD simulation of 30 ps at 300 K in an NPT ($P = 0$) ensemble was performed for equilibrium before each deformation operation. To analyze the atomistic structures generated by MD simulations, we used the polyhedral template matching (PTM) [117] and the grain segmentation method to identify BCC matrix, BCC twin, and α'/α" phase [19]. In addition, we also applied OVITO to visualize all the MD results [183].

2.2.5 Calculations of Twinning Pathway

To evaluate the energy landscape for both the twinning and anti-twinning deformation that may occur to a pre-existing twin embryo observed in our MD simulations, we define a twin-

ning pathway through homogeneous displacements between different parts of a crystal near an existing {112} twin boundary to generate a type of defects named as "twin growth faults" and calculate the related energy variations. The simulation box used for calculations of the twinning pathway and the related twin growth fault energies is shown in Figure 2.5 (a). Here, we construct an orthogonal supercell with basis vectors of $30[111]\times30[\bar{1}10]\times12[11\bar{2}]$ (72 atomic layers along $[11\bar{2}]$ direction) in the unit of conventional BCC lattice vectors. The supercell contains {112} twin boundary located in the middle(viewing along $[\bar{1}10]$ direction). Red dashed line separates the supercell into two regions that have different orientations: atoms colored in green are in the BCC twin, which are in the same orientation as the twin region in Figure 2.3 (c)-(e); atoms colored in light brown are in the BCC matrix, which is in the same orientation of BCC matrix in Figure 2.3 (c)-(e). The color correspondences (light brown color for BCC matrix and green color for BCC twin) are consistent with the following sections of this paper. Here, to more clearly identify the twin boundary and locations of twin growth faults, we also mark two atomic layers just at the boundary in white color.

To generate twin growth faults at the twin boundary, we displace the atoms in the BCC matrix (the upper crystal above the twin boundary) with certain fault displacements in the way of homogeneous displacements. Figure 2.5 (b) shows an example of the creation of a 2-layer twin growth fault. We shift the upper atomic layer adjacent to the twin boundary (the red dashed line) along [111] direction by the magnitude of $\lambda \times \frac{1}{2}[111]$ relative to the bottom crystal; we also shift all the upper layers (except the atomic layer that is adjacent to the twin boundary and is already shifted) along [111] direction with the magnitude of $2\lambda\times\ \frac{1}{2}[111]$ relative to the bottom crystal, where λ ranging from 0 to 1 in the interval of 0.01. So the maximum fault displacement is the length of one or two full Burgers vectors in BCC lattice (when λ approaches 1), which is the smallest unit length of structure periodicity along [111] direction in BCC lattice. The method of twin growth faults energy calculation is similar to the twinning pathway designed by Ogata et al.[156] and also recently applied by Gröger et al. [78] to investigate the energy landscape of deformation twinning in BCC metals.

However, the difference is that the two-layer displacements were applied in a perfect BCC lattice to generate a two-layer stacking fault in previous studies[156, 78], but we apply the two-layer homogeneous displacement mechanism near an existing {112} twin boundary in a bicrystal structure to simulate the twinning and anti-twinning deformation during the twin growth process. So the defects generated during this homogeneous displacement process are not simply stacking faults in a perfect crystal. Thus, we name this type of defect generated in Figure 2.5 (b) as "twin growth fault".

To calculate the energy profile along the twinning pathway by the twin growth fault generation, we use the conjugated gradient (CG) minimization method [15]. The relaxation convergence for force is 1×10^{-6} eV/Å and the energy tolerance is 1×10^{-6}. During the relaxation minimization, the bottom and top regions along $[11\bar{2}]$ direction in the supercell are frozen (grey regions in Figure 2.5) to ensure that only atoms near the twin boundary are included in the calculation and no energy contribution from extra surfaces. Meanwhile, the thicknesses of the frozen part should be large enough to avoid the interactions between movable atoms and atoms in the top/bottom frozen regions. As for the unfrozen part of the supercell, atoms are only relaxed along $[11\bar{2}]$ direction perpendicular to the $(11\bar{2})$ twin boundary plane after the homogeneous displacements are applied. Here, we define the energy of twin growth faults induced by homogeneous displacements, $\gamma^n_{\mathrm{TGF}}(\lambda)$, using Eq. 2.1 below

$$\gamma^n_{\mathrm{TGF}}(\lambda) = \frac{E^n_\lambda - E_0}{A} \tag{2.1}$$

Here E^n_λ is the relaxed energy of the supercell that contains n-layer twin growth faults with the magnitude of $\lambda \times \frac{1}{2}[111]$ of homogeneous displacements as described in Figure 2.5(b) (Here $n = 2$). E_0 is the relaxed energy of the supercell without any twin growth faults. A is the area of one fault plane defined by the supercell size. In the following sections, we simplify the name of energy of the twin growth fault as γ_{TGF} for convenience because we always study 2-layer twin growth faults. A key reason for presenting the results of 2-layer twin growth faults is that the energy barriers in 2-layer twin growth faults are smaller than those in other

n-layer (n= 1,2 and 3) twin growth faults cases based on our calculations. Similarly, 2-layer stacking faults are also found to be the pathway with the minimum energy barriers for the stacking fault generation in many BCC transition metals (Nb, Ta, etc.) according to a recent computational study by Gröger et al. [78]

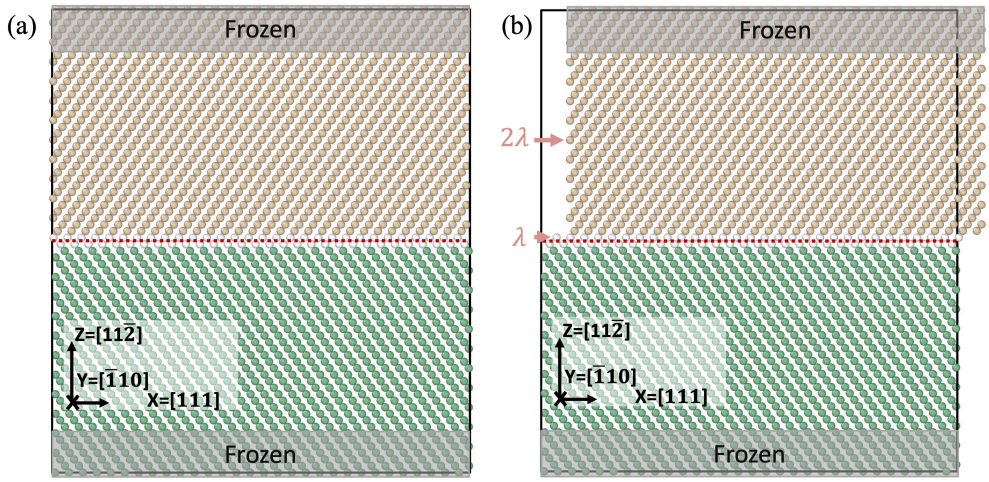


Figure 2.5: Schematic illustration for a twin pathway through homogeneous displacement mechanism near an existing {112} twin boundary in a bicrystal structure. (a) is the bicrystal structure that contains a (11$\bar{2}$) twin boundary in the middle, viewing along [1$\bar{1}$0] direction. Atoms in green color have the same orientation as BCC twin in Figure 2.3 while atoms in light brown color have the same orientation as BCC matrix in Figure 2.3. The twin boundary between two (11$\bar{2}$) atomic planes is indicated by a red dashed line. White color atoms are on (11$\bar{2}$) atomic planes adjacent to the twin boundary. (b) is the bicrystal structure under a twinning pathway created by homogeneous displacements between different parts of the upper crystal. Atoms in the first (11$\bar{2}$) atomic layer adjacent to the twin boundary shift together by $\lambda \times \frac{1}{2}[111]]$ relative to the lower crystal. Atoms above the first (11$\bar{2}$) atomic layer adjacent to the twin boundary shift together by $2\lambda \times \frac{1}{2}[111]$ relative to the lower crystal. $\frac{1}{2}[111]$ is the full Burgers vector and λ ranges from 0 to 1 at the interval of 0.01. Atoms in grey shade regions are fixed during the energy minimization and the atoms out of the grey regions are only allowed to be relaxed in the Z direction normal to (11$\bar{2}$).

2.2.6 Experimental Characterizations of Twin Boundary Structures

To verify the structures of twin boundaries obtained from the above atomistic simulations, the atom configurations at the $\{112\}\langle 11\bar{1}\rangle$ type twin boundary were characterized in the β Ti-

24Nb-4Zr-8Sn (wt. %, Ti-2448) alloy. Since we want to investigate how {112} twin-induced ω phase affects the {112} stability and configurations and so pre-existing athermal ω phase should be avoided. Here, we carefully choose this composition and the addictive Zr and Sn can help suppress the quenched-in athermal ω phase [85, 84, 86] We use conventional transmission electron microscopy (TEM) and aberration-corrected z-contrast high angle annular dark field-scanning transmission electron microscopy (HAADF-STEM) for characterization. Ti-2448 was β solution treated at 1000°C for 30 min followed by water quenching to room temperature, and then cold-rolled by 20% reduction in thickness. The β solution treated and cold rolled Ti-2448 was cross-sectioned, mounted, and ground for characterization following conventional routes. Site-specific TEM lift-out lamella for TEM and HAADF-STEM was prepared across the {112} twin boundary using Thermo Scientific Scios 2 dual-beam focus ion beam (DB-FIB), and further cleaned using Fischione 1040 nanomill. Conventional TEM was performed using FEI Talos F200s transmission electron microscope at 200kV, and atomic resolution HAADF-STEM imaging was performed using aberration-corrected Thermo Scientific Themis Z scanning transmission electron microscope at 300kV.

2.3 Results

2.3.1 Structures and Stability of {112} Twin Embryos at 0 K

Examples of atomistic structures in DFT-relaxed supercells are shown in Figure 2.3 (b), (f), (g), and (h), respectively, for the perfect BCC lattice and twin embryos of Ti_3Nb (108-atom supercell, VEC = 4.25). More snapshots of fully relaxed twin embryo structures for Ti_3Nb (VEC=4.25) and Ti_3Mo (VEC=4.5) can be found in B.1. By comparing Figure 2.3 (a) and (b), we do not observe a perfect ω matrix in the relaxed supercell, which initially was in an ideal BCC lattice. This is consistent with the conclusion that spontaneously β to ω phase transformation hardly occurs when VEC is equal to or greater than 4.25, as discussed in Section 2.2.2. However, in supercells that contain twin embryos before relaxations, local

atomistic structures with the structural features of ω phase can be identified at locations where twin embryos were generated. The structural features for the atomistic structure of ω phase are clearly shown in Figure 2.1 (b). Generally, if two adjacent atoms on two nearest neighbor $(11\bar{2})$ layers align in a line parallel to $[11\bar{2}]$ from the view of $[\bar{1}10]$ direction in a relaxed supercell, we can regard the local atomistic structures of these two atoms have the structural features of ω phase. When the number of $(11\bar{2})$ layers of the original twin embryo in the unrelaxed structure equals 3 or 6, most atoms in the twin regions (grey shape areas in Figure 2.3 (f) and (g)) have the structural features of ω phase by aligning to adjacent atoms along $[11\bar{2}]$ direction. Even when the number of $(11\bar{2})$ layers of the original twin embryo increases to 9, a large portion of atoms in the twin region (grey shape areas in Figure 2.3 (h)) still have the structural features of ω phase. However, when VEC increases to 4.5, the structural features of ω phase are hardly observed in the relaxed supercells. The snapshots of relaxed supercells (VEC = 4.5 cases) are shown in Appendix B B.1.

We also quantitatively estimated the energy costs of these twin embryos in all the DFT relaxed supercells by using twin boundary (TB) energy γ_{TB} defined as the follow [209]:

$$\gamma_{\mathrm{TB}} = \frac{E_{\mathrm{twin}} - E_{\mathrm{perfect}}}{2A} \tag{2.2}$$

Here, E_{twin} is the energy of a relaxed twinned supercell, E_{perfect} is the energy of the corresponding relaxed supercell in the perfect BCC lattice, and A here represents the supercell area parallel to $(11\bar{2})$ twin boundary plane. Typically, γ_{TB} is greater than 0 and this parameter can indicate the energy cost to form a twin embryo. The calculated γ_{TB} values for different Ti alloys are plotted in Figure 2.6. The "violin" plots here are implemented by the Python package from Seaborn [211]. Each sub-figure in Figure 2.6 contains γ_{TB} calculated by using all the fully relaxed twinned supercells at a given composition (indicated at the top of each sub-figure).

As we discussed in Section 2.2.1, we generated 18 different supercells for each SQS-

optimized lattice occupation of a given composition with a fixed number of twin layers in the middle of the supercell. Therefore, in each sub-figure of Figure 2.6, each column has 18 different data points, each of which corresponds to different local chemical compositions and lattice occupations in an alloy with the same average chemical composition. These data points are marked as black dots in the middle of each "violin" graph. Meanwhile, the width of the "violin" graph features a kernel density estimation of the data distribution. In this case, the widest location is where the most data is distributed. The dots linked by solid lines mark the location where the mean value of γ_{TB} distribution for the corresponding alloy composition.

Clearly shown by different alloy compositions in Figure 2.6, the average γ_{TB} increases as the VEC increases. This trend coincides with the fact that the β phase becomes stable relative to other phases (α', α", and ω) as the VEC increases [95, 114], so there should be less energetic driving forces of spontaneous β to ω phase transformation at twin boundaries. In addition, as for γ_{TB} distribution of different twinned supercells for each composition, especially when VEC is equal or greater than 4.33, we can see that the γ_{TB} variation becomes smaller as the number of $(11\bar{2})$ layer in the twin embryo increases. This indicates that a 3-layer twin embryo may not be stable and spontaneously disappear by diffusionless transformation. This is consistent with the observations of atomistic structures in Appendix B B.1. For example, when VEC = 4.5, ω phase can still be observed in the configurations of 3-layer twin cases, while ω phase totally disappeared when $(11\bar{2})$ layer of the twin embryo increases to 6.

Moreover, γ_{TB} distributions for two alloy compositions of VEC equal to 4.25 (Figure 2.6 (a) and (d)) are mainly distributed at values that close or even less than 0. This indicates that the initially constructed twin embryos spontaneously induce a large portion of β phase in both the matrix and twin regions transforming into a lower energy state, more specifically, ω phase depending on the local chemical compositions. Even a 9-layer twin embryo plotted in Figure 2.6 (a) and (d) is not thick enough to survive for low VEC cases because the

calculated γ_{TB} are still close to 0. Compared with higher VEC cases, we can conclude that for β-Ti alloys, the existing {112} twin embryos can induce the β to ω phase transformation depending on both the average alloy compositions (VEC) and the local lattice occupations, and vice versa, twin-induced ω phase impede the formation of stable twin embryos with a small number of $(11\bar{2})$ layer.

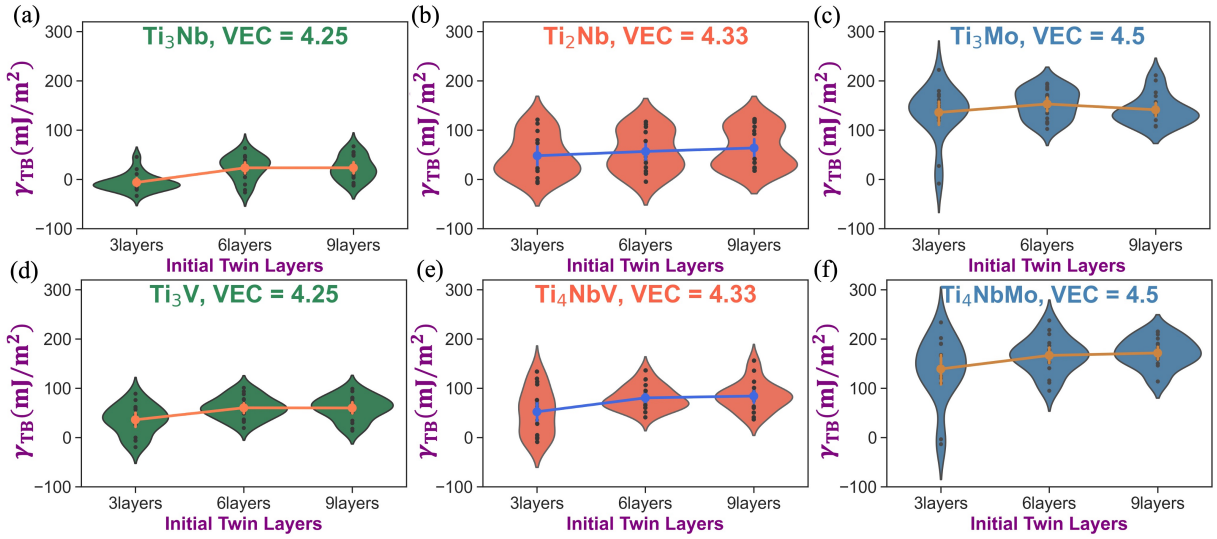


Figure 2.6: Twin boundary energy γ_{TB} defined in Equation 2.2 vs. the number of $(11\bar{2})$ layers of twin embryos for alloys with different VEC values. All cases were calculated by DFT using a supercell of 108 atoms plotted in Figure 2.3 (a). For each type of twin embryo structure at a given alloy composition, there are 18 possible cases to locate the twin embryo with different $(11\bar{2})$ layer indexes plotted in Figure 2.3 (a). So the "violin" plots of these 18 data points are used to illustrate the distribution and the mean value of γ_{TB} for each twin embryo structure at a given alloy composition. The detailed alloy compositions and the corresponding VEC values are shown at the top of each subfigure.

To confirm our conclusion on the quantitative correlation between twin embryo stability and phase stability, we employ the structure descriptor $d_{[111]}$ defined in Figure 2.3 (i) to distinguish atoms in ω phases and those in β phases. Here, We calculate the $d_{[111]}$ for all atoms in all supercells we generated so far. The histogram plots of $d_{[111]}$ for all atoms in different supercells are shown in Figure 2.7. Because all the supercells contain 108 atoms and there are 18 different atomic configurations for each composition with a given number of twin layers, each subfigure in Figure 2.7 is the histogram for the $d_{[111]}$ values of 18×108

= 1944 atoms (except those in Figure 2.7(a) and (e)for the perfect BCC lattices with twin embryos, which are histograms for the $d_{[111]}$ values of 108 atoms).

As explained in Figure 2.3 (i) and Section 2.2.3, since the value of $d_{[111]}$ is normalized by the value of $\frac{1}{2}[111]_{\beta}$, so if the peak of the histogram is located at 0.333 and no data points drop at 0, then statistically we can claim that the corresponding supercells are in β phase with a BCC lattice and ω phase does not appear. If there is a peak in the histogram located at 0, there are a significant amount of local ω phases in these supercells. In Figure 2.7 (a)- (h), we present histograms for two compositions: Ti_3Nb (VEC=4.25) and Ti_3Mo (VEC=4.5). The histograms for the other compositions can be found in Appendix B B.2. As far as Ti_3Mo is concerned (Figure 2.7 (e)-(h)), there are no evident peaks near $d_{[111]} = 0$ in neither perfect lattice nor twinned supercells. Nevertheless, we can still observe a small portion of data points near the $d_{[111]} = 0$ region for 3-twin supercells (Figure 2.7 (f)). This is consistent with the energy data shown in Figure 2.6 (f), where we can see a large variation of γ_{TB} distribution for those 3-layer twin supercells. This indicates that the 3-layer twin embryo is not thick enough to stabilize for Ti_3Mo and collapses to ω phase. Meanwhile, as for other supercells for Ti_3Mo, there are almost no data points less than 0.1. In contrast, when VEC = 4.25 (Figure 2.7 (a)-(d)), there are two comparable peaks for all the supercells except no-twin lattices: one is near $d_{[111]} = 0$ and the other one is near $d_{[111]} \approx 0.3$, suggesting that a large portion of β phase can transform to ω phase because of the low stability of β phase when the VEC value is low. Compared to the perfect lattice in Figure 2.7 (a), the peaks near $d_{[111]} = 0$ increase significantly for the twinned supercells in Figure 2.7 (b)-(d)), suggesting the introductions of twin embryo enhance $\beta \rightarrow \omega$ transformation remarkably. In addition, the case of the 9-layer twin embryo in Figure 2.7 (d) still has slightly stronger peaks near the $d_{[111]} = 0$ region compared with the case of 6-layer twin embryo in Figure 2.7 (c), suggesting that the twin embryos are still unstable when there are 9 $(11\bar{2})$ layers in the twin region.

To conclude, both our energetic descriptor (γ_{TB}) and structural descriptor ($d_{[111]}$) indicate

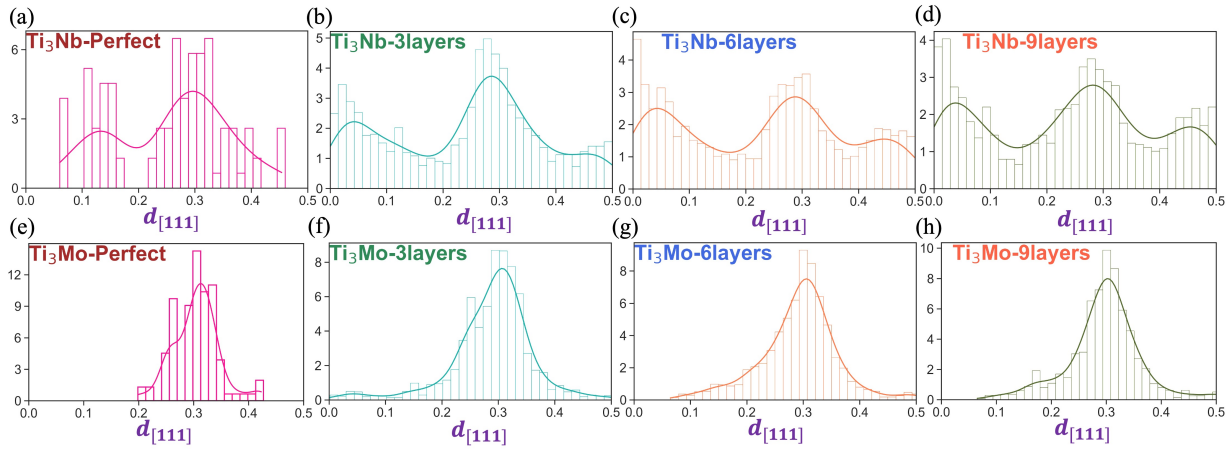


Figure 2.7: Histograms of $d_{[111]}$ values (normalized in the unit of the length of $\frac{1}{2}[111]_\beta$) for DFT-relaxed supercells of different alloy compositions and twin embryo structures. From left to right the subfigures in each row are for the perfect BCC matrix, 3-layer twin, 6-layer twin, and 9-layer twin embryo structure for a specific composition, respectively. (a)-(d) are for Ti_3Nb (VEC=4.25); (e)-(h) are for Ti_3Mo (VEC=4.5).

that the minimum thickness of a stable twin embryo varies with the VEC value of Ti alloy; a thicker twin embryo is required for be stable in β-Ti alloy a lower VEC; {112} twin boundaries can induce the β to ω phase transformation at low VEC and thus increase the difficulty of forming a stable twin embryo. However, these DFT supercell sizes are still too small to include the effects of local concentration fluctuations, and we have not investigated the stability and growth kinetics of twin embryos at different temperatures under external loading conditions. These size/temperature effects and growth kinetics are discussed in the following sections.

2.3.2 Stability of {112} Twin Embryos at Room Temperature

First, we investigated the twin embryos' stability at room temperature based on MD simulations using Ti-Nb MEAM potential [57]. The MD settings are described in Section 2.2.4. The snapshots for supercells after 200 ps of MD simulations under the NPT ensemble ($P = 0$ and $T = 300$ K) are plotted in Figure 2.8. Subfigures in each column from left to right in Figure 2.8 stand for supercells that initially (before MD relaxations) have the perfect BCC

lattice, 3-layer twin embryo, 6-layer twin embryo, and 9-layer twin embryo, respectively, in different alloy systems. The light brown color represents the BCC matrix while the green color represents the BCC twin identified based on the Polyhedral Template Matching (PTM) method [117]. Figure 2.8 (a)-(d) show atomistic structures of the unrelaxed supercells for all the alloy cases, where twin embryos are always added to the middle of a supercell through a layer-by-layer mechanism, and all supercells are constructed in the same way as described in Section 2.2.1).

Figure 2.8 (e)-(h) are MD-relaxed supercells of Ti_3Nb (VEC=4.25). It clearly shows that both 3-layer and 6-layer twin embryos disappear while the 9-layer twin embryo survives after MD relaxations. In addition, the boundaries between twin and matrix regions in Figure 2.8 (h) are not as flat as those in the unrelaxed supercell in Figure 2.8 (d). Figure 2.8 (i)-(l) and Figure 2.8 (m)-(p) are MD-relaxed supercells of Ti_2Nb (VEC=4.33) and TiNb (VEC=4.5), respectively. For both alloy cases, 3-layer twin embryos disappear, but both 6-layer and 9-layer twin embryos survive after MD relations. In addition, twin boundaries in both the relaxed Ti_2Nb and TiNb become more flat compared to those of Ti_3Nb. Figure 2.8 (q)-(t) are MD-relaxed supercells of Pure Nb (VEC=5), where all twin embryos survive and all twin boundaries are almost as flat as those in the unrelaxed supercells. In summary, the critical thickness of a stable twin embryo increases as the VEC value decreases: 3 atomic layers for Pure Nb (VEC=5), 6 atomic layers for TiNb (VEC=4.5) and Ti_2Nb (VEC=4.33), 9 atomic layers for Ti_3Nb (VEC=4.25). This trend is also consistent with DFT results in Section 2.3.1: alloy compositions with low VEC values increase the difficulty of identifying stable twin embryos with BCC lattice due to the local $\beta \rightarrow \omega$ transformation. This transformation usually is intensified on twin boundaries. Thus, the ultra-thin twin embryos with two twin boundaries too close to each can not survive after MD relaxations because ω phases on two twin boundaries can interact with each other, transforming almost all atoms inside the twin region into ω phase.

To further confirm the effects of ω phases on twin embryo stability in these MD simula-

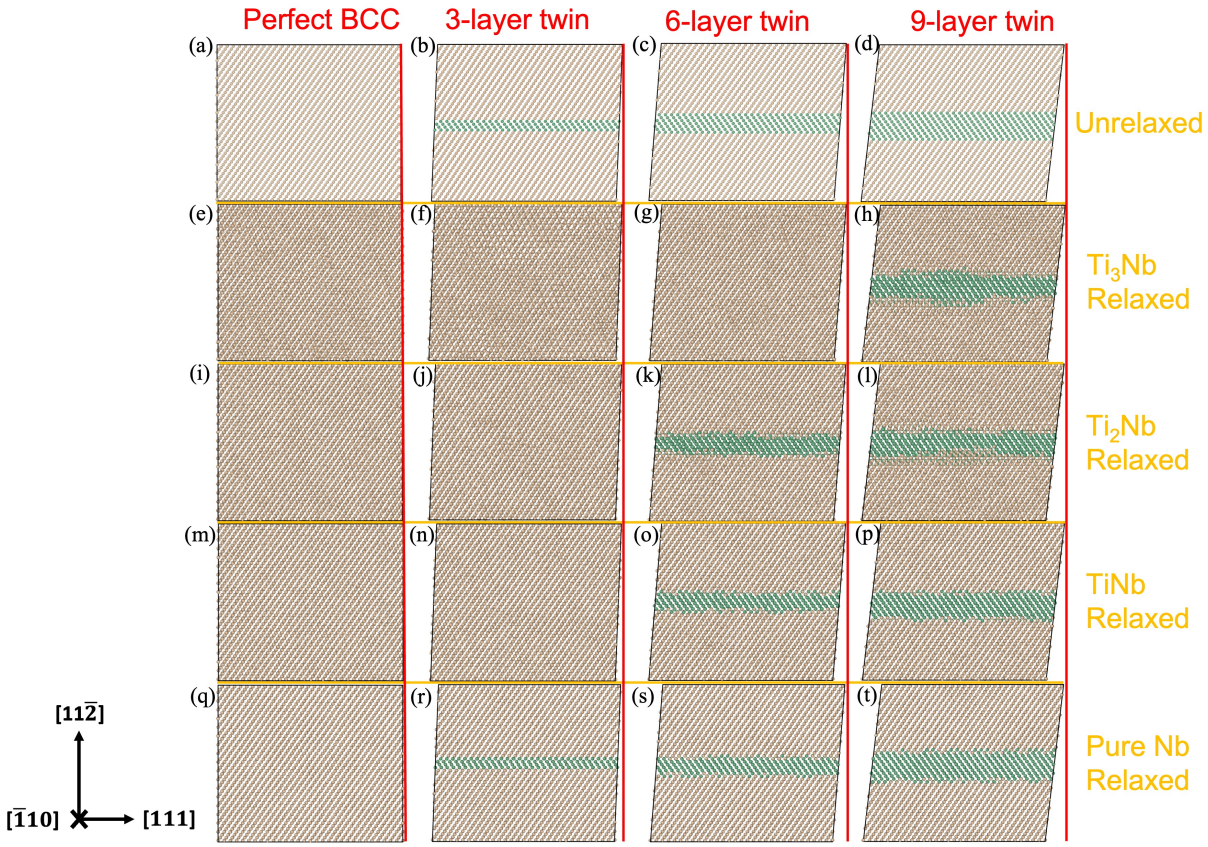


Figure 2.8: Configurations of {112} twin embryos in Ti-Nb alloys after MD simulations (200 ps and the NPT ensemble ($P = 0$ and $T = 300$ K)). Subfigures of each column from left to right are supercells that initially (before MD relaxations) have the perfect BCC lattice, 3-layer twin embryo, 6-layer twin embryo, and 9-layer twin embryo, respectively, in different alloys. Subfigures of each row are supercells for different alloys. (a)-(d): Unrelaxed supercells of all alloy cases before MD relaxations. (e)-(h): Relaxed Ti_3Nb supercells. (i)-(l): Relaxed Ti_2Nb supercells. (m)-(p): Relaxed TiNb supercells. (q)-(t): Relaxed pure Nb supercells. The light brown color represents the BCC matrix while the green color represents the BCC twin. Phase identification is conducted by Polyhedral template matching (PTM) [117]and phase variants identification (BCC matrix and BCC twin) is conducted by Grain segmentation method [19] in the current version of OVITO [183]

tions, we applied quantitative methods to identify the ω phases on twin boundaries in the relaxed supercells that contain stable twin embryos with the minimum number of atomic layers (6 atomic layers for TiNb (VEC=4.5) and Ti_2Nb (VEC=4.33), 9 atomic layers for Ti_3Nb (VEC=4.25)). We employed the same descriptor $d_{[111]}$ defined in Figure 2.3 (i) to quantitatively define the extent of $\beta \rightarrow \omega$ transformation of each atom according to its first-nearest-neighbor environment in these selected supercells. In addition, for each relaxed supercell after MD simulations, we first run 10 steps of conjugated gradient (CG) minimization to remove the noises due to thermal vibrations [15]. Here, even though ω phases and α'/α" phase have some similarities viewing from $[\bar{1}10]$ direction (both of them have 0 projection distance of two adjacent $(11\bar{2})$ planes), occur of $\beta \rightarrow \alpha$'/α" phase needs external shear stresses [103] and α'/α" phase can not survive without external stresses. Hence, $d_{[111]}$ is still an efficient structural descriptor to identify ω phases in the supercells if they are free of external stresses. Figure 2.9 (a)-(c) are snapshots of some selected supercells after the CG minimization. We calculated $d_{[111]}$ for all the atoms in these supercells. Similar to the distribution shown in Figure 2.7, the $d_{[111]}$ values have a continuous distribution. In order to distinguish the local ω phase, here we assign two discrete values (0 and 1) to each atom based on the corresponding $d_{[111]}$. Value 0 indicates ω phase while 1 indicates β phase. If $d_{[111]}$ of the atom is less or equal to 0.1, then we assume this atom is in the ω phase. Otherwise, we treat the atom as β phase. Here, we make $d_{[111]} = 0.1$ as the cutoff value for phase identification is based on the histogram plot in Figure 2.7 (h). In 9-layer twinned supercells of Ti_3Mo (VEC= 4.5), β phase should be stable, and $\{112\}$ twin boundaries should not induce $\beta \rightarrow \omega$ phase transformations, so the corresponding 9-layer twin embryo supercells should do contain almost zero atoms with local atomistic structures with the structural features of ω phase. Also, we notice that there are almost no distributions of $d_{[111]}$ value less than 0.1 in Figure 2.7 (h). So 0.1 can be a valid and efficient cut-off to separate ω-like phase and β-like phase by considering the local atomistic structures. Here, we do not choose a histogram of perfect BCC lattice of Ti_3Mo as a reference to decide the cutoff value (in Figure 2.7 (e),

there are almost no distributions of $d_{[111]}$ value less 0.2). The reason is that twin boundary structures can trigger local lattice distortion and change the value of $d_{[111]}$, so we should allow a large variation of $d_{[111]}$ values for atoms in β phase that contains twin boundaries.

Figure 2.9 (d)-(f) is the heatmap of supercells shown in Figure 2.9 in (a)-(c) based on assigned two-phase identification values of $d_{[111]}$. When VEC equals 4.25, we can see 4 to 5 layers of ω phases (marked in black color in Figure 2.9 (d)) stacking along the top and bottom twin boundaries (enclosed in red and green dashed lines). Also, the twin boundaries in Figure 2.9 (d) are not homogeneous and we can see some kinks and steps along the twin boundaries (marked in green color) due to the variations of ω phase locations. This is why the twin phase (green region) in Ti_3Nb shown in Figure 2.9 (a) are thick and rough compared with those in Ti_2Nb and TiNb shown in Figure 2.9 (b) and (c). The structural features are consistent with those observed in the aberration-corrected high-angle annular dark field scanning transmission electron microscopy (HAADF-STEM) images shown in Figure 2.9 (g) and (h). In Figure 2.9 (g), the twin boundaries are composed of stacked ω structures ranging from 2 to 4 atomic layers in thickness. These structures (both simulation results in Figure 2.9 (d) and experimental results in Figure 2.9 (g)) are also consistent with the findings in Section 2.3.1 that $\{112\}$ twins activate the β to ω structural transformation. In addition, in Figure 2.9 (d), we can observe that a part of the twin regions is collapsed to a 4-layer of ω phase; we can also find some ω phase located away from the twin embryo in Figure 2.9 (d). These features of ω phase distributions are because the local VEC is much less than 4.25 due to local concentration fluctuations and the original local β phase can spontaneously transfer to ω phase. When VEC increases in Figure 2.9 (e) and (f), the portion of atoms in ω phase (marked in black color) significantly reduces. We can see atoms in ω phase along each of the two twin boundaries form a thin and discontinuous line in Ti_2Nb (Figure 2.9 (e)), and almost no atoms in ω phase are identified in TiNb (Figure 2.9 (e)).

Meanwhile, we also measure the thicknesses of ω phase at twin boundaries in different VEC cases from this study and several published papers. [132, 60, 111, 239, 215, 37, 205], as

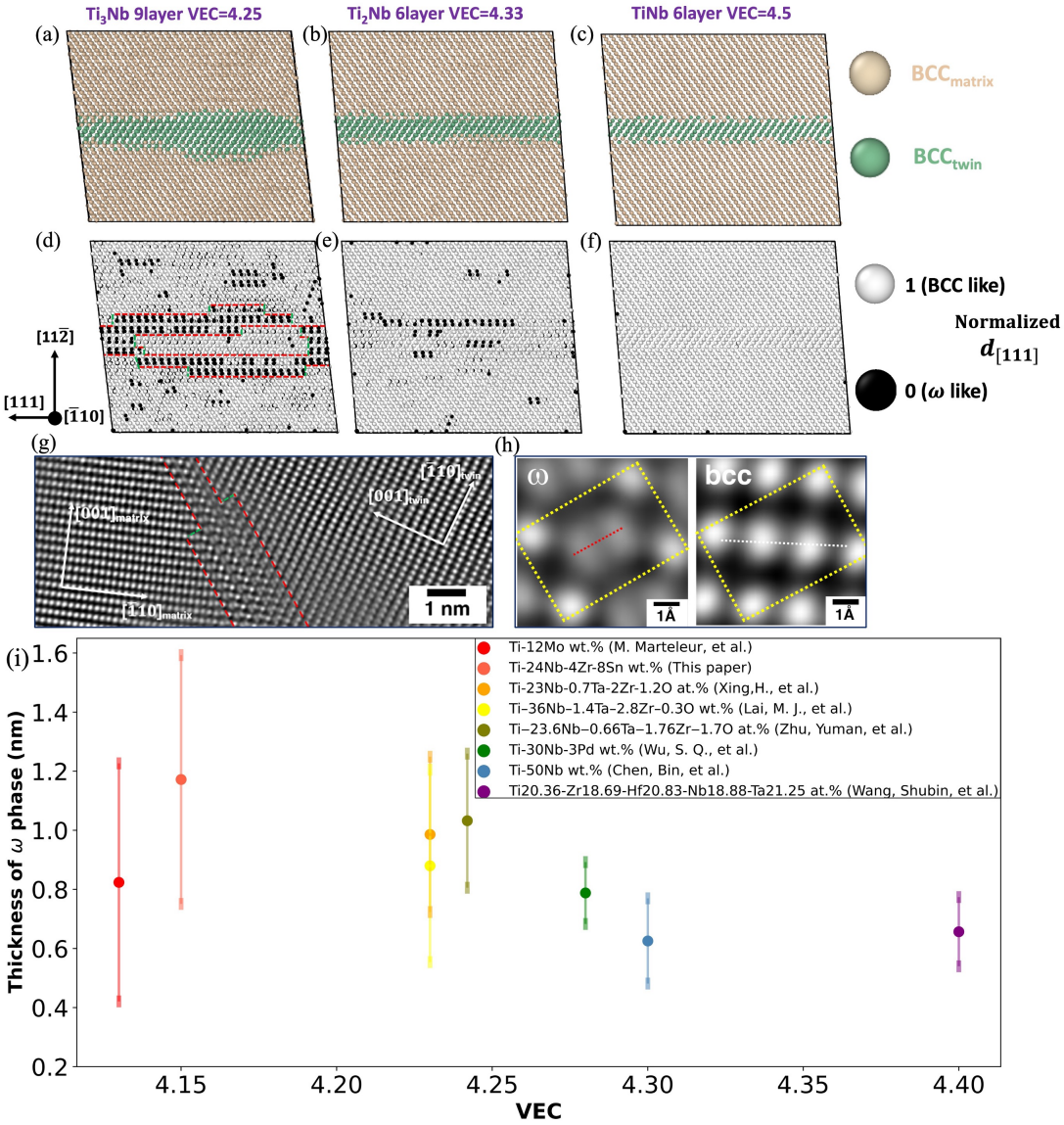


Figure 2.9: Atomistic structures of {112} twin boundaries from MD simulations and experiments. (a)–(c) Relaxed supercells containing stable twin embryos with the minimum number of atomic layers: (a) 9 layers for Ti_3Nb (VEC = 4.25), (b) 6 layers for Ti_2Nb (VEC = 4.33), and (c) 6 layers for TiNb (VEC = 4.5); brown and green atoms represent the BCC matrix and BCC twin, respectively.(d)–(f) Corresponding phase-identified snapshots of (a)–(c), where white and black atoms represent the β (BCC) and ω phases, respectively; red dashed lines mark twin boundaries aligned with the twinning plane and green dashed lines mark twin boundary steps, with thick boundary regions in (d) highlighted by both colors indicating ω phase formation.(g)–(h) Aberration-corrected HAADF-STEM images of the ω phase at a {112} twin boundary in 20% cold-rolled Ti-24Nb-4Zr-8Sn: (g) nanoscale ω layer at the twin boundary; (h) unit cells of hexagonal ω and BCC β phases.(i) Distribution of ω phase thicknesses at twin boundaries across different VEC values compiled from published data [132, 60, 111, 239, 215, 37, 205]; solid points indicate the length-weighted average thickness and error bars represent the weighted standard deviation.

shown in Figure 2.9 (i). The methods for thickness measurement are presented in Appendix B B.3. Here, the solid circles in Figure 2.9 (i) represent the average thickness of local ω phases weighted by the lengths that parallel to the {112} twin planes. The error bars in solid lines are estimated by the weighted standard deviations of thicknesses of local ω phases in the experiment data. Generally, based on these experimental results, the average thicknesses of ω phase at twin boundaries decrease with the increase of VEC values of alloy compositions, especially in the Ti-Nb alloy system, which is consistent with our observations in our DFT calculations in Figure 2.7 and MD simulations Figure 2.9 (d)-(f). The only outlier is Ti-12Mo wt.% [132], which has a relatively small average thickness of ω phases at low VEC (VEC=4.13). This indicates that, although VEC is still the dominant factor, it is not the only factor that affects β to ω phase transformations at {112} twin boundaries. These factors may include oxygen effects and thermomechanical processing procedures, which are not in the scope of this paper but will be explored in the future. Besides, as indicated by the error bar magnitudes, the fluctuations of ω phase thicknesses also decrease as VEC increases, which means that twin boundaries are rough in low VEC cases due to the fluctuations of many local ω phases on the boundaries, while they become flat as VEC increases. This trend is also consistent with observations in our MD simulations in Figures 2.8 and 2.9 (d)-(f).

Above all, the experimental observations of the morphology of ω phases at the twin boundaries and the VEC effect on ω phases formation behavior at twin boundaries are generally consistent with the observations in DFT and MD simulation results. However, it should be emphasized that the above analyses are based on the results of electron microscopy characterizations from different sources. The accuracy of these results depends on the quality of characterizations and the sampling of different locations in alloy samples. These factors are difficult to control. Thus, the results in Figure 2.9(i) can only be used as supportive evidence of our conclusions about {112} twin boundary structures in β-Ti alloys.

2.3.3 Growth of {112} Twin Embryos

So far, our DFT calculations and MD simulations reveal the correlation between the stability of {112} twin embryos and $\beta \rightarrow \omega$ phase transformation at {112} twin boundaries. In the next step, we deformed the twinned supercells by applying the shear loading to examine the growth kinetics of the stable twin embryo with the minimum {112}-layer thickness for each composition identified from Figure 2.8 (3 layers for pure Nb, 6 layers for TiNb and Ti_2Nb, and 9 layers for Ti_3Nb). Thus, after the MD relaxations in Section 2.3.2, we deformed the supercells with the stable twin embryos using a constant engineering shear strain rate along [111] direction on $(11\bar{2})$ plane at 300 K. The corresponding shear stress-strain curves are plotted in Figure 2.10. As shown in Figure 2.10 (b), (c), and (d), the twin embryos in pure Nb, TiNb, and Ti_2Nb can smoothly grow under the applied shear loading. From the inserted snapshots in the plots of Figure 2.10 (b)-(d), the twin regions all become much thicker than the initial twin embryos when the shear strain increases to 0.20. Another interesting finding is that the shear stress needed for twin boundary migration in pure Nb is around 0.7 GPa, which is much larger than the other two alloys (Ti_2Nb and TiNb). The increase in the critical stress for twin migration is likely related to the high twin boundary energy of pure Nb (278.7 mJ/m^2 from our calculation) compared with those of Ti_2Nb and TiNb shown in Figure 2.6.

In addition, the stress-strain curve in pure Nb in Figure 2.10 (d) behaves like periodic peaks and each peak has almost the same maximum stress. It suggests the twin migration in pure Nb is triggered by just one type of mechanism with the same critical stress, such as the twin boundary step nucleation. However, the stress-strain curves for Ti_2Nb and TiNb in Figure 2.10 (b) and (c) have more fluctuations on the maximum value of each local peak, especially for Ti_2Nb where there are still some ω phases on twin boundaries as shown in Figure 2.9 (e). Since each peak of the stress-strain curve corresponds to the critical stress to trigger the twin boundary migration, these fluctuations suggest the variations of

local chemical concentrations may change the detailed mechanism of the rate-limiting step of twin migration. Since there are stronger fluctuations in the stress-strain curve of Ti_2Nb (Figure 2.10 (b)) than those for TiNb (Figure 2.10 (c)), ω phases on twin boundaries of Ti_2Nb could affect the critical stress that triggers the rate-limiting step of twin migration by considering that there are much more ω phase or ω-like structures on twin boundaries of Ti_2Nb (Figure 2.9 (e)) than those on twin boundaries of TiNb (Figure 2.9 (f)).

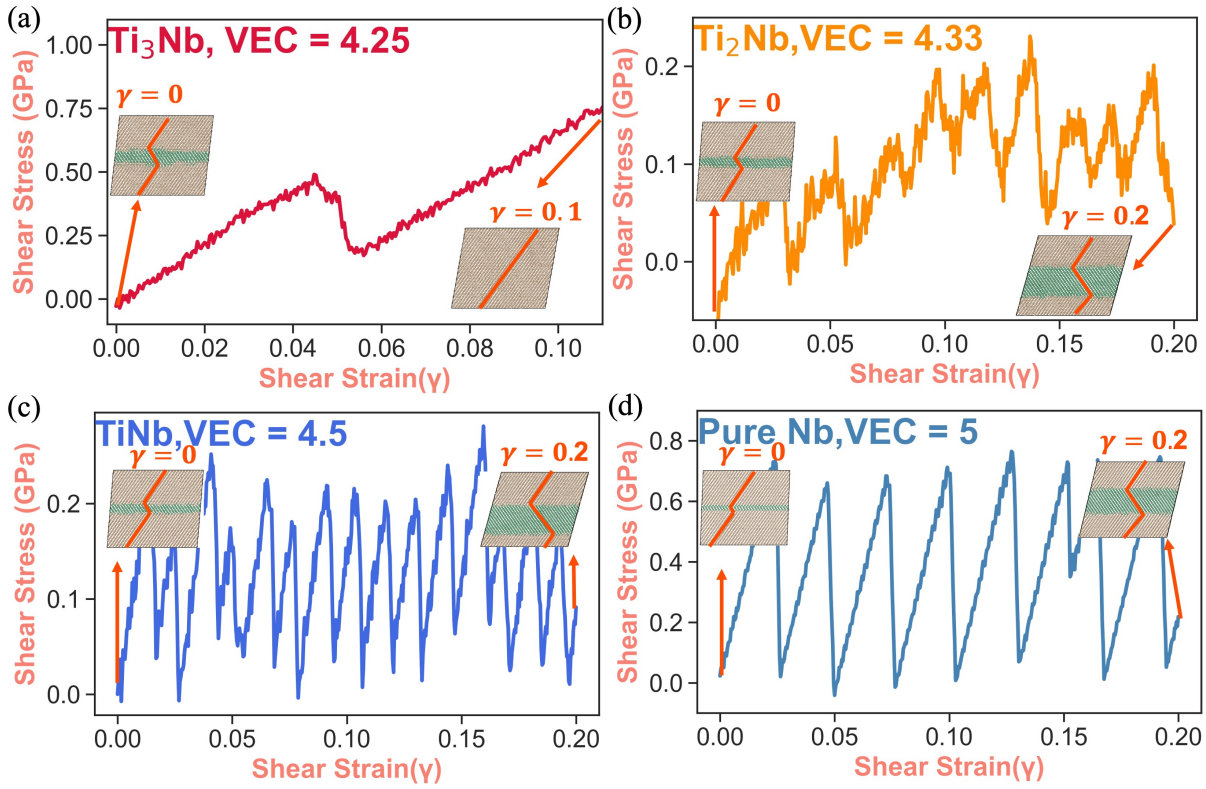


Figure 2.10: Stress-strain curves and atomistic structure changes when constant shear loading is applied to supercells that contain stable twin embryos with the minimum {112}-layer thickness for different Ti alloys. Inserted graphs in each subfigure are the snapshots at the initial state and the final state of the shear process. (a) Ti_3Nb starting from a relaxed 9-layer twin embryo. (b) Ti_2Nb starting from a relaxed 6-layer twin embryo. (c) TiNb starting from a relaxed 6-layer twin embryo. (d) Pure Nb starting from a relaxed 3-layer twin embryo. Atoms marked in light brown color in the inserted figures are in the BCC matrix while atoms marked in green color in the inserted figures are in the BCC twin. The orange solid lines in the inserted figures indicate the crystal orientations of the BCC phase.

In contrast, the stress-strain curve and the corresponding twin embryo evolution for Ti_3Nb

shown in Figure 2.10 (a) are abnormal compared with all other alloys in Figure 2.10. Even though a 9-layer twin can survive after a long-time MD relaxation at room temperature, its twin boundaries do not move and the twin embryo does not grow as the shearing strain increases from zero. This low twin boundary mobility could be related to the high ratio of ω phases on twin boundaries shown in Figure 2.9 (a) and (d), which could significantly increase the roughness of twin boundary energy landscape and the energy barriers for twin boundary migration. When the shear strain is above $\sim$0.03, a slope change of the stress-strain curve occurs due to some internal structural variations, which are found to be diffusionless phase transformation inside the twin embryo as analyzed in the following section. This twin embryo even starts to shrink when the shear strain increases above 0.0448 and completely disappears when the shear strain reaches $\sim$ 0.06. Then the shear stress continues to increase with the shear strain without further twinning behavior. When the shear strain approaches 0.1, we can only see a single crystal without a twin embryo according to the right inserted graph in Figure 2.10 (a).

Figure 2.11 demonstrates the detailed evolution of atomistic structures during the shrinkage of the twin embryo for Ti_3Nb shown in Figure 2.10 (a). As shown in Figure 2.11 (a), we present several snapshots of the twin region at/near some critical points of this detwinning process. We can observe α'/α" phases (purple color atoms) accumulate in the twin region and then disappear during the detwinning process. Here, we use the PTM method to identify different phases, but the PTM method cannot distinguish the difference between α' (HCP) and α" (orthorhombic) phases due to their similar atomistic structures (PTM simply identifies α' and α" phase as HCP phase). In the following sections, to more rigorously elaborate and avoid any misunderstanding, we use the α'/α" phase to represent the PTM-identified HCP phase. We also analyze the dynamic change of volume fraction of α'/α". Based on the analysis, we find that α'/α" phases continuously increases and approaches a maximum value close to detwinning state. This indicates BCC twin $\rightarrow$ α'/α" phase requires the accumulation of enough stress inside the twin embryo. When shear strain further increases, based on the

stress-strain curve in Figure 2.10 (a) and the snapshots in Figure 2.11 (a), the sudden stress drop together with the detwinning behavior should be related to the α'/α" phase $\rightarrow$ BCC matrix within the twin embryo. Meanwhile, we can observe low mobility of twin boundary (specifically lower twin boundary) in the Figure 2.11 (a) during the detwinning process, which is for the sake of pinning effect from ω phase at the twin boundary.

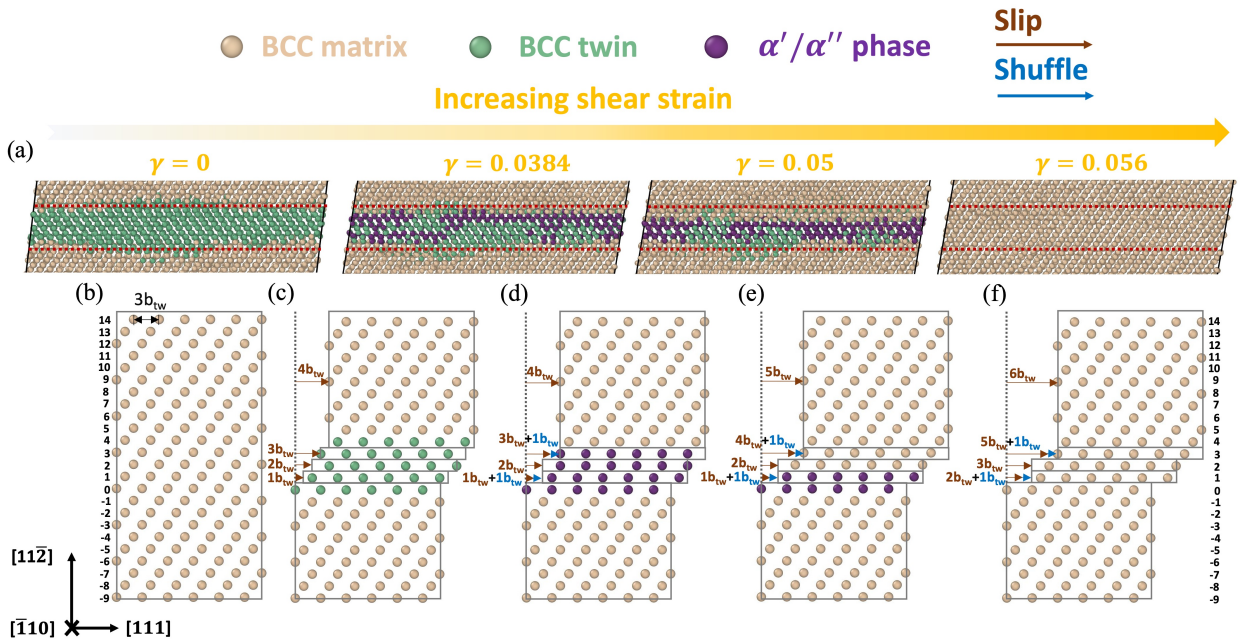


Figure 2.11: Evolution of atomistic structures during the shrinkage of the twin embryo in Ti_3Nb under the increasing shear strain along the twinning direction. (a) shows the snapshots of the twin region (green color) at/near some critical points of this detwinning process during the MD simulations. (b)-(f) are schematic illustrations for the whole process of the initial twinning from a perfect single crystal and the later detwinning process in Ti_3Nb assisted by reversible β (BCC twin variant) to α'/α" phase to β (BCC matrix variant) phase transformation. Here BCC matrix is in light brown color, α'/α" phase is in purple color, and BCC twin is in green color. During the twinning and detwinning process, atomic displacements by slip are marked in dark brown arrows, while atomic displacements by shuffle are marked in blue arrows. The magnitudes of atomic displacements shown in (c)-(f) are calculated in reference to the initial state of the perfect crystal in (b). The label index of each atomic layer along [11$\bar{2}$] direction is shown on the left side of (b) and the right side of (f). Here one twin Burgers vector $b_{\mathrm{tw}} = \frac{1}{6}[111]$.

To more thoroughly analyze the phase transformation behaviors during the detwinning process in the twin region, we compare the structures of twin regions at some critical states of

detwinning process, as shown in Figure 2.11 (a). Red dashed lines mark the initial locations of twin boundaries before shear is applied. When shear strain γ is 0.0384, there are some small local α'/α" phases mainly distributed at the upper twin boundary and the volume of the twin region has a tendency to decrease compared to the initial state (γ equals to 0). As the shear strain γ increases to 0.05, the twin region further shrinks. Compared to the structure of the twin region when γ is 0.0384, the initial α'/α" phases (purple color) have transformed to BCC matrix (light brown) and more atoms in the middle part of twin region (green color) becomes α'/α" phases. Further, when shear strain γ slightly increases to 0.056, the twin region disappears and totally transforms into BCC matrix, and the intermediate α'/α" phases no longer survive. Based on this boundary to interior detwinning process within the twin region, we propose a α'/α"phases-assisted detwinning mechanism, and we illustrate the step-by-step process in Figure 2.11(b)-(f).

As shown in Figure 2.11 (b), to illustrate the detwinning process in Ti_3Nb more clearly, we start from the perfect single crystal. Here we assign the label index for each atomic layer along $[11\bar{2}]$ direction, ranging from -9 to 14 shown on the left side of Figure 2.11(b). Then we construct a 4-layer twin embryo in the middle of the supercell following the layer-by-layer twin dislocation slip mechanism, as shown in Figure 2.11 (c). Even though {112} twin nucleation in Ti_3Nb and other metastable β-Ti alloys may not follow this slip mechanism, the net relative fault displacements in the twinned region compared to the initial perfect crystal state should be independent of the specific twin formation pathway. At the stage in Figure 2.11 (c), when the twin embryo is hard to grow even under external shear along the twinning direction (possibly due to the pinning effect of ω phase at the twin boundaries), α'/α" phase-assisted detwinning behavior happens inside the twin region. As shown in Figure 2.11 (d), by shuffling Layer 1 and Layer 3 along [111] direction in the magnitude of one twin Burgers vector ($b_{\mathrm{tw}} = \frac{1}{6}[111]$), four atomic layers of the distorted α'/α" phase form (purple atoms). This stage corresponds to the stage when γ is 0.0384 in Figure 2.11 (a). Further, Layer 3 to Layer 14 undergo a rigid slip in the magnitude of 1 b_{tw}, approaching

the stage shown in Figure 2.11 (e). Compared to Figure 2.11 (d), the upper twin region (Layer 2 and Layer 4) has transformed back to BCC matrix from the intermediate α'/α" phase, which is similar to the stage when γ is 0.05 in Figure 2.11 (a). Similarly, from Figure 2.11 (e) to Figure 2.11 (f), the lower part of α'/α" phase totally transforms into the BCC matrix by slipping Layer 1 to Layer 14 for 1 b_{tw}, and finally all twin region disappears as shown in Figure 2.11 (f). In total, compared to the original perfect structure (Figure 2.11 (b)), atoms in Layer 1 and Layer 2 have a total displacement of 3 b_{tw} (equivalent to one full Burgers vector), while atoms in Layer 3 and above part are displaced by 6 b_{tw} (equivalent to two full Burgers vectors). The magnitudes of net displacements are also consistent with our MD results by analyzing the average atomic displacements.

Here, for simplicity, we use a 4-layer twin embryo structure for illustration. Moreover, the smallest thickness to identify α'/α" phase along $[\bar{1}10]_{\beta}$ || $[010]_{\alpha''}$ || $[000\bar{1}]_{\alpha'}$ direction is a length of 4 atomic layers as shown in Figure 2.1 (a). Indeed, the whole detwinning process presented in Figure 2.11 (c)-(f) can be assumed as the detwinning process of the upper twin region of 9-layer twinned supercell in Ti_3Nb. In general, the detwinning process for a stable twin embryo in metastable β Ti alloys can happen by repeating the steps from stage in Figure 2.11 (d) to stage in Figure 2.11 (f), starting from a twin boundary to the interior of the twin region.

Even though the detwinning behavior can happen with the assistance of α'/α" phase, it needs the premise of low mobility of the twin boundaries even under loading conditions. In other words, twin boundaries in Ti_3Nb are relatively hard to move along the twinning direction. Meanwhile, the extra displacements within the twin region induced by shuffle illustrated in Figure 2.11 (d) and (e) have the anti-twinning sense, which indicates that twinning in BCC matrix region and anti-twinning in BCC twin region become competitive in metastable β Ti alloys. Direct investigation of twinning and anti-twinning behaviors in metastable β Ti alloys under loading conditions is difficult, but we can indirectly compare the twinning and anti-twinning preference by investigating the energy barriers of twin growth

fault generation at twin boundaries by applying homogeneous displacements as described in Section 2.2.5 and Figure 2.5. The corresponding results and detailed discussion are shown in the following part.

Figure 2.12 shows the results of energy barriers and stability of 2-layer twin growth faults vs the magnitude of the homogeneous displacements for pure Nb and different Ti-Nb alloys. Detailed illustrations for the twin growth faults generation and twin growth fault energy calculation are explained in Section 2.2.5. Figure 2.12 (a) shows the structure snapshots at some critical points during the 2-layer twin growth faults generation process in pure Nb. Green color represents BCC twin and light brown color represents BCC matrix. The orientations of BCC twin and BCC matrix are consistent with the BCC twin and BCC matrix defined in the previous sections. White atoms at the twin boundary and twin growth faults are in other orientations. Snapshot A is the initial structure before twin growth faults generation. Snapshot B, C, and D are atomistic structures at the transition state of the first energy barrier, the local energy minimum, and the transition state of the second energy barrier in the twin growth fault energy profile, respectively. Snapshot E is the structure containing 2-layer twin growth faults with one full Burgers vector displacement fault magnitude. From the crystallography view, Structure A and structure E should be the same for pure metals and the energy states should also be similar for alloys as long as the area of stacking planes defined by the supercell is large enough.

Figure 2.12 (b) is the energy profile of 2-layer twin growth faults by homogeneous displacements as described in Figure 2.5 along the twinning directions for Ti-Nb alloys and pure Nb. Theoretically, based on the classical layer-by-layer twin dislocation slip mechanism, there is a local energy minimum when λ is $\frac{1}{3}$ (equivalent to the magnitude of one twin Burgers vector b_{tw}), indicating twin growth by one $\{112\}$ atomic layer (From stage A to stage C). However, because of an isosceles feature of $\{112\}$ twin boundaries [198, 28, 176, 78], the positions of local energy minimum may vary. If we continue to increase the magnitude of fault displacements along the twinning direction after the local energy minimum, the twin growth

fault structure first increases and then decreases to approach stage E, so the structure evolution through C to E can be regarded as the detwinning behavior of the twin region through slip along the twinning direction. Meanwhile, since stage E is structurally equivalent to stage A, twin growth can be achieved either by shearing one twin Burgers vector along the twinning direction (from stage A to stage C) or two twin Burgers vectors along the opposite direction (anti-twinning direction) (from stage E to stage C). In pure Nb and other BCC transition metals, the energy barrier for twin growth along the anti-twinning direction (from stage E to stage C), which is close to the energy barrier for detwinning behavior (from stage C to stage E), is much larger than the energy barrier along the twinning direction (from stage A to stage C) [78]. This indicates that in most BCC transition metals, {112} twins prefer to grow by shearing along the twinning direction, and the anti-twinning or detwinning phenomenon is hard to observe under loading conditions.

As we compare the energy profiles of 2-layer twin growth faults in Ti3Nb with pure Nb and other Ti-Nb alloys shown in Figure 2.12 (b), it is evident that the difference of the energy barrier for anti-twinning (marked by star symbols) and the energy barrier for twinning (marked by hexagon symbols) greatly reduces. The ratio of the energy barriers for anti-twinning ($\gamma^{\mathrm{AT}}_{\mathrm{TGF}}$) and twinning ($\gamma^{\mathrm{TW}}_{\mathrm{TGF}}$) is around 17 in pure Nb, and the values of $\gamma^{\mathrm{AT}}_{\mathrm{TGF}}/\gamma^{\mathrm{TW}}_{\mathrm{TGF}}$ decrease as the VEC of the alloys decreases: 8.5 for TiNb, 3.4 for Ti_2Nb and 1.48 for Ti_3Nb. Clearly, the small difference of energy barriers for twinning and anti-twinning in Ti_3Nb alloy means that twin growth behavior in the BCC matrix and anti-twinning in BCC twin (alternately speaking, detwinning behaviors) are competitive given the applied shear strain along the twinning direction, making the detwinning behavior through the anti-twinning mechanism through C to E in Figure 2.12(a) much more likely to occur. In summary, the energy profile for 2-layer twin growth faults can indicate the intrinsic energetic preference of twinning behavior in the BCC matrix and anti-twinning behavior in the BCC twin (or detwinning behavior). When energy barriers are comparable, and intermediate α'/α" phases in Figure 2.11 can further promote the detwinning event and so the twin embryos do not

grow even though applying shear along twinning directions.

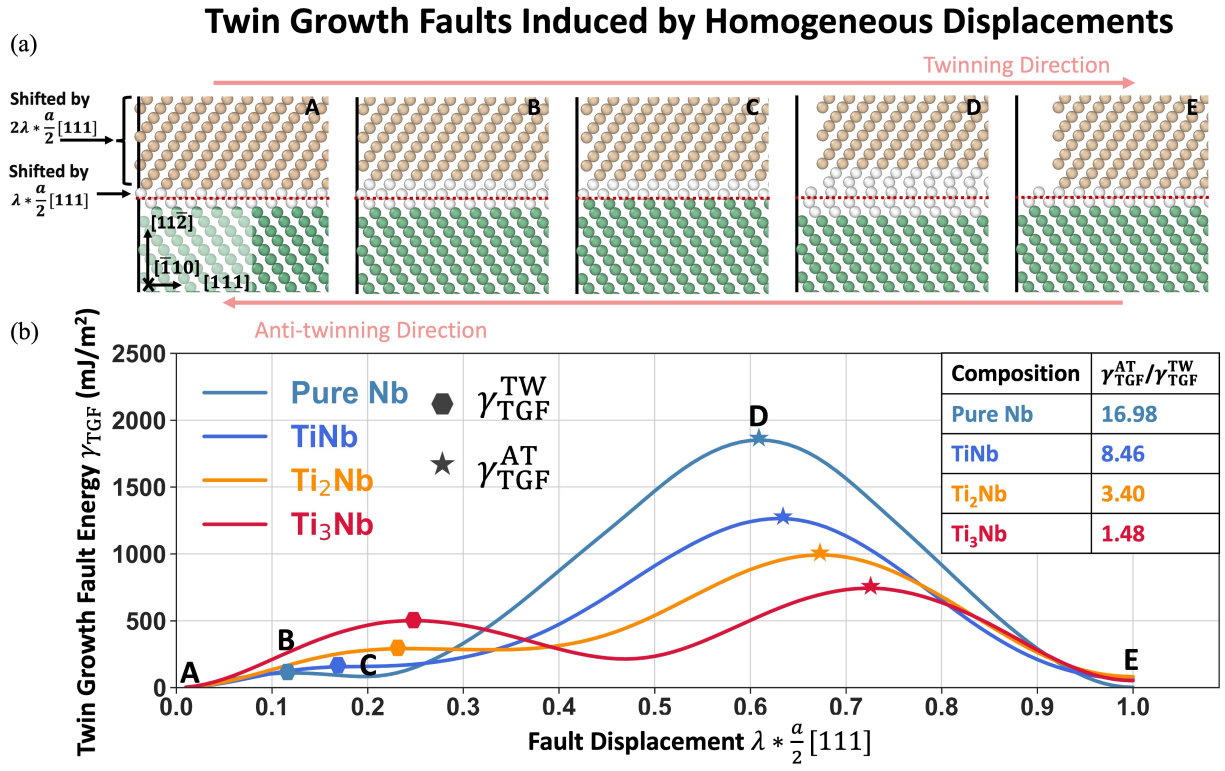


Figure 2.12: The energy profiles of 2-layer twin growth faults induced by $\lambda \times \frac{1}{2}[111]$ homogeneous displacements (described by Section 2.2.5) in Ti-Nb alloys and pure Nb. (a) shows the structure snapshots at some critical stages during the 2-layer stacking twin growth faults generation process in pure Nb. Stage A is the initial state before twin growth faults generation (λ=0). Stage B, C, and D are at the transition state of the first energy barrier, the local energy minimum, and the transition state of the second energy barrier of the twin growth fault energy profile, respectively. Stage E is the state when the displacement fault magnitude equals one full Burgers vector (λ=1). (b) shows the plots of the energy profile of 2-layer twin growth faults for different Ti-Nb alloys and pure Nb as a function of $\lambda \times \frac{1}{2}[111]$ displacements. The star symbols in the plots mark the Stage D location of energy barriers for anti-twinning (γ^{AT}_{TGF}), while the hexagon symbols indicate the Stage B location of energy barriers for twinning (γ^{TW}_{TGF}). The inserted table shows the value of $\gamma^{AT}_{TGF}/\gamma^{TW}_{TGF}$ in metal/alloys with different compositions.

Based on the detwinning phenomena for Ti_3Nb described above, two different reversible phase transformations occur: $\beta \leftrightarrow \omega$ transformations at twin boundaries and $\beta \leftrightarrow \alpha$'/$\alpha$" transformations inside twin embryos. A large amount of $\beta \rightarrow \omega$ transformations on {112} twin boundaries for Ti_3Nb reduce the twin mobility and increase the stress level that can

be reached inside the twin embryos. Such high stress and relative low β phase stability for Ti_3Nb at 300 K together induce the β twin $\rightarrow \alpha'/\alpha'' \rightarrow \beta$ matrix transformations inside twin embryos. In addition, the close distances between two {112} twin boundaries in this 9-layer twin embryo also play a role in activating the final detwinning behavior. We also constructed an 18-layer twinned supercell for Ti_3Nb and performed the same shear loading. The twin embryo does not smoothly grow as well (only locally grow/shrink) under the applied stress, confirming $\beta \rightarrow \omega$ transformations on {112} twin boundaries for Ti_3Nb reduce the twin mobility independent of the twin embryo size. Meanwhile, α'/α'' -phase-like structures frequently form locally but they would not continue to grow to bulk α'/α'' phase and disappear shortly. In all, the 18-layer twin growth behavior compared to the 9-layer twin detwinning behavior indicates that total detwinning is conditional and requires a narrow twin embryo in these MD simulations with high strain rates.

2.3.4 Controlling {112} Twin Growth by Tuning β Phase stability

By analyzing the MD results thus far, we have investigated how different phase transformations affect the {112} twin embryo growth. The next question is whether we can control the growth of {112} twin by tuning the thermodynamics of phase transformations. Reversible phase transformations are highly related to relative phase stability, which can be tuned by both temperature and alloy compositions. Therefore, we investigate how temperature and alloy compositions affect the detwinning/twinning phenomena of a 9-layer twin embryo in alloys with compositions similar to Ti_3Nb.

The detailed results are in Figure 2.13 (all compositions in Figure 2.13 are in the atomic fraction). As for the temperature factor for a Ti-Nb alloy with fixed 25% Nb composition, by comparing the shear stress-strain curves of Figure 2.13 (a)-(d), we find that the detwinning behavior is suppressed and the twin embryo can smoothly grow when the temperature increase to 400K. Based on the fitting results of interatomic potential [57] we use in our study, β phase is thermodynamically stable in Ti_3Nb when temperature greater than 410

K. Meanwhile, we find that when the temperature approaches 400 K, there are fewer ω structures along twin boundaries compared to those in 300 K. The increase of BCC phase stability can suppress the formation of the local ω phase inside twin boundaries. Without too many local ω-like structures forming along the twin boundaries, though we can still observe stress-induced α'/α" nuclei frequently form within the twin embryo, α'/α" phase nuclei are hard to grow. This is because the local stress within the twin embryo is hard to accumulate but would be released by fast {112} twin boundary migration.

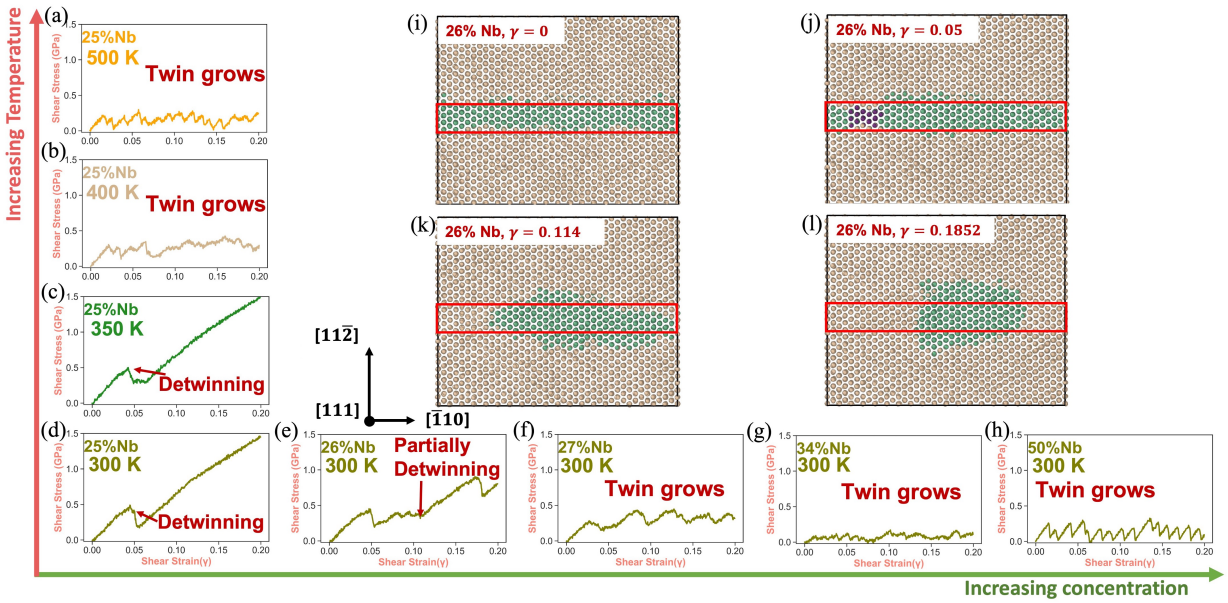


Figure 2.13: Shear stress-strain curves for 9-layer twin embryo for different compositions under different temperatures. (a)-(d) are all for Ti_3Nb but at different temperatures. (d)-(h) are all at 300K but at different compositions. (i)-(l) are the snapshots for $Ti_{0.74}Nb_{0.26}$ during deformation viewed from the shear direction [111]. The red rectangle in the (i)-(l) represents the twin boundary of the stable twin embryo before applying the shear loading. Light brown color in (i)-(l) represents BCC matrix, purple color represents α'/α" phase, and green color is for BCC twin. The phase identification is completed by Polyhedral template matching (PTM) [117]and Grain segmentation method [19].

Moreover, we also investigate how compositions affect detwinning behavior at a constant temperature (e.g., 300 K). Based on the fitting results of Ti-Nb MEAM potential [57], Ti_3Nb is very close to the critical composition where ω phase is relatively unstable compared to β phase at 0 K. Hence, we gradually increase the Nb concentration and observe the stress-

strain curves and the corresponding twin embryo evolution kinetics at 300 K. When Nb concentration equals 26 % in Figure 2.13 (e), an interesting partial detwinning behavior occurs, with the snapshots of the supercells at different shear strains viewed from the twin Burgers vector direction [111] in Figure 2.13 (i)-(l). As we can see from Figure 2.13 (j) and (e), when shear strain approaches 0.05, the stress drops and the partial twin embryo becomes the α'/α" phase. Thereafter, the twin boundary has a tendency to migrate locally (green color outside the red rectangle that defines the initial twin embryo region in Figure 2.13(i)). The reduced stress when the strain is larger than 0.05 is achieved by both for local BCC twin $\rightarrow$ α'/α" phase transformation and local twin migration. With the further increase of shear strain to 0.114 (Figure 2.13 (e)), the partial detwinning occurs since the local α'/α" phase Figure 2.13 (i) totally transforms into a BCC matrix as plotted in Figure 2.13 (k). Then the twin boundaries of the surviving twin embryo migrate slowly. Compared to Ti_3Nb, twin boundaries in $Ti_{0.74}Nb_{0.26}$ have a slightly higher twin mobility. Hence, local stress within the twin embryo can be partially released when twin boundaries migrate locally. At this stage, the local stress concentration can not be satisfied for a complete BCC twin $\rightarrow$ α'/α" phase $\rightarrow$ BCC matrix phase transformation.

As shown in Figure 2.13 (d)-(g), when the Nb concentration approaches 27 % and above, the twin can smoothly migrate under the applied shear stress. It is worth noticing that the critical stress for twin migration has a tendency to drop as Nb concentration increases initially by comparing the case with 34 % Nb in Figure 2.13 (g) ($\sim$ 0.1 GPa for twin migrations) to the case with 27 % Nb in Figure 2.13 (f) ($\sim$ 0.4 GPa for twin migrations). Then the critical stress for twin migration increases when the Nb concentration further increases as shown in the case with Nb concentration equal to 0.5 in Figure 2.13 (h) ($\sim$ 0.3 GPa for twin migrations). This trend would be further kept with the increasing Nb concentration since the critical stress for twin migration in pure Nb in Figure 2.10(d) reaches $\sim$ 0.7 GPa. (In B.4 of Appendix B Materials, we provide stress-strain curves of more compositions in the region of Nb atomic concentrations from 27% to 50% (VEC value of the Ti-Nb alloy

increases from 4.27 to 4.5, correspondingly). Since the increases of Nb concentrations can reduce the stability and amount of ω phases on twin boundaries as shown in Figures 2.7-2.9, these variations of Nb effects suggest that there could be multiple factors that determine the roles of ω phases on {112} twin migration kinetics, which will be discussed in the next section.

2.4 Discussions

In this study, we shed light on the role of ω phase in the {112} twin growth in β-Ti alloys, and the results uncover the fact that it may highly depend on the ω phase stability compared to the β phase. Many previous studies have observed that {112} twins in β-Ti alloys have close relationships with structural phase transformation between ω and β phase [114, 132, 37, 215, 112, 218, 121, 124, 216, 169, 52, 239]. Nevertheless, there is a long debate on whether ω phase can promote or impede {112} twin growth. In this study, shear stress-strain curves shown in Figures 2.10 and 2.13 combined with twin boundary configurations shown in Figure 2.9 (d)-(f) indicate that both promotion and impediment behaviors of ω phase can happen under different conditions as described in Section 2.3.4. These opposite effects indicate that the kinetics of {112} twins in β-Ti alloys may be related to complex mechanisms of diffusional phase transformations between ω and β phase that are decided by multiple factors and parameters.

A schematic illustration of the possible mechanism to explain the above concentration-dependent ω phase effects is shown by the free energy landscape for the homogeneous diffusionless β matrix $\rightarrow$ ω phase $\rightarrow$ β twin transformations in Figure 2.14. In this plot, as the VEC decreases from Figure 2.14 (a) to (c), ω phase becomes more stable, so the free energy of ω phase at its ground state goes down, and it is reasonable to assume that the local curvature of the free energy curve (the reciprocal of the local curvature radius) at its ground state may also increase because the energy cost to break its ground-state symmetry structure generally arises with its enhanced stability; meanwhile, under the same trend of

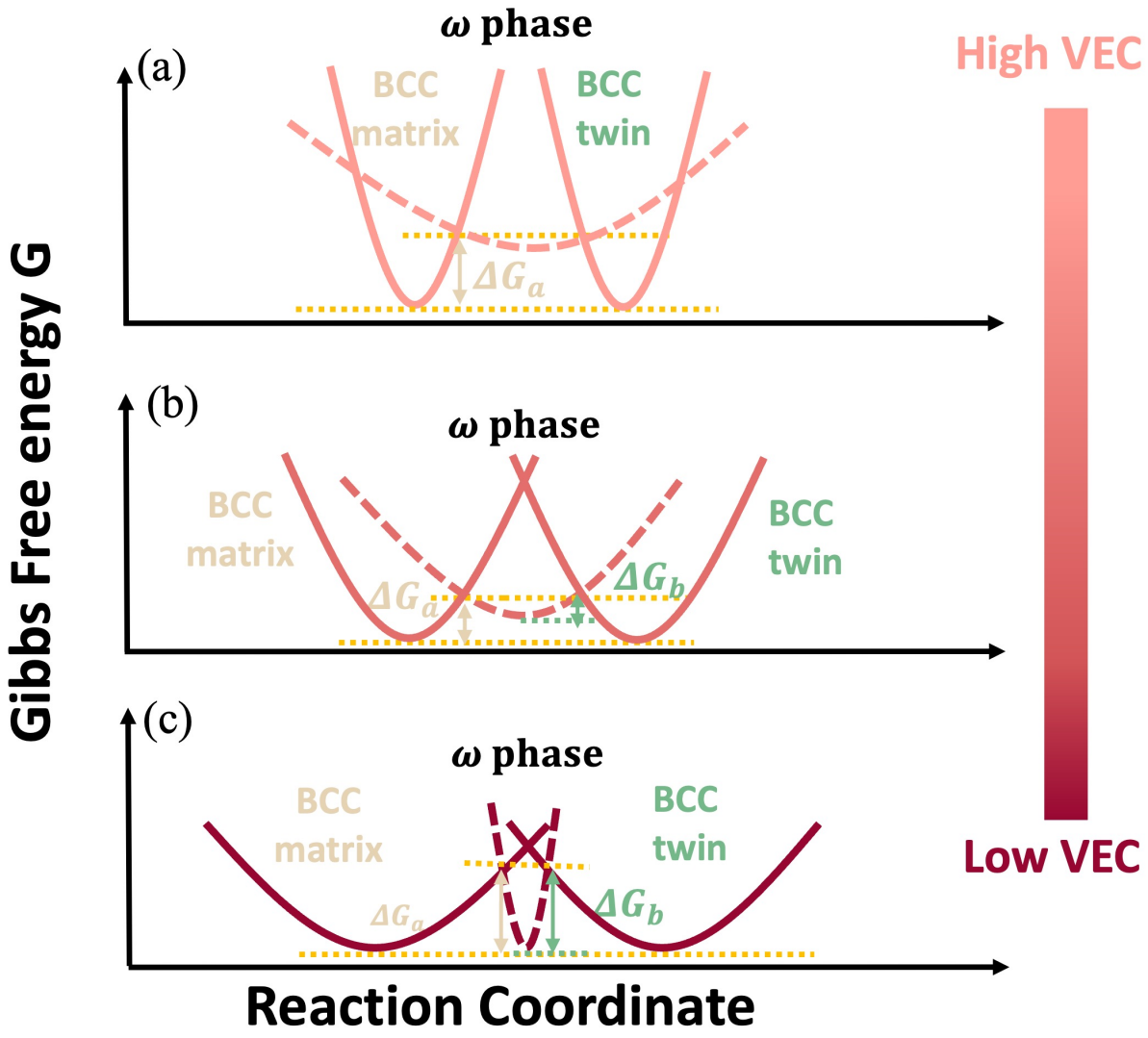


Figure 2.14: Schematic draw of the free energy landscape variations for the homogeneous diffusionless transformations to indicate the variation of twin boundary migration kinetics. In each subfigure, solid curves represent the BCC matrix and BCC twin (left and right), respectively; the dashed curve in the middle is for the ω phase. The color bar for the free energy landscape curves is shown on the right of the figure. Darker red is for lower VEC Ti alloys while lighter red is for higher VEC Ti alloys. ΔG_a in the plots represents the energy barrier of BCC matrix $\rightarrow$ ω phase transformation and ΔG_b represents the energy barrier of ω phase $\rightarrow$ BCC twin transformation. Since ΔG_b in (a) is very small, we do not mark it there.

VEC changes from Figure 2.14 (a) to (c), the free energy of β phase at its ground state goes up relative to that of ω phase, and the local curvature of the free energy curve may also decrease at the ground state of β phase because the energy cost to break its ground-state symmetry structure generally drops with its weakened stability. Because of the existence of ω phases on the {112} twin boundaries in many β-Ti alloys, we can assume the free energy landscape of the homogeneous diffusionless transformation of β matrix $\rightarrow$ ω phase $\rightarrow$ β twin is strongly correlated to the kinetics of {112} twin boundary migration, so a low/high energy barrier along the free energy landscape of this homogeneous transformation can correspond to the fast migration kinetics. As shown in Figure 2.14, there is an energy barrier of ΔG_a from the ground state of β matrix to the ground state of ω phase, and there is another energy barrier ΔG_b from the ground state of ω phase to the ground state of β twin. Thus, the overall twin migration kinetics could be related to the larger value of ΔG_a and ΔG_b in this whole transformation path from β matrix to β twin.

Due to the changes in the positions and shapes (local curvatures near the ground states) of free energy curves of both β and ω phases illustrated in Figure 2.14, we can see the variations of the larger value of ΔG_a and ΔG_b can be used to explain the role of ω phase on the {112} twin growth kinetics. When VEC is large ($\sim$ 4.5 at 300 K), ΔG_a is much larger than ΔG_b (Figure 2.14 (a)), indicating there could be large barriers to achieve the transformation path from β matrix to β twin through ω phase as the intermediate phase, and the twin migration can be achieved by other mechanisms (such as the twin dislocation mechanisms[198]). When VEC decreases ($\sim$4.33 at 300 K), ΔG_a decreases and ΔG_b is also not large (Figure 2.14 (b)), indicating ω phase as the intermediate phase can provide a low-barrier transformation path from β matrix to β twin. When VEC further decreases ($\sim$ 4.25 at 300 K), both ΔG_a and ΔG_b can increase again compared with those in Figure 2.14 (b), indicating the twin migration kinetics is slowed down again. Meanwhile, as ω phase become stable at low VEC conditions, they can locally form in different orientations and can grow or shrink in different directions under loading conditions, which further complicates

the {112} twinning pathways. Here we have to emphasize that the plots of free energy landscape are used for illustration purposes only. They should not only be governed by VEC but also other factors, such as chemical composition variations beyond the d-band filling effects, temperature, applied stress, etc. An accurate free energy landscape of metastable phases in Ti alloys will be investigated in future work to provide quantitative guidance on manipulations of twin activities based on thermodynamic phase stability. In addition, the quantitative correlation between the free energy landscape in the homogeneous diffusionless transformation and the twin migration kinetics through heterogeneous mechanisms (e.g., twin boundary step formation and migration) should also be studied in detail. A possible strategy is to investigate how the free energy landscape in the homogeneous diffusionless transformation affects the energy profiles of twin growth faults in Figure 2.12, which can be regarded as simplified mechanisms of the realistic twin boundary migration kinetics. The free energy landscape of reversible phase transformations can be accurately explored for complex alloy compositions based on atomistic simulations and CALPHAD (CALculation of PHAse Diagrams) methods, and twin growth fault energy profiles can also be calculated by atomistic simulations with accurate interatomic potentials or direct first-principles calculations.

Though our results illustrate that the stability and growth kinetics of the pre-existing {112} twin embryos are highly related to the diffusionless transformation between metastable phases in β Ti alloys, we did not investigate the correlation between phase transformation and {112} twin nucleation in this study. In experiments, {112} twin nuclei were observed inside the ω nano-particles in β Ti alloys, so it was proposed that {112} twins were nucleated from the ω phase [215], but the real dynamics of twin nucleation is difficult to be captured experimentally. In this work, we do not intend to extensively investigate the relationship of phase transformations and {112} twins nucleation in various types of Ti alloys. Instead, we apply MD simulations to demonstrate that {112} twins in Ti_3Nb prefer to nucleation from grain boundaries instead of local ω clusters or particles. Specifically, we compare the twin nucleation behaviors in Ti_3Nb alloy under three different conditions: 1) shearing along the

twinning direction for a perfect single crystal, 2) shearing along the anti-twinning direction for a perfect single crystal, and 3) shearing a bicrystal containing twist grain boundaries [62]. The detailed description of twist grain boundary construction is in Appendix B B.5.1. According to the stress-strain curves shown in Appendix B B.5.2, {112} twins can nucleate either by shearing along twinning or anti-twinning directions with a comparable critical shear stress, which is consistent with the results of $\gamma^{\mathrm{AT}}_{\mathrm{TGF}}/\gamma^{\mathrm{TW}}_{\mathrm{TGF}}$ for Ti_3Nb in Figure 2.12 (c). In addition, compared to the twin nucleation behaviors in single crystals, twins can nucleate more easily under relatively smaller shear stress and much smaller shear strain from grain boundaries in the bicrystal case. In Appendix B B.5.3, we also present the snapshots of the whole process of twin nucleation and evolution. The results show twins directly nucleate from the grain boundaries and then annihilate under the increased strain, consistent with the detwinning behavior of the twin embryo in Ti_3Nb plotted in Figure 2.10(a) and Figure 2.11 (a). Meanwhile, we do not observe a significant amount of local ω phases before twin nucleation in all three cases, but we can observe thick ω phases form around the twin boundaries from the cross-section views after twin nucleation. The formed thick ω phases do not promote the twin growth and totally disappear once the twin totally shrinks. These MD simulations suggest that, at least for Ti alloys with VEC values $\sim$ 4.25 or higher at 300 K, the local ω phases are more likely to be products of {112} twins formed from grain boundaries and other defects, which are preferred twin nucleation sites compared with local ω phases. However, for Ti alloys with even lower VEC values and a large amount of athermal ω phases, {112} twin nucleation promoted by ω phases could be possible.

Besides effects of ω phase and defects like grain boundaries on {112} twinnability, oxygen is also an important factor controlling the {112} twinnability, which is not mentioned in this study. In experiments, oxygen is highly soluble in Ti alloys and solubility of oxygen is inevitable during mechanical processing [8]. Meanwhile, it is widely acknowledged that oxygen content plays important roles in deformation mechanisms and phases stability in β-Ti alloys [140, 42, 44, 23, 69, 56], especially ω phase stability, α'/α" phase stability, and phase

transformation between multiple metastable phases [44, 140, 23, 207, 214, 7]. Generally, it is widely observed that high-level oxygen content can suppress the formation of ω phase [207, 44] and increase the stability of β phase in the β-Ti alloys [140, 23]. Hence, oxygen can also affect the free energy landscape of ω phase and β phase and so further control the {112} twin growth. Meanwhile, the solubility of oxygen can reduce the volume fraction of stress-induced α'/α" phase in β phase and so increase the difficulty of β phase $\rightarrow$ α'/α" phase transformation [137, 23]. Therefore, it is necessary to include oxygen effects in the future twinnability investigation in Ti alloys.

Our MD results reveal the α'/α" phase-assisted detwinning of {112} twin (Figure 2.11). However, this detwinning behavior may be hard to be observed in experiments. As illustrated in the above discussion, one possible reason is that the solubility of oxygen in real experiments can suppress the β phase $\leftrightarrow$ α'/α" phase and so α'/α" phase may not serve as the intermediate state for reversible β phase transformations in {112} twins as explained in Figure 2.11 (b). Other possible reasons are that the shear strain rates in MD simulations are much larger than those in experiments and microstructures of alloy in real experiments contain complex defects that change the free energy landscape of twin nucleation and growth. As illustrated in Section 2.3.4, detwinning behavior is decided by competition between BCC phase $\leftrightarrow$ α'/α" phase inside twin embryo and BCC phase $\leftrightarrow$ ω phase along twin boundaries. So detwinning behavior happens at the condition of low twin mobility of twin boundaries and large stress accumulating inside the twin embryo in a short time. In experiments, the samples contain various types of defects to release external stress and/or trigger the twin migration under much lower shear strain rates compared with MD simulations. Moreover, twin propagation and growth are generally in the intersonic speed [61] and in-situ techniques are hard to capture the intermediate phase for twinning and detwinning. Nevertheless, whether the detwinning could occur to the stable {112} twin embryo under experimental conditions, our MD simulations indeed confirm that {112} twin embryo growth can become much more difficult when the VEC is below a critical value ($\sim$ 4.25 at 300 K).

2.5 Conclusions

In summary, we conduct DFT calculations and classical MD simulations to investigate the {112} twin embryo stability and growth behaviors in β-Ti alloys comprehensively by varying twin embryo sizes, alloy compositions, and temperatures. Our findings are listed below:

1) Dependent on alloy compositions and the related VEC values, {112} twin boundary structures would activate the local β to ω phase transformations along the twin boundaries. As the VEC value decreases, ω phases on twin boundaries become thicker and increase the roughness of twin boundary planes. These tendencies are generally in agreement with experimental characterizations of {112} twin boundary structures in different β-Ti alloys from this study and literature [132, 60, 111, 239, 215, 37, 205]. Consistent with tendencies, both DFT results at 0 K and MD results at 300 K reveal that stable stacked ω structures would destabilize the twin embryo in low VEC cases (equal or less than 4.25 in this study), so the twin embryo should be much thicker (at least 9 atomic layers of {112} twin planes) for survival than those β-Ti alloys with high VEC values (6 or 3 atomic layers of {112} twin planes when VEC equal or greater than 4.5). This stability requirement for twin embryos can significantly reduce the {112} twin nucleation kinetics/rates in certain β-Ti alloys, where both β phase and ω phase have similar thermodynamic stability.

2) Besides twin embryo nucleation, β to ω phase transformations in β-Ti alloys can also affect the {112} twin growth under the applied shear stress and the effects vary with alloy compositions. In low VEC cases (equal or less than 4.25 at 300K in this study), ω phase transferred from metastable β phase at twin boundaries can greatly impede the twin migration; meanwhile, BCC twin $\rightarrow$ α'/α" phase $\rightarrow$ BCC matrix phase transformations can also be triggered within the {112} twin embryos by the external shear stress and result in twin embryo eliminations. The occurrence of this α'/α" phase-mediated detwinning behavior may benefit from a small difference between the energy barrier of the twinning behavior in BCC matrix and the energy barrier of the anti-twinning behavior in BCC twin region, where

both barriers are calculated by the twin growth fault energy profiles defined by a twinning pathway through homogeneous displacements near the pre-existing twin boundary (details in Figure 2.12). When we further increase VEC (around 4.34 at 300 K), ω phases at twin boundaries behave beneficially and they reduce the critical resolved shear stress (only $\sim$ 0.1 GPa along twin Burgers vector on twin plane) for twin boundary migration and {112} twin embryos can smoothly grow. When VEC further increases (greater than 4.5 at 300K), β to ω phase transformations are not favorable at twin boundaries, and {112} twin embryos can grow by standard twin dislocation formation/migration mechanism with relatively large critical stress ($\sim$ 0.3 GPa for VEC equal to 4.5 and $\sim$ 0.7 GPa for VEC equal to 5.0 (pure Nb)).

3) The effects of β to ω phase transformations on {112} twin embryo growth also depend on temperature. An increase in temperature can enhance the relative stability of β phase compared to other metastable phases, which can suppress the transformations detrimental to twin embryo growth, such as β to ω phase transformations at twin boundaries and reversible β to α'/α" phase transformations within the twin embryo. For example, a 9-layer twin embryo in Ti alloys with VEC equal to 4.25 can grow smoothly under small critical stress (only 0.2 $\sim$ 0.33 GPa) at 400 K.

4)The composition-and-temperature-dependent effects of ω phase on {112} twin embryo growth kinetics may originate from the free energy landscape of the homogeneous diffusionless β matrix $\rightarrow$ ω phase $\rightarrow$ β twin transformations illustrated in Figure 2.14.

CHAPTER 3

Interfacial Structure Evolution and Growth Kinetics of {332} Twin

The $\{332\}\langle 11\bar{3}\rangle$ twinning mode is a characteristic and mechanistically unique deformation mode in metastable β-Ti alloys, yet the atomic-scale mechanisms governing its stability and growth remain poorly understood. This chapter presents a systematic MD investigation of {332} twin embryo stability and boundary migration kinetics across a range of compositions and temperatures in Ti-Nb and Ti-Mo alloy systems. Twin embryo relaxation simulations reveal a critical thickness of stable twin embryo, which increases with decreasing β-phase stability. A transitional α'/α'' interfacial phase forms spontaneously at the twin boundary across all compositions, with its thickness decreasing systematically as the alloy approaches the stable BCC regime. Bicrystal shear simulations show that the twin boundary migration stress is primarily governed by temperature through thermally activated atomic shuffles, while composition plays a secondary role. Atomic displacement analysis reveals a composition-dependent switch in growth mechanism: metastable alloys grow via a $\beta \rightarrow \alpha'' \rightarrow \beta$ transformation pathway, whereas more stable alloys follow the crystallographically predicted minimum-shuffle path. Despite these mechanistic differences, neither embryo survival nor boundary migration is prohibitively difficult in the stable composition range where {332} twinning is experimentally absent. This points to early-stage twin nucleation and propagation as the rate-determining step, motivating the atomistic nucleation study presented in the following chapter.

3.1 Introduction

Among all deformation twinning modes reported in BCC metallic systems, the $\{332\}\langle 11\bar{3}\rangle$ twin (short as $\{332\}$ twin in following parts) is arguably the most unusual and the most consequential from a materials design perspective. Unlike the $\{112\}\langle 11\bar{1}\rangle$ twinning mode (shorten as $\{332\}$ twin in following parts) that operates across virtually all stable BCC metals such as iron, tungsten, molybdenum, tantalum, niobium; and metstable β Ti alloys in this thesis. $\{332\}$ twin is essentially absent in elemental BCC metals and appears almost exclusively in metastable β-Ti alloys, where the β-phase is held in a thermodynamically unstable state by β-stabilising alloying elements such as Mo, Nb, V, and Ta [123]. First predicted experimentally identified by Blackburn and Williams in 1971 in Ti-11.5Mo-6Zr-4.5Sn [16], the $\{332\}$ twin has since been reported across a wide range of binary and multicomponent metastable β-Ti systems, including Ti-V, Ti-Mo, Ti-Nb, and Ti-Zr-based alloys [123]. The misorientation across the $\{332\}$ twin boundary is 50.5°, characterised by the twinning elements $K_1 = \{332\}$, $K_2 = \{11\bar{2}\}$, $\eta_1 = \langle 11\bar{3}\rangle$, $\eta_2 = \langle 111\rangle$, a twinning shear of $s = 0.3536$, and a plane of shear $P = \{1\bar{1}0\}$ [189]. This relatively low shear magnitude combined with the requirement of atomic shuffles for one half of the atoms in each twinning layer, places the $\{332\}$ mode in the class of shear-shuffle compound twins whose operative mechanism is fundamentally different from the pure-shear $\{112\}$ mode in stable BCC alloys. In terms of mechanical consequences, the $\{332\}$ twin imparts a low yield strength, substantial elongation, and a high sustained work hardening rate to metastable β-Ti alloys, making it one of the primary carriers of the TWIP effect in this alloy class [123]. Critically, the activation of $\{332\}$ twinning is strongly composition-dependent: as the β-phase stability increases with alloying content, the operative deformation mode transitions systematically from $\{332\}$ twinning to $\{112\}$ twin and dislocation slip, and the mechanical response shifts correspondingly from low yield strength with high elongation to high yield strength with limited ductility. This composition-controlled mode transition positions the $\{332\}$ twin as a central design

lever in the engineering of metastable β-Ti alloys for structural and biomedical applications.

Despite the extensive experimental characterisation of {332} twins in metastable β-Ti alloys, two fundamental mechanistic questions remain unresolved. First, no systematic atomistic study has examined how the twin boundary core structure - including the character, thickness, and stability of the transitional α'' or ω interfacial layer – evolves as a function of alloy composition and temperature. Existing experimental observations are necessarily limited to post-mortem snapshots at fixed compositions, and the dynamic structural evolution at the moving boundary under different thermomechanical conditions is entirely inaccessible to current experimental techniques. Second, it remains unclear whether the strong preference for {332} twinning in metastable β and stable BCC Ti alloys is governed primarily by the nucleation stage or the growth stage of the twinning process. If the preference is set at nucleation, it implies that the energy barriers for embryo formation on {332} and {112} planes differ decisively between metastable and stable BCC systems, likely through the coupling to the $\beta \rightarrow \alpha''$ transformation pathway discussed above. If instead growth kinetics are controlling, then the twin boundary migration stress is the quantity that determines mode selection. Disentangling these two contributions is essential for any predictive model of deformation mode competition in metastable β-Ti alloys, yet no study has addressed this question from an atomistic perspective.

The unresolved questions identified above define the central objectives of the atomistic investigation in this chapter. First, we use molecular dynamics (MD) simulations with both classical interatomic potentials and machine-learning potentials to examine the structural evolution of the interfacial twin boundary during migration under controlled shear loading. We consider both Ti-Nb and Ti-Mo alloy systems, covering compositions from the metastable regime to the more stable β regime over a wide temperature range. Structurally, we observe a change in twin-boundary migration behavior as the alloy composition shifts from the metastable to the stable regime. Energetically, We then examine whether these different atomic migration mechanisms lead to a corresponding change in the stress required for

twin-boundary motion. Surprisingly, the critical shear stress does not differ dramatically between metastable and stable Ti alloys. This result indicates that the difficulty of forming {332} twins in stable BCC alloys is not primarily caused by poor twin-boundary mobility during growth. Instead, it suggests that the rate-limiting step for {332} twinnability is twin nucleation, which will be investigated in the next chapter.

3.2 Methods

3.2.1 Supercell Setup

As for the simulation box setting for twin stability, 41040 atoms were included in a supercell with basis vectors of $15[113]\times18[\bar{1}10]\times7[\bar{3}\bar{3}2]$ in the unit of conventional BCC lattice vectors. For chemical compositions of Ti alloys, we chose three different compositions: Ti_3Nb (VEC = 4.25), Ti_2Nb (VEC =4.33), TiNb (VEC = 4.5). Besides, each composition was applied to generate 4 different structures: 5-layer twin embryo, 11-layer twin embryo, 17-layer twin embryo and 22-layer twin embryo. As for the simulation box setting for twin migration, 31500 atoms were included in a supercell in bicrystal with basis vectors of $10[113]\times9[\bar{1}10]\times16[\bar{3}\bar{3}2]$ in the unit of conventional BCC lattice vectors. Meanwhile, we add 10 angstrom vacuum at top and bottom layer. The twin boundary is at middle. Here we investigate two different alloy systems, Ti-Nb and Ti-Mo. As for chemical compositions of Ti-Nb alloys, we chose three different compositions: Ti_3Nb (VEC = 4.25), Ti_2Nb (VEC =4.33), TiNb (VEC = 4.5). As for chemical compositions of Ti-Mo alloys, we chose four different compositions in weight percent: Ti-10Mo, Ti-12Mo, Ti-15Mo and Ti-25Mo.

3.2.2 MD Simulations

Molecular dynamics (MD) simulations were performed by Large-scale Atomic/Molecular Massively Parallel Simulator (LAMMPS) [170]to investigate Ti-Nb and Ti-Mo binary alloys. Ti-Nb systems we use modified embedded atom method (MEAM) potential developed

by Ehemann et al. [57] while Ti-Mo systems we employ Ti-Nb-Ta-Mo machine learning potential developed by Zheng et al. [236]. For examinations of twin embryo stability at room temperature, MD simulations were performed on the supercells at a constant temperature of 300K under the isothermal-isobaric (NPT) ensemble ($P = 0$) for 200 ps. The time step was set to be 1 fs. The energy and structure of the system were calculated every 1 ps. Furthermore, to investigate temperature and composition-dependent twin migration behaviors, we deformed the supercells that contain the bicrystal by applying shear stress with a constant engineering shear strain rate of 1 $\times 10^7$ s^{-1} along [113] direction on $(\bar{3}\bar{3}2)$ plane. The time step for the deformation simulation was also 1 fs. An MD simulation of 30 ps at target temperatures in an NPT ($P = 0$) ensemble was performed for equilibrium before each deformation operation. To analyze the atomistic structures generated by MD simulations, we used the polyhedral template matching (PTM) [117] and the grain segmentation method to identify BCC matrix, BCC twin, and α'/α" phase [19]. In addition, we also applied OVITO to visualize all the MD results [183].

3.3 Results

3.3.1 {332} Twin Stability

Figure 3.1 presents the MD-relaxed structures of {332} twin embryos of varying thickness (5, 11, 17, and 22 atomic layers) across three Ti–Nb compositions spanning a range of β-phase stability: Ti_3Nb (VEC = 4.25), Ti_2Nb (VEC = 4.33), and TiNb (VEC = 4.50), and Figure 3.2 presents the corresponding results for three Ti–Mo compositions (in weight percent): Ti-12Mo (VEC = 4.13), Ti-66.7Mo (VEC = 5.00), and pure Mo (VEC = 6.00), all at 300 K. Several composition- and thickness-dependent trends emerge consistently across both alloy systems. With respect to twin embryo stability, a critical twin thickness exists below which the embryo spontaneously collapses back into the β matrix upon relaxation, and this critical thickness increases systematically with decreasing β-phase stability across both sys-

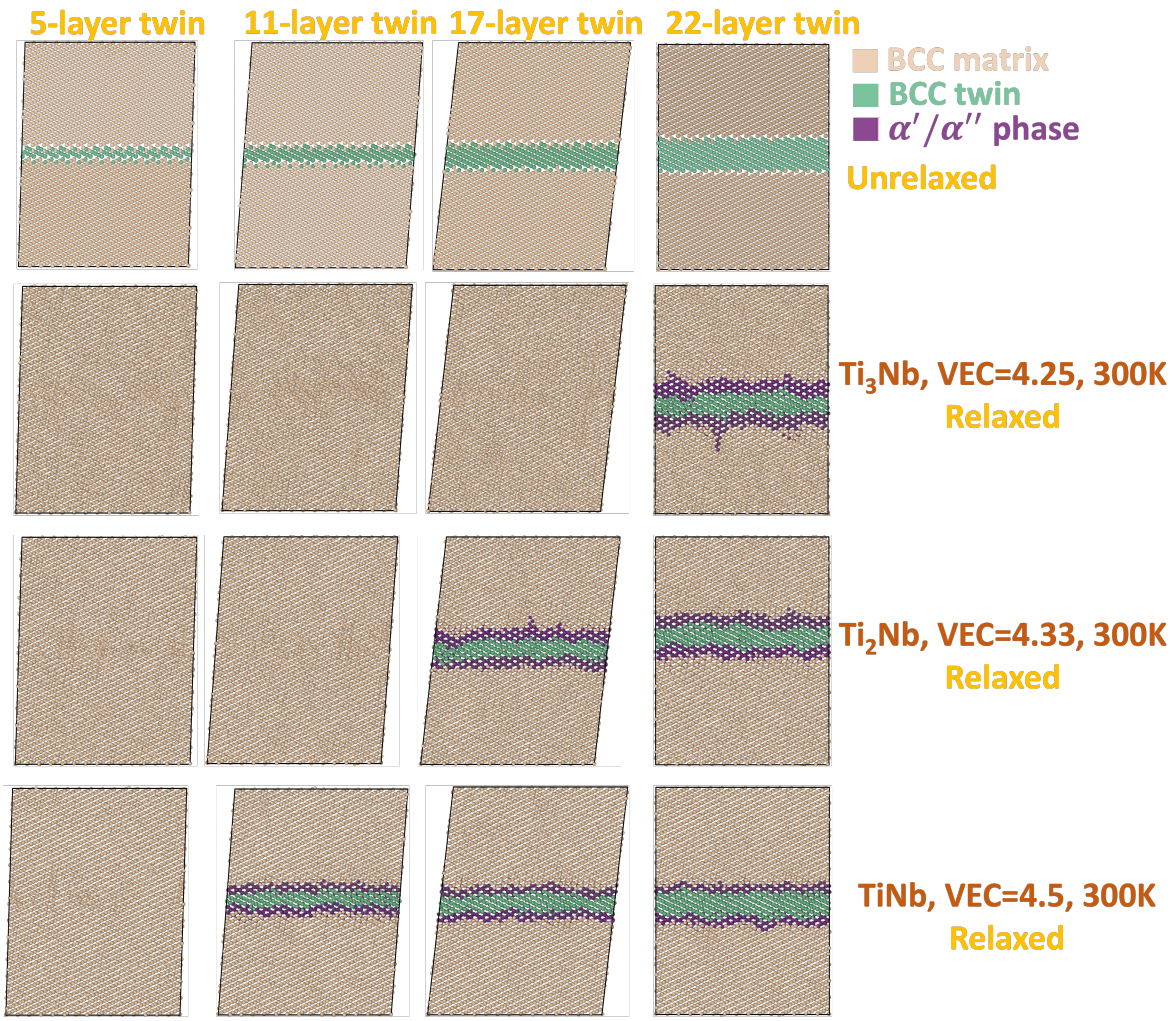


Figure 3.1: Stability analysis of pre-inserted {332} twin embryos in Ti–Nb alloys at 300 K. The columns show initial twin thicknesses of 5, 11, 17, and 22 atomic layers. The first row shows the unrelaxed configurations, in which the BCC twin embryo is embedded in the BCC matrix. The following rows show the relaxed structures for Ti_3Nb, Ti_2Nb, and TiNb, corresponding to VEC values of 4.25, 4.33, and 4.50, respectively. Beige atoms indicate the BCC matrix, green atoms indicate the BCC twin, and purple atoms indicate the spontaneous transferred α'/α'' phase. The relaxation results reveal a strong dependence of {332} twin stability on composition and embryo thickness. Thin twin embryos are unstable and tend to disappear during relaxation, whereas thicker embryos can be retained and are accompanied by local α'/α'' transformation near the twin interface. This behavior suggests that the stability of {332} twins in metastable Ti–Nb alloys is closely coupled to local martensitic transformation and depends on both alloy composition and twin embryo size.

tems: in TiNb (VEC = 4.50), a stable twin embryo is already established at 11 layers, whereas in Ti_2Nb (VEC = 4.33) a minimum of 17 layers is required, and in Ti_3Nb (VEC = 4.25) even the 22-layer embryo remains marginally stable at 300 K; in the Ti–Mo system, pure Mo (VEC = 6.00) retains stable embryos at all thicknesses without interfacial transformation, Ti-66.7Mo (VEC = 5.00) requires a minimum of 17 layers, and Ti-12Mo (VEC = 4.13) exhibits structural disordering even at 22 layers, reflecting its proximity to the martensitic transformation boundary. Regarding the interfacial twin boundary structure, a physically significant observation is the spontaneous formation of an α'/α'' interfacial phase at both twin boundaries upon relaxation in the metastable compositions of both systems. This is not a pre-imposed structural constraint but emerges naturally from the energy minimization of the as-constructed {332} embryo, providing direct atomistic confirmation that the transitional martensitic layer at the {332} twin boundary is thermodynamically intrinsic to this twinning mode and is not an artifact of deformation history or specimen preparation, consistent with experimental observations [38, 113].

Critically, the thickness of this interfacial α'/α'' layer decreases systematically as β-phase stability increases — from Ti_3Nb to TiNb in the Ti–Nb system, and from Ti-12Mo toward pure Mo in the Ti–Mo system. This reflects the diminishing thermodynamic driving force for martensitic transformation as the alloy composition moves away from the $\beta \rightarrow \alpha''$ transformation boundary toward the stable BCC region, where the interfacial α'/α'' phase is completely absent, as seen in pure Mo This compositional dependence of the interfacial phase thickness across two chemically distinct alloy systems demonstrates that the coupling between phase transformation and twin boundary structure is a general feature of twinning in metastable β alloys, analogous to the ω-mediated interfacial layer at the {112} twin boundary reported in the preceding chapter, and operative across different twinning modes through a common underlying lattice instability mechanism. Then it raises a question that how these interfacial phases affects the twin migration behaviors, which will be discussed in the following part.

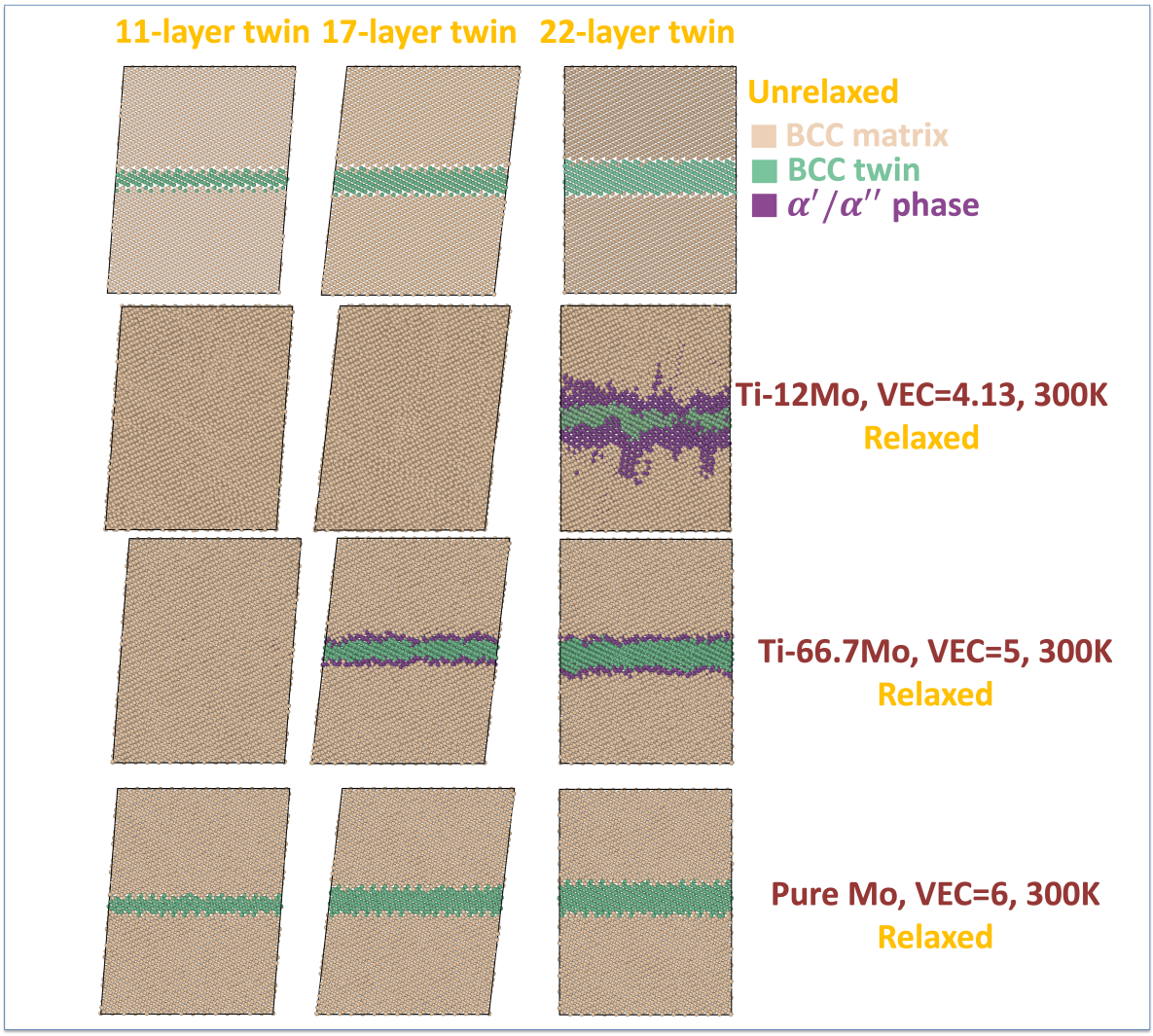


Figure 3.2: Stability analysis of pre-inserted {332} twin embryos in Ti–Mo alloys at 300 K. The columns show initial twin thicknesses of 11, 17, and 22 atomic layers. The first row shows the unrelaxed configurations, in which the BCC twin embryo is embedded in the BCC matrix. The following rows show the relaxed structures for Ti–12Mo (wt.%), Ti–66.7Mo (wt.%), and Pure Mo, corresponding to VEC values of 4.13, 5, and 6, respectively. Beige atoms indicate the BCC matrix, green atoms indicate the BCC twin, and purple atoms indicate the spontaneous transferred α'/α'' phase.

3.3.2 {332} Twin Growth

Figure 3.3 and Figure 3.4 present the shear stress–strain responses of {332} twin boundary migration in Ti-Nb (25, 33, and 50 at.% Nb) and Ti-Mo (10, 12, 15, and 25 wt.% Mo) bicrystal systems, respectively, simulated across a range of temperatures. In both alloy systems, the stress-strain curves share a consistent characteristic shape: an initial elastic loading regime, followed by a stress drop marking the onset of twin boundary migration, and a subsequent lower plateau reflecting the steady-state glide of the twin boundary across the simulation cell. This behavior confirms that the critical stress extracted from each curve corresponds to the twin boundary migration stress.

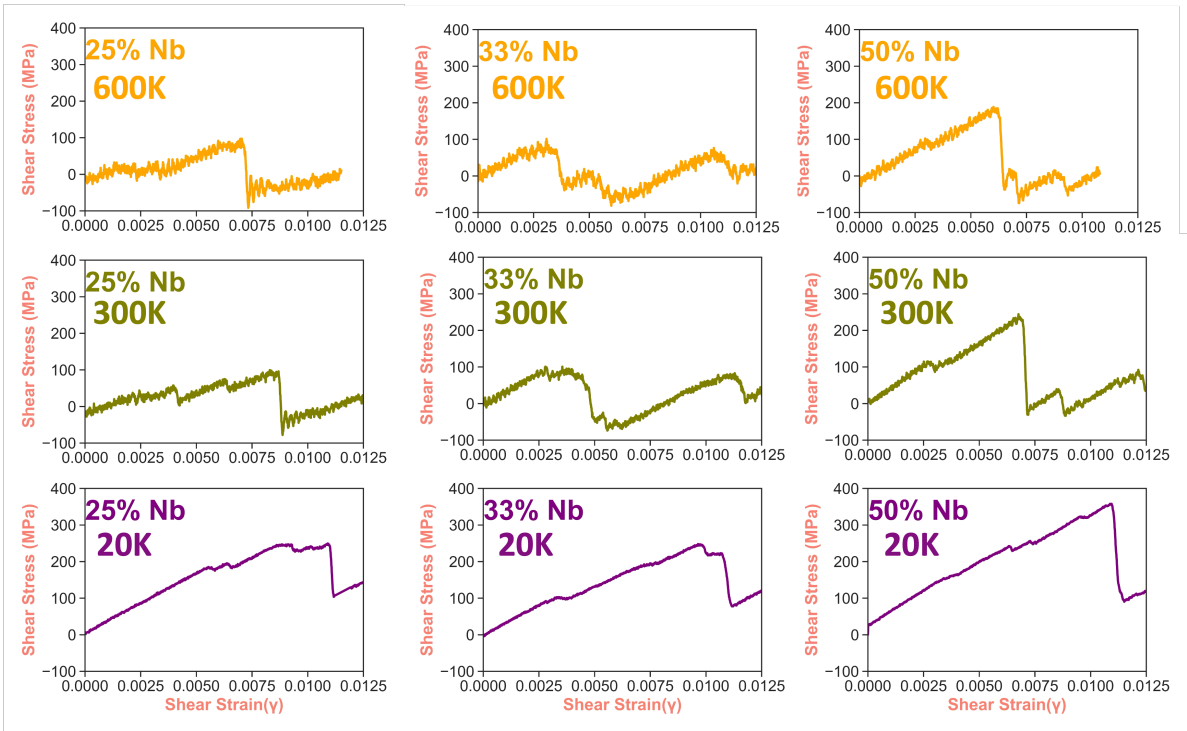


Figure 3.3: Shear stress–strain curves for {332} twin-boundary migration in Ti–Nb bicrystal models under engineering strain rate of 1×10^7 s^{-1}. The columns correspond to Nb contents of 25, 33, and 50 at.%, respectively. The rows correspond to temperatures of 600, 300, and 20 K, respectively. Orange, olive, and purple curves denote simulations at 600, 300, and 20 K, respectively. The vertical axis shows the shear stress in MPa, and the horizontal axis shows the imposed shear strain γ.

The most pronounced and systematic trend in both datasets is the strong sensitivity of

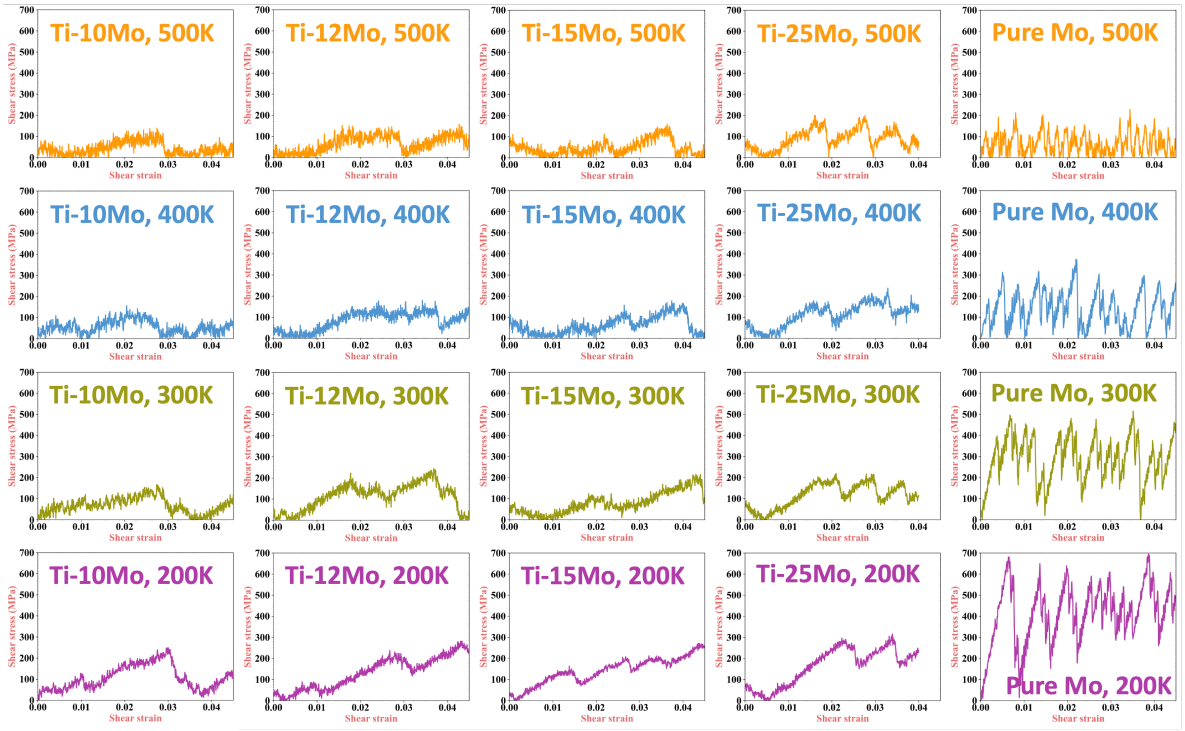


Figure 3.4: Shear stress–strain curves for {332} twin-boundary migration in Ti–Mo bicrystal models under engineering strain rate of 1×10^8 s^{-1}. The columns correspond to Mo contents of 10, 12, 15, 25 wt.% and pure Mo, respectively. The rows correspond to temperatures of 500, 400, 300, and 200 K, respectively. Orange, blue, olive, and purple curves denote simulations at 500, 400, 300, and 200 K, respectively. The vertical axis shows the shear stress in MPa, and the horizontal axis shows the imposed shear strain γ.

the twin boundary migration stress to temperature. In the Ti-Nb system, the migration stress decreases dramatically as temperature increases from 20 K to 600 K: at 25 at.% Nb, the peak migration stress drops from approximately 260 MPa at 20 K to below 100 MPa at 300 K, and falls further to near zero-stress-plateau behaviour at 600 K, where thermal activation alone is sufficient to drive boundary motion at the applied strain rate. Qualitatively identical behavior is observed in the Ti-Mo system: across all four Mo compositions, the migration stress decreases by a factor of two to three as temperature rises from 200 K to 500 K, with the stress–strain curves at elevated temperatures exhibiting a notably noisier, more diffuse yield point that reflects thermally activated boundary fluctuations rather than a sharp mechanical instability. This strong temperature sensitivity is physically consistent with the shuffle-mediated {332} growth mechanism discussed in the preceding section: unlike pure-shear {112} growth driven by twinning partial glide, the cooperative atomic shuffles required for {332} boundary advancement carry a finite thermal activation barrier that is progressively overcome as temperature increases, rendering the effective migration stress highly temperature-dependent.

In contrast, the effect of composition on the twin boundary migration stress is comparatively modest in both alloy systems. In the Ti-Nb system, increasing the Nb content from 25 to 50 at.%, β-phase stability increases and then eliminates the α'' interfacial layer at the twin boundary as demonstrated in the preceding section. which raises the migration stress only marginally at a given temperature: at 300 K, the peak stress increases from $\sim$90 MPa at 25 at.% Nb to $\sim$240 MPa at 50 at.% Nb, a notable but not dramatic change considering the large compositional interval spanned. Similarly in the Ti-Mo system, the migration stress shows only a moderate increase with Mo content across the four compositions at each temperature, with no qualitative change in the shape or character of the stress–strain response. This relative composition-insensitivity of the migration stress reinforces the interpretation that twin boundary growth in both alloy systems is predominantly governed by thermal activation of the atomic shuffle pathway rather than by the local phase stability of

the boundary. The composition controls primarily whether the α'' interfacial layer is present at the boundary, which modifies the effective migration stress through the energetics of the transformation-coupled pathway, but the dominant kinetic lever remains temperature. Taken together, these results establish a clear hierarchy: temperature is the primary control variable for {332} twin growth kinetics, with composition playing a secondary but non-negligible role through its influence on the interfacial phase character. This temperature-dominant, composition-modulated behavior constitutes the quantitative physical basis for the kinetics model of twin developed in the subsequent chapter.

3.3.3 Composition-dependent {332} Twin Growth Mechanisms

The preceding sections established the temperature- and composition-dependent twin stability and migration stress in Ti-Nb and Ti-Mo alloys. However, the underlying atomic growth mechanism remained uncharacterised. Here we analyse the atomic displacements during {332} twin boundary migration to resolve how the boundary advances at the atomic scale, and how this differs between metastable and stable compositions.

Figure 3.5 presents the atomic displacement profiles during twin growth in Ti_3Nb and TiNb at 300 K. Two displacement components are examined independently: the displacement along the twinning direction $X = [11\bar{3}]$ (shear component) and the displacement along the twinning normal $Z = [\bar{3}\bar{3}2]$ (shuffle component). A non-zero displacement along Z would be absent in a pure-shear twinning mechanism. Both systems show clear, finite displacements along Z across the twin layers. This directly confirms that {332} twin growth is not a pure shear process. It proceeds by a combined shear-plus-shuffle mechanism, consistent with the crystallographic requirement discussed in Chapter 1. Despite this common feature, the two compositions show qualitatively distinct displacement characters in the Z direction. In Ti_3Nb (metastable, VEC = 4.25), the Z-displacements are large in magnitude and broadly distributed across layers L1–L12 without a well-defined layer-by-layer sequence. This diffuse, irregular pattern deviates significantly from the minimum-displacement shuf-

fle path proposed by Tobe et al. [189]. Instead, it suggests that atoms do not follow the shortest crystallographic path between parent and twin positions. We attribute this to the $\beta \rightarrow \alpha'' \rightarrow \beta$ transformation pathway operating at the boundary: atoms traverse an intermediate α'' structural configuration, which carries a larger and more distributed displacement field than the direct shuffle path. Full atomic trajectories supporting this interpretation are provided in Appendix C.

In TiNb (more stable, VEC = 4.50), the behaviour is markedly different. The Z-displacements across layers L1–L10 are small in magnitude and display a rigid, alternating up-and-down pattern from layer to layer. This ordered, low-amplitude displacement profile is in close agreement with the minimum-shuffle mechanism proposed by Tobe et al. [189], in which each twinning layer undergoes the smallest geometrically admissible shuffle to reach the twin configuration. Although a thin α'' interfacial layer is still present in TiNb as shown in the preceding section, its influence on the bulk of the twin layers is evidently minor. The growth mechanism is dominated by the direct shear-shuffle path rather than the transformation pathway.

These results reveal a composition-dependent switch in the atomic growth mechanism of {332} twins. In metastable alloys, growth is mediated by the transformation pathway, with atoms traversing an α'' intermediate state and producing a diffuse, large-amplitude shuffle field. In more stable alloys, growth follows the minimum-shuffle path, with atoms executing small, ordered displacements layer by layer. This mechanistic transition is directly coupled to the thickness and stability of the α'' interfacial phase characterized earlier: a thicker, more stable α'' layer promotes the transformation-pathway growth mechanism, while a thin or absent interfacial phase permits the minimum-shuffle mechanism to dominate. The two mechanisms carry different energy barriers and different sensitivities to temperature, which provides a physical basis for the composition-modulated migration stress observed in Figures 3.3 and 3.4.

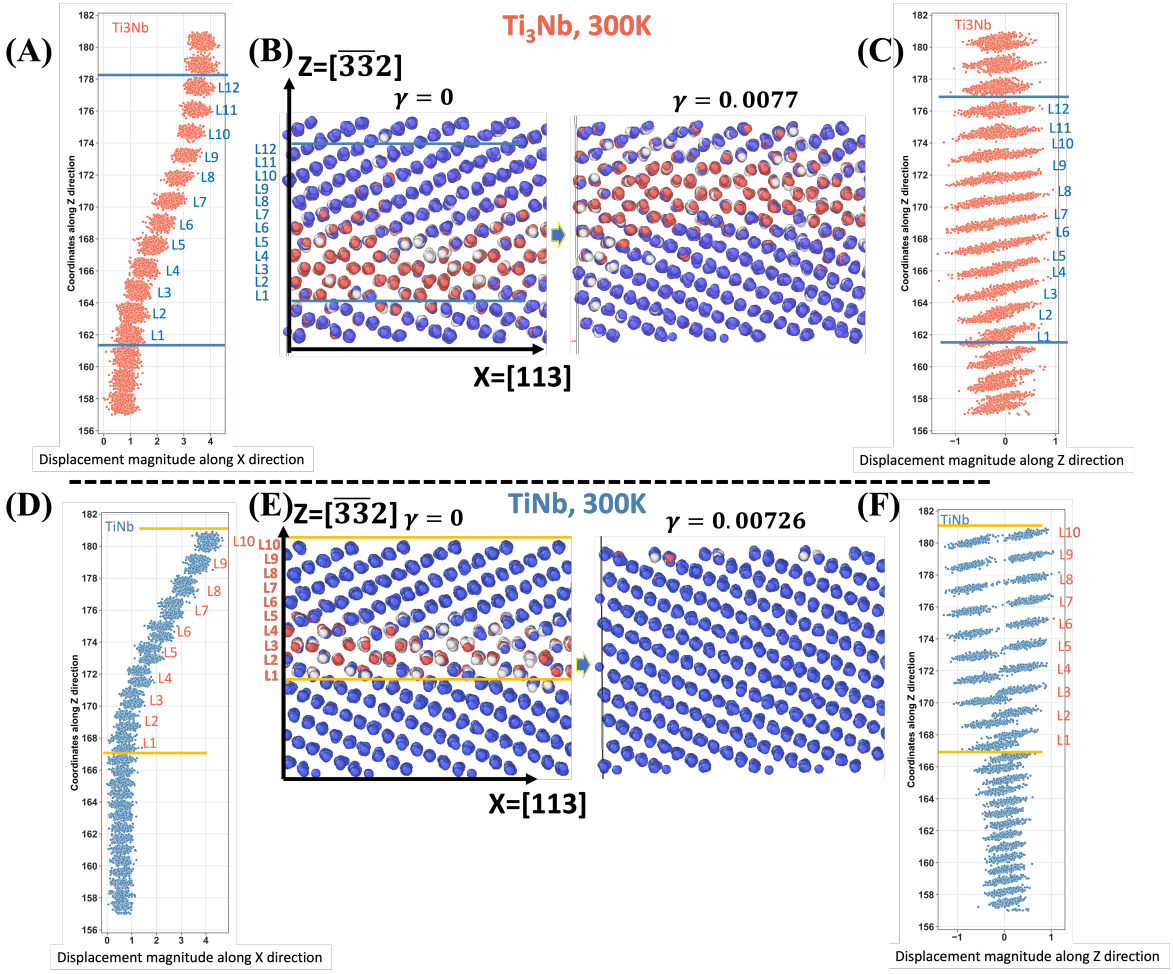


Figure 3.5: Atomic displacement analysis during {332} twin growth in Ti–Nb alloys at 300 K. Panels (A)–(C) show the Ti_3Nb system, and panels (D)–(F) show the TiNb system. Panels (B) and (E) show atomic configurations before and after shear deformation, with the initial states at $\gamma = 0$ and the deformed states at $\gamma = 0.0077$ for Ti_3Nb and $\gamma = 0.00726$ for TiNb. The viewing directions are indicated by the in-plane axes $X = [113]$ and $Z = [\bar{3}\bar{3}2]$. Blue horizontal lines mark the analyzed twin region. Panels (A) and (D) plot the displacement magnitude along the X direction as a function of atomic coordinate along the Z direction. Panels (C) and (F) plot the displacement magnitude along the Z direction as a function of atomic coordinate along the Z direction. Layer labels L1–L12 for Ti_3Nb and L1–L10 for TiNb identify the atomic layers within the analyzed twin region. The displacement is normalized by the average atomic layer distance along each direction.

3.4 Discussion

In this study we focus on {332} twin stability and growth kinetics in metatsable Ti alloys, primarily in Ti-Nb and Ti-Mo alloy systems. As for twin stability, the comparison of critical embryo thicknesses across compositions, raises an apparent inconsistency with experimental observation. The present results show that lower β-phase stability requires a thicker critical embryo to survive under room temperature — a trend observed consistently in both Ti–Nb (Ti_3Nb requiring the largest critical thickness) and Ti–Mo (Ti-12Mo exhibiting structural disordering even at 22 layers) — suggesting a higher energetic cost for stable embryo formation in more metastable alloys. This appears to contradict the well-established experimental finding that {332} twinning is more prevalent in alloys of lower β-stability, and is essentially absent in fully stable BCC metals. This apparent inconsistency, however, dissolves when the role of the interfacial α'/α'' phase is considered carefully. In the low-stability alloys, the thick α'/α'' layer at the twin boundary carries a significant fraction of the transformation eigenstrain associated with the $\beta \rightarrow \alpha''$ pathway, which acts to destabilize the thin embryo energetically. In other words, the interfacial phase does not simply accommodate the twin. Instead it competes with it for structural identity in the early-thickness regime, requiring the embryo to attain a minimum thickness before the twin core energy dominates over the interfacial transformation penalty. This is precisely why small embryos in the low-stability alloys collapse: they are partially converted back to BCC matrix via α'' rather than surviving as a geometrically coherent twin. The critical thickness therefore reflects not the difficulty of the twinning shear alone, but the energetic competition between twinning and phase transformation at the embryo boundary.

As for twin boundary migration stress, taken together with the interfacial α'/α'' thickness trends established in the preceding section, reveal a physically consistent picture: as β-phase stability increases and the interfacial α'/α'' layer progressively thins and ultimately vanishes, the twin boundary migration stress increases accordingly, confirming that the inter-

facial α'/α'' phase actively promotes {332} twin growth by lowering the effective migration barrier through the transformation-coupled shuffle pathway. However, when the {332} migration stresses are compared directly against the {112} twin boundary migration stresses established in Chapter 3, an apparent inconsistency with experimental observation emerges at the stable BCC composition range. In the metastable regime, the comparison is fully consistent with experiments: {332} twins exhibit migration stresses that are substantially lower than, or at most competitive with, those of {112} twins, providing a clear energetic rationale for the experimental prevalence of {332} twinning in metastable β-Ti alloys. In the high-stability regime, however, the {332} migration stress remains competitive with that of {112} twins — for instance, both modes exhibit migration stresses on the order of $\sim 200\,\mathrm{MPa}$ in TiNb at $300\,\mathrm{K}$ — yet experimentally, {332} twinning is rarely, if ever, observed in alloys of comparable or higher β-phase stability. This persistent inconsistency between the growth stress comparison and experimental mode selection strongly suggests that the rarity of {332} twinning in stable β alloys is not governed by twin growth kinetics, but is instead controlled at the nucleation stage, a conclusion that motivates the systematic nucleation analysis presented in the subsequent chapter.

Reconciling this with the experimental prevalence of {332} twinning in metastable alloys requires recognizing that embryo stability, boundary migration, and twin nucleation are distinct physical processes that must be considered separately. The atomistic results presented in this chapter demonstrate that, once a {332} embryo has attained its critical thickness, boundary migration proceeds readily across a wide range of compositions and temperatures in both Ti–Nb and Ti–Mo systems, and that even in the high-stability regime — where {332} twinning is experimentally rare — the migration stress remains competitive with that of {112} twins; neither embryo survival nor boundary migration is therefore dramatically more difficult in stable BCC alloys, and if both are achievable across the full composition range examined, the experimental rarity of {332} twinning in stable β alloys cannot be attributed to any limitation in sustaining or thickening a pre-existing embryo. The rate-determining

step must therefore lie at an earlier stage — the nucleation and early propagation of the twin before a stable embryo is established — and we propose that the decisive factor is the barrier for forming the first few twinning layers via the coupled $\beta \rightarrow \alpha'' \rightarrow \beta$ transformation pathway: in metastable alloys, the proximity to the $\beta \rightarrow \alpha''$ instability substantially lowers this nucleation barrier by providing a low-energy intermediate structural pathway through the α'' state, whereas in stable BCC metals the α'' pathway is either inaccessible or energetically prohibitive, removing the primary nucleation advantage that makes {332} twinning viable. The {332} twin preference in metastable β-Ti alloys is therefore a nucleation-controlled phenomenon, mediated by the coupled $\beta \rightarrow \alpha'' \rightarrow \beta$ transformation pathway, and this conclusion motivates the investigation presented in the following chapter, where the early-stage nucleation and propagation of {332} twins and the transformation-coupled mechanism that governs them are examined directly.

3.5 Conclusion

This chapter presented a systematic MD investigation of {332} twin stability, growth kinetics, and atomic growth mechanisms in metastable β-Ti alloys (Ti-Nb and Ti-Mo alloy systems) across a range of compositions and temperatures in different alloy systems. The key findings are summarized as follows:

- A critical twin embryo thickness exists below which the {332} embryo collapses into the β matrix upon relaxation. This critical thickness increases with decreasing β-phase stability, reflecting the reduced chemical driving force for twinning in more metastable compositions.

- Spontaneous formation of a transitional α'/α'' interfacial phase at the {332} twin boundary is observed upon relaxation across all compositions studied. This interfacial phase is thermodynamically intrinsic to the {332} twinning mode and is not an artefact of deformation history. Its thickness decreases systematically with increasing β-phase

stability, mirroring the ω-mediated interfacial behaviour at {112} twin boundaries reported in the preceding chapter.

- The twin boundary migration stress is strongly sensitive to temperature in both Ti-Nb and Ti-Mo alloy systems. Across all compositions, the migration stress decreases by a factor of two to three as temperature increases from the cryogenic regime to 500–600 K. This temperature sensitivity is attributed to the thermally activated atomic shuffle pathway that governs {332} boundary advancement.

- The effect of composition on the twin boundary migration stress is comparatively modest. While increasing β-phase stability raises the migration stress moderately, no qualitative change in the character of the stress–strain response is observed. Temperature is the primary control variable for {332} twin growth kinetics; composition plays a secondary but non-negligible role through its influence on the interfacial phase character.

- Atomic displacement analysis reveals a composition-dependent switch in the {332} twin growth mechanism. In metastable Ti_3Nb, the growth proceeds via the $\beta \rightarrow \alpha'' \rightarrow \beta$ transformation pathway, producing large and broadly distributed displacements along the twinning normal direction. In the more stable TiNb, growth follows the minimum-shuffle path proposed by Tobe et al., with small, up-and-down displacements layer by layer.

- Despite this mechanistic difference, neither the critical embryo thickness nor the twin boundary migration stress becomes prohibitively large in the high-stability compositions where {332} twinning is experimentally absent. This demonstrates that embryo survival and boundary thickening are not the rate-limiting steps for {332} twin formation.

- The combined evidence points to early-stage twin nucleation and propagation as the

determining step governing the presence or absence of {332} twinning across different BCC alloy systems. The transformation-coupled nucleation pathway, operative in metastable alloys through the proximity to the $\beta \rightarrow \alpha''$ instability, is proposed as the critical factor that enables {332} twinning in metastable β-Ti alloys and suppresses it in conventionally stable BCC metals. This conclusion motivates the early-stage nucleation study presented in the following chapter.

CHAPTER 4

Energetic Model for Nucleation of Deformation Modes

Metastable alloys, such as β-phase titanium (Ti) alloys with a body-centered cubic (BCC) lattice, exhibit exceptional mechanical properties through the interplay of multiple deformation mechanisms-diffusionless phase transformations, deformation twinning, and dislocation slip. However, understanding how these mechanisms compete or cooperate across a wide range of metastable alloys and mechanical loading conditions remains a fundamental challenge. Here, we employ molecular dynamics (MD) simulations to investigate the nucleation behavior of competing deformation modes in metastable β Ti-Nb alloys as functions of temperature, composition, and loading conditions. We reveal that twinning pathways emerge through reversible transformations between the β phase and the orthorhombic α'' phase, in agreement with crystallographic theory. Quantitative analyses show that the dominant deformation mechanisms and preferred twinning-plane orientations are governed by two key energetic parameters: the free energy barrier for homogeneous $\beta \leftrightarrow \alpha''$ transformations and the misfit strain energy along specific phase boundaries. These energetic quantities vary systematically with thermodynamic and mechanical conditions, thereby explaining the deformation-mode transitions observed in both simulations and experiments.

4.1 Introduction

The increasing demand from energy, transportation, biomedical, and aerospace sectors for structural materials that simultaneously exhibit high strength, excellent ductility, strong work-hardening capacity, and reliable performance under extreme conditions has intensified efforts to design meta-stable alloys [171]. Such alloys enable the activation of multiple deformation mechanisms to achieve superior mechanical properties. Among them, metastable β-titanium (β-Ti) alloys are particularly attractive owing to their low density, outstanding corrosion and high-temperature resistance, and excellent biocompatibility [105, 168]. In these β-Ti alloys, the interplay among twinning-induced plasticity (TWIP) from deformation twinning, transformation-induced plasticity (TRIP) arising from diffusionless phase transformations, and dislocation slip plays a critical role in optimizing mechanical properties [99, 45, 46, 174, 25, 55, 63, 64, 162, 8, 26, 31, 120, 151, 133, 87, 123]. Comparable complex deformation behaviors are also observed in metastable BCC refractory high-entropy alloys (HEAs) that exhibit exceptional mechanical performance [204, 126, 94, 203, 230, 205]. Achieving superior properties requires activating these mechanisms in the proper sequence and to the appropriate extent, which demands precise engineering of their thermodynamic and kinetic characteristics as well as processing pathways [35, 71, 81, 141, 185, 17, 229]. Despite decades of research, however, a comprehensive and robust strategy for guiding the controllable activation of these mechanisms in β-Ti and similar alloy systems has yet to be fully established.

A major challenge in accurately predicting deformation mode activation and their interactions in β-Ti alloys arises from the coexistence and strong coupling of multiple metastable phase transformations and deformation twinning modes. The principal metastable phases in Ti alloys include the β phase with a BCC lattice, the α' phase with a hexagonal close-packed (HCP) structure, the α'' phase with an orthorhombic lattice, and the ω phase with a hexagonal lattice [73, 74]. Among deformation twins, the conventional

$\{112\}\langle 11\bar{1}\rangle$ twinning system is common in BCC transition metals and alloys [78]. However, in β-Ti alloys, high-index twinning systems (Miller indices > 2) are frequently observed [229, 4], most notably the $\{332\}\langle 11\bar{3}\rangle$ twin as the dominant twinning behavior [51, 189, 82, 228, 38, 113, 158, 159, 17, 80]. The $\{332\}$ twins frequently coexist with $\{112\}$ twins, producing complex hierarchical microstructures. For example, Figure 4.1 (A-C) shows TEM images of $\{112\}$ and $\{332\}$ twins in a Ti-24Nb-4Zr-8Sn (Ti2448) alloy after 5% cold rolling, with schematic illustrations of the corresponding twin orientations in Figure 4.1 (D-E). Experimental procedures are in Section S1.1 of the Appendix C. Crystallographic theory further predicts a strong interplay between reversible diffusionless phase transformations and deformation twinning [74, 13]. As illustrated in Figure 4.1 (F), one possible pathway for twin formation involves a reversible $\beta_{\text{matrix}} \rightarrow \alpha'' \rightarrow \beta_{\text{twin}}$ transformation [74], wherein both $\{332\}$ and $\{112\}$ twins emerge as conjugate solutions of the kinematic compatibility condition between the β matrix and the twin variant. The coupling between transformations and twinning is further supported by experimental and computational observations of ω and α'' phases at twin boundaries [215, 39, 113, 41, 187, 237, 38, 36].

The coupling between phase transformations and twinning suggests that the preferred deformation modes can be correlated with, and even predicted by, the phase stability of metastable Ti alloys [83, 234]. For instance, in Ti-Nb alloys, the $\{332\}$ twin dominates when BCC stability is low (low Nb concentration). As BCC stability increases slightly, its formation becomes temperature- and orientation-dependent, with a transition to $\{112\}$ twinning and eventually to dislocation slip [82]. Similar correlations between deformation modes and BCC stability have also been observed in Ti-V and Ti-Mo alloys [83]. To rationalize these trends, the empirical $\overline{\text{Bo}}$–$\overline{\text{Md}}$ diagram, inspired by Hume–Rothery rules [145], relates deformation mode variations to the mean electronic parameters $\overline{\text{Bo}}$ (bond order) and $\overline{\text{Md}}$ (metal d-orbital energy level), and has successfully explained general trends in Ti alloys [147]. However, the $\overline{\text{Bo}}$–$\overline{\text{Md}}$ diagram breaks down in more complex alloy systems [48] and provides no guidance on temperature effects or processing conditions. A more recent model based on

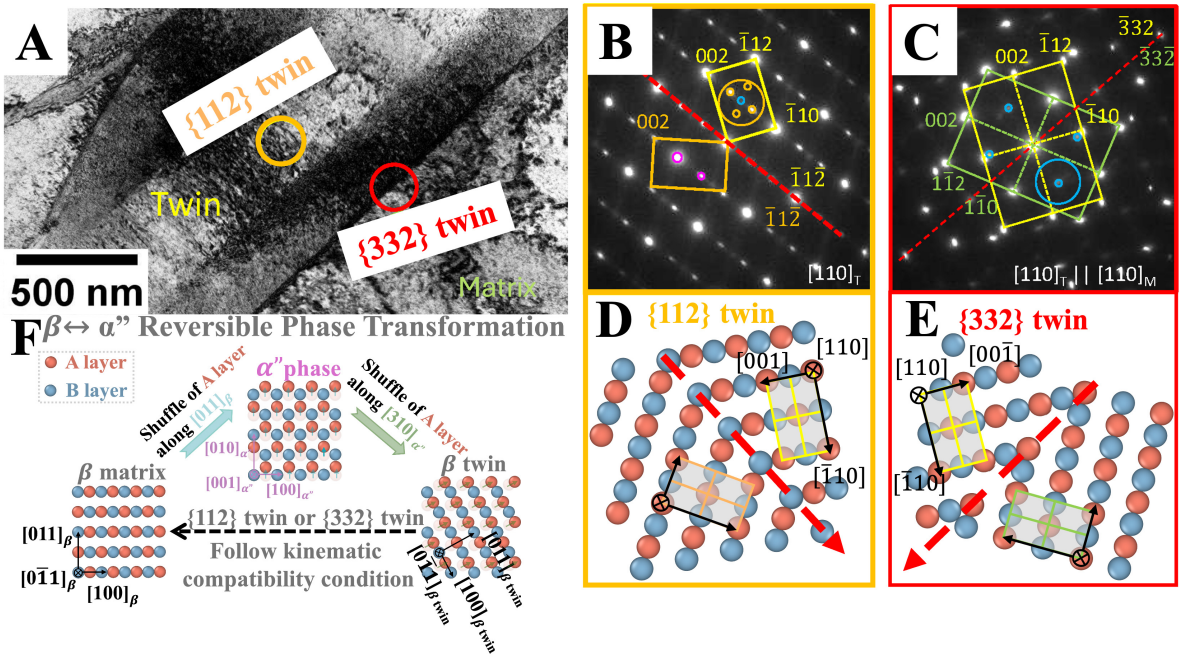


Figure 4.1: **Coexistence of {112} twin and {332} twin in 5% cold-rolled Ti2448 (Ti-24Nb-4Zr-8Sn) sample. A** is the TEM figure illustrating morphology of {112} twin and {332} twin, red circle mark the boundary of {332} twin, and orange circle mark the boundary of secondary {112} twin located inside the {332} twin region. **B-C** are the diffraction patterns at the boundary of{112} twin and {332} twin. **D-E** are schematic draws for the {112} twin boundary and {332} twin boundary.**F** show an example of formation of BCC twin phase via reversible β-α" phase transformations.

first-principles calculations of equilibrium elastic properties at 0 K also fails to capture temperature effects, twinning competitions, or dynamic deformation behavior under load [128]. Similarly, a physics-based model that estimates free energy barriers for phase transformation nucleation under external force predicts preferred deformation modes (TRIP, TWIP, or dislocation) but cannot distinguish between different twinning modes [234]. A key shortcoming of these approaches is the lack of accurate consideration of free energy variations along the full twinning pathway. Gao *et al.* [74] proposed a rigorous framework in which twin formation occurs via multi-step reversible phase transformations, suggesting a promising route to construct energetic models along these pathways for more accurate predictions of TWIP and TRIP behavior.

To elucidate the formation mechanisms and energetics of different deformation modes, particularly the complete twinning pathway, we employ MD simulations to systematically probe the nucleation of deformation modes in representative Ti–Nb and Ti–Mo alloys. The simulations quantitatively reveal how temperature, chemical composition, and loading conditions govern the competition among different deformation modes. We demonstrate that both {112} and {332} twinning pathways emerge via reversible transformations between the β and α'' phases, consistent with crystallographic models [74]. Quantitative analyses further show that the dominant deformation modes and preferred twinning-plane orientations ({112} vs. {332}) are dictated by both the chemical free energy changes along the $\beta_{\text{matrix}} \rightarrow \alpha'' \rightarrow \beta_{\text{twin}}$ transformation pathway and by the misfit strain energies between these phases along the corresponding twinning-plane orientations. These energetic parameters vary systematically with temperature, composition, and loading method, thereby explaining the deformation-mode transitions observed in both simulations and experiments. Notably, the contributions of misfit strain energies to the twinning nucleation barrier are generally comparable to those of chemical free energy changes, indicating that models based solely on thermodynamic phase stability and related parameters are insufficient to capture all key factors governing twinning-mode selection [147]. Finally, we propose a conceptual flowchart based on these

energetic metrics to guide the design of Ti alloys with tailored mechanical performance. This framework, grounded in these two critical energetic parameters, is extendable to metastable Ti alloys and refractory HEAs and adaptable for machine-learning–assisted high-throughput computational screening, thereby accelerating alloy discovery.

4.2 Materials and Methods

This section outlines the computational and analytical methods employed in this study. Section 4.2.1 describes the simulation setups used to investigate the atomic-scale nucleation of various deformation modes under different compositions, temperatures, and loading conditions. Section 4.2.2 details the metadynamics approach used to characterize the free energy landscape associated with the $\beta \rightarrow \alpha''$ phase transformation, which governs the selection of deformation modes and is further discussed in Section 4.3. Section 4.2.3 presents the procedures for calculating elastic constants and lattice parameters, which serve as essential inputs for estimating the misfit strain energy relevant to twin nucleation and twinning mode selection. Finally, Section 4.2.4 describes the methods used to compute misfit strains between grains of different phases under applied deformation, providing critical insights into the strain energy penalty for twin nucleation and the influence of external loading conditions on twinning behavior.

4.2.1 MD Simulations on Nucleation of Defects

We use the Large-Scale Atomic/Mol-ecular Massively Parallel Simulator (LAMMPS [170, 188]) to perform MD simulations. We investigate temperature-, chemical composition- and loading condition- dependent twin nucleation in Ti-Nb binary alloy system using Modified Embedded Atom Method (MEAM) potential developed by Ehemann et al. [57]. As for Ti-Mo binary alloy system, we employ MLP developed by Zheng et.al [236]. As for the simulation box setting, a supercell containing 405504 atoms with basis vectors of

$32[311]\times12[\bar{2}33]\times48[01\bar{1}]$ in the unit of conventional BCC lattice vectors. As for temperature and chemical composition setting, we perform loading operations under 77 K (liquid nitrogen temperature) and 300 K (room temperature), which are two common operation temperatures in experiments. Meanwhile, we selected three different compositions that cross the compositional boundaries between the unstable–metastable and metastable–stable regions of the BCC phase: Ti_5Nb (Ti-27 wt%Nb, close to Nb concentration in experimental sample in Figure 4.1),Ti_4Nb (Ti-33 wt%Nb)and Ti_2Nb (Ti-49 wt%Nb). As for the loading conditions, we apply shear loading along [311] direction on $(\bar{2}33)$ with two ways of setting the boundary conditions: The first boundary condition corresponds to a confined simple shear state. By controlling strain condition, only the shear strain is applied and the other strain components should be constrained to 0:

$$\varepsilon_{ij}^{(\text{confined simple shear})} = \begin{bmatrix} 0 & \gamma_{xy} & 0 \\ 0 & 0 & 0 \\ 0 & 0 & 0 \end{bmatrix} \quad \text{in basis: } X = [3\,1\,1], \quad Y = [\bar{2}\,3\,3], \quad Z = [0\,1\,\bar{1}] \tag{4.1}$$

The second setting on boundary condition is to apply non-confined simple shear for the system. By controlling stress condition, only shear stress is applied and the other non-shear stress components should relax to 0 and in a symmetric Cauchy stress tensor form:

$$\sigma_{ij}^{(\text{non-confined simple shear})} = \begin{bmatrix} 0 & \tau_{xy} & 0 \\ 0 & 0 & 0 \\ 0 & 0 & 0 \end{bmatrix} \quad \text{in basis: } X = [3\,1\,1], \quad Y = [\bar{2}\,3\,3], \quad Z = [0\,1\,\bar{1}] \tag{4.2}$$

Before dynamic loading, we hold the simulation box under isothermal-isobaric (NPT) Nose-Hoover dynamics[135] ($P = 0$, and T is consistent with further loading temperature) for 50 ps to achieve thermal equilibrium. The timestep is set to 1 fs and the engineering shear strain rate is 1×10^8/s.

4.2.2 Metadynamics for Phase Transformation Barriers

To explore the free energy landscape associated with the BCC–α" phase transformation, we employ well-tempered metadynamics using the PLUMED plugin [191, 49].The whole simulation box is under isothermal–isobaric conditions using Parrinello–Rahman–type barostat (NPH) combined with canonical sampling via velocity rescaling with Hamiltonian dynamics (temp/csvr) at target temperature [178, 33]. Here we do not use conventional NPT method to simulate isothermal–isobaric conditions since NPH+temp/csvr can be more reliably to control the system temperature during bias deposition at non-equilibrium state. The orientation of simulation box along the BCC crystal directions: $8[100] \times 6[011] \times 6[0\bar{1}1]$, with a total of 1152 atoms. Here the supercell size is smaller than the supercell size (18000 atoms) for lattice constants calculation. This choice ensures that the entire simulation cell can undergo a homogeneous lattice transformation along the Burgers pathway, enabling efficient exploration of the free energy surface. Larger systems are not suitable for this type of metadynamics study because they introduce heterogeneous nucleation and significantly increase the computational cost, without affecting the intrinsic homogeneous chemical free energy barrier we aim to quantify. Two collective variables (CVs) are chosen to follow Burgers [32] transformation mechanisms: (i) the relative shuffle displacement between adjacent {110} planes, computed as the z-component of the center-of-mass distance between two groups of atoms on alternative {110} planes, and (ii) the axial strain represented by the b/a ratio, evaluated as the ratio of the simulation cell lengths along the [011] and [100] directions, respectively.

The metadynamics bias is applied using Gaussian hills of height 0.05 meV/atom, deposited every 200 steps. The width (sigma) of the Gaussians for each CV was set to 5% of its typical fluctuation range to ensure resolution without over-biasing. A bias factor of 30 is used to modulate the bias deposition in accordance with the well-tempered metadynamics protocol, enabling efficient exploration of metastable states while avoiding oversampling of already

visited configurations. All the metadynamics simulations are performed for a total of 100 nanoseconds to ensure sufficient sampling and convergence of the free energy surface.

4.2.3 Calculations of Lattice Constants and Elastic Constants

To calculate lattice constants of β phase and α" phase at stress-free condition under finite temperatures, we construct supercells in perfect BCC and HCP phase and then relax at finite temperatures. As for the supercell in perfect BCC phase, the basis is $20[100]\times15[011]\times15[0\bar{1}1]$ in the unit of conventional BCC lattice vectors. As for supercell in perfect HCP phase, the basis is $20/3[11\bar{2}0]\times15[\bar{1}100]\times15[0001]$. We then relax the supercells at finite temperature (77 K or 300 K) and hold the simulation box under isothermal-isobaric (NPT) Nose-Hoover dynamics [135] ($P = 0$) for 100 ps to achieve thermal equilibrium. Then we average the lattice parameters of last 100 timesteps. Since at metastable β (slightly deviated from perfect BCC phase) region, β phase can locally transfer to other metastable phases (ω or α" phase) and so we first use PTM methods to filter out the atoms in β (BCC-like) phase. Then we calculate the unit length along X=[100],Y=[011] and Z=$[0\bar{1}1]$ within β phase. Here unit length along $[011]/[0\bar{1}1]$ is not rigorously equal to $\sqrt{2}$ a_β(unit length of [100]) in metastable β Ti alloys. Finally we can obtain average lattice constant a_β of β phases at equilibrium state. As for lattice constants of α" phase, once the supercells in HCP phase is relaxed at finit temperature, the simulation box will spontaneously transfer to metastable α" phase. Similar to the case of β phase, we first use PTM method to extract atoms in α" (HCP-like) phase. Then we calculate unit length along $[11\bar{2}0]_{\mathrm{HCP}}\|[100]_{\alpha"}$,$[\bar{1}100]_{\mathrm{HCP}}\|[010]_{\alpha"}$ and $[0001]_{\mathrm{HCP}}\|[001]_{\alpha"}$. The unit lengths of corresponding directions are length of $a_{\alpha"}$, $b_{\alpha"}$ and $c_{\alpha"}$, respectively.

To determine the elastic constants of the BCC phase, we employed the finite-deformation (perturbation) method [172, 235] using LAMMPS. This approach applies small homogeneous strains to the equilibrium structure and measures the resulting stress response. For BCC systems, only three independent elastic constants exist: C_{11}, C_{12}, and C_{44}. These constants

were evaluated by applying three symmetry-appropriate deformation modes to the simulation cell. A uniaxial strain $\varepsilon_{xx} = \delta$ was used to obtain C_{11} from the corresponding stress σ_{xx}, whereas a volume-conserving orthorhombic strain ($\varepsilon_{xx} = \delta$, $\varepsilon_{yy} = -\delta$) provided $C_{11} - C_{12}$ from the stress difference $\sigma_{xx} - \sigma_{yy}$. A simple shear deformation $\varepsilon_{xy} = \delta$ yielded C_{44} from the shear stress σ_{xy}. Small strain magnitudes ($\delta = \pm 0.001$) were used to ensure a linear elastic response consistent with Hooke's law. All calculations were performed at 0 K to eliminate thermal fluctuations and isolate the intrinsic lattice response [154]. Here, though all deformations nucleate at finite temperature, metastable Ti-Nb alloys often exhibit an Elinvar-like anomaly and so elastic constants are very weakly dependent on temperature [76]. Meanwhile, 0 K calculations can be an efficient way to estimate the elastic parameters for later twin nucleation metrics calculations. All calculated elastic constants are summarized in Section S2.6 of the Appendix C

4.2.4 Misfit Strain along Interfaces between Phase Boundaries

To calculate misfit strain along interphase boundaries at deformed state, we need information on deform state of β parent phase and nucleated α" phase. Since under deformed state, the grains undergo stretch and rotation, the structure of phases are deviated from stress-free state and we cannot directly calculate needed lattice constants. The information on deformed state of lattices of β and α" phase can be extracted from elastic deformation gradient matrix obtained from PTM method from OVITO. In brief, we first choose the reference state for β phase and α" phase and define corresponding deformed state under loading conditions. Both reference state and deformed state are described by elastic deformation gradient matrix at the global reference of perfect BCC and HCP unit cell defined in OVITO [117]. Further, elastic deformation gradient matrix of deformed state relative to reference state we choose will be then used for misfit strain calculations. Here we can perform polar decomposition on

the elastic deformation gradient matrix to obtain pure stretch part and pure rotation part:

$$\mathbf{F} = \mathbf{R} \cdot \mathbf{U} \tag{4.3}$$

Here $\mathbf{U}$ is the right stretch tensor (symmetric and positive-definite), and $\mathbf{R}$ is the rotation matrix (proper orthogonal). And right stretch tensor $\mathbf{U}$ can be extracted as:

$$\mathbf{U} = \sqrt{\mathbf{F}^{\mathrm{T}} \cdot \mathbf{F}} \tag{4.4}$$

Elastic stretch $\mathbf{U}$ here only characterize the shape of current deformed state relative to reference state. For example, if the lattice isotopically expand 2% while relative ratio of unit length of coordination system is unchanged compared to reference state, the elastic stretch tensor will remain in the identity matrix. Hence if we want to obtain the real unit length along different directions, we need to transfer the elastic stretch tensor to real stretch tensor by multiplying the lattice constants at deformed state. In Section S1.7 of Appendix C, we present step-by-step procedures on how to calculate misfit strain along two interphase boundaries defined in Equation 4.8 from information on deformed state of lattice and lattice constants under deformed state.

4.3 Results

4.3.1 MD Simulations on Deformation Modes

We first examine the atomistic-scale nucleation behaviors of common deformation modes in β-Ti alloys as functions of temperature, composition, and loading conditions. These modes include stress-induced diffusionless transformations (primarily α''), {112} twinning, {332} twinning, and dislocation slip. Among them, the nucleation of {332} twins is particularly complex, and few atomistic studies have reproduced it in a manner consistent with experimental observations. To address this, we apply shear loading along the [311] direction on

$(\bar{2}33)$ planes, which provides the most favorable driving force for {332} twin formation [189]. Since alternative mechanisms may still dominate under certain conditions [82], we perform MD simulations across a range of alloy compositions, temperatures, and boundary conditions to investigate deformation mode selection under different thermomechanical environments. Specifically, two representative temperatures are considered: 77 K (liquid nitrogen temperature) and 300 K, both widely used in experiments. For compositional variations, we select Ti_5Nb (close to the Nb concentration in the experimental sample shown in Figure 4.1), Ti_4Nb, and Ti_2Nb, representing alloys spanning distinct regimes of β-phase stability. For mechanical boundary conditions under shear loading, we employ two setups: "Non-Confined Simple Shear" (NSS) and "Confined Simple Shear" (CSS). In the NSS case, shear strain is incrementally applied while keeping all normal and non-applied shear stresses zero, simulating pure shear deformation under stress-free conditions. In the CSS case, shear strain is incrementally applied while keeping all non-shear strain components fixed at zero, simulating mechanically constrained environments such as local confined grains in bulk samples. Further details of the MD settings are provided in the Section 4.2.1.

Figure 4.2 shows MD simulation results for the nucleation and early-stage growth of different deformation modes. The chemical composition, temperature, and loading conditions for each case are listed on the left of each row. Because β-phase stability in Ti–Nb alloys increases with both Nb content and temperature [57, 39], we qualitatively rank the four cases in Figure 4.2 by increasing stability: Ti_5Nb at 77 K (Figure 4.2(A–F)) exhibits the lowest β stability, Ti_4Nb at 300 K (Figure 4.2(G–I)) shows intermediate stability, and Ti_2Nb at 300 K (Figure 4.2(J–L)) displays the highest stability. Each row corresponds to a specific alloy system and includes, from left to right: (i) the initial stress-free atomic configuration prior to shear loading; (ii) atomic snapshots under shear deformation; and (iii) the time evolution of the volume fraction of metastable phases and twinning regions. Atoms are color-coded to distinguish the β phase (with different orientations due to twinning) from other metastable phases. Details of the phase-classification procedures are in Section S1.3 of the Appendix C

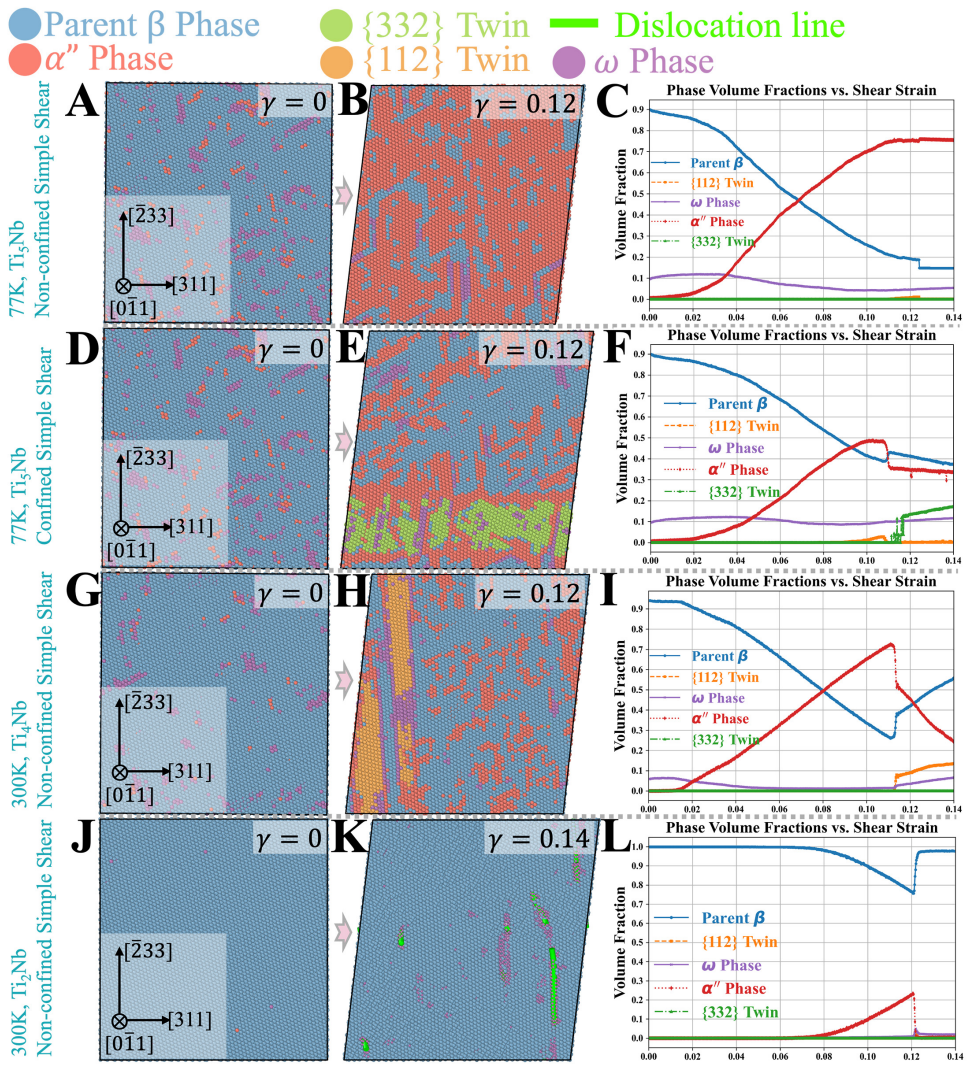


Figure 4.2: **Atomistic structural evolution and deformation modes of Ti-Nb alloys under varying temperature, composition, and stress/strain conditions by MD simulations. In all cases, the shear loading is along [311] direction on ($\bar{2}$33) planes.** Temperature, composition and stress/strain conditions are fixed in each row: **(A-C)** is Ti_5Nb under 77 K, non-confined simple shear condition; **(D-F)** is Ti_5Nb under 77 K, confined simple shear condition; **(G-I)** is Ti_4Nb under 300 K, non-confined simple shear condition; **(J-L)** is Ti_2Nb under 300 K, non-confined simple shear condition. From top to down, **(A,D,G,J)** are snapshots of atomistic structures before loading applied; **(B,E,H,K)** are snapshots of atomistic structures when applied shear strain is 0.12 and different deformation modes produced; **(C,F,I,L)** illustrate nucleation of different metastable phases during shear loading and dynamic volume fraction change. Color interpretation of atoms in the MD snapshots locating at the top of the figure. dominant deformation mode of each row is different: **(A-C)** is α" martensite; **(D-F)** is {332} twin; **(G-I)** is {112} twin and **(J-L)** is dislocation slip.

and misorientation calculations are provided in Section S1.4 of the Appendix C.

When both the Nb concentration and temperature are relatively low, specifically for Ti_5Nb at 77 K, our MD simulations reveal the formation of locally distributed ω and α'' phases (Figure 4.2(A,D)), consistent with typical diffusionless transformations in metastable β-Ti alloys [8]. As mentioned above, two distinct shear loading conditions are examined: NSS (Figure 4.2(A–C)) and CSS (Figure 4.2(D–F)). Under NSS condition, a large fraction of the β matrix (blue atoms) transforms into the α'' phase (red atoms), with the phase fraction rapidly increasing and saturating at approximately 80% when the applied shear strain reaches 0.12 (Figure 4.2(C)). Throughout this deformation, minimal formation of new β twin variants is observed, indicating that the dominant mechanism is a direct $\beta \rightarrow \alpha''$ diffusionless transformation, which is retained under strain, exemplifying classical TRIP behavior widely reported in low-stability β-Ti alloys [8]. Interestingly, when the loading condition is changed to CSS condition, the dominant deformation mechanism shifts. As shown in Figure 4.2(E), the nucleation and growth of α'' are significantly suppressed, with the phase fraction plateauing at about 50% at a shear strain of 0.11 (Figure 4.2(F)). Beyond this point, the α'' fraction abruptly decreases by around 15%, coinciding with the sudden appearance and growth of {332} twin structures, whose volume fraction increases from zero to 15% (green curve). By analyzing time-resolved atomic snapshot, we find that {332} twin nucleation initiates within the α'' phase. This twin formation mechanism induced by reversible β-α'' transformations is supported by numerous experimental studies [113, 41, 187, 237, 38, 36]. As shear strain continues to increase, the α'' phase fraction remains relatively stable but localized primarily near {332} twin boundaries. Simultaneously, the β matrix fraction decreases, suggesting that {332} twins continue to grow at the expense of the parent phase.

With increasing β-phase stability, as in Ti_4Nb at 300 K (Figure 4.2(G–I)) and Ti_2Nb at 300 K (Figure 4.2(J–L)) under NSS, the dominant deformation mechanisms shift from $\beta \rightarrow \alpha''$ transformation and {332} twinning to {112} twinning and dislocation slip. In

Ti_4Nb at 300 K, a twin domain (orange in Figure 4.2H) is identified as a {112} twin (shown in Section S2.2 of the Appendix C). Phase evolution tracking (Figure 4.2I) shows that, between strains of 0 and 0.11, the β parent fraction (blue) decreases while α'' (red) increases. Beyond this point, α'' rapidly transforms into the {112} twin (orange), indicating a sequence of $\beta \rightarrow \alpha'' \rightarrow \beta\{112\}$ twin. After nucleation, however, the {112} twin fraction remains nearly constant, while the β matrix continues to grow. This suggests that although twin formation from α'' is energetically favorable, subsequent twin growth is kinetically hindered, likely due to pinning by ω particles (purple in Figure 4.2H) observed in metastable β-Ti alloys [39, 215]. In Ti_2Nb at 300 K, where β stability is highest, phase transformations are largely suppressed (Figures 4.2(J,K)). The α'' phase nucleates only at higher strains ($\varepsilon \approx 0.08$, Figure 4.2L), reaches a modest fraction ($\sim$20%), and subsequently reverts to β with the onset of dislocation slip, confirming that slip dominates deformation in highly stable β-Ti alloys.

Table 4.1: Deformation mechanisms of Ti-Nb alloys at different temperatures. (shear strain rate is $10^8/s$), Here "CSS" in the table is short for "Confined Simple Shear","NSS" in the table is short for "Non-confined Simple Shear".

	77 K		300 K		Predicted by $\overline{\text{Bo}}$–$\overline{\text{Md}}$
Alloy	CSS	NSS	CSS	NSS	
Ti_5Nb	{332}	α''+ {112}	{332}	α''+ {112}	TRIP
Ti_4Nb	{332}	{112}	{112}	{112}	TWIP
Ti_2Nb	Dislocation	{112} + Dislocation	Dislocation	Dislocation	Dislocation

Beyond the four representative cases in Figure 4.2, the dominant deformation modes across all simulated conditions are summarized in Table 4.1. We also show a graph illustrating the temperature, chemical composition and loading condition- dependent deformation modes already summarized in Table 4.1. These simulations span a wide range of thermodynamic β-phase stabilities, from the unstable/metastable boundary to the metastable/stable regime [57, 39]. At low stability, exemplified by Ti_5Nb at 77 K, deformation is dominated by $\beta \rightarrow \alpha''$ transformation and {332} twinning, with the prevailing mechanism depending on the loading condition (NSS vs. CSS). These behaviors are characteristic of TRIP and

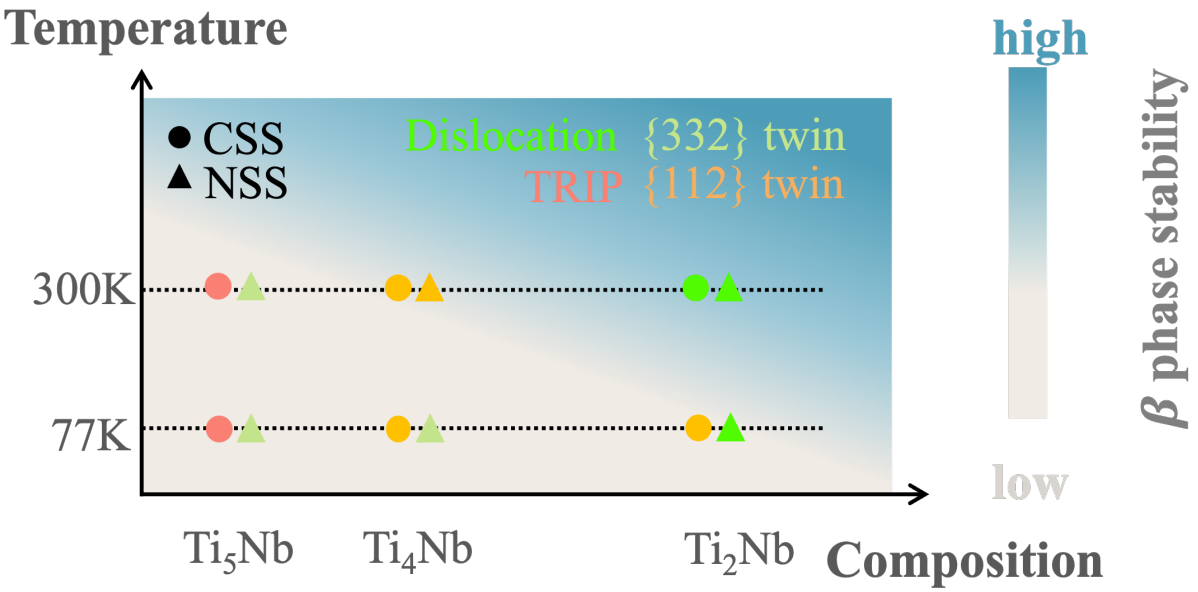


Figure 4.3: **Schematic illustration of temperature- and composition-dependent deformation mechanisms in metastable β Ti alloys.** The background color qualitatively represents the stability of the β phase, increasing from lower left (sand color) to upper right (sea blue color). The corresponding deformation modes are consistent with Table 4.1. Colors of data points represent different dominate deformation modes: red is TRIP; orange is {112} twin; light green is {332} twin and bright green is dislocation. Shape of data points represent different loading condition: circle is NSS and rectangle is CSS. The transition between mechanisms is strongly temperature, chemical composition and loading condition-dependent, highlighting the competition between nucleation-controlled deformation modes in metastable alloys.

TWIP effects commonly observed in metastable β-Ti alloys. With moderate stability (e.g., Ti_4Nb at 77 K), $\beta \rightarrow \alpha''$ transformation is less favorable, and deformation is primarily governed by {332} or {112} twinning, again depending on loading conditions, consistent with TWIP-dominated behavior. At higher stability, as in Ti_4Nb at 300 K and Ti_2Nb at 77 K, {332} twinning is strongly suppressed, while {112} twinning and dislocation slip become dominant. Overall, these results demonstrate a clear correlation between deformation mode selection and β-phase stability. Importantly, our simulations show excellent agreement with experimental observations [234, 128, 38, 83, 125, 82, 220, 226, 177, 231, 77], as discussed in the next section.

4.3.2 Experimental Observations of Deformation Modes

To assess consistency with experimental observations, we compile literature data on deformation modes in Ti–Nb alloys across a range of compositions and temperatures (Figure 4.4A). Data points are color-coded by the reported dominant mechanism. In the low-stability regime (pink rectangle), experiments frequently show a mixture of $\beta \rightarrow \alpha''$ transformation and {332} twinning, consistent with our simulations of Ti_5Nb at 77 K that exhibit coexisting TRIP and TWIP (Figure 4.2A–F, Table 4.1). With slightly higher Nb content or temperature (green-circled region), {332} twinning predominates across 77–300 K [83], though {112} twins occasionally appear under specific loading conditions, in agreement with our simulations for Ti_5Nb at 300 K and Ti_4Nb at 77 K. At higher β stability (orange triangle region), {332} twins are limited to cryogenic conditions under carefully controlled loading, while deformation is otherwise dominated by dislocation slip [83]. Although experimental data here are sparse, our simulations of Ti_4Nb at 300 K and Ti_2Nb at 77 K show dominant {112} twinning and slip with suppressed {332} twinning. In the fully stable regime (>47 wt% Nb, purple), no {332} twinning has been reported; deformation occurs almost exclusively by dislocation slip, as in conventional BCC metals. This trend matches our Ti_2Nb simulation at 300 K (Figure 4.2J–L, Table 4.1), where slip dominates and transformations or twinning

are minimal. Overall, these comparisons demonstrate strong agreement between simulations and experiments, confirming the predictive fidelity of our framework.

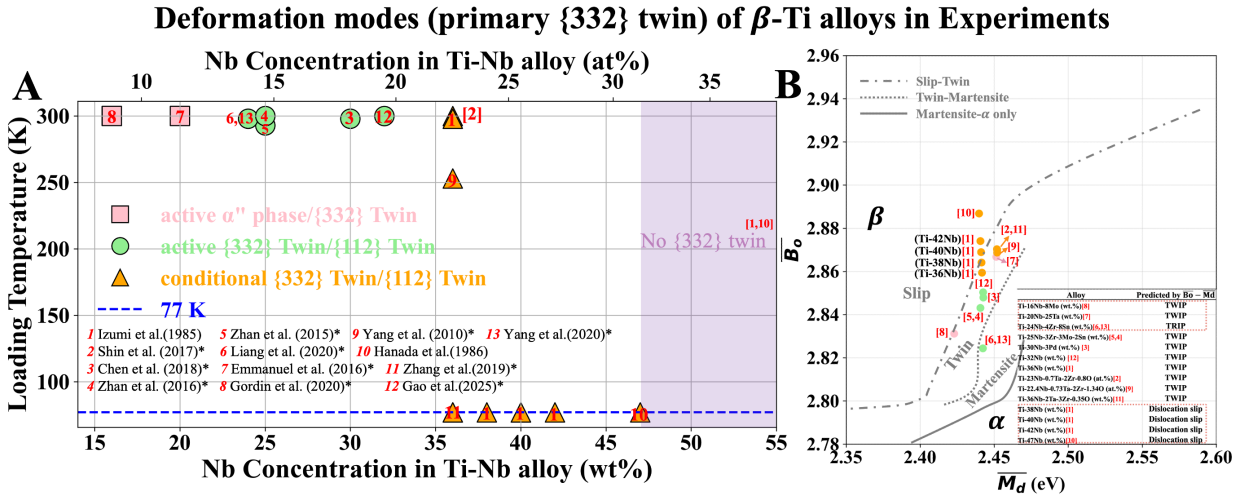


Figure 4.4: **Temperature and composition conditions for {332} twin nucleation for Ti-Nb alloys in experiments [83, 82, 220, 226, 177, 38, 125, 231, 77, 219, 75, 227, 12].** In **A**, data points marked in pink rectangle (Nb concentration is less than 24 wt%) indicates that dominant deformation mode is α" martensite and {332} twin. {332} twin (and small volume of {112} twin) can form insensitive to temperature and loading condition when Nb concentration is between 25 wt% and 36 wt% (data points in light green circle). {332} twin can form by carefully controlling loading condition under cryogenic temperatures (Nb concentration is between 36 wt% and 47 wt%). Within this region, {112} twin and slip can also form and compete with {332} twin nucleation. When Nb concentration is larger than 47 wt%, shown in purple region, {332} twin can not form in any condition and dislocation slip is the dominant deformation mode. As for alloys that marked with "*", Nb is the dominant β stabilizer element in the composition but the alloy is not binary, they also include small amount of neutral elements and oxygen in addition. In **B**, we also present the predicted deformation modes of samples in **A** by $\overline{\text{Bo}} - \overline{\text{Md}}$ diagram. The definition of colors of data points in **B** are consistently based on the deformation modes observed in experiments in **A**.The experimental-fitted boundaries for different deformation modes are from Morinaga [146]. Clearly, compared to experimental observations of deformation modes in the samples shown in **A**, there are large deviation compared to $\overline{\text{Bo}} - \overline{\text{Md}}$ prediction, especially those marked in red rectangles.

Both our MD results (Table 4.1) and published experimental data (Figure 4.4A) reveal a consistent trend in β-Ti alloys: as β-phase stability increases, the dominant deformation mechanisms shift from α'' formation (TRIP) to {332} and {112} twinning (TWIP), and eventually to dislocation slip. This trend agrees with prior datasets [234, 128, 48, 233]. It

can also be partially rationalized by the well-established $\overline{\text{Bo}}$–$\overline{\text{Md}}$ diagram [147], which uses concentration-averaged electronic structural parameters. Figure 4.4B plots the corresponding $\overline{\text{Bo}}$ and $\overline{\text{Md}}$ values for alloys in Figure 4.4A, with deformation boundaries based on Morinaga's experimental fitting [146]. In this diagram, β stability generally increases from lower right to upper left, and the observed TRIP $\rightarrow$ TWIP $\rightarrow$ slip sequence is broadly reproduced. The inset table in Figure 4.4B summarizes the predicted modes. However, significant deviations remain, particularly in cases marked by dashed rectangles, where experimental results diverge from the $\overline{\text{Bo}}$–$\overline{\text{Md}}$ predictions. Notably, the diagram cannot distinguish between {332} and {112} twinning within the TWIP regime, nor does it capture the strong dependence of deformation behavior on temperature and loading conditions. These limitations highlight the need for more accurate, physically grounded models to describe deformation mode transitions under complex thermodynamic and mechanical environments.

These findings highlight a critical gap in our understanding of deformation in metastable β-Ti alloys. Specifically, three fundamental questions arise: (1) How does the free energy landscape of diffusionless transformations at finite temperature shape deformation pathways, beyond the zero-Kelvin stability predictions of the $\overline{\text{Bo}}$–$\overline{\text{Md}}$ diagram? (2) What additional energetic parameters, beyond phase stability, govern the competition among deformation modes? (3) Can universal thermodynamic or kinetic metrics be identified to predict transitions between modes in the same alloy under different loading conditions? Addressing these questions requires moving beyond empirical descriptors toward an energetics-based framework. To this end, we analyze our MD simulations using advanced free energy methods and crystallographic models linking twinning and diffusionless phase transformations. Our goal is to establish a predictive framework that connects temperature, composition, and loading conditions to deformation-mode selection, providing new principles for the design of β-Ti alloys with tailored mechanical performance through the controlled activation of competing mechanisms.

4.3.3 β Phase Stability and $\beta - \alpha$" Transformation Reversibility

We begin by exploring free energy parameters related to β-phase stability to accurately capture their effects on deformation mode transition. Thus, we construct a free energy landscape (FEL) for homogeneous $\beta \leftrightarrow \alpha''$ transformations using metadynamics simulations with PLUMED [49, 191, 20]. Following the Burgers path [32], we adopt two collective variables: the shuffle magnitude between two adjacent $(01\bar{1})$ planes along [011] and the b/a ratio, where b and a are the unit lengths of $\langle 011 \rangle$ and $\langle 100 \rangle$ in the β phase. In the ideal β phase (perfect BCC lattice), $b/a = \sqrt{2}$ and the shuffle magnitude is zero. In the orientation relationship between β and the ideal HCP α phase, $b/a = \sqrt{3}$ and the shuffle magnitude is $b/6$, typically ranging from 0 to 0.1 nm depending on $\langle \bar{1}100 \rangle$ length in HCP. The α'' phase can thus be regarded as an intermediate state between the perfect BCC and HCP structures, with its equilibrium b/a ratio and shuffle magnitude dependent on alloy composition and temperature. Further computational details are provided in the **Section 4.2.2**.

Figure 4.5(A–D) shows the FELs of the $\beta \leftrightarrow \alpha''$ transformation of four different cases in which TRIP, TRIP/TWIP, and dislocation are dominate, respectively. By comparing alloy systems with different Nb concentrations and temperatures, we examine how β-phase stability influences $\beta \leftrightarrow \alpha''$ transformation behavior. To quantify the reversibility between the β and α'' phases, we introduce a parameter $P_{\text{chem}}^{\beta \leftrightarrow \alpha''}$, defined as follows:

$$P_{\text{chem}}^{\beta \leftrightarrow \alpha''} = \exp\left(-\frac{\left|\Delta F_{\beta \leftrightarrow \alpha''}^{\text{A}}\right|}{K_{\text{B}}T}\right) \tag{4.5}$$

Here

$$\left|\Delta F_{\beta \leftrightarrow \alpha''}^{\text{A}}\right| = \max\{\Delta F_{\beta \to \alpha''}^{\text{A}}, \Delta F_{\alpha'' \to \beta}^{\text{A}}\} \tag{4.6}$$

Here, $\Delta F_{\beta \to \alpha''}^{\text{A}}$ and $\Delta F_{\alpha'' \to \beta}^{\text{A}}$ denote the activation free energies for the $\beta \to \alpha''$ and $\alpha'' \to \beta$ transformations along the minimum energy path (MEP), respectively. The parameter $P_{\text{chem}}^{\beta \leftrightarrow \alpha''}$ ranges from 0 to 1, with lower values indicating reduced kinetic favorability for the reversible $\beta \leftrightarrow \alpha''$ transformation, and higher values indicating the opposite. The corresponding

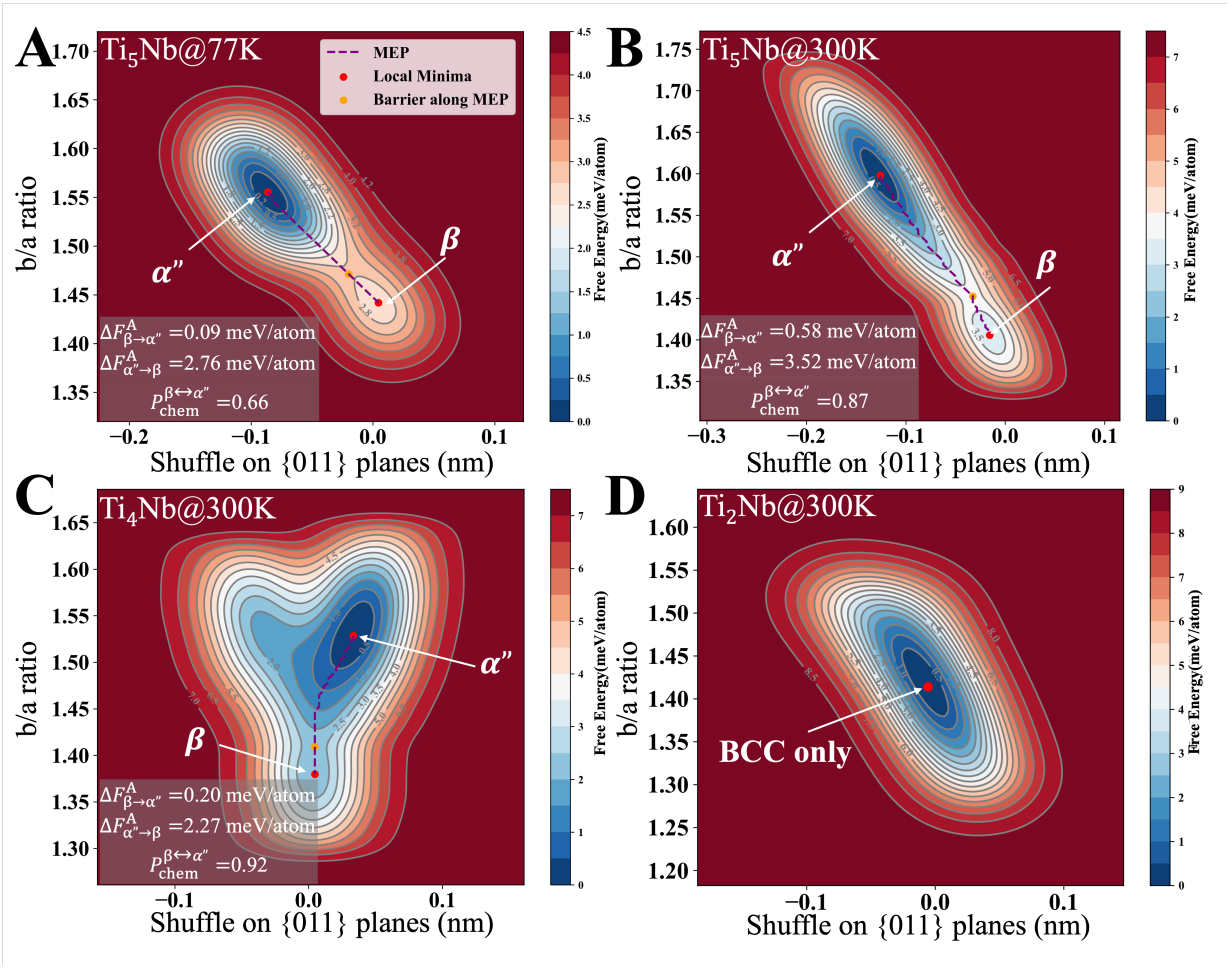


Figure 4.5: β-α" **energy landscape for Ti alloys, including unstable BCC Ti-alloy (α-Ti alloys), metastable BCC Ti-alloys and stable BCC Ti-alloy.** Here we choose two collective variables: shuffle magnitude between (011) planes along $[0\bar{1}1]$ directions and "b/a" ratios ("b" is the length of $\langle 0\bar{1}1\rangle$ in BCC and "a" is the length of $\langle 100\rangle$ in BCC phase). Positions of BCC and α"/α phase are marked in the figure. **A** is for Ti_5Nb at 77 K. **B** is Ti_5Nb at 300 K and **C** is Ti_4Nb at 300 K. **D** is the case of stable BCC Ti-alloys, which we can only observe one global minima at BCC phase and no local minima for α" phase. The corresponding transformation barriers and $P_{\text{chem}}^{\beta\leftrightarrow\alpha''}$ are label in the sub figures.

values are reported in the subfigures of Figure 4.5. Details of the procedures for locating local minima and determining the MEP from the FEL are provided in Section S1.5 of the Appendix C.

Figure 4.5(A) shows the energy landscape of Ti_5Nb at 77 K, where the dominant deformation modes are α'' formation or {332} twinning (Table 4.1). In this highly metastable state, the activation barrier for the $\beta \rightarrow \alpha''$ transformation is only 0.09 meV/atom, and $P_{\text{chem}}^{\beta \leftrightarrow \alpha''}$ is 0.66, which is the lowest among all cases, indicating poor reversibility. Raising the temperature to 300 K (Figure 4.5B) improves β stability, increasing $P_{\text{chem}}^{\beta \leftrightarrow \alpha''}$ to 0.87. Higher reversibility enables TWIP, allowing the system to escape the α'' well under loading. The dominant modes here are {112} or {332} twinning, depending on loading conditions (Table 4.1). Composition also tunes the landscape: increasing Nb from Ti_5Nb to Ti_4Nb at 300 K (Figure 4.5C) raises $P_{\text{chem}}^{\beta \leftrightarrow \alpha''}$ to 0.92, with TWIP still dominant. At higher Nb (Ti_2Nb, 300 K; Figure 4.5D), only a single global minimum corresponding to the β phase remains. Here, the α'' phase is unstable at zero stress, reversible transformation is negligible, and deformation occurs solely by dislocation slip (Table 4.1).

In summary, these four representative cases demonstrate how $P_{\text{chem}}^{\beta \leftrightarrow \alpha''}$ characterizes the effects of temperature and composition on $\beta \leftrightarrow \alpha''$ reversibility, correlating phase stability with the selection of TRIP, TWIP, or slip, consistent with Figure 4.4. In Section S2.4 of the Appendix C, we also provide FEL for the Ti_4Nb at 77 K and Ti-10Mo (wt.%) at 300 K. However, $P_{\text{chem}}^{\beta \leftrightarrow \alpha''}$ alone cannot distinguish between twinning modes within the TWIP regime (e.g., Figures 4.5B and C). Additional material properties beyond the FEL must therefore be considered, as discussed in the following section.

4.3.4 Evaluations of Misfit Strain Energies during β-α" Transformation

We next consider factors beyond the FEL that determine the selection of specific twinning modes within the TWIP regime. Assuming twinning proceeds through a reversible $\beta \leftrightarrow \alpha''$

transformation, the preferred mode is that with the lowest nucleation barrier. This barrier includes four main contributions: the chemical driving force $\Delta G^{\mathrm{A}}_{\mathrm{chem}}$, interfacial free energy $\Delta G^{\mathrm{A}}_{\mathrm{int}}$, elastic strain energy from nucleus–matrix misfit $\Delta G^{\mathrm{A}}_{\mathrm{elast}}$, and the external work W_{ext}. The total nucleation barrier ΔG^{A} can therefore be expressed as:

$$\Delta G^{\mathrm{A}} = \Delta G^{\mathrm{A}}_{\mathrm{chem}} + \Delta G^{\mathrm{A}}_{\mathrm{int}} + \Delta G^{\mathrm{A}}_{\mathrm{elast}} - W_{\mathrm{ext}} \tag{4.7}$$

Deformation twinning through reversible phase transformations typically forms coherent or semi-coherent twin boundaries [99]. Consequently, $\Delta G^{\mathrm{A}}_{\mathrm{int}}$ is usually negligible and not rate-controlling [99]. Instead, the nucleation barrier is primarily governed by $\Delta G^{\mathrm{A}}_{\mathrm{chem}}$, $\Delta G^{\mathrm{A}}_{\mathrm{elast}}$ and external work W_{ext}. The chemical term reflects the reversible $\beta \leftrightarrow \alpha''$ transformation barrier (related to $P^{\beta\leftrightarrow\alpha''}_{\mathrm{chem}}$ defined in the previous section), while the elastic penalty arises if the nucleus grows along a plane other than the invariant plane of the corresponding transformation [99, 153]. These invariant planes dictate the twin orientation relationship with the parent lattice and, consequently, the selection of twinning modes [99, 153]. Additionally, external work due to external loading can also alter the total twin nucleation barrier. Thus, the interplay between transformation reversibility and invariant-plane formation under loading condition is central to understanding deformation-mode selection in metastable β-Ti alloys.

Within this framework, twinning via reversible transformations proceeds in two steps: (1) β (matrix) $\rightarrow \alpha$", and (2) α" $\rightarrow \beta$ (twin lattice). Each step ideally occurs along a distinct invariant plane, the habit plane for the phase transformation and the twin plane for twinning, thereby minimizing misfit strain energy [232]. Along the lowest free energy pathway, α'' nucleates and grows along the habit plane in step (1). After saturation, it transforms back to β in step (2), initially along the same habit plane and ultimately along the twin plane between the β matrix and the β twin lattice. Under strong local driving forces (e.g., stress concentrations near nucleation sites), however, the α'' phase in step (1) may deviate from its ideal invariant-plane orientation to accelerate kinetics, incurring higher misfit energy that can significantly contribute to ΔG^{A}. For example, experimental characterizations of $\beta \rightarrow \alpha \rightarrow \alpha''$

transformations often reveal semi-coherent interfaces that follow the Burgers Orientation Relationship (BOR): $\{1\bar{1}2\}_{\beta} \parallel \{0\bar{1}10\}_{\mathrm{HCP}} \parallel \{110\}_{\alpha''}$ and $\langle\bar{1}11\rangle_{\beta} \parallel \langle\bar{2}110\rangle_{\mathrm{HCP}} \parallel \langle\bar{1}10\rangle_{\alpha''}$ [206]. To evaluate the resulting misfit strain energies, we next analyze atomistic structures, with particular focus on the $\beta \parallel \alpha''$ interfaces at the twin nucleation stage shown in Figure 4.6. Figure 4.6(A) illustrates the $(\bar{2}33)_{\beta}$ plane (green), where shear deformation is later applied

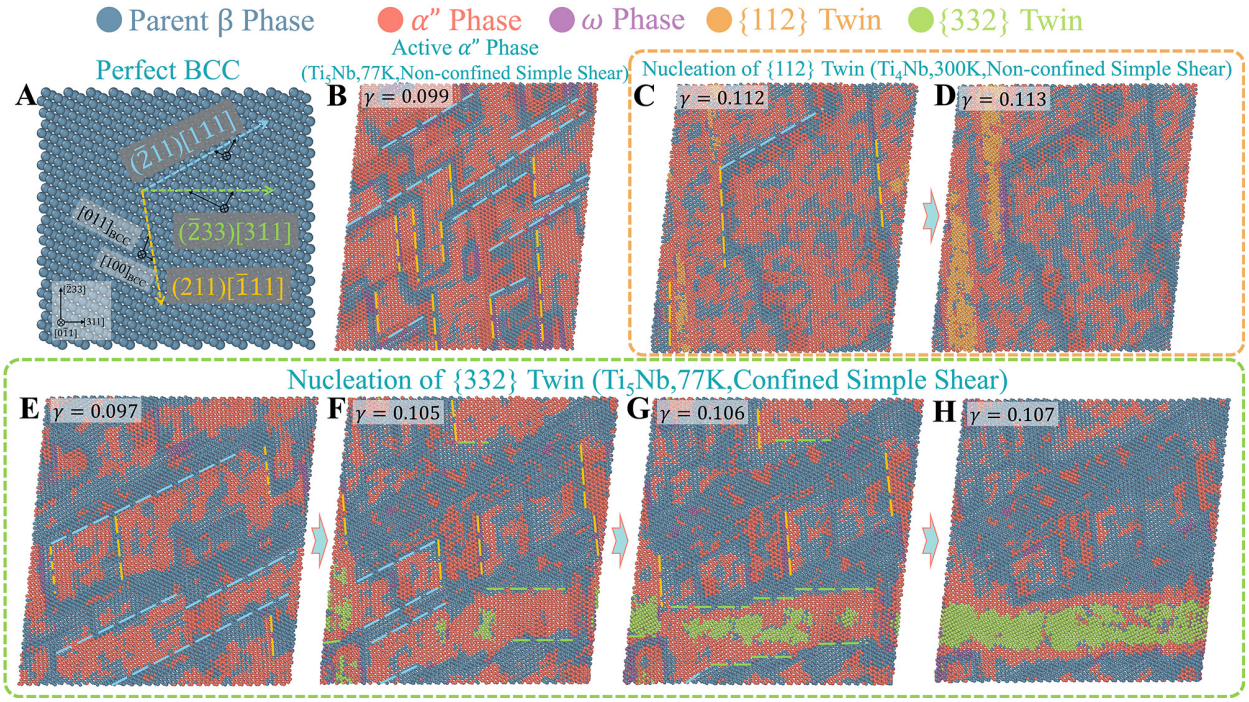


Figure 4.6: **Facted interfaces of BCC and nucleated α" phase before nucleation of different deformation modes. (A)** is illustration on the all conventional coherent $\beta\|\alpha$" interfaces (marked in orange and blue) consistent with the BOR and defined by $\{211\}$ planes with in-plane $\langle\bar{1}11\rangle$ directions, lying in the [311]–$[\bar{2}33]$ zone. We also mark the $(\bar{2}33)$ plane along [311] direction (green line) that closely align to the $\{332\}$ twin boundary formed under shear loading. The coordinate system in **(A)** is consistent with that of initial state of simulation box in **(B-H)**. **(B)** is the snapshot when the system close to the stage of α" phase nucleation saturation. Corresponding setting is consistent with the case in Figure 4.2 (A-D). **(C-D)** are snapshots of critical stage of $\{112\}$ twin nucleation in the case of Figure 4.2 (I-L). **(E-H)** are the snapshots of $\{332\}$ twin nucleation process in the case of Figure 4.2 (E-H). Here we want to present how the interfaces of $\beta\|\alpha$" (bottom of the figures) tilt from blue lines to green lines that closely align with $\{332\}$ twinning plane. Definitions on the colors of atoms are consistent with the definition in Figure 4.2. Lines in **(B-H)** mark some facted interfaces between BCC and nucleated α" phase. Lines with the same color as **A)** correspond to closely related orientation.

along the $[311]_\beta$ direction; and two typical $\beta \parallel \alpha''$ semi-coherent interfaces (blue and yellow) lying in the $[\bar{2}33]_\beta$–$[311]_\beta$ plane that follow the BOR introduced earlier. Figures 4.6(B–H) show representative faceted interfaces observed at different stages: near α'' saturation (Figure 4.6(B), corresponding to Ti_5Nb at 77 K under NSS loading shown in Figure 4.2B), during {112} twin nucleation (Figures 4.6(C–D), corresponding to Ti_4Nb at 300 K under NSS loading shown in Figure 4.2H), and during {332} twin nucleation (Figures 4.6(E–H), corresponding to Ti_5Nb at 77 K under CSS loading plotted in Figure 4.2E). In the case of α'' formation plotted in Figure 4.6(B), α'' nucleation and growth is strongly favored for Ti_5Nb at 77 K under NSS loading. The large α'' volume fraction promotes the formation of multiple coherent and semi-coherent interfaces to minimize interfacial energy. Two of the most prominent align closely with {211} planes [Figure 4.6(A)], consistent with the BOR as well as prior experimental and computational studies [149, 175, 206]. With further shear, only small {112} twin nuclei are observed, reflecting both the low reversibility and the tendency of this loading condition to stabilize α''. For {112} twin nucleation (Figures 4.6(C–D)), a long, flat $\beta \parallel \alpha''$ interface forms nearly parallel to the $(211)_\beta$ plane along $[\bar{1}11]_\beta$ (marked in orange), corresponding to the theoretical invariant plane of the {112} twin shown in Figure 4.2(J).

In the case of {332} twin nucleation [Figure 4.6(E–H)], we observe uncommon faceted $\beta \parallel \alpha''$ interfaces (marked in green) oriented near the $(\bar{2}33)_\beta$ plane, which later becomes the invariant plane of the nucleated {332} twin. Initially, however, the $(\bar{2}33)_\beta$ plane along $[311]_\beta$ is not the preferred $\beta \parallel \alpha''$ interface [Figure 4.6(E)]. When local {332} twin domains form within the α'' band at the bottom of the cell, the band adopts a curved shape [Figure 4.6(F–G)], and the emerging {332} twins tend to reorient the $\beta \parallel \alpha''$ interface toward alignment with the {332} twinning plane (green line), progressively flattening the interface. As additional {332} twin domains form, the faceted $\beta \parallel \alpha''$ interface gradually becomes parallel to the {332} twinning planes [Figure 4.6(H)]. To our knowledge, this represents the first atomic-scale observation of dynamic {332} twin nucleation from the α'' phase, consistent with in-situ experiments [113]. This finding also confirms our assumption that the

formation of the twin invariant plane requires the $\beta \parallel \alpha''$ interface to align with the twin plane. Considering the two critical steps of twin nucleation discussed above, we regard the alignment of α'' along faceted $\beta \parallel \alpha''$ interfaces toward the twin-invariant orientation as an intermediate step connecting them. Accordingly, in our model, the in-plane misfit strain energy density of coherent or semi-coherent $\beta \parallel \alpha''$ interfaces aligned with twin-invariant planes is treated as the dominant contribution to the misfit strain energy governing twin nucleation and, ultimately, twin selection.

As shown in Figure 4.7, crystallographic analysis demonstrates that the $\beta \parallel \alpha''$ interfaces and the associated twin-invariant plane orientations observed in Figure 4.6 can be obtained through the reversible $\beta \leftrightarrow \alpha''$ phase transformation along the well-defined Burgers path for the transformation between β and α phase in the HCP structure, because the α'' phase can be treated as a distorted α phase deviated from the ideal c/a ratio and the perfect hexagonal basal plane [32, 74]. In Figure 4.7(A), different atom colors highlight the ABAB stacking sequence along $[0\bar{1}1]_\beta$, while the $\beta \rightarrow \alpha''$ transformation involves a homogeneous compressive strain along $[100]_\beta$ together with an additional atomic shuffle of $(0\bar{1}1)_\beta$ planes along $[011]_\beta$. Based on the observations in Figure 4.6, once the α'' phase nucleates and grows into a large band or grain within the parent β matrix, two key $\beta \parallel \alpha''$ coherent/semi-coherent interfaces aligned with different twin-invariant planes can be identified (Figures 4.7(B–E)). Figures 4.7(B–C) correspond to the formation of the {112} twin, consistent with the MD results in Figures 4.6(C–D), while Figures 4.7(D–E) correspond to the formation of the {332} twin, consistent with Figures 4.6(E–H). From a crystallographic perspective, and following the Hadamard jump condition [46, 74], the intermediate α'' phase connecting the parent β variant and the twin variant ({112} or {332}) exhibits the following orientation relationship (OR) with the β phase:

$$\begin{aligned} &\text{For } \{112\} \text{ twin: } (211)_\beta \parallel (110)_{\alpha''}, \quad [\bar{1}11]_\beta \parallel [\bar{1}10]_{\alpha''}, \\ &\text{For } \{332\} \text{ twin: } (\bar{2}33)_\beta \parallel (\bar{1}30)_{\alpha''}, \quad [311]_\beta \parallel [310]_{\alpha''}. \end{aligned} \tag{4.8}$$

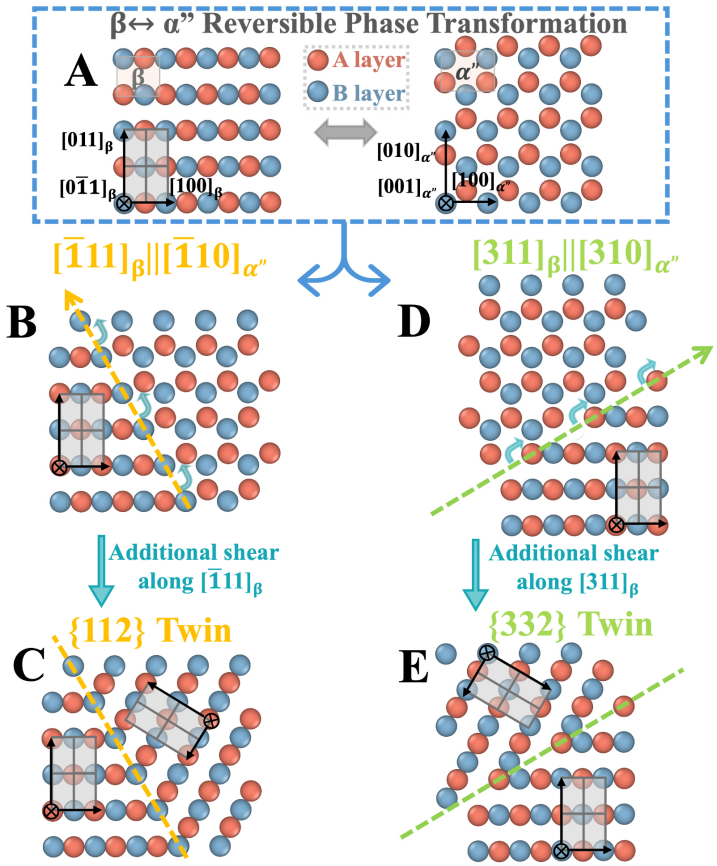


Figure 4.7: **Schematic draw on BCC-to-α" phase transformation and two BCC-α" interphase boundary align with twinning plane. A** illustrate BCC-α" phase transformation pathway by shuffling (0$\bar{1}$1) planes along [011] direction. Color of atoms indicating ABAB stacking. In addition to shuffle, the lattice also undergo lateral strain along [100] directions during transformation. To simplify illustration, we do not draw here. α" phase is similar to HCP phase, and the real atomic structure of α" phase varies with different metastable alloys under different temperature, we draw perfect HCP here as an example. **B** and **D** are two theoretical calculated BCC-α" interphase boundaries align with twinning planes during BCC-α" phase transformation. Orange and green arrows indicate the directions that parallel to the interface. **C** and **E** illustrate two types of BCC twin boundary structure after α" phase transfering back to BCC phases under shear along the directions marked in blue arrows. **A-B-C** is the pathway for {112} twin formation by BCC-to-α" phase reversible phase transformation and **A-D-E** is the pathway for {332} twin formation by BCC-to-α" phase reversible phase transformation. In real cases (both in MD and experiments), there are phase transformation behaviors along twin boundaries. Since we here is to illustrate structural relationships of α", twin and matrix, we do not draw the real twin boundary structure. The illustrations and snapshots of twin boundaries are in Section S2.1 of the Appendix C.

Based on the above orientation relationships, we next estimate the in-plane misfit strain energy along the $\beta \parallel \alpha''$ interfaces, assuming that the local interfaces behave orthotropically. Thus, the in-plane stress–strain relation (neglecting out-of-plane components) follows the orthotropic form [96]. Furthermore, using Eshelby's theory [58] in combination with the orthotropic stress–strain relation, we derive the general expression for the in-plane misfit strain energy density, denoted as $W_{\text{twin}}^{\text{misfit}}$ (in units of eV/atom), as:

$$W_{\text{twin}}^{\text{misfit}} = \frac{1}{2}\left(\frac{E_1}{1-\nu_{12}\nu_{21}}\varepsilon_{11}^2 + \frac{E_2}{1-\nu_{12}\nu_{21}}\varepsilon_{22}^2 + 2\frac{\nu_{12}E_2}{1-\nu_{12}\nu_{21}}\varepsilon_{11}\varepsilon_{22} + G_{12}\gamma_{12}^2\right)\Omega_\beta \tag{4.9}$$

where direction "1" denotes the longitudinal in-plane axis ($[\bar{1}11]_\beta$ or $[311]_\beta$ in Equation 4.8), and direction "2" denotes the transverse in-plane axis (given by the cross product of the plane normal and the longitudinal direction in Equation 4.8); in this study, the transverse in-plane axis is $[0\bar{1}1]_\beta$, which is parallel to the Z axis. E_1 and E_2 represent the Young's moduli along the longitudinal and transverse directions, respectively; ν_{12} and ν_{21} are the corresponding Poisson's ratios, with ν_{12} describing the transverse strain induced by longitudinal stress and ν_{21} the reverse. G_{12} is the in-plane shear modulus, γ_{12} the in-plane shear strain, ε_{11} and ε_{22} the misfit strains along the longitudinal and transverse directions, and Ω_β the atomic volume of the β phase.

Following Equation 4.9, we summary the explicit definitions of each elastic parameter and misfit strain to calculate misfit strain energy density along specific interfaces in Table 4.2:

In Section S1.6 of the Appendix C, we provide the general formula of directional Young's modulus, directional shear modulus and directional Poisson's ratio for cubic systems. In Section S1.7 of the Appendix C, we provide step-by-step procedures to calculate the misfit strain for $\beta \parallel \alpha''$ interfaces associated with the {112} and {332} twins under deformed state. Here, the misfit strain energy is defined relative to the β phase, since the nucleated α'' domains act as inclusions embedded within the parent β matrix, and the surrounding

Table 4.2: Elastic parameters and misfit strains for different alloy systems.

Parameters	$\{112\}$ twin	$\{332\}$ twin
E_1	$E_{\langle 111\rangle}$	$E_{\langle 311\rangle}$
E_2	$E_{\langle 011\rangle}$	$E_{\langle 011\rangle}$
G_{12}	$G_{\{111\}\langle 0\bar{1}1\rangle}$	$G_{\{311\}\langle 0\bar{1}1\rangle}$
ν_{12}	$\nu_{[\bar{1}11]\rightarrow[0\bar{1}1]}$	$\nu_{[311]\rightarrow[0\bar{1}1]}$
ν_{21}	$\nu_{[0\bar{1}1]\rightarrow[\bar{1}11]}$	$\nu_{[0\bar{1}1]\rightarrow[311]}$
ε_{11}	$\dfrac{d^{\beta}_{[\bar{1}11]} - d^{\alpha''}_{[\bar{1}10]}}{d^{\beta}_{[\bar{1}11]}}$	$\dfrac{d^{\beta}_{[311]} - d^{\alpha''}_{[310]}}{d^{\beta}_{[311]}}$
ε_{22}	$\dfrac{d^{\beta}_{[0\bar{1}1]} - d^{\alpha''}_{[001]}}{d^{\beta}_{[0\bar{1}1]}}$	$\dfrac{d^{\beta}_{[0\bar{1}1]} - d^{\alpha''}_{[001]}}{d^{\beta}_{[0\bar{1}1]}}$
γ_{12}	$\gamma_{\{111\}\langle 0\bar{1}1\rangle}$	$\gamma_{\{311\}\langle 0\bar{1}1\rangle}$

β lattice accommodates the misfit. Accordingly, all elastic constants and Poisson's ratios used in this study correspond to the β parent phase. The specific $\beta \parallel \alpha''$ interfaces used to calculate $W^{\text{misfit}}_{\text{twin}}$ for both twin modes, $W^{\text{misfit}}_{\{332\}\text{ twin}}$ and $W^{\text{misfit}}_{\{112\}\text{ twin}}$, follow the orientation relationships defined in Equation 4.8.

4.3.5 Twin Nucleation Metric

Figure 4.6 and Figure 4.7 suggest approximate methods to describe the twin nucleation path through the $\beta \leftrightarrow \alpha''$ reversible phase transformation for both $\{112\}$ and $\{332\}$ twins. Based on these descriptions of reaction paths and each term in Eq.4.7 for the nucleation barrier, we here now propose a twin nucleation metric (TNM):

$$\Delta g^{*}_{\text{twin}} = \left|\Delta F^{\text{A}}_{\beta\leftrightarrow\alpha''}\right| + W^{\text{misfit}}_{\text{twin}} \tag{4.10}$$

Here $\Delta g^{*}_{\text{twin}}$ characterizes the total free energy barrier per atom if the twinning is achieved by the reversible transformation between BCC and α" phase with the critical intermediate α" phase growing along the twin invariant planes. $\left|\Delta F^{\text{A}}_{\beta\leftrightarrow\alpha''}\right|$ defined in Eq. 4.6 (correlate

$\Delta G^{\mathrm{A}}_{\mathrm{chem}}$ in Eq. 4.7) characterizes the chemical free energy contribution to the barrier and is mainly dependent on temperature and composition. $W^{\mathrm{misfit}}_{\mathrm{twin}}$ from Eq. 4.9 estimates the misfit strain energy costs (correlate $\Delta G^{\mathrm{A}}_{\mathrm{elas}}$ and W_{ext} in Eq. 4.7), which are dependent on temperature, composition, and loading conditions. Then we use it to evaluate the twin nucleation behaviors we summarize in Table 4.1 and to investigate how and why temperature, composition, and loading condition tune the twinnability.

Table 4.3: Summary on the energetic descriptors for twinning nucleation behaviors and reversibility between β and α" phase. Unit of all energetic parameters is meV/atom. $P^{\beta\leftrightarrow\alpha''}_{\mathrm{chem}}$ is dimensionless. "DM" is short for deformation modes.

Alloy System	$\left\|\Delta F^{\mathrm{A}}_{\beta\leftrightarrow\alpha''}\right\|$	$w^{\mathrm{misfit}}_{\{112\}\mathrm{Twin}}$	$w^{\mathrm{misfit}}_{\{332\}\mathrm{Twin}}$	$\mathbf{P}^{\beta\leftrightarrow\alpha''}_{\mathrm{chem}}$	$\Delta g^{*}_{\{112\}\mathrm{twin}}$	$\Delta g^{*}_{\{332\}\mathrm{twin}}$	**DM**
Ti_5Nb@77 K	2.76	5.33	5.23	**0.66**	**8.09**	**7.99**	α"/**{332}**
Ti_5Nb@300 K	3.52	3.16	6.74	**0.87**	**6.68**	**10.26**	**{332}/{112}**
Ti_4Nb@77 K	1.35	3.22	5.74	**0.82**	**4.57**	**7.09**	**{332}/{112}**
Ti_4Nb@300 K	2.27	1.84	6.81	**0.92**	**4.10**	**9.08**	**{112}**
Ti10Mo@300 K	2.75	8.88	0.30	**0.90**	**11.63**	**3.05**	**{332}**

Table 4.3 summarizes the critical energetic descriptors for twinning nucleation behavior, including those defined in Eq. 4.10, for four Ti–Nb alloy systems prior to loading (the corresponding dominant twinning modes after loading are listed in the rightmost column): Ti_5Nb at 77 K, Ti_5Nb at 300 K, Ti_4Nb at 77 K, and Ti_4Nb at 300 K. In addition, one experimental dataset (Ti–10Mo wt.% at 300 K, the corresponding lattice constants are: a_β= 0.329 nm; $d^{[011]}_\beta$=0.475 nm; $a_{\alpha"}$=0.321 nm and $b_{\alpha"}$=0.503 nm.) beyond the Ti–Nb system is also included.In the sample, only {332} twin is found. Experimental procedures are shown in Section S1.2 of the Appendix C. Detailed procedures for calculating the equilibrium lattice constants of the BCC and α'' phases are described in the Section 4.2.3. $P^{\beta\leftrightarrow\alpha''}_{\mathrm{chem}}$, $\Delta g^{*}_{\{112\}\ \mathrm{twin}}$, and $\Delta g^{*}_{\{332\}\ \mathrm{twin}}$ are obtained from $\left|\Delta F^{\mathrm{A}}_{\beta\leftrightarrow\alpha''}\right|$, $w^{\mathrm{misfit}}_{\{112\}\mathrm{twin}}$, and $w^{\mathrm{misfit}}_{\{332\}\mathrm{twin}}$ according to Equation 4.8 and Equation 4.9. The magnitudes of these energetic parameters fall within a reasonable range compared with experimental results for Ti alloys [234]. In all cases shown in Table 4.3, the misfit strain energy density is comparable to, or even higher than, the

activation energy barrier for the phase transformation. This finding indicates that, in some cases, the elastic strain energy can be more critical than the chemical free energy (i.e., BCC phase stability) in determining the twinnability and the selection of the preferred twinning mode.

In the case of Ti_5Nb at 77 K, $P_{\text{chem}}^{\beta\leftrightarrow\alpha''}$ is relatively low compared to the other cases, indicating that the reversibility between the BCC and α'' phases is limited. As confirmed by the MD simulations, the α'' phase can be retained even under severe deformation in specific loading conditions. For Ti_5Nb at 300 K and Ti_4Nb at 77 K, $P_{\text{chem}}^{\beta\leftrightarrow\alpha''}$ is closer to 1, suggesting a higher reversibility between the BCC and α'' phases than in Ti_5Nb at 77 K. Consequently, the α'' phase acts as an intermediate stage, and twinning becomes easier to initiate under applied loading. In both cases, the twin nucleation metric (TNM) $\Delta g^*_{\{112\}\text{ twin}}$ is about 2.5–3.5 meV/atom lower than $\Delta g^*_{\{332\}\text{ twin}}$, indicating that the {112} twin is intrinsically more favorable. However, external loading conditions can compensate for the difference in Δg^*_{twin}, making {332} twin nucleation energetically competitive. Therefore, both {112} and {332} twins may form depending on the specific loading environment. For Ti_4Nb at 300 K, the high $P_{\text{chem}}^{\beta\leftrightarrow\alpha''}$ (0.92) ensures a strong propensity for twin nucleation. In this case, $\Delta g^*_{\{112\}\text{ twin}}$ is significantly smaller (by approximately 5 meV/atom) than $\Delta g^*_{\{332\}\text{ twin}}$, indicating that even under loading conditions that nominally favor {332} twinning, only {112} twins are likely to form. Conversely, for Ti–10Mo wt.% at 300 K, $\Delta g^*_{\{332\}\text{ twin}}$ is about 8.6 meV/atom lower than $\Delta g^*_{\{112\}\text{ twin}}$, which explains why only {332} twins are observed experimentally, despite the complexity of the loading conditions. In Section S2.7 of Appendix C, we also provide loading condition dependent Δg^*_{twin} in other cases we investigated in Table 4.1. In summary, Δg^*_{twin} in the undeformed state, when combined with $P_{\text{chem}}^{\beta\leftrightarrow\alpha''}$, reflects the intrinsic tendency for twinning and twin mode selection, which is independent of external loading effects to some extent. We next investigate how loading conditions influence deformation mode selection by analyzing the evolution of Δg^*_{twin} during dynamic shear loading.

Figure 4.8 shows the evolution of Δg^*_{twin} during dynamic loading for different alloy sys-

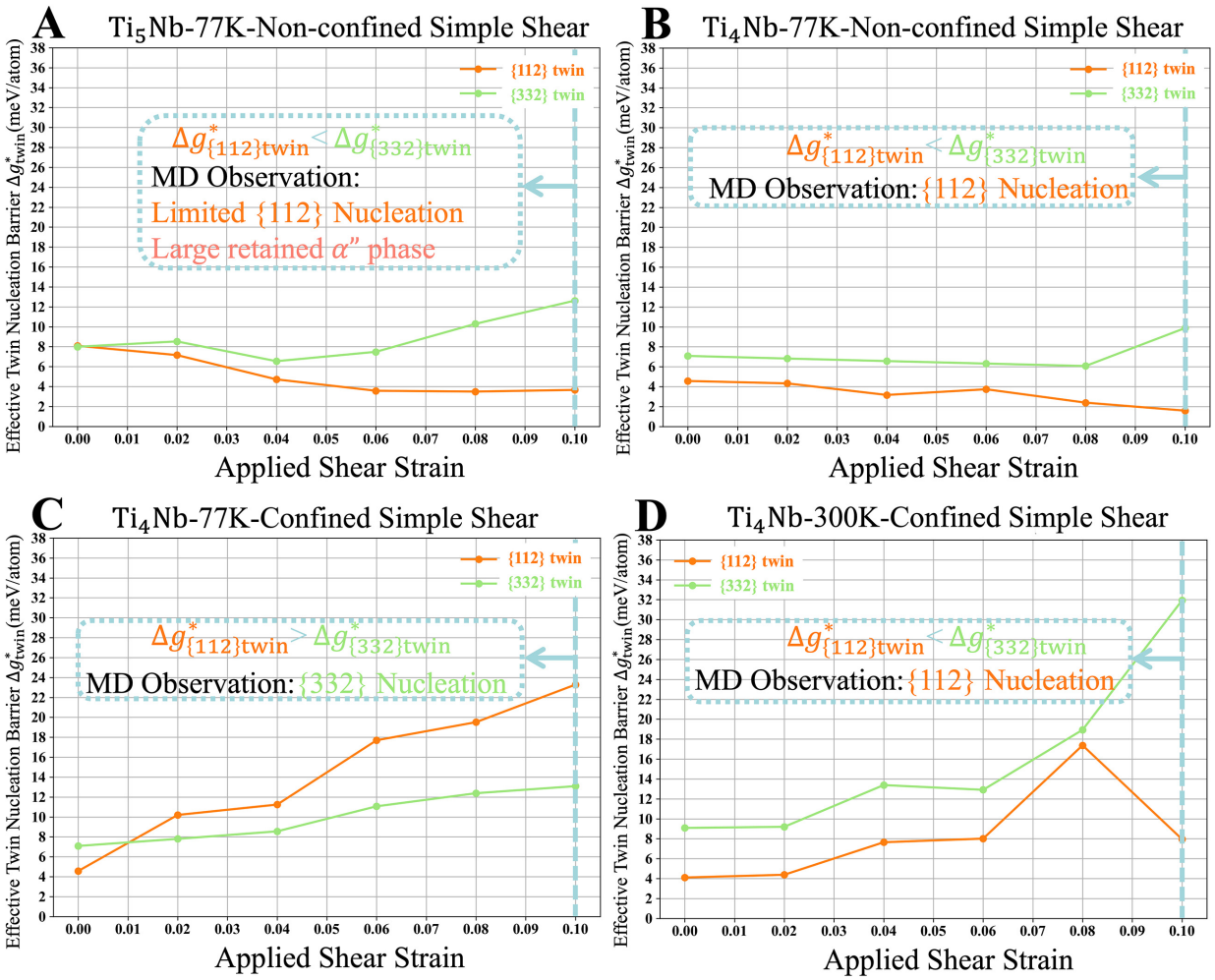


Figure 4.8: **Dynamic change of twin nucleation metric, Δg^*_{twin} under different stress/strain conditions for different alloy systems.** In all cases, the volume of nucleated α" phase saturates when applied shear strain is around 0.1. And twins starts to nucleate right after. The orange curves represent $\Delta g^*_{\{112\}\text{twin}}$ under loading conditions while the green curves correspond to $\Delta g^*_{\{332\}\text{twin}}$ under loading conditions. The alloy composition, temperature and loading type are at top of each subfigure. In each subfigure, we compare the magnitude of $\Delta g^*_{\{112\}\text{twin}}$ and $\Delta g^*_{\{332\}\text{twin}}$ at critical stage (external shear strain is 0.1,marked in light blue lines). Meanwhile, we mark the MD observations on the type of twin about to nucleate. All the snapshots of final deformed simulation box are in Section S2.3 of the Appendix C.

tems. Details of the Δg^*_{twin} calculation under deformed states are provided in the Section , and analyses of atomic structure evolution and deformation mode nucleation for the cases shown in Figure 4.8 are included in Section S2.3 of the Appendix C. During shear deformation, β–α'' phase transformations are observed in all cases, and the volume fraction of the nucleated α'' phase saturates when the applied shear strain reaches approximately 0.1. Subsequently, the nucleated α'' phase transforms into different deformation modes, depending on the temperature, composition, and corresponding stress/strain conditions. The detailed simulation parameters are labeled at the top of each subplot.

For Ti_5Nb at 77 K under non-confined simple shear (Figure 4.8(A)), $\Delta g^*_{\{112\}\text{ twin}}$ and $\Delta g^*_{\{332\}\text{ twin}}$ are initially similar. Upon applying shear strain, the loading condition alters these values differently: $\Delta g^*_{\{112\}\text{ twin}}$ decreases, while $\Delta g^*_{\{332\}\text{ twin}}$ increases. At the critical stage, where the α'' phase fraction reaches saturation, $\Delta g^*_{\{112\}\text{ twin}}$ becomes approximately 8 meV/atom lower than $\Delta g^*_{\{332\}\text{ twin}}$, making {112} twin nucleation more favorable. However, as discussed in Table 4.3, the reversibility between the BCC and α'' phases is low. Consistently, the MD simulations show that the dominant deformation mode remains the α'' phase, accompanied by a few localized {112} twin nuclei. Even when {112} twins form, their volume fraction remains small, and the system largely retains the α'' structure. The limited twin volume fraction can also be attributed to the large barrier associated with twin growth [39], which lies beyond the scope of this study but will be addressed in future work.

If we increase the Nb concentration from Ti_5Nb to Ti_4Nb while keeping the same temperature and loading condition [Figure 4.8(B)], $P^{\beta\leftrightarrow\alpha''}_{\text{chem}}$ increases (as already shown in Table 4.3), indicating higher reversibility between the BCC and α'' phases. Meanwhile, the overall trend in the evolution of Δg^*_{twin} remains similar to that in Figure 4.8(A). In this case, the α'' phase is not retained, and evident {112} twin nucleation behavior is observed. In contrast, if we keep the same composition and temperature but change the loading condition (comparing Figure 4.8(B) and (C)), the twinning nucleation behavior changes dramatically. The loading condition in Figure 4.8(C) increases both $\Delta g^*_{\{112\}\text{ twin}}$ and $\Delta g^*_{\{332\}\text{ twin}}$, but the increase in

$\Delta g^*_{\{112\}\ \text{twin}}$ is much larger. As a result, although $\Delta g^*_{\{112\}\ \text{twin}}$ is initially about 2.5 meV/atom lower than $\Delta g^*_{\{332\}\ \text{twin}}$, under loading it becomes roughly 10 meV/atom higher at the stage where the α'' phase fraction saturates. Consequently, {332} twin nucleation becomes much more favorable than {112} twinning, consistent with the MD observations.

Temperature also affects twinning mode selection, as revealed by the evolution of Δg^*_{twin}. Comparing the cases in Figure 4.8(C) and (D), where alloy composition and loading conditions are identical but temperature differs, we find that in Figure 4.8(D), $\Delta g^*_{\{112\}\ \text{twin}}$ is initially much smaller than $\Delta g^*_{\{332\}\ \text{twin}}$ compared to the case in Figure 4.8(C). Even though further loading significantly increases $\Delta g^*_{\{112\}\ \text{twin}}$, $\Delta g^*_{\{332\}\ \text{twin}}$ remains higher at the critical stage. As a result, {112} twinning, rather than {332}, is still observed. In summary, consistent with the discussion in Table 4.3, a large nucleation energy difference between $\Delta g^*_{\{112\}\ \text{twin}}$ and $\Delta g^*_{\{332\}\ \text{twin}}$ under stress-free conditions limits the influence of loading effects, and the twinning mode preferentially follows the pathway with the lower Δg^*_{twin}.

In summary, here we provide a workflow for calculating energetic parameters to assess the deformation modes in metastable β-Ti alloys. Meanwhile, it is extendable to other metastable BCC refractory high entropy alloys.

4.4 Discussion

So far, our proposed Δg^*_{twin} illustrates how temperature, composition, and loading conditions influence twinning mode selection in the metastable BCC region, while $P^{\beta\leftrightarrow\alpha''}_{\text{chem}}$ indicates how temperature and alloy composition affect the competition among TWIP, TRIP, and dislocation slip. By integrating these two parameters, we introduce a conceptual flowchart in Figure 5.2 to illustrate how deformation modes can be tuned via temperature, composition, and loading conditions. We first examine whether the α'' phase exists at the stress-free state to determine when dislocation slip dominates, represented by the left branch of the flowchart. In this study, Ti_2Nb at 300 K serves as a representative example of this regime. If the α'' phase can exist at the stress-free state and corresponds to a local minimum in the FEL,

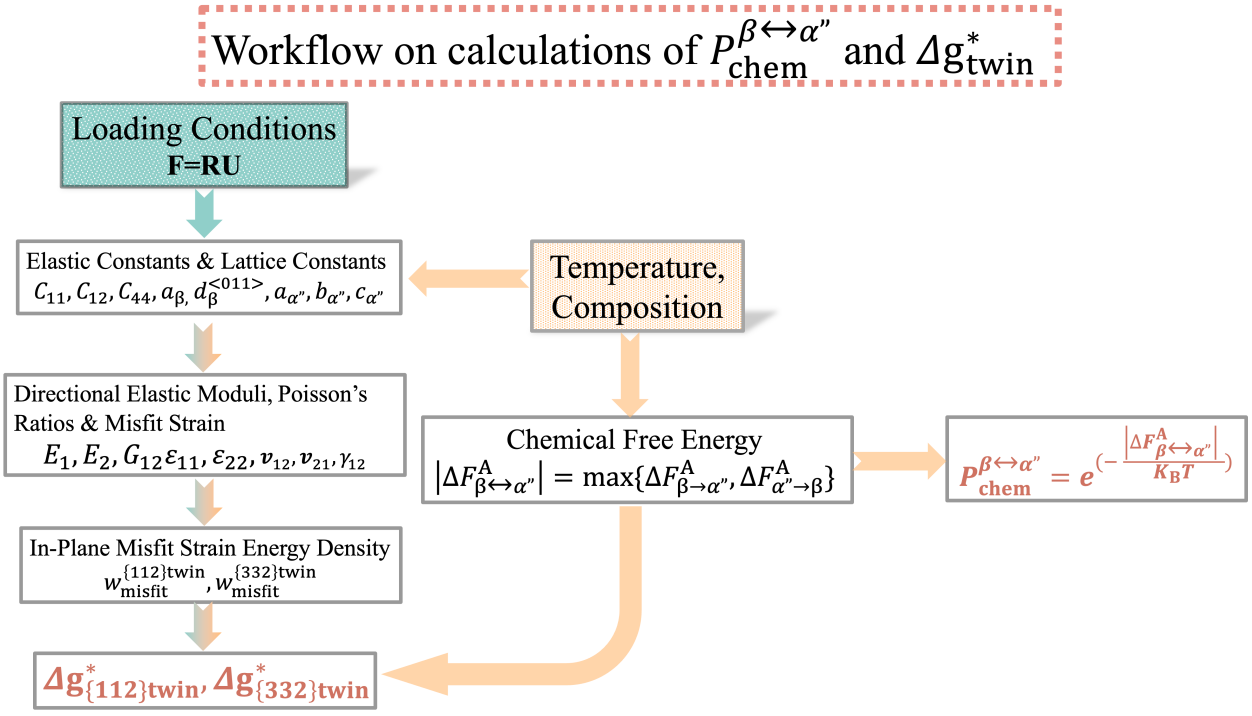


Figure 4.9: **A step-by-step workflow to calculate energetic parameters to distinguish deformation modes in metastable BCC alloys.**

we then evaluate the reversibility between the BCC and α'' phases and the twin nucleation metric to identify the competition among TRIP, {112} twinning, and {332} twinning. This corresponds to the right branch of the flowchart. We first assess $P_{\text{chem}}^{\beta\leftrightarrow\alpha''}$. Although no strict threshold is defined here, a low reversibility (with $P_{\text{chem}}^{\beta\leftrightarrow\alpha''}$ close to 0) indicates that twinning is difficult to nucleate via reversible phase transformations, and the α'' phase can be retained under certain loading conditions. Conversely, when the reversibility between the BCC and α'' phases is high, twins can form more readily. Under this condition, we then compare $\Delta g_{\text{twin}}^{*}$ for {112} and {332} twins. Although loading conditions can strongly modify the twin nucleation barriers, particularly near the critical stage of α'' phase saturation, a large intrinsic (i.e., under the loading-free condition) difference in $\Delta g_{\text{twin}}^{*}$ between the two twinning modes makes the mode with the lower $\Delta g_{\text{twin}}^{*}$ value more favorable and less sensitive to external loading. Representative examples include the {112} twin in Ti_4Nb at 300 K and the {332} twin in Ti–10Mo wt.% at 300 K.

When $\Delta g_{\text{twin}}^{*}$ for the {112} and {332} twins are comparable, the determining factor is no longer the intrinsic material property but rather the specific loading condition. Representative examples are Ti_5Nb at 300 K and Ti_4Nb at 77 K. This explains why conventional theoretical approaches that rely primarily on β-phase stability cannot distinguish twinning modes within the TWIP regime. Moreover, both TWIP and TRIP can also be tuned by loading conditions when $P_{\text{chem}}^{\beta\leftrightarrow\alpha''}$ lies between 0 and 1, as exemplified by Ti_5Nb at 77 K. A quantitative investigation of how loading conditions influence deformation mode selection will be an important topic for future studies.

Compared to the widely used $\overline{\text{Bo}}$–$\overline{\text{Md}}$ method, $P_{\text{chem}}^{\beta\leftrightarrow\alpha''}$ in our framework more clearly captures the correlation between temperature-dependent β-phase stability, its reversibility, and deformation mode selection. Taking the alloys in this study as examples, the ($\overline{\text{Bo}}$, $\overline{\text{Md}}$) values for Ti_5Nb, Ti_4Nb, and Ti_2Nb are (2.8415, 2.4431), (2.8518, 2.4424), and (2.8930, 2.3933), respectively. Although these temperature-independent $\overline{\text{Bo}}$–$\overline{\text{Md}}$ parameters are quite similar, their deformation modes differ significantly. In particular, Ti_5Nb and Ti_4Nb are

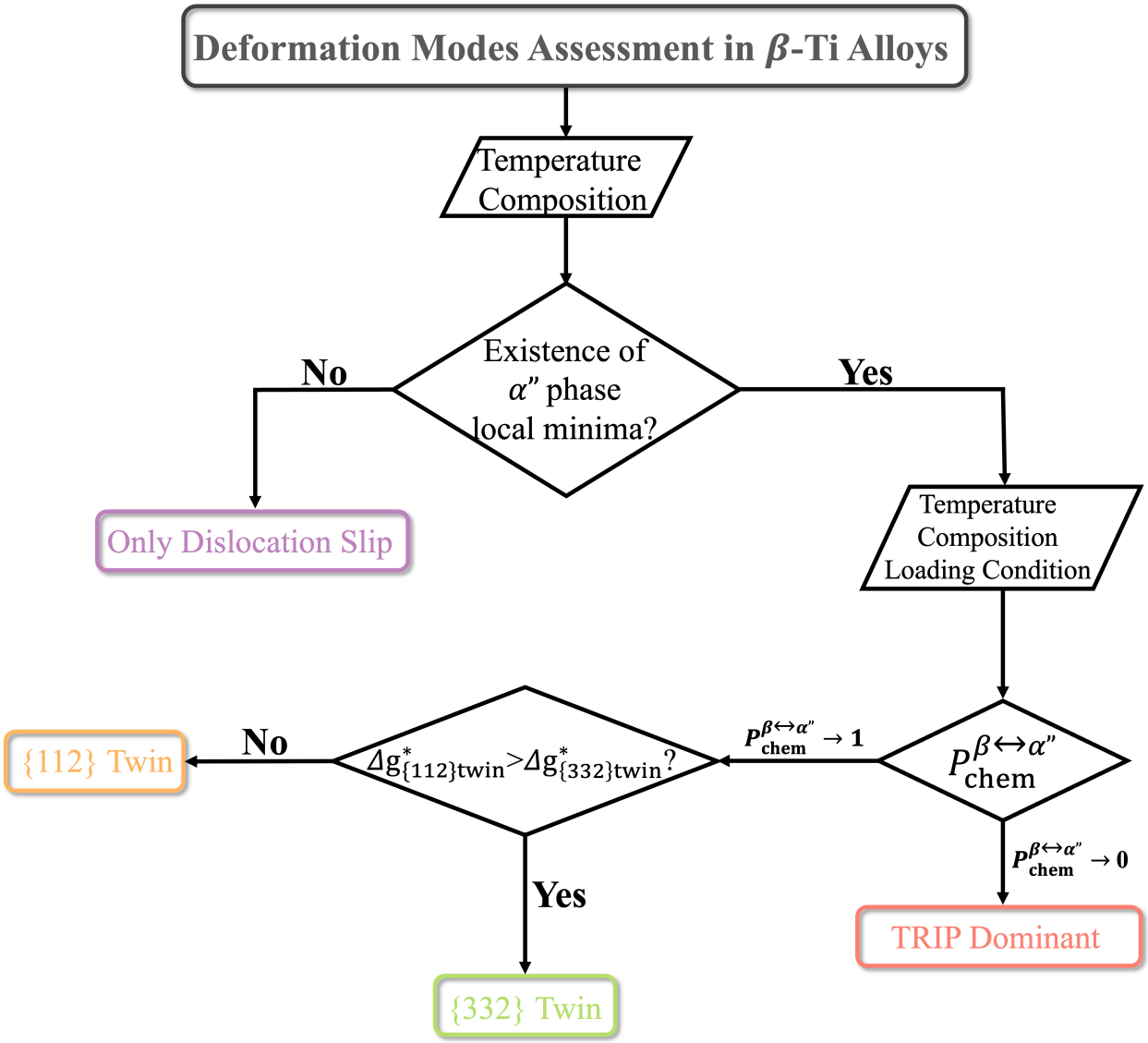


Figure 4.10: **A conceptual flowchart for criteria of deformation modes selection in metastable β-Ti alloys.**

located near the TRIP–TWIP boundary in the $\overline{\text{Bo}}$–$\overline{\text{Md}}$ diagram (see Figure 4.4B). However, this TRIP/TWIP boundary in the $\overline{\text{Bo}}$–$\overline{\text{Md}}$ diagram is based on empirical fitting rather than a physically derived criterion, making it ambiguous for data points near the boundary. Furthermore, as summarized in Table 4.1, the effect of temperature on deformation mode selection cannot be neglected.

Another advantage of this framework over conventional semi-empirical methods is its ability to provide insights into twinning mode selection within the TWIP regime under mechanical loading. Since both twinning modes occur via the same reversible β–α'' phase transformation, the elastic strain free energy associated with twinning nucleation plays a more critical role. This elastic strain energy is strongly correlated with the strain state (or structural distortion) of the β phase and the nucleated α'' phase. The equilibrium structures of the α'' and β phases vary with alloy composition, temperature, and loading conditions. Due to the metastability of the β phase and its relatively low elastic moduli, it is highly susceptible to lattice distortion under applied loading. Moreover, many metastable β-Ti alloys contain neutral elements such as Sn and Zr, which do not significantly affect β phase stability but can substantially modify lattice parameters, elastic moduli, and elastic constants of both β and α'' phases, thereby influencing the elastic strain energy penalty for twin nucleation [100, 84]. In addition, α''-stabilizing elements such as oxygen, which are often introduced during materials processing, can also induce lattice distortions and alter the equilibrium lattice parameters of both β and α'' phases [155, 43, 150, 202, 186]. Therefore, structural distortions and lattice modulations in β and α'' phases can become significant under mechanical loading but are poorly captured by existing empirical alloy design methods. The strain state of metastable phases is represented by a second-order tensor field, making it difficult to directly link to twin nucleation barriers. In our theoretical framework, Δg^*_{twin} effectively connects the strain states of the β and α'' phases to the misfit strain energy density, thereby determining the competition between different twinning modes. Δg^*_{twin} at the undeformed state reveals the intrinsic tendency for twinning mode selection, while Δg^*_{twin}

at the deformed state illustrates how loading conditions influence twin nucleation behavior and provides guidance for tuning twinning modes through mechanical loading.

Beyond the Ti–Nb and Ti–Mo binary systems included in this study, our deformation mode assessment flowchart is readily extensible to multicomponent metastable β-Ti alloys, making it a potentially useful tool for alloy design. All these input parameters in this framework of Figure 5.2 can be obtained through both computational and experimental approaches and are not limited to specific alloy systems. Compared with case-by-case MD simulations of complete deformation processes, which require large supercells and entail high computational cost, the parameters needed for our assessment can be obtained much more efficiently. Therefore, this workflow enables high-throughput screening of compositional space to identify alloys that intrinsically favor targeted deformation mechanisms. Furthermore, machine-learning interatomic potentials (MLIPs) trained on high-quality *ab initio* data can further accelerate the prediction of the required energetic and elastic parameters across broad compositional and temperature ranges. Compared with direct atomistic simulations of deformation mechanisms using very large supercells, it is also far more practical to train accurate MLIPs to compute $P_{\text{chem}}^{\beta\leftrightarrow\alpha''}$ and $\Delta g_{\text{twin}}^{*}$ using relatively small cells. Overall, the proposed theoretical framework, when combined with machine-learning techniques, offers a data-efficient prescreening strategy for rapidly identifying alloys with an intrinsic propensity for specific deformation modes [144, 3, 148, 66].

Another limitation of the current framework is the lack of information on dynamic growth behaviors. In particular, within the TWIP regime, the final volume fraction of twins in the material, which correlates with their contribution to plasticity, is highly dependent on twin growth behavior. For the {112} twin in metastable Ti alloys, the growth behavior is closely related to the stability of the ω phase [39], and the growth kinetics can be tuned by controlling the reversibility between the β and ω phases. In contrast, {112} twin nucleation and growth in stable BCC materials do not necessarily require phase transformations and can instead be triggered by successive slip on {112} planes [123]. Since our focus is on

the metastable region, we do not consider this successive slip mechanism here, particularly because dislocation slip is the dominant carrier of plastic deformation compared to {112} twinning in stable BCC materials. For the {332} twin in metastable Ti alloys, α'' phase is often observed along twin boundaries [113, 38] (including in this study), suggesting twin growth via reversible β–α'' phase transformation. However, the atomistic motion of twin boundaries during growth remains under debate and does not strictly follow the Burgers path [189, 110]. To fully evaluate the growth kinetics of {332} twins, detailed investigations of atomic motions at twin boundaries are still required in future studies.

As for mechanical loading aspect, we do not consider the strain rate effect. Strain rate can affect both nucleation and growth kinetics for all four deformation behaviors. For example, researchers use surface mechanical rolling treatment (SMRT) method investigate strain rate-dependent deformation modes in β Ti-12Mo ally and observe the shift of dominant deformation modes from low to high strain rate: stress-induced α" martensite $\rightarrow$ {332}/{112} twins $\rightarrow$ dislocation slip and shear bands [210]. Strain rate can significantly affect value of Δg^*_{twin}. This is out of the scope of current study but worth investigations.

4.5 Conclusion

Here, we summarize the key findings and conclusions from the atomistic simulations conducted and theories proposed in this study:

(1) Our atomistic simulations capture the full spectrum of common deformation modes in metastable β-Ti alloys. Thermodynamically, we reveal temperature and composition-dependent deformation modes selection. The trend is well consistent with experimental observations. Especially, there is a long time puzzle for dynamic nucleation behavior of unique {332} twin in metastable β-Ti alloys. Crystallographic theory propose the phase transformation-induced twinning path while experimental technique capture the phase transformation behaviors surrounding the {332} twin nuclei. For the first time, Our atomistic simulations for {332} twin nucleation fill the gap between crystallographic theory and exper-

iments. The dynamic nucleation process are in well agreement with both crystallographic theory and experiments.

(2) By systematic energetic and structural analysis during reversible phase transformations and twin nucleation processes, combine with crystallographic theory, we then derive a $P_{\text{chem}}^{\beta\leftrightarrow\alpha''}$–$\Delta g_{\text{twin}}^{*}$ flowchart, which incorporates both the free energy barriers for homogeneous transformations and the misfit strain energy along specific phase boundaries. This conceptual flowchart provides clear criteria for the nucleation of different deformation modes, with parameters that correlate temperature, alloy composition, and loading conditions during mechanical deformation. In Section S1.8 of the Appendix C, we also provide a step-by-step workflow for calculating all key parameters in the flowchart. The applicability of this framework is not limited to the alloys studied here; it can be extended to multicomponent metastable β-Ti alloys and to the future design of metastable BCC refractory high-entropy alloys using high-throughput atomistic simulations of defect-free bulk systems based on accurate MLIPs.

CHAPTER 5

Theoretical Prediction on Twin Nucleation Strength

Metastable β-Ti alloys exhibit complex deformation behaviors governed by competing mechanisms including stress-induced martensitic transformation, deformation twinning, and dislocation slip, whose interplay determines macroscopic yield strength. Building on the energetic framework established for binary Ti-Nb alloys, we extend the twin nucleation metric, the free energy barrier Δg^*_{twin}, into classical nucleation theory (CNT) to predict the yield strength of ternary Ti-Nb-Mo alloys without requiring computationally expensive molecular dynamics simulations on deformation dynamics. The predicted yield strengths show strong agreement with experimental data, reproducing both the compositional and temperature dependence observed across the metastable region. We demonstrate that within the metastable compositional space, fine-tuning the Mo fraction selectively modifies the misfit strain energy for twin boundary formation, thereby shifting the preferred twinning mode and enabling targeted alloy design. Temperature serves as an orthogonal handle that modulates the chemical free energy driving force, providing independent control over the overall yield strength. This computationally efficient framework is readily extendable to other metastable β-Ti alloy systems and even metastable BCC high entropy alloys, offering a physics-based pathway for accelerated metastable BCC alloy design guided by thermodynamic and crystallographic principles.

5.1 Introduction

Metastable β-phase titanium (Ti) alloys have attracted sustained interest as structural materials due to their exceptional combination of high strength, low density, and tunable mechanical response [105, 168]. Their mechanical behavior is governed by competing deformation mechanisms, making metastable β-Ti alloys highly designable through composition- and thermodynamics-guided selection of the dominant deformation mode. Significant progress has been made in developing compositional design strategies for metastable β-Ti alloys, with the overarching goal of identifying alloy compositions that activate desired deformation mechanisms. The molybdenum equivalency ($\mathrm{Mo_{eq}}$) concept reduces a multicomponent alloy to a single scalar measure of β-phase stability by weighting each alloying element according to its stabilizing potency relative to Mo [67, 9]. Another widely used strategy is based on the d-electron theory. Morinaga and co-workers correlates deformation-mode tendencies with the average d-orbital energy level ($\bar{B}_o$) and metal d-orbital energy ($\overline{M_d}$), providing an electronic-structure-informed map that partitions the compositional space into regions prone to SIM transformation, twinning, or dislocation slip [147]. Besides these widely used strategy, in Chapter 4, we also estimate a theoretical framework that connect the deformation modes selection with temperature, composition and mechanical loading condition, potentially can further improve materials design strategy.

However, a fundamental limitation shared by these design strategies is only link the thermomechanical (mostly composition only) condition with deformation mode. The quantitative correlation between deformation modes and mechanical properties (such as yield strength, work hardening rate) is totally empty. This gap becomes particularly consequential in metastable Ti alloy design scenarios where multiple candidate compositions are predicted to operate within the same deformation regime. For instance, among a set of Ti-Nb-Mo alloys all predicted to exhibit the TWIP effect based on $\mathrm{Mo_{eq}}$ or d-electron descriptors, existing classification frameworks offer no basis for discriminating which candidate will deliver

the most favorable strength-ductility combination. Alloy selection in such cases therefore remains largely empirical, relying on iterative synthesis and mechanical testing rather than on predictive physical models.

Efforts to establish a more quantitative connection between deformation mechanisms and mechanical properties have been pursued in related material systems, but with important limitations that preclude direct application to metastable β-Ti alloys. In TWIP steels, dislocation-density-based crystal plasticity models have been developed that incorporate twin nucleation and volume fraction evolution to predict flow stress and strain-hardening behavior [24]. While physically grounded, these models require extensive microstructural parameters calibrated against experimental stress–strain curves, and are not predictive a priori from composition alone. In shape memory alloys, Peierls–Nabarro-based twin nucleation models have been used to predict the critical twinning stress from first-principles twinning energy pathways, achieving good agreement with experimental data [200]. However, these approaches are system-specific, rely on density functional theory (DFT) inputs for each composition, and are not readily scalable for compositional screening. More recently, machine learning frameworks have been proposed that chain a deformation-mode classification model with a yield strength regression model for β-Ti alloys [164], providing a practical data-driven tool. Nevertheless, such approaches require large experimental training datasets for each alloy system, and lack the physical interpretability needed to guide mechanistic understanding or extrapolate to new compositions.

In the present chapter, we extend the deformation assessment framework in Chapter 4 to ternary Ti-Nb-Mo alloys and incorporate Δg^*_{twin} directly into classical nucleation theory (CNT) to yield quantitative predictions of macroscopic yield strength from deformation modes. The addition of Mo as a third alloying element is of both scientific and practical interest: Mo is a strong β-stabilizer whose concentration modulates the misfit strain energy at twin-matrix interfaces, providing fine-grained control over twinning mode preference. Meanwhile, temperature independently tunes the chemical free energy contribution to

Δg^*_{twin}, enabling decoupled optimization of yield strength. We show that the predicted yield strengths across the metastable Ti-Nb-Mo compositional space agree well with experimental measurements, capturing both compositional trends and temperature dependence. Beyond the specific Ti-Nb-Mo system, the framework is formulated in terms of quantities that are broadly accessible for other metastable β-Ti alloys, suggesting a general and computationally efficient route toward physics-based alloy design.

5.2 Methods

The computational methods employed in this chapter follow the same general framework established in Chapter 4, encompassing 1) metadynamic simulations for free energy barrier calculations of the $\beta \leftrightarrow \alpha''$ phase transformation; 2) calculations of lattice constants and elastic constants for the relevant phases, and 3) evaluation of misfit strain energies along β/α'' phase boundaries. The primary distinction in the present chapter is the adoption of a different Machine Learning Potential (MLP), we here utilize the moment tensor potential (MTP) for Ti-Nb-Mo ternary alloys developed by Zheng et al. [236], which extend chemical space into ternary system and has been validated against density functional theory (DFT) calculations for structural, elastic, and thermodynamic properties across the Ti-Nb-Mo compositional space. All molecular dynamics simulations are performed using this MTP within the same simulation protocols described in Chapter 4.

5.3 Results

5.3.1 Heterogeneous Nucleation Framework

So far, the twin nucleation metric we proposed in Chapter 4 can reveal how temperature, composition and loading conditions affect the twin nucleation competition. Nevertheless, the metric is a per atom energetic parameter while real nucleation barrier is inherently

size dependent. To bridge this gap, We then incorporate the atomistic nucleation metric into a heterogeneous nucleation framework, thereby connecting local energetic descriptors to physically realistic nucleation processes. Within this framework, the nucleation barrier is reasonably linked to the corresponding critical stress required to activate deformation and so further enable to predict yield strength.

According to a heterogeneous nucleation process, we assume the nuclei in an oblate ellipsoid shape with diameter a in lateral dimension and with thickness of c. The the total free energy change associated with twin nucleus formation is expressed as [173, 234]:

$$\Delta G = 2\pi a^2 \gamma_0 + \frac{4}{3}\pi a^2 c \left(\Delta g_{\text{chem}} + \Delta g_{\text{str}} - \tau_T \gamma_T\right), \tag{5.1}$$

where a and c are the lateral and thickness dimensions of the nucleus, γ_0 is the interfacial energy, Δg_{chem} is the chemical driving force (taken as the transformation barrier and in the unit of J/m^3), Δg_{str} is the elastic misfit strain energy density and in the unit of J/m^3, τ_T is the applied shear stress, and γ_T is the characteristic twinning shear. Specially, both for $\{112\}$ and $\{332\}$ twin, the twinning shear is $\frac{1}{2\sqrt{2}} \approx 0.3536$, assuming twinning via lattice modulation [189]. In stable BCC alloy system, many studies treat twinning shear for $\{112\}$ twin is $\frac{2}{2\sqrt{2}} \approx 0.7071$, assuming twinning via pure shear without atomic shuffle. This is unrealistic large for metastable BCC system where twinning is via lattice modulation. [189]

At the critical nucleus size, the stationary conditions satisfy that:

$$\begin{cases} \dfrac{\partial \Delta G}{\partial a} = 0 \;\Rightarrow\; \Delta g_{\text{chem}} + \Delta g_{\text{str}} + \dfrac{3}{2c}\gamma_0 = \tau_T \gamma_T \\ \dfrac{\partial \Delta G}{\partial c} = 0 \;\Rightarrow\; \Delta g_{\text{chem}} + \Delta g_{\text{str}} = \tau_T \gamma_T \end{cases} \tag{5.2}$$

Therefore, a lower-bound condition for twin nucleation is:

$$\tau_T = \frac{\Delta g_{\text{chem}} + \Delta g_{\text{str}}}{\gamma_T}. \tag{5.3}$$

In this work, the chemical contribution Δg_{chem} is obtained from metadynamics-derived transformation barriers (e.g., $\beta \rightarrow \alpha''$), while the elastic contribution Δg_{str} is represented by the misfit strain energy density $W^{\text{misfit}}_{\{112\}\text{twin}}$ and $W^{\text{misfit}}_{\{332\}\text{twin}}$ corresponding to {112} and {332} twinning modes, respectively. This yields a mode-dependent critical shear stress:

$$\tau^{\text{twin}}_{\text{crit}} = \frac{\Delta g^{*}_{\text{twin}}}{\gamma_{\text{twin}} \times \Omega} = \frac{\left|\Delta F^{\text{A}}_{\beta \leftrightarrow \alpha''}\right| + W^{\text{misfit}}_{\text{twin}}}{\gamma_{\text{twin}} \times \Omega} \tag{5.4}$$

where Ω is atomic volume.

For polycrystalline materials, we further estimate the macroscopic critical stress for twin using the Taylor factor M (M=3 in this study):

$$\sigma^{\text{twin}}_{\text{crit}} = M \times \tau^{\text{twin}}_{\text{crit}}. \tag{5.5}$$

Finally, since {332} twin and {112} twin are two dominant twinning modes, the final predicted yield stress is determined by the twinning mode with smaller nucleation stress:

$$\sigma^{\text{twin}}_{\text{yield}} = \min\left\{\sigma^{\{332\}\text{Twin}}_{\text{crit}},\ \sigma^{\{112\}\text{Twin}}_{\text{crit}}\right\}. \tag{5.6}$$

This framework provides a unified pathway linking atomistic energetics (transformation barriers and misfit strain energies) to macroscopic mechanical response, like yield strength, enabling quantitative comparison of competing twinning modes and prediction of dominant deformation mechanisms. We then employ it to a wider composition space, and the results are shown in following part.

5.3.2 Metastability of Ti-Nb-Mo Ternary Alloys

We now employ the nucleation framework to other Ti alloy systems. We previously develop the theoretical model via a series of atomistic simulation in Ti-Nb binary system. This is because the MEAM Ti-Nb potential we employ in this study is reliable to capture dynamic

deformation process, especially martensite phase transformation and phase transformation induced twinning [39, 57]. Therefore, it enables describe the transient nucleation process with good physics fidelity. In real experiments, {332} twin is more prevalent in Ti-Mo binary or multi-component Ti system containing Mo [185, 234, 83, 80] and TRIP/TWIP effects have been extensively studied in the those alloy systems [236]. To better compare the experiment and theoretical predicted yield stress, we then extend the framework to Ti-Mo-Nb alloy employing Ti-Mo-Nb-Ta MTP machine learning potential. Since we directly employ the nucleation framework, so we do not need potential to accurately simulate deformation behaviors. Instead, it only needs to accurately describe lattice constants, elastic constants and phase stability in the wide chemical space. We select this potential is because its training data includes random solid solution structures in various chemical compositions at different temperature.

We first identify the temperature-dependent metastable region (where β and α" coexist) for Ti-Mo-Nb system using the MTP potential, results are in the Figure 5.1. Gray region are compositions in which only HCP-like α'/α" and the structure will spontaneously transfer to α'/α" once relaxation. In contract, light yellow region are compositions in which structure will stay at perfect BCC phase and will not sustain at α" phase. If the structure initially in perfect BCC lattice but spontenously transfer to α" with b/a larger than 1.5, we mark it in gray color. If the structure initially in perfect HCP lattice but spontenously transfer to BCC with b/a no larger than 1.415, we mark it in light yellow color. Compositions in gray or light yellow regions are out of metastable region and have no TRIP/TWIP effect. We therefore focus the remaining compositions where β and α" coexist.

We present the heatmap of $W^{\text{misfit}}_{\{332\}\text{twin}}$-$W^{\text{misfit}}_{\{112\}\text{twin}}$ for remaining compositions. Within metastable region, compositions in blue colors may favors {332} twin nucleation since negative values of $W^{\text{misfit}}_{\{332\}\text{twin}}$-$W^{\text{misfit}}_{\{112\}\text{twin}}$ while compositions in red colors show positive values of $W^{\text{misfit}}_{\{332\}\text{twin}}$-$W^{\text{misfit}}_{\{112\}\text{twin}}$, indicating {112} twin favors. Although we have not calculate chemical free energy contribution for these compositions, the competition between twinning is by

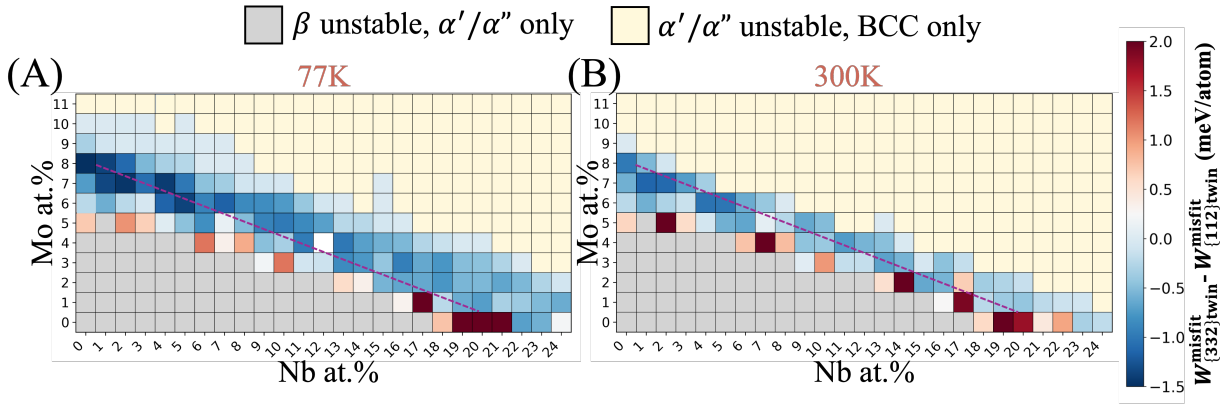


Figure 5.1: **Composition-dependent map of metastability in the Ti-Mo-Nb system at 77 K (A) and 300 K (B).** The color bar represents the difference in misfit strain energy density between twinning modes, $W^{\text{misfit}}_{\{332\}\text{twin}}$ - $W^{\text{misfit}}_{\{112\}\text{twin}}$ (meV/atom), where negative values (blue) indicate preference for {332} twinning and positive values (red) favor {112} twinning. Grey and yellow regions have no metastable phases and only one phase exists. Grey regions correspond to compositions where the β phase is unstable and only α'/α'' exist, while light-yellow regions indicate stable β (BCC) where α'/α'' is unstable. The dashed purple line marks a compositional pathway along which all alloys remain metastable in both temperature with respect to the $\beta \rightarrow \alpha'/\alpha''$ transformation. Compositions along this metastable pathway are selected for subsequent analysis to evaluate the predicted yield stress based on competing twinning modes.

misfit strain energy only in our model. Clearly, both in 77 K and 300 K, compositions close to binary Ti-Mo with little to none Nb (darker blue region) are favorable for {332} twin. Instead, compositions close to binary Ti-Nb with little to none Mo (darker red region) are favorable for {112} twin. This composition dependent twin selections are generally consistent with experimental fact: {332} twin favors in many Ti-Mo binary alloys while few experimental reports for {332} twin nucleation in Ti-Nb binary alloys [185, 234, 83, 80]. Neutral elements are often added into Ti-Nb based alloys to form {332} twin, as we previously shown in Figure 4.4 [83, 82, 220, 226, 177, 38, 125, 231, 77, 219, 75, 227, 12].

5.3.3 Macroscopic Yield Stress Prediction via Twin Nucleation Metric

Within the narrow metastable region, besides misfit strain energy, to estimate the corresponding yield stress, we need to further calculate chemical free energy barrier between β and α" phase. Since relatively intense computation cost for Metadynamics calculations, we here pick representative compositions within metastable region. As shown in Figure 5.1, compositions along purple line across the metastable region are remain in metastable under both 77 K and 300 K. Meanwhile, compositions along the purple line are away from BCC unstable/metastable and BCC metastable/stable boundaries where TRIP may dominate. Compositions along purple line satisfy:

$$\mathrm{Ti}_{92-0.6x}\mathrm{Nb}_x\mathrm{Mo}_{8-0.4x}, \quad 0 \leq x \leq 20 \text{ (at.\%)} \tag{5.7}$$

Assuming TWIP is dominant deformation modes within the compositions in Equation 5.7 at 77 K and 300 K, Figure 5.3 (A) and (B) shows the predicted critical stress $\sigma_{\mathrm{crit}}^{\mathrm{twin}}$ for twin nucleation. Orange solid line with circle markers represent $\sigma_{\mathrm{crit}}^{\{112\}\mathrm{Twin}}$ while green solid line with square markers represent $\sigma_{\mathrm{crit}}^{\{332\}\mathrm{Twin}}$. Star markers represent experimental measured yield strength. Dominant deformation mode found in experiment for Green star is

{332} twin; while orange star marker represent corresponding dominant deformation mode is {112} twin (combined with TRIP in some cases). The predicated yield stress, $\sigma_{\text{yield}}^{\text{twin}}$, is $\min\left\{\sigma_{\text{crit}}^{\{332\}\text{Twin}},\ \sigma_{\text{crit}}^{\{112\}\text{Twin}}\right\}$, defined in Equation 5.6. In general, the predict yield stress are at the same magnitude of experimental data under 77 K and 300 K. As for twin selection at 77 K, trend is consistent with results in Figure 5.1, $\sigma_{\text{crit}}^{\{332\}\text{Twin}}$ is evidently smaller than $\sigma_{\text{crit}}^{\{112\}\text{Twin}}$ when Nb concentration is less than 16 at.%, indicating {332} twin is more favorable (So $\sigma_{\text{yield}}^{\text{twin}}$=$\sigma_{\text{crit}}^{\{332\}\text{Twin}}$). When Nb concentration is larger than 16 at.%, corresponding Mo concentration is less than 1.6 at.%, {332} twin is not favorable thermodynamically since $\sigma_{\text{crit}}^{\{112\}\text{Twin}}$ is much smaller, and so $\sigma_{\text{yield}}^{\text{twin}}$=$\sigma_{\text{crit}}^{\{112\}\text{Twin}}$. Meanwhile, predict yield stress is generally correlate with alloy composition. Adding Nb and reducing Mo contents will leads to decrease of yield stress. Though we have limited experimental data at 77 K, experimental measured yield stress of Ti-Nb binary alloy at 77 K are no larger than 400 MPa [82, 122], which is much smaller than 810 MPa for Ti-8.1 at.%Mo. Meanwhile, experimental data confirm decrease of yield strength with increase of Nb in Ti-10Mo-Nb (wt.%) alloy [217] and increase of yield strength with increase of Mo in Ti-Mo-26Nb(wt.%). Therefore, experimental observation can indirectly confirm the trend at 77 K shown in Figure 5.3 (A).

As for twin selection at 300 K shown in Figure 5.3 (B), {332} twin is also favorable when Nb concentration is small and unfavorable thermodynamically when Nb concentration is large. However,as for predicted yield stress $\sigma_{\text{yield}}^{\text{twin}}$, it is not monotonically decreases with increase Nb concentration. Instead, it has a pick at middle when Nb concentration is around $11-13$ at.%, where $\sigma_{\text{yield}}^{\text{twin}}$ is comparable to Ti-8 at.%Mo. Meanwhile, {332} twin is favorable at that narrow composition region. Compared to experimental data in Figure 5.3 (B), the predicted yield stress, without fitting parameters, are reasonable agreement with experimental measurements, especially correlation between composition and yield stress. Meanwhile, Zain et.al conduct shape memory effect test on a series of metastable β Ti-(0-4)Mo-(12-28)Nb (at.%) alloy at room temperature and notice that yield strength achieves maximum when the alloy contain moderate amount Mo and Nb ($Ti_{84}Mo_4Nb_{12}$ (at.%)) [1], which is

close to the composition ($Ti_{84.8}Mo_{3.2}Nb_{12}$)with maximum yield strength in Figure 5.3 (B). Besides comparison of predicted and experimental measured yield strength, the predicated dominant deformation modes are also consistent with experimental observation.

So far we explore composition effects on yield strength under different temperatures, we then explore the temperature effect. Increasing temperature from 77 K to 300 K leads to a systematic reduction in twin nucleation stress for both twinning modes. In conventional stable BCC alloys, it is widely acknowledged that temperature affect barriers of kink-pair nucleation, barriers of dislocation motion and so affect the total yield strength [181, 143]. However, quantitative investigation of temperature effect on yield strength of metastable BCC alloys (dislocation is no longer dominant deformation mechanism) are still limited so far. Moreover, strain free energy and chemical free energy are both non-trivial term for nucleation of deformation twinning in metastable system, so we need to analyze them separately. Following Equation 5.4 and Equation 5.6, we can separate chemical contribution $\sigma_{\text{chem}}^{\text{Twin}}$ and strain contribution $\sigma_{\text{misfit}}^{\text{Twin}}$ of predict yield strength:

$$\sigma_{\text{chem}}^{\text{Twin}} = M \times \frac{\left|\Delta F_{\beta\leftrightarrow\alpha''}^{\text{A}}\right|}{\gamma_{\text{twin}} \times \Omega}, \quad \sigma_{\text{misfit}}^{\text{Twin}} = M \times \frac{W_{\text{twin}}^{\text{misfit}}}{\gamma_{\text{twin}} \times \Omega} \tag{5.8}$$

Following Equation 5.8, we then plot the decomposition of predicted yield strength for Ti-Mo-Nb we investigated in Figure 5.3 (C) and (D).Orange dashed line with circle markers represent $\sigma_{\text{misfit}}^{\{112\}\text{Twin}}$ while green dashed line with square markers represent $\sigma_{\text{misfit}}^{\{332\}\text{Twin}}$. Gray solid line with triangle markers represent $\sigma_{\text{chem}}^{\text{Twin}}$. As for temperature effect on misfit strain energy, misfit strain energy slightly increase with decrease of temperature, especially at composition region where Nb content (x $\leq$ 10) is dilute. Instead, the temperature effect on change of misfit strain energy is limited when Nb concentration is relatively higher (x $>$ 10). The magnitude of misfit strain contribution on yield strength is mainly depends on the composition. In contrast, temperature effect on chemical free energy of phase transformations are remarkable. $\sigma_{\text{chem}}^{\text{Twin}}$ undergoes around 100 MPa (1 meV/atom for $\left|\Delta F_{\beta\leftrightarrow\alpha''}^{\text{A}}\right|$)

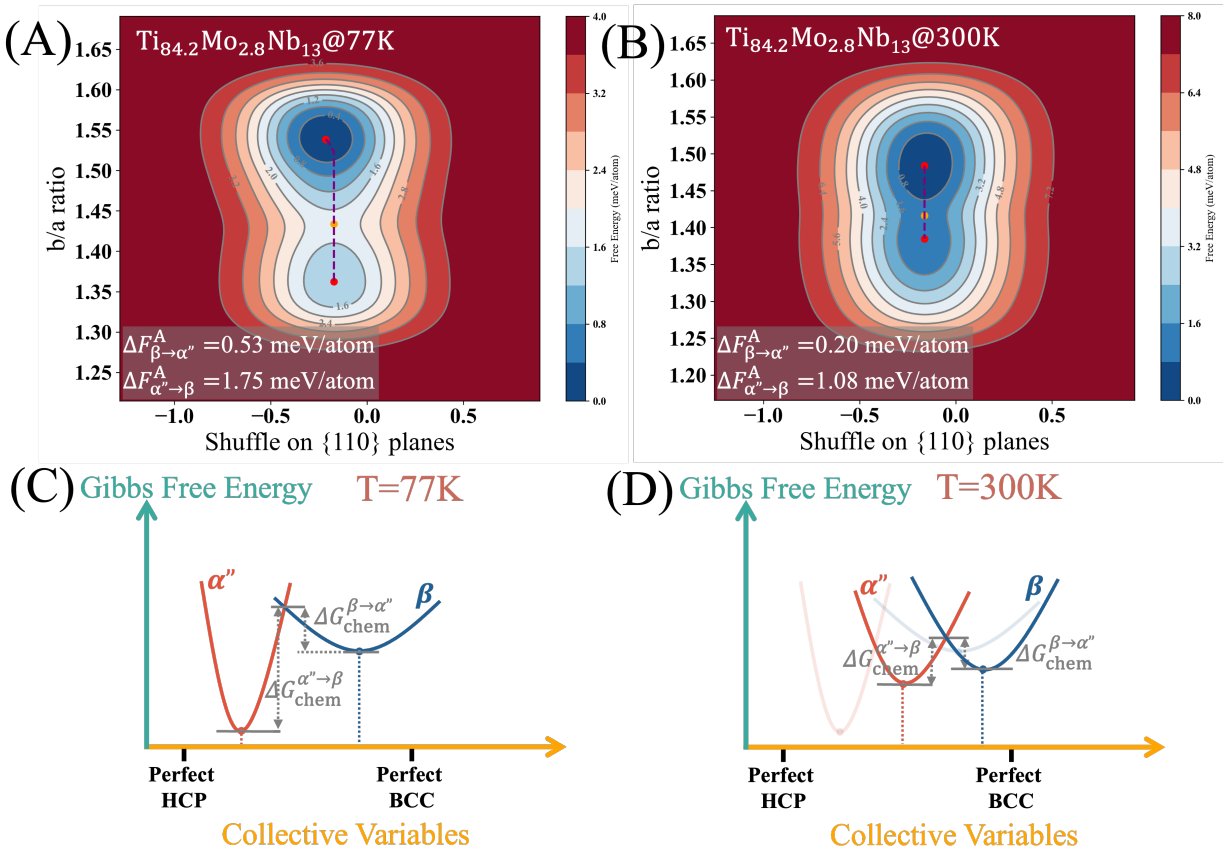


Figure 5.2: **A conceptual flowchart for criteria of deformation modes selection in metastable β-Ti alloys.**

reduction for all compositions when temperature increases from 77 K to 300 K. Meanwhile, $\sigma_{\text{chem}}^{\text{Twin}}$ variation between different compositions under same temperature is scattered and no dramatic difference, which indicates fine tuning alloy composition within the metastable region has limited effect on phase transformation barriers. When it comes to the magnitude of $\sigma_{\text{chem}}^{\text{Twin}}$ and $\sigma_{\text{misfit}}^{\text{Twin}}$, it clearly shows that $\sigma_{\text{misfit}}^{\text{Twin}}$ is remarkably larger than $\sigma_{\text{chem}}^{\text{Twin}}$. $\sigma_{\text{chem}}^{\text{Twin}}$ strongly correlate with phase stability and $\sigma_{\text{misfit}}^{\text{Twin}}$ contains important information on strain energy. It indicates that, in metastable system, focusing on phase stability only have limited ability to predict twinning mode competition and twinning nucleation behaviors. Instead, strain energy can play critical roles on twin competition.

The preference for {332} twinning in Ti–Mo systems can be understood from the competition between chemical and elastic contributions. The relatively low transformation barrier in these alloys promotes reversible $\beta \leftrightarrow \alpha''$ transformation, which facilitates twin nucleation, while the misfit strain energy associated with {332} twins is lower than that of {112} twins due to more favorable lattice correspondence and reduced elastic incompatibility. As a result, {332} twinning becomes the dominant deformation mode. However, despite this favorable nucleation condition, the overall stress level remains relatively high, indicating that Ti–Mo alloys can simultaneously favor {332} twinning and maintain a high yield strength. This combination arises because the nucleation barrier, while lower for {332} compared to {112}, is still significant in absolute magnitude due to the contribution of transformation energetics.

Importantly, when compared with Ti–Nb systems, a fundamentally different behavior is expected. Ti–Nb alloys are characterized by higher reversibility of the $\beta \leftrightarrow \alpha''$ transformation and lower effective nucleation barriers, which promotes TRIP-dominated deformation and superelasticity. In such systems, the critical stress for transformation and twinning is significantly reduced, leading to lower macroscopic yield stress. Therefore, while Ti–Mo alloys favor {332} twinning at relatively high stress levels, Ti–Nb alloys exhibit enhanced transformation plasticity and superelastic behavior due to their lower energetic barriers and higher phase stability tunability.

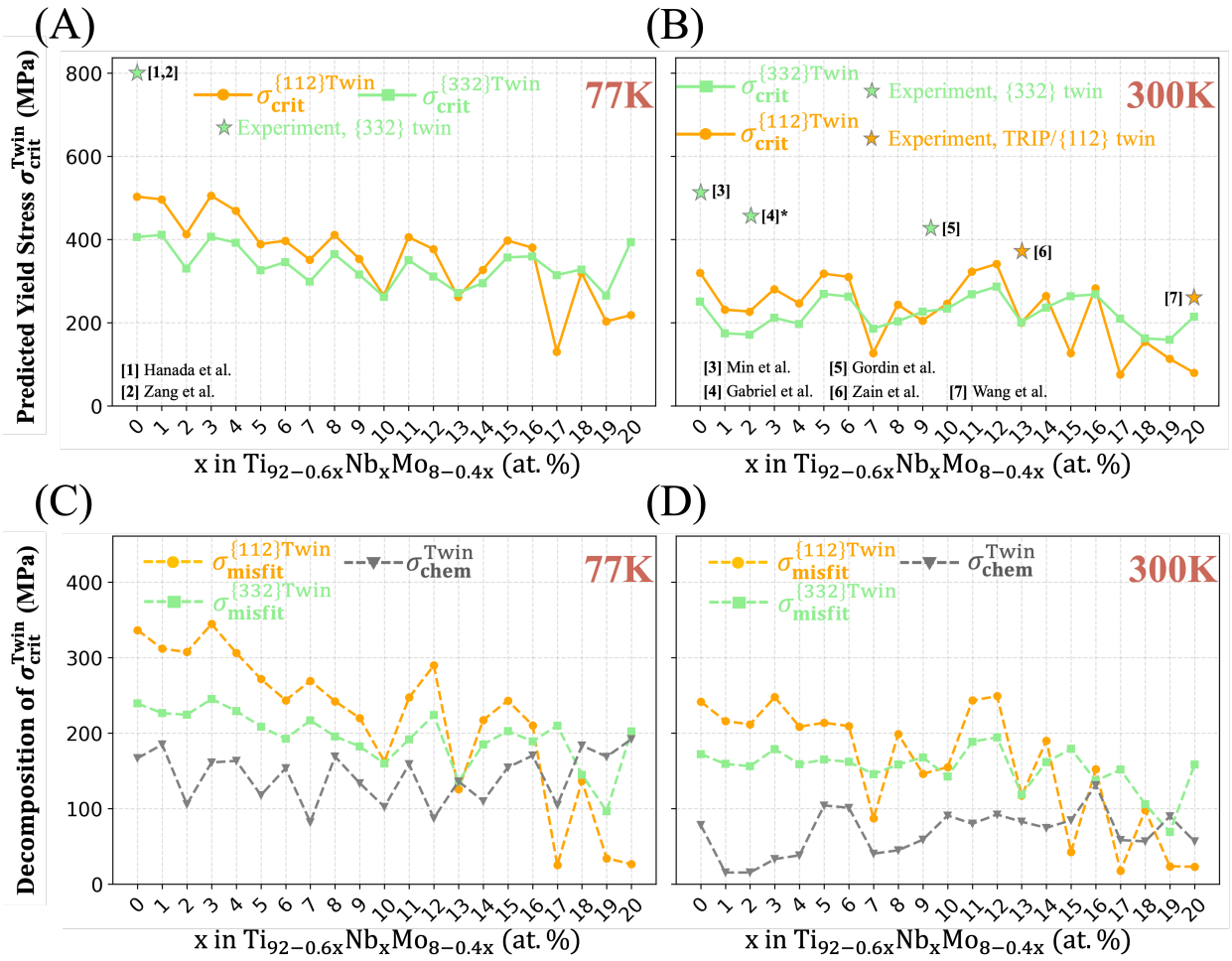


Figure 5.3: **Comparison of critical stress for {112} and {332} twinning modes as a function of Nb concentration at 77 K and 300 K for $Ti_{92-0.6x}$-$Mo_{8-0.4x}$-Nb_x alloy system.**Figure 5.3 (A) and (B) shows the predict critical stress for {112} and {332} twinning modes. Orange solid line with circle markers represent $\sigma_{\text{crit}}^{\{112\}\text{Twin}}$ while green solid line with square markers represent $\sigma_{\text{crit}}^{\{332\}\text{Twin}}$. Star markers represent experimental measured yield strength. Dominant twinning mode for green star markers are {332} twin while dominant twinning mode for orange star markers are {112} twin (mix with TRIP). Figure 5.3 (C) and (D) show the decomposition of $\sigma_{\text{crit}}^{\text{Twin}}$. Orange dashed line with circle markers represent $\sigma_{\text{misfit}}^{\{112\}\text{Twin}}$ while green dashed line with square markers represent $\sigma_{\text{misfit}}^{\{332\}\text{Twin}}$. Gray solid line with triangle markers represent $\sigma_{\text{chem}}^{\text{Twin}}$. Nb concentration uniquely defines the alloy composition (with Mo varying linearly and therefore not shown explicitly). [101, 77, 234, 141, 208, 224, 83, 141, 70, 1]

Overall, these results highlight that the proposed nucleation-based metric not only captures the selection between {112} and {332} twinning modes, but also provides a quantitative link between atomistic energetics and macroscopic mechanical response, enabling predictive understanding of deformation mechanisms across different alloy systems.

5.4 Discussion

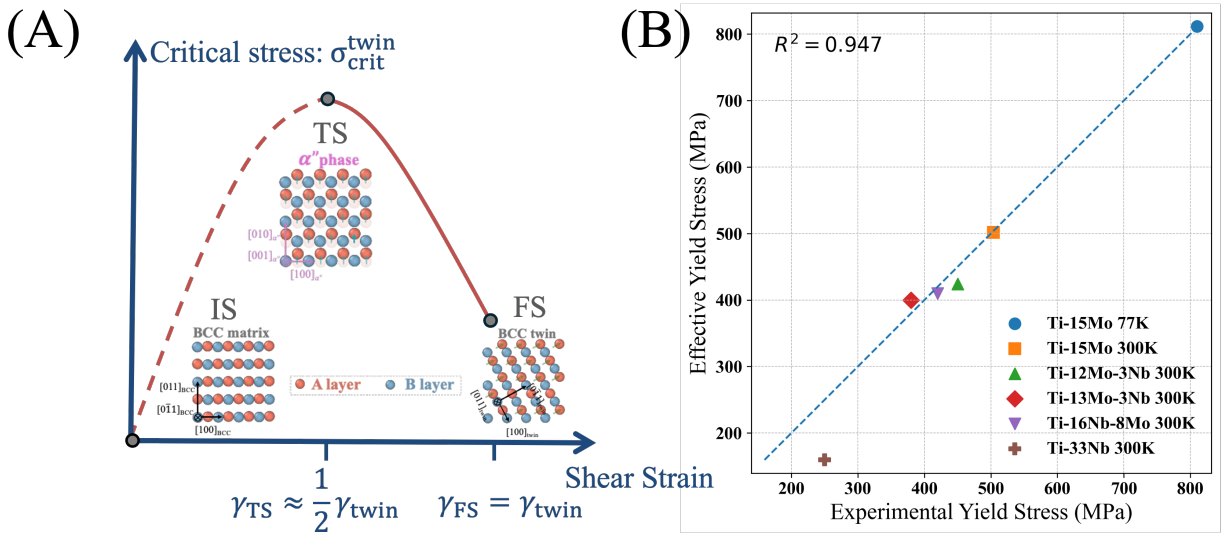


Figure 5.4: **Schematic framework and validation of the twin nucleation-based yield stress model for TWIP dominant metastable β Ti alloys. The model modified the Equation 5.4 and introduces an effective twinning strain to link the twin nucleation barrier with a measurable stress scale.**(A) is a schematic illustration of the twin nucleation pathway in terms of critical stress as a function of shear strain. The process evolves from the initial state (IS, β matrix) to the final state (FS, β twin) through a transition state (TS, α" phase). Before TS, α" phase have not formed, essential step for twin nucleation is not satisfied and so it is dashed line. Twin can form only after TS. The effective shear strain at the transition state is approximated as $\gamma_{TS} \approx \frac{1}{2}\gamma_{twin}$, while $\gamma_{FS} = \gamma_{twin}$, defined in Equation 5.4. (B) is comparison between the calculated effective yield stress obtained from twinning nucleation model and the experimental yield stress for metastable Ti-based alloys. The high coefficient of determination ($R^2 = 0.947$) indicates strong agreement. [101, 77, 234, 141, 208, 224, 83, 141, 70, 1]

To establish a direct connection between the nucleation metric and experimentally measurable mechanical properties, we further extend our theoretical framework and introduce a

stress parameter, $\sigma_{\text{yield}}^{\text{twin}}$, to predict the yield strength of metastable Ti–Nb–Mo alloys. This nucleation-controlled yield stress enables quantitative prediction of both the magnitude of yield strength and the selection of twinning modes as functions of temperature and composition, showing good agreement with available experimental observations. These results highlight the robustness of the proposed framework. Within the metastable regime, our analysis reveals a clear separation of thermodynamic roles: temperature predominantly influences the chemical free energy associated with phase transformation, whereas composition primarily governs the misfit strain energy. The competition between twinning modes is primarily governed by the misfit strain energy, which exhibits weak temperature dependence. This characteristic enables reliable prediction of twinning behavior using 0 K calculations, highlighting the potential for high-throughput screening across a broad compositional space.

So far, the theoretical predicted $\sigma_{\text{yield}}^{\text{twin}}$ is totally free of any fitting parameter and any experimental corrections. When it comes to the comparison of experimental yield strength and $\sigma_{\text{yield}}^{\text{twin}}$ (equals to $\min\left\{\sigma_{\text{crit}}^{\{332\}\text{Twin}},\ \sigma_{\text{crit}}^{\{112\}\text{Twin}}\right\}$), experimental yield strength is around two times of $\sigma_{\text{yield}}^{\text{twin}}$. This is because the overestimation of twinning shear. As shown in Figure 5.4(A), the twinning shear γ_{twin} calculated by crystallography theory [189] is the shear strain required from initial state (IS, β matrix) to final state (FS, β twin). However, the chemical free energy and misfit strain energy for twin nucleation is at the transition state (TS), the corresponding shear strain should be smaller than $\gamma_{\text{FS}} = \gamma_{\text{twin}}$. A reasonable assumption is shear strain at transition state $\gamma_{\text{TS}} \approx \frac{1}{2}\gamma_{\text{twin}}$. We then substitute γ_{TS} for γ_{twin} in Equation 5.4 -5.6, and further define the effective yield stress:

$$\sigma_{\text{yield}}^{\text{twin}*} = 2 \times \sigma_{\text{yield}}^{\text{twin}} \tag{5.9}$$

We then compare the calculated effective twinning yield stress, $\sigma_{\text{yield}}^{\text{twin}*}$, with experimentally measured yield stresses, as shown in Figure 5.4(B). Overall, a strong quantitative correlation ($R^2 = 0.947$) is obtained between theory and experiment, demonstrating that the proposed

nucleation-based framework captures the trend of composition- and temperature-dependent yield strength across metastable Ti alloys. Among all data points, the largest deviation occurs for Ti-33Nb wt.% (Ti-20Nb at.%) at 300 K, where the model underestimates the experimental yield stress. This discrepancy likely arises because deformation in this alloy is dominated by stress-induced α'' martensitic transformation accompanied by α'' variant reorientation and localized transformation banding, mechanisms frequently observed in TRIP-dominated Ti alloys but not explicitly incorporated in the present twinning-based framework [208]. Despite this physically explainable deviation, the strong correlation between predicted and measured strengths across diverse compositions and temperatures highlights the robustness of the model and suggests its potential for extension to broader compositional and temperature spaces through high-throughput screening.

Despite the strengths of the theoretical framework discussed above, one important limitation is that the proposed twin nucleation metric does not explicitly account for interfacial energy. This simplification is adopted to enable efficient evaluation over a wide compositional space, as incorporating interfacial contributions would require detailed knowledge of interface structure and morphology, significantly increasing computational cost and reducing the feasibility of high-throughput screening. However, this approximation introduces inherent limitations. In realistic systems, interfacial energy is not a constant but depends on the morphology of the twin embryo, including its shape, size, orientation, and crystallographic character. Unlike the spherical nuclei assumed in classical nucleation theory, twin embryos in metastable Ti alloys typically exhibit plate-, wedge-, or needle-like geometries, which arise from the minimization of total free energy under mechanical constraints [127, 99, 118, 119, 223, 221, 123].Furthermore, the presence of spontaneous phase transformation behavior at twin boundaries in metastable Ti alloys [37, 39, 113] suggests that the interfacial structure can be significantly more complex than that of conventional twin boundaries, further complicating the determination of interfacial energy. Although interfacial energy is generally smaller in magnitude than the volumetric contributions from chemical

free energy and misfit strain energy, its variation with interface structure and morphology may still influence the relative nucleation barriers of competing twinning modes, particularly when the differences in bulk energetics are small. Therefore, while neglecting interfacial energy enables an efficient and scalable framework, a more rigorous treatment of twin nucleation should incorporate orientation-dependent interfacial energy and realistic embryo geometries. It is worth investigating a unified method to estimate interfacial energy of twin boundaries in metastable Ti alloys.

Another limitation of the current framework is the lack of information on dynamic growth behaviors. In particular, within the TWIP regime, the final volume fraction of twins in the material, which correlates with their contribution to plasticity, is highly dependent on twin growth behavior. For the {112} twin in metastable Ti alloys, the growth behavior is closely related to the stability of the ω phase [39], and the growth kinetics can be tuned by controlling the reversibility between the β and ω phases. In contrast, {112} twin nucleation and growth in stable BCC materials do not necessarily require phase transformations and can instead be triggered by successive slip on {112} planes [123]. Since our focus is on the metastable region, we do not consider this successive slip mechanism here, particularly because dislocation slip is the dominant carrier of plastic deformation compared to {112} twinning in stable BCC materials. For the {332} twin in metastable Ti alloys, α'' phase is often observed along twin boundaries [113, 38] (including in this study), suggesting twin growth via reversible β–α'' phase transformation. However, the atomistic motion of twin boundaries during growth remains under debate and does not strictly follow the Burgers path [189, 110]. To fully evaluate the growth kinetics of {332} twins, detailed investigations of atomic motions at twin boundaries are still required in future studies.

As for prediction on yield stress via twin nucleation metric, the present framework is that provides an estimate of the "intrinsic" yield stress, therefore reflects an idealized material response that is independent of prior processing history. In practical materials, however, the measured yield strength is strongly influenced by extrinsic factors such as heat treat-

ment [6], pre-strain [142], and thermomechanical processing (e.g., cold rolling) ([222]). These processes modify the microstructural state by introducing defects, residual stresses, and heterogeneous nucleation sites, including dislocations, grain boundaries, and phase interfaces [5]. Such features can significantly alter the effective nucleation barrier and activation pathway of deformation mechanisms, thereby shifting the observed yield stress away from the intrinsic value predicted by the current model. Moreover, mechanical pre-conditioning can either promote or suppress specific deformation modes by changing the local stress state and defect density, further complicating the relationship between intrinsic energetics and macroscopic response. As a result, while the present framework is well suited for capturing fundamental trends associated with composition and temperature, it does not explicitly account for microstructure-dependent strengthening mechanisms.Incorporating the effects of microstructural heterogeneity and processing history—such as defect-assisted nucleation and strain hardening—would be necessary to extend the model toward more quantitative prediction of experimentally measured yield strength.

5.5 Conclusion

Here, we summarize the key findings and conclusions from the atomistic simulations conducted and theories proposed in this study:

We further incorporate proposed twin nucleation metric (Δg^*_{twin}) into classical nucleation theory, and to evaluate yield strength for metastable Ti-Nb-Mo ternary alloys. The predicted yield strength have good agreement with experimental data, especially the trend on temperature and composition dependence for yields strength. Within the metastable region, fine tuning elemental fraction in Ti-Nb-Mo can efficiently change the twinning mode preference by affecting misfit strain energy for twin nucleation; temperature optimization can effectively changing the overall yield strength by changing the chemical free energy contribution. Free of simulating complex deformation behaviors with accurate interatomic or machine learning potential, this yield strength prediction framework can be efficiently extendable to other

metastable Ti alloys systems for new Ti alloy design.

CHAPTER 6

Summary

6.1 Remark

The previous four chapters presented the main studies in this thesis. As shown in Figure 6.1, the left part of the flow chart summarizes the key topics of the research across chapters, while the right part situates these studies within a broader materials design workflow.

6.1.1 Bridging Fundamental Mechanisms and Alloy Design

As for fundamental understanding on structural evolution of twinning, though crystallography theories previous predict reversible phase transformations-mediated twinning pathways and experimental studies show the complex atomic structure early-stage stable twin embryos, there is a gap between these two parts. This thesis fills this gap. Simulations conducted in this thesis present the dynamic nucleation (Chapter 4) and growth kinetic of {112} twin and {332} twin (Chapter 2-3) from scratch. The dynamic structural evolutions consistent with crystallography prediction while final twin embryo morphologies are consistent with experimental observation.

As for materials design strategies, current alloy design strategies for metastable β-Ti alloy design, both in industry and academia, remain largely confined to establishing composition–deformation modes connections. There is no guidance on how to tune temperature and loading conditions to optimize the deformation modes selection in materials. Meanwhile,

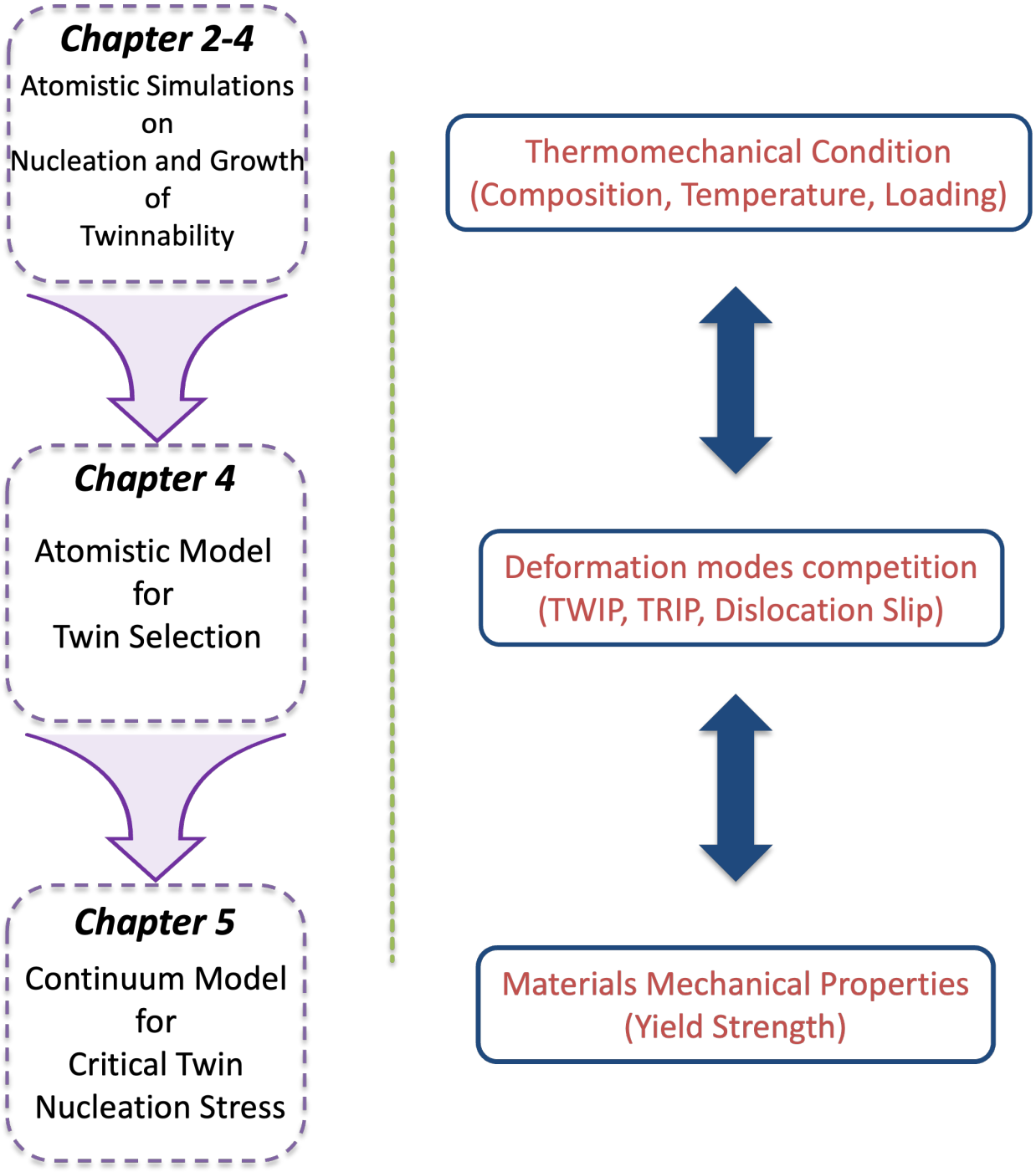


Figure 6.1: Illustrations on overall summary of this thesis. Left part is the main contents for the thesis. Right part is the overall objectives. In brief, it is to make quantitative connections between thermomechanical conditions-deformation modes-mechanical properties.

there is no general quantitative approaches that connect dominant deformation modes and mechanical properties. In this thesis, we shed light on the quantitative relationship between **thermodynamic conditions–deformation mode selection–macroscopic critical twin nucleation stress** (Chapter 5) (strong correlate to yield strength for TWIP Ti alloys).

6.1.2 Toward Physics-Based Alloy Design

A persistent and practically important puzzle in metastable β-Ti alloy design is the characteristically **low yield strength** and **limited strain-hardening capacity** of TWIP-active compositions. Ti alloys exhibiting the TWIP effect frequently show yield strengths in the range of 200–500 MPa, substantially below those of slip-dominated or precipitation-strengthened β-Ti alloys (500–1000 MPa). The framework developed in this thesis offers a mechanistic and quantitative explanation for this observation.

Yield strength is governed by the nucleation stress of the dominant deformation mode, which in TWIP-active compositions is twin nucleation. Following the twin nucleation metric established in Chapter 4, the critical nucleation barrier Δg^*_{twin} receives contributions from two energetic terms: the chemical free energy barrier $\Delta g_{\beta\to\alpha''}$ for the homogeneous $\beta \leftrightarrow \alpha''$ transformation, and the misfit strain energy Δg_{misfit} accumulated along specific β/α'' phase boundaries. In the TWIP regime, both contributions are intrinsically limited. The metastable nature of the β phase places these alloys close to the thermodynamic boundary of α'' stability, where the chemical free energy difference between the parent and product phases is small by definition, so $\Delta g_{\beta\to\alpha''}$ is necessarily low and provides only a modest resistance to twin nucleation. The misfit strain energy term, while quantitatively larger than the chemical contribution, is similarly bounded: because both the β and α'' phases are structurally closely related and so the lattice parameter mismatch across the β/α'' habit planes is inherently modest, and Δg_{misfit} cannot grow arbitrarily large without destabilizing the transformation pathway entirely. Consequently, Δg^*_{twin} is structurally self-limited in

metastable β-Ti alloys: the very thermodynamic proximity to α'' that activates twinning as a deformation mechanism simultaneously caps the nucleation barrier and, through the CNT-based yield strength model of Chapter 5, caps the resulting yield strength. This provides a physically transparent explanation for why TWIP-active β-Ti alloys are in low yield strength region.

Nevertheless, following this thesis, two possible strategies are potentially increase the yield strength for TWIP Ti alloys. The first strategy operates through the chemical free energy barrier $\Delta g_{\beta\to\alpha''}$. Since this quantity reflects the thermodynamic driving force for the $\beta \to \alpha''$ transformation, it can be raised by shifting the alloy composition toward the stable side of the metastable β region — increasing β-stabilizer content moves the alloy away from the α'' stability boundary, enlarging $\Delta g_{\beta\to\alpha''}$ and raising the chemical resistance to twin nucleation. Equivalently, operating at elevated temperatures reduces the thermodynamic driving force for the transformation, providing a thermal handle on the same quantity. However, this strategy carries an inherent trade-off: pushing too far into the stable β region eventually suppresses twinning entirely and transitions the dominant deformation mode to dislocation slip, exiting the TWIP regime altogether.

The second and more efficient strategy operates through the misfit strain energy Δg_{misfit}. Unlike the chemical free energy term, which is set primarily by composition and temperature, Δg_{misfit} retains an additional degree of freedom through the mechanical loading condition: the applied stress state determines which β/α'' habit planes are mechanically activated and therefore which components of the misfit strain tensor are penalized. This opens two distinct levers. First, loading conditions can be tailored to suppress α'' nucleation along low-misfit habit planes, effectively delaying twin nucleation to higher applied stresses and raising the apparent yield strength without altering the alloy composition. A similar idea is performed by Gao et.al. [71] Second, alloying additions that asymmetrically modify the β and α'' lattice parameters can selectively increase Δg_{misfit} along active habit planes (both $\{112\}$ twin and $\{332\}$ twin), imposing a larger strain energy penalty on twin nucleation and raising the yield

strength while preserving the TWIP deformation mode. Because Δg_{misfit} is quantitatively the dominant contribution to $\Delta g^{*}_{\text{twin}}$ across the metastable compositions studied in this thesis, this second strategy offers a more direct and compositionally efficient route to yield strength improvement than chemical free energy tuning alone.

Limited strain-hardening capacity is another fundamental constraint of metastable TWIP β-Ti alloys, and the atomistic studies presented in Chapter 2 and Chapter 3 shed light on its mechanistic origins, even though a fully quantitative strain-hardening model is lack in the present thesis.

The two dominant twinning systems in metastable β-Ti alloys contribute to strain hardening through fundamentally different pathways. As demonstrated in Chapter 2, $\{112\}\langle 111\rangle$ twins are inherently unstable upon growth: the ω phase, which mediates the $\{112\}$ twinning pathway, simultaneously destabilizes the growing twin embryo and arrests its thickening. As a consequence, $\{112\}$ twins remain thin and carry limited external strain, contributing relatively little to the progressive grain subdivision that underpins the dynamic Hall–Petch effect. On the other hand, Chapter 3 reveals that $\{332\}\langle 113\rangle$ twins grow readily and exhibit low sensitivity to alloy composition. The α''-mediated $\{332\}$ pathway has a shallow energy landscape that permits facile twin propagation across a wide range of metastable compositions. While this growth facility makes $\{332\}$ twins the dominant carrier of plastic strain in most TWIP β-Ti alloys, it is precisely this ease of growth that limits their strain-hardening contribution: coarse, rapidly growing $\{332\}$ twins saturate in number early in deformation, leaving insufficient twin boundary area per unit volume to sustain effective dislocation storage and Hall–Petch grain subdivision at higher strains. Compounding both effects, the concurrent stress-induced α'' martensite provides an additional strain accommodation mechanism that further dilutes the strain-hardening response by relieving local stress concentrations that would otherwise drive dislocation accumulation.

Two strategies emerge from this mechanistic picture to overcome these limitations. From a materials design perspective, interstitial oxygen additions represent a particularly promis-

ing route: oxygen segregates preferentially to {332} twin boundaries, pinning twin migration and restricting twin thickening, thereby promoting more extensive twin nucleation over twin growth. The resulting finer twin spacing reduces the dislocation mean free path more efficiently, sustaining the dynamic Hall–Petch effect to higher strains. Simultaneously, a strong {332} texture in the β matrix limits the mean free path available for {332} twin propagation, further constraining twin growth and enhancing boundary density. From a mechanical loading perspective, tailoring the stress state to reduce the Schmid factor for $\{332\}\langle 113\rangle$ while simultaneously favoring $\{112\}\langle 111\rangle$ activation would slow down the $\{332\}\langle 113\rangle$ twin thickening and so enhance the strain-hardening effect. Although {112} twins individually carry less strain, their higher boundary density per unit volume and stronger resistance to thickening make them more effective dislocation barriers, potentially delivering a higher and more sustained strain-hardening rate than {332}-dominated deformation.

6.2 Conclusion

Metastable β-Ti alloys offer an exceptional combination of mechanical properties through the interplay of stress-induced martensitic transformation and deformation twinning, yet the atomistic mechanisms governing this interplay have remained poorly understood, limiting the rational design of these alloys. This thesis addressed these questions through computation simulation and theoretical modeling, combining thermodynamic and kinetics, to develop a mechanistic and predictive understanding of twinning and transformation in metastable β-Ti alloys from the atomic scale to macroscopic mechanical response.

Chapter 2 investigated the stability and growth of $\{112\}\langle 11\bar{1}\rangle$ twins in metastable β-Ti alloys. The key finding is that the twin boundary structure and growth kinetics are intimately coupled to the relative thermodynamic stability between the ω and β phases. The ω phase forms spontaneously as a transitional interfacial layer at the {112} twin boundary. This establishes that {112} twin growth in metastable β-Ti alloys is not a pure-shear process but is inherently coupled to the local phase transformation behavior at the boundary.

Chapter 3 extended this investigation to the $\{332\}\langle 11\bar{3}\rangle$ twinning mode, which is unique to metastable β-Ti alloys and absent in conventional stable BCC metals. Systematic MD simulations of twin embryo stability and bicrystal boundary migration across Ti-Nb and Ti-Mo compositions revealed that the twin boundary migration stress is primarily controlled by temperature through thermally activated atomic shuffles, with composition playing a secondary role. Atomic displacement analysis uncovered a composition-dependent switch in growth mechanism: metastable alloys grow via a $\beta \rightarrow \alpha$" $\rightarrow \beta$ transformation pathway, while more stable alloys follow the minimum-shuffle path. Critically, neither embryo survival nor boundary migration was found to be prohibitively difficult in the stable composition range where $\{332\}$ twinning is absent experimentally, pointing to early-stage nucleation and propagation as the rate-determining step for $\{332\}$ twin formation.

Chapter 4 develop a theoretical model for assessing deformation mode competition in metastable β-Ti alloys. The model captures the competition among dislocation slip, stress-induced $\beta \rightarrow \alpha''$ transformation, and $\{332\}$ deformation twinning through a Boltzmann-factor-based nucleation metric that incorporates the chemical driving force, the misfit strain energy, and the twin boundary energy as its physical inputs. Despite its relative simplicity, the model successfully rationalizes the complex composition- and temperature-dependent transitions between TRIP- and TWIP-dominated regimes observed experimentally across multiple alloy systems. It provides a clear and interpretable physical picture of the competing energetic contributions that govern mode selection, without recourse to empirical fitting parameters.

Chapter 5 extended the nucleation framework into a generalized yield strength prediction model for metastable β-Ti alloys. By incorporating the misfit strain energy, the chemical free energy barrier into a unified analytical expression, the model predicts the yield stress as a function of alloy composition and temperature with no fitting parameters. All inputs are either experimentally measurable or directly computable from DFT calculations. The model shows good quantitative agreement with experimental yield strength data across a range of

Ti-Nb, Ti-Mo and Ti-Nb-Mo alloy compositions, and correctly captures the non-monotonic composition dependence and the temperature sensitivity of yielding that characterize TRIP- and TWIP-active alloys. The clarity of the physical picture, the absence of adjustable parameters, and the accessibility of the inputs suggest that this framework could serve as a practical tool for alloy design.

Overall, the findings of this thesis establish a coherent multi-scale understanding of metastability-driven deformation in β-Ti alloys, from the atomic-scale structure and dynamics of twin boundaries to macroscopic yield behavior. The central message is that the exceptional mechanical properties of metastable β-Ti alloys are ultimately governed by the thermodynamic and kinetics of phase transformation at the earliest stages of twin nucleation – a regime that is accessible to atomistic computation and amenable to physical modeling, and that offers a principled basis for the rational design of alloys in which twinning, transformation, and slip are deliberately orchestrated to achieve targeted mechanical performance.

6.3 Future Work

Building upon the key findings of this thesis and motivated by the long-term goal of enhancing the yield strength and strain hardening rate of metastable β-Ti alloys, several promising directions for future theoretical and computational work are identified below:

- **Quantitative framework for transformation-mediated twin growth.** This thesis reveals a close correlation between twin boundary migration and phase transformation behaviour at both {112} and {332} twin boundaries. However, no quantitative theoretical framework currently exists to predict the twin growth stress from the underlying interfacial phase thermodynamics. Developing such a framework – one that connects the interfacial phase character, its transformation driving force, and the resulting boundary mobility to the macroscopic twin growth stress and strain hardening capacity. Furthermore, since the interfacial phase at a twin boundary is a special case

of a grain boundary phase, the theoretical framework developed here is directly transferable to the broader problem of grain boundary complexion transitions in other alloy systems, offering a physically grounded approach to understanding how grain boundary phases (complexity) govern microstructure evolution and mechanical properties beyond the β-Ti context.

- **Critical Boltzmann factor for TRIP–TWIP transition.** The twin nucleation metric proposed in this thesis employs a Boltzmann factor to qualitatively distinguish TRIP- and TWIP-dominated deformation regimes. While this provides a physically motivated criterion for mode selection, the critical value of this factor that marks the boundary between TRIP and TWIP behavior remains quantitatively undefined. Systematic experimental validation across a wider range of compositions and temperatures, combined with higher-fidelity free energy calculations, would allow this threshold to be calibrated quantitatively, transforming the current qualitative indicator into a predictive design criterion.

- **Efficient evaluation of the chemical free energy barrier.** The current nucleation metric incorporates a chemical free energy term evaluated through metadynamics simulations, which, while physically rigorous, remains computationally expensive and not straightforwardly scalable to high-throughput screening. Developing a more efficient approach to evaluate the transformation free energy barrier – for example through CALPHAD-informed Landau models, machine-learning-accelerated free energy perturbation methods, or analytical approximations calibrated against metadynamics results – would substantially reduce the computational cost without sacrificing the physical fidelity of the nucleation model.

- **Phase-field /Constitutive modelling of microstructure evolution.** To understand and investigate how texture and loading condition change the twin evolution and corresponding yield strength the strain hardening effect. The twin bound-

ary energies, migration kinetics, and nucleation metrics derived in this thesis constitute a physically rigorous and directly usable set of inputs for phase-field modelling of dynamic microstructure evolution in metastable β-Ti alloys under different loading conditions. Coupling the present atomistic framework to a multi-order-parameter phase-field model would enable the simulation of TRIP- and TWIP-active microstructure evolution – including variant selection, domain coarsening, and the feedback between transformation strain and subsequent deformation – under realistic thermomechanical processing conditions, at length and time scales inaccessible to MD.Specifically,$\Delta g^{*}_{\text{twin}} = |\Delta F^{A}_{\beta\leftrightarrow\alpha''}| + W^{\text{misfit}}_{\text{twin}}$ proposed in Chapter 4 can be incorporated into a multi-order-parameter phase-field total free energy functional of the form:

$$F_{\text{tot}} = F_{\text{chem}} + F_{\text{int}} + F_{\text{elas}} + F_{\text{load}} \tag{6.1}$$

where F_{chem} encodes the composition- and temperature-dependent driving force for twin nucleation via $|\Delta F^{A}_{\beta\leftrightarrow\alpha''}|$, F_{int} governs twin boundary energy and migration, which can be obtained via twin boundary energy. F_{elas} captures the elastic misfit strain field arising from twin-matrix incompatibility, which be implemented by $W^{\text{misfit}}_{\text{twin}}$ and F_{load} couples the evolving microstructure to the applied thermomechanical loading condition. In this way, we bridge the atomistic insights of this thesis to microstructure-level predictions relevant for processing and alloy design.

- **High-throughput screening for new TWIP-active β-Ti alloys.** The results of Chapter 5 demonstrate that the simple predicted twinning nucleation stress have strong correlation to experimental measured yield strength of metastable TWIP Ti alloys across wide temperature and compositions. This opens the possibility of high-throughput screening of multicomponent Ti alloy compositions by universal machine learning potential to identify new TWIP-active systems that combine economical alloying content with high yield strength and sustained strain hardening. Concretely,

the screening criterion proposed here is based on the twin yield strength defined as:

$$\sigma_{\text{yield}}^{\text{twin}} = \min\left\{\sigma_{\text{crit}}^{\{332\}\,\text{twin}},\ \sigma_{\text{crit}}^{\{112\}\,\text{twin}}\right\} \tag{6.2}$$

where $\sigma_{\text{crit}}^{\{332\}\,\text{twin}}$ and $\sigma_{\text{crit}}^{\{112\}\,\text{twin}}$ are the critical nucleation stresses for {332} and {112} twinning, respectively, both of which can be evaluated from the nucleation framework developed in Chapter 5 using universal machine learning potential. A good candidate alloy should satisfy two criteria. First, candidate alloys should exhibit a high $\sigma_{\text{yield}}^{\text{twin}}$, ensuring that the alloy possesses sufficient strength before the onset of twinning-mediated plasticity Second the two critical twin nucleation stresses should be closely matched to ensures that both twinning modes are simultaneously active during deformation. This co-activation not only maximizes the geometric diversity of operative twin systems but also enlarges the microstructural design space. For example, through independent control of twin boundary spacing, twin volume fraction, and the relative activity of each mode — thereby providing greater freedom to optimize and tailor the overall strain hardening rate and the resulting strength–ductility balance beyond what is achievable when a single twinning mode dominates.

- **Extension to other metastable engineering alloy systems.** Metastability engineering is emerging as a broadly applicable alloy design paradigm beyond β-Ti alloys, encompassing metastable high-entropy alloys, medium-entropy alloys, and shape memory systems. However, atomistic studies of deformation kinetics in these systems remain limited, in part because existing machine-learning interatomic potentials are predominantly fitted to ground-state configurations and lack the physical fidelity to describe transition states and intermediate metastable phases along transformation pathways. Capturing the complex free energy landscape of metastable multi-component alloys – including the energy barriers between competing phases, the soft-mode instabilities that precede transformation, and the coupling between transformation and

plasticity – requires interatomic potentials that explicitly include transition states and intermediate structural configurations in their training sets. Developing transferable machine-learning potential fitting frameworks that systematically incorporate these non-equilibrium states, particularly for complex multicomponent alloys, represents one of the most important methodological frontiers for the atomistic study of metastability-driven deformation.

- **Interstitial oxygen effects on TWIP Ti alloys** An extension of the present framework is to systematically investigate how interstitial oxygen affects twin nucleation and growth kinetics in metastable β-Ti alloys, and how these effects propagate to yield strength and strain-hardening capacity. This investigation is still rely on MD technique. However, it is a very challenging but promising direction to develop Oxygen-contained interatomic/machine learning potential for Ti alloys. Developed potential can be employed for metadynamics simulations of the $\beta \leftrightarrow \alpha''$ transformation should be performed as a function of oxygen content, directly quantifying how oxygen modifies the chemical free energy barrier $\Delta g_{\beta\to\alpha''}$. Complementarily, lattice parameter calculations for oxygen-doped β and α'' phases would quantify the change in misfit strain energy Δg_{misfit} along specific habit planes. Both quantities feed directly into the twin nucleation metric $\Delta g^{*}_{\text{twin}}$, from which the oxygen-dependent yield strength can be predicted through the classical nucleation theory framework of Chapter 5. Meanwhile, developed oxygen-contained potential can study twin boundary velocity and pinning force as functions of oxygen segregation energy and coverage. The results can then be further input into a dynamic Hall–Petch model to predict the strain-hardening rate as a function of oxygen content.

Appendix A

General Mathematical Solution for Invariant Plane Strain

A.1 Deformation Gradient and Invariant Plane Condition

A deformation that satisfies the invariant plane strain (IPS) condition requires the existence of a plane whose vectors remain undistorted and unrotated upon transformation. Such a deformation gradient $\mathbf{F}$ takes the general form:

$$\mathbf{F} = \mathbf{I} + \mathbf{d} \otimes \mathbf{n} \tag{A.1}$$

where $\mathbf{n}$ denotes the unit normal to the invariant plane and $\mathbf{d}$ is the displacement (shear) vector. The deformation described by Eq. (A.1) is geometrically equivalent to a simple shear superimposed on the identity, leaving the plane with normal $\mathbf{n}$ macroscopically undistorted.

A.2 Hermitian Form and Eigenvalue Decomposition

To determine the conditions under which a given transformation can be described as an IPS, we construct the symmetric Hermitian form $\mathbf{F}^T\mathbf{F}$:

$$\begin{aligned} \mathbf{F}^T\mathbf{F} &= (\mathbf{I} + \mathbf{d} \otimes \mathbf{n})^T(\mathbf{I} + \mathbf{d} \otimes \mathbf{n}) \\ &= (\mathbf{I} + \mathbf{n} \otimes \mathbf{d})(\mathbf{I} + \mathbf{d} \otimes \mathbf{n}) \\ &= \mathbf{I} + \left(\mathbf{d} + \frac{\mathbf{d} \cdot \mathbf{d}}{2}\,\mathbf{n}\right) \otimes \mathbf{n} + \mathbf{n} \otimes \left(\mathbf{d} + \frac{\mathbf{d} \cdot \mathbf{d}}{2}\,\mathbf{n}\right) \end{aligned} \tag{A.2}$$

Since $\mathbf{F}^T\mathbf{F}$ is a symmetric positive-definite matrix, it admits a spectral decomposition in terms of its eigenvalues η_i^2 and orthonormal eigenvectors $\mathbf{v}_i$:

$$\mathbf{F}^T\mathbf{F} = \eta_1^2\,\mathbf{v}_1 \otimes \mathbf{v}_1 + \eta_2^2\,\mathbf{v}_2 \otimes \mathbf{v}_2 + \eta_3^2\,\mathbf{v}_3 \otimes \mathbf{v}_3 \tag{A.3}$$

A.3 Necessary Condition for IPS

Using the identity $\mathbf{I} = \sum_i \mathbf{v}_i \otimes \mathbf{v}_i$, Eq. (A.3) can be rewritten as:

$$\mathbf{F}^T\mathbf{F} = \mathbf{I} + (\eta_1^2 - 1)\,\mathbf{v}_1 \otimes \mathbf{v}_1 + (\eta_2^2 - 1)\,\mathbf{v}_2 \otimes \mathbf{v}_2 + (\eta_3^2 - 1)\,\mathbf{v}_3 \otimes \mathbf{v}_3 \tag{A.4}$$

Comparing Eq. (A.4) with Eq. (A.2), the rank-two structure of $\mathbf{F}^T\mathbf{F} - \mathbf{I}$ imposes a necessary condition on the eigenvalues. For an IPS to exist, one eigenvalue must equal unity, one must be less than unity, and one must be greater than unity:

$$\eta_1^2 < 1, \qquad \eta_2^2 = 1, \qquad \eta_3^2 > 1 \tag{A.5}$$

Under this condition, Eq. (A.4) reduces to:

$$\mathbf{F}^T\mathbf{F} = \mathbf{I} + \mathbf{P} \otimes \mathbf{n} + \mathbf{n} \otimes \mathbf{P} \tag{A.6}$$

where the two solutions for the invariant plane normal $\mathbf{n}$ and the associated vector $\mathbf{P}$ are:

$$\begin{cases} \mathbf{n}_1 = \sqrt{\dfrac{\eta_3^2 - 1}{\eta_3^2 - \eta_1^2}}\,\mathbf{v}_3 + \sqrt{\dfrac{1 - \eta_1^2}{\eta_3^2 - \eta_1^2}}\,\mathbf{v}_1 \\ \mathbf{P}_1 = \dfrac{1}{2}(\eta_3^2 - \eta_1^2)\left(\sqrt{\dfrac{\eta_3^2 - 1}{\eta_3^2 - \eta_1^2}}\,\mathbf{v}_3 - \sqrt{\dfrac{1 - \eta_1^2}{\eta_3^2 - \eta_1^2}}\,\mathbf{v}_1\right) \end{cases} \tag{A.7}$$

$$\begin{cases} \mathbf{n}_2 = \sqrt{\dfrac{\eta_3^2 - 1}{\eta_3^2 - \eta_1^2}}\,\mathbf{v}_3 - \sqrt{\dfrac{1 - \eta_1^2}{\eta_3^2 - \eta_1^2}}\,\mathbf{v}_1 \\ \mathbf{P}_2 = \dfrac{1}{2}(\eta_3^2 - \eta_1^2)\left(\sqrt{\dfrac{\eta_3^2 - 1}{\eta_3^2 - \eta_1^2}}\,\mathbf{v}_3 + \sqrt{\dfrac{1 - \eta_1^2}{\eta_3^2 - \eta_1^2}}\,\mathbf{v}_1\right) \end{cases} \tag{A.8}$$

yielding two geometrically distinct IPS solutions.

A.4 Recovery of the Shear Vector

Comparing Eqs. (A.7)–(A.8) with Eq. (A.2), the displacement vector $\mathbf{d}$ can be recovered from $\mathbf{P}$ via:

$$\mathbf{d} + \frac{\mathbf{d}\cdot\mathbf{d}}{2}\,\mathbf{n} = \mathbf{P} \tag{A.9}$$

The two explicit solutions are:

$$\mathbf{d}_1 = (\eta_3^2 - \eta_1^2)\left(\eta_1\sqrt{\frac{\eta_3^2 - 1}{\eta_3^2 - \eta_1^2}}\,\mathbf{v}_3 - \eta_3\sqrt{\frac{1 - \eta_1^2}{\eta_3^2 - \eta_1^2}}\,\mathbf{v}_1\right) \tag{A.10}$$

$$\mathbf{d}_2 = (\eta_3^2 - \eta_1^2)\left(\eta_1\sqrt{\frac{\eta_3^2 - 1}{\eta_3^2 - \eta_1^2}}\,\mathbf{v}_3 + \eta_3\sqrt{\frac{1 - \eta_1^2}{\eta_3^2 - \eta_1^2}}\,\mathbf{v}_1\right) \tag{A.11}$$

Note that $\mathbf{n}$ is defined up to a scalar multiple in the derivation above; normalization of $\mathbf{n}$ requires a corresponding rescaling of $\mathbf{d}$, leaving the deformation gradient $\mathbf{F}$ in Eq. (A.1) invariant.

A.5 Rotation Correction and Physical Solutions

Because the derivation above is based on the symmetric form $\mathbf{F}^T\mathbf{F}$ rather than $\mathbf{F}$ itself, the solutions for $\mathbf{d}$ and $\mathbf{n}$ do not directly guarantee satisfaction of Eq. (A.1). Instead, they satisfy the more general condition:

$$\mathbf{R}\,\mathbf{F} = \mathbf{I} + \mathbf{d} \otimes \mathbf{n} \qquad \text{or equivalently} \qquad \mathbf{R}\,\mathbf{F} - \mathbf{I} = \mathbf{d} \otimes \mathbf{n} \tag{A.12}$$

where $\mathbf{Q}$ is a unitary matrix satisfying $\mathbf{R}^T\mathbf{R} = \mathbf{I}$. For the solution to be physically meaningful in continuum mechanics, $\mathbf{Q}$ must be a proper rotation matrix with $\det(\mathbf{R}) = 1$. In three dimensions, Eq. (A.12) involves 8 independent unknowns (3 in $\mathbf{Q}$, 3 in $\mathbf{d}$, and 2 in $\mathbf{n}$ after normalization) subject to 9 constraints, making the system generically over-determined. A physical IPS solution therefore exists only when the eigenvalue condition in Eq. (A.5) is satisfied, which provides the additional degree of freedom necessary for compatibility.

Appendix B

Stability and Growth Kinetics of {112} Twin

B.1 DFT Relaxation

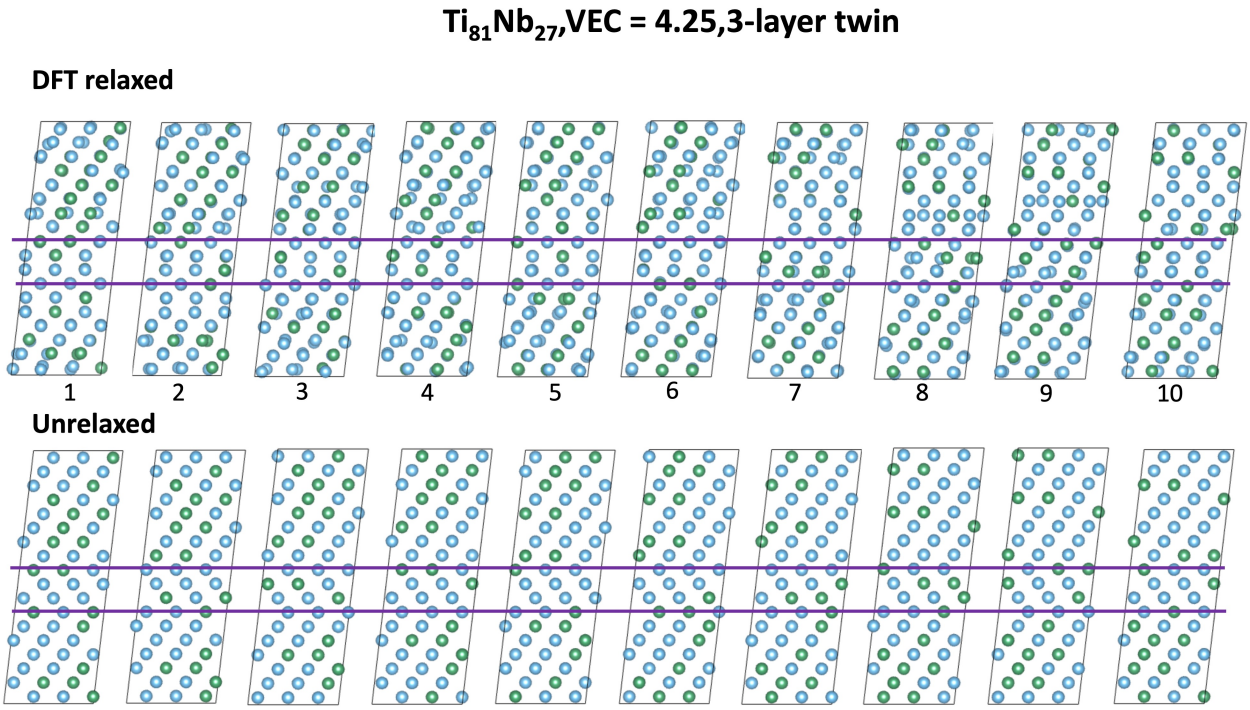


Figure B.1: Snapshots for unrelaxed and DFT fully relaxed atomic structures of 3-layer twin embryo in Ti_3Nb. Blue color is for Ti atoms, green color is for Nb atoms and region between two dark purple lines indicated the initial location of twin boundaries.

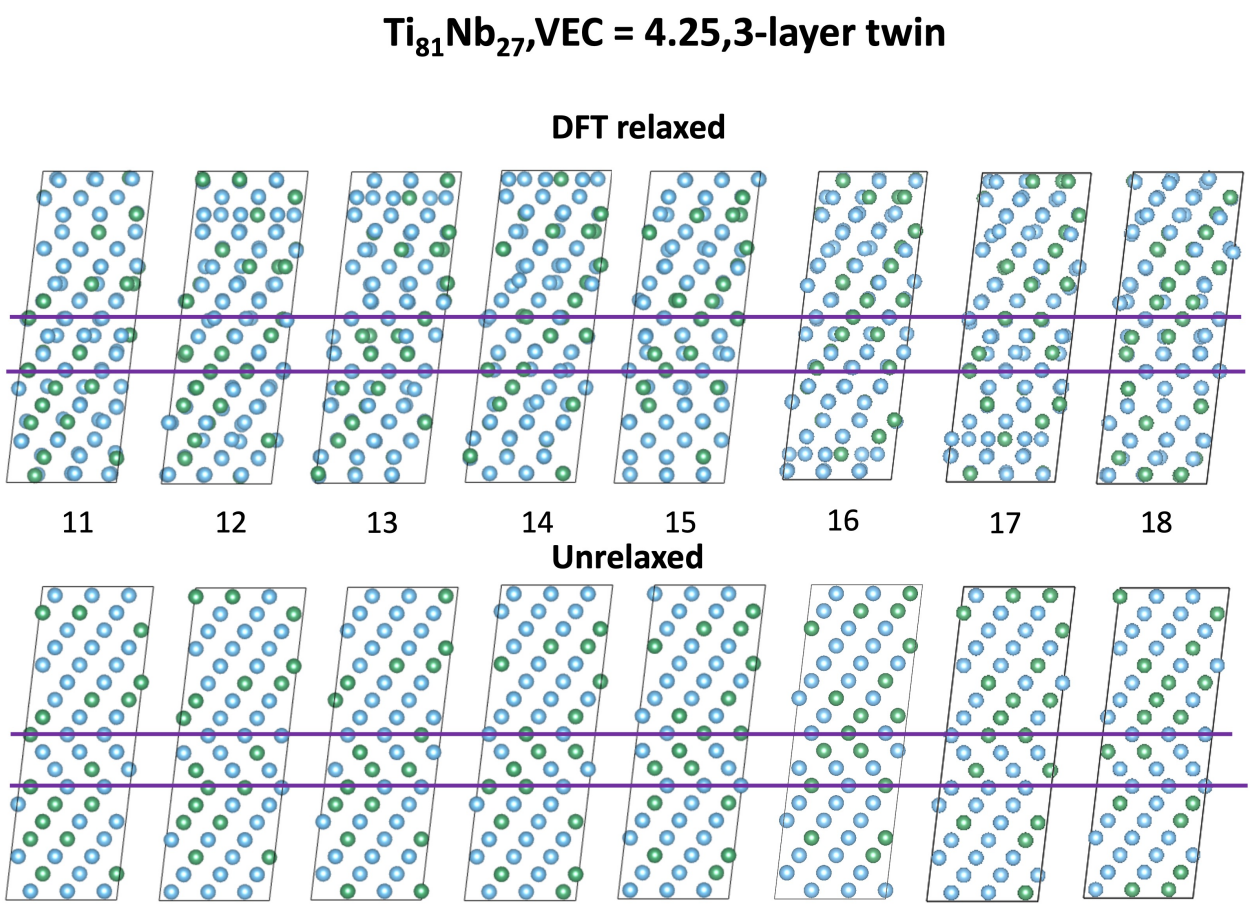


Figure B.2: Snapshots for unrelaxed and DFT fully relaxed atomic structures of 3-layer twin embryo in Ti_3Nb. Blue color is for Ti atoms, green color is for Nb atoms and region between two dark purple lines indicated the initial location of twin boundaries.

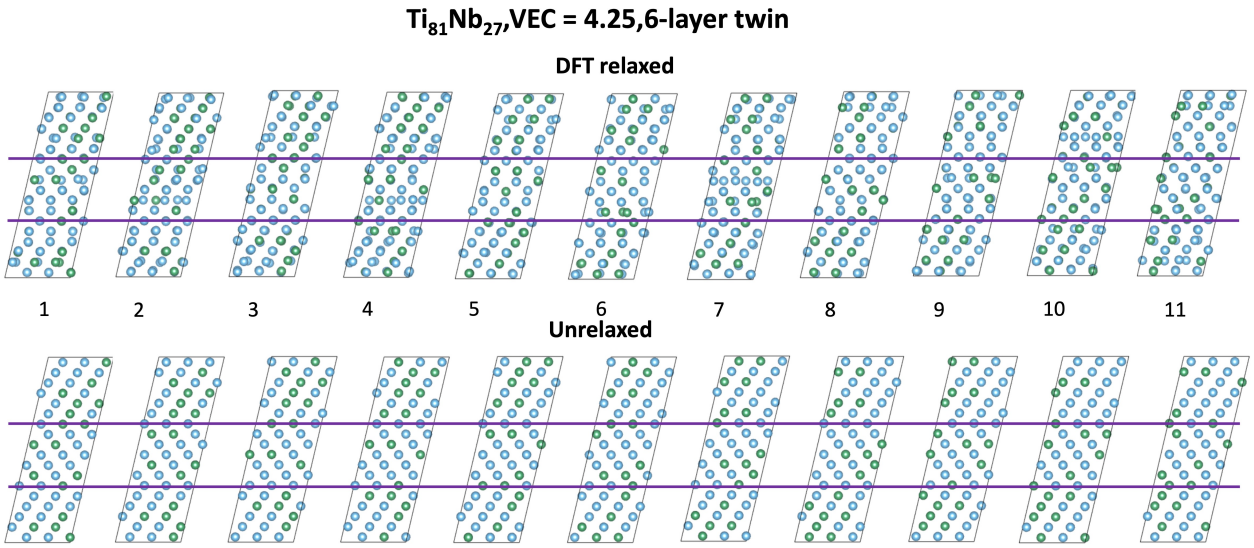


Figure B.3: Snapshots for unrelaxed and DFT fully relaxed atomic structures of 6-layer twin embryo in Ti_3Nb. Blue color is for Ti atoms, green color is for Nb atoms and region between two dark purple lines indicated the initial location of twin boundaries.

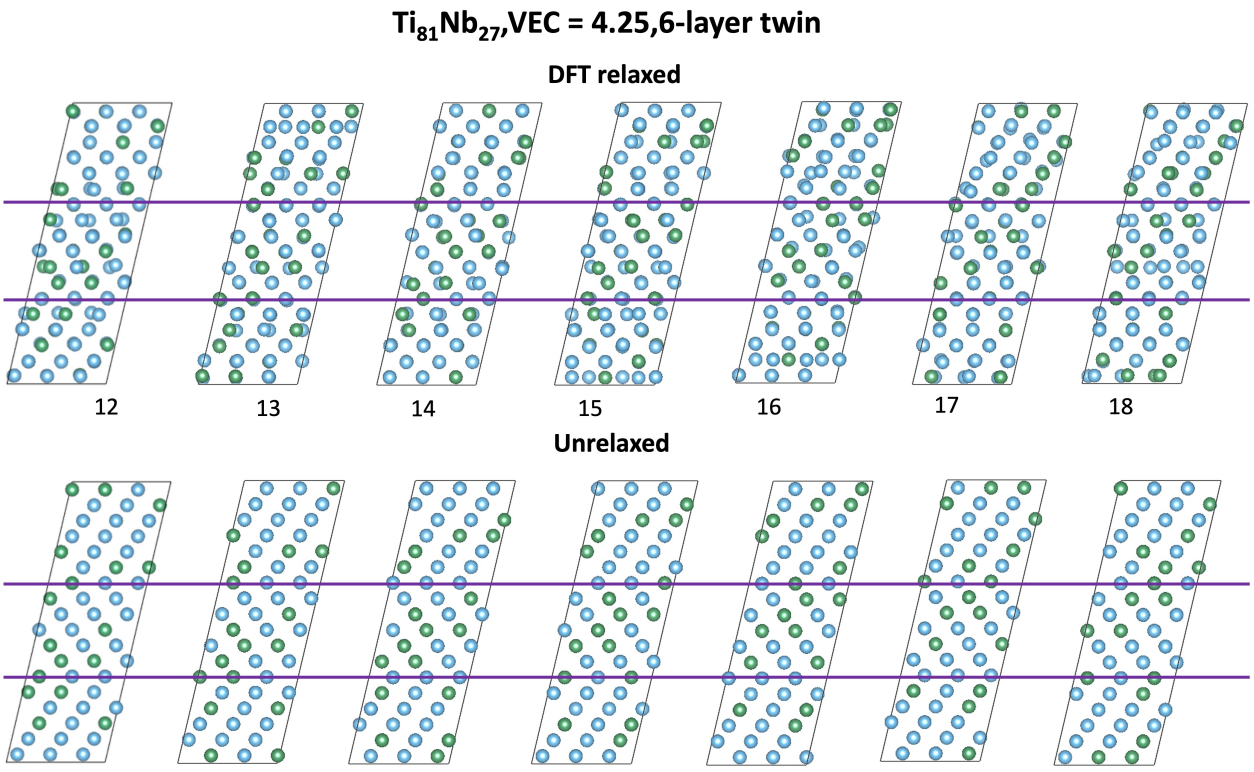


Figure B.4: Snapshots for unrelaxed and DFT fully relaxed atomic structures of 6-layer twin embryo in Ti_3Nb. Blue color is for Ti atoms, green color is for Nb atoms and region between two dark purple lines indicated the initial location of twin boundaries.

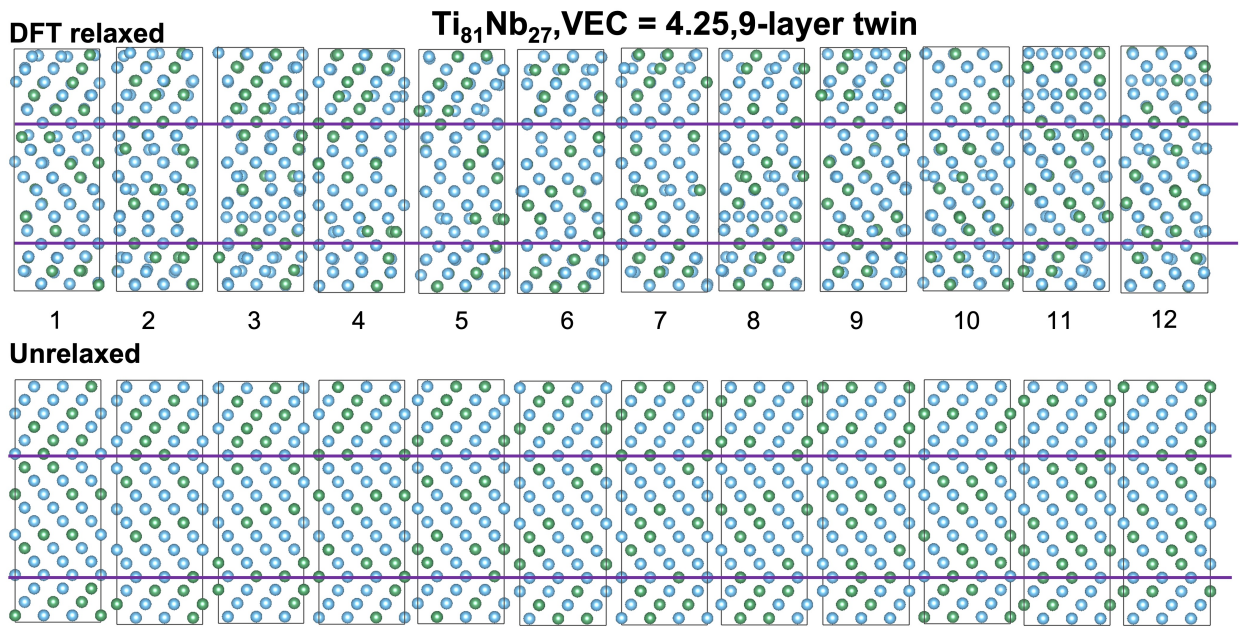


Figure B.5: Snapshots for unrelaxed and DFT fully relaxed atomic structures of 9-layer twin embryo in Ti_3Nb. Blue color is for Ti atoms, green color is for Nb atoms and region between two dark purple lines indicated the initial location of twin boundaries.

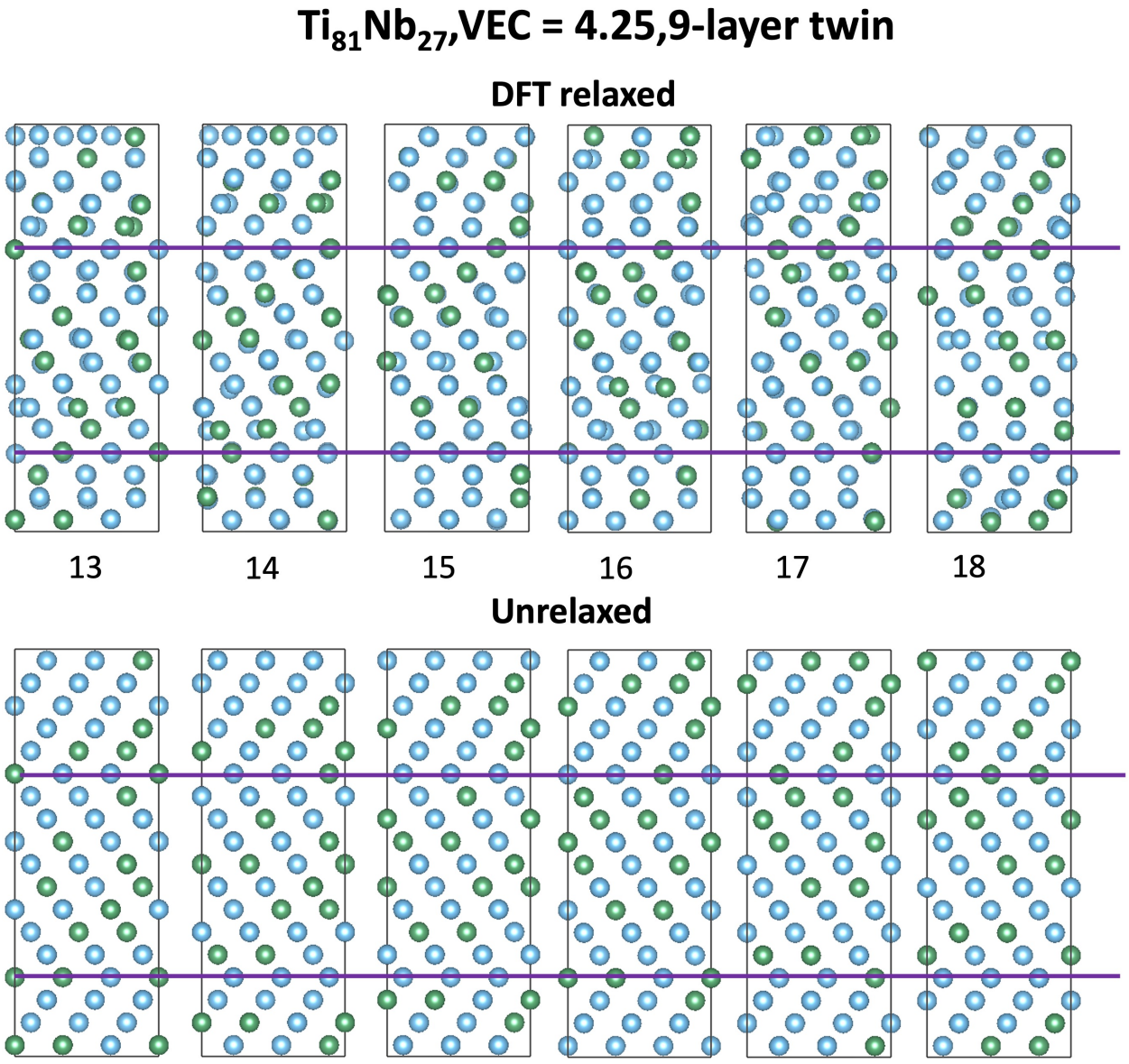


Figure B.6: Snapshots for unrelaxed and DFT fully relaxed atomic structures of 9-layer twin embryo in Ti_3Nb. Blue color is for Ti atoms, green color is for Nb atoms and region between two dark purple lines indicated the initial location of twin boundaries.

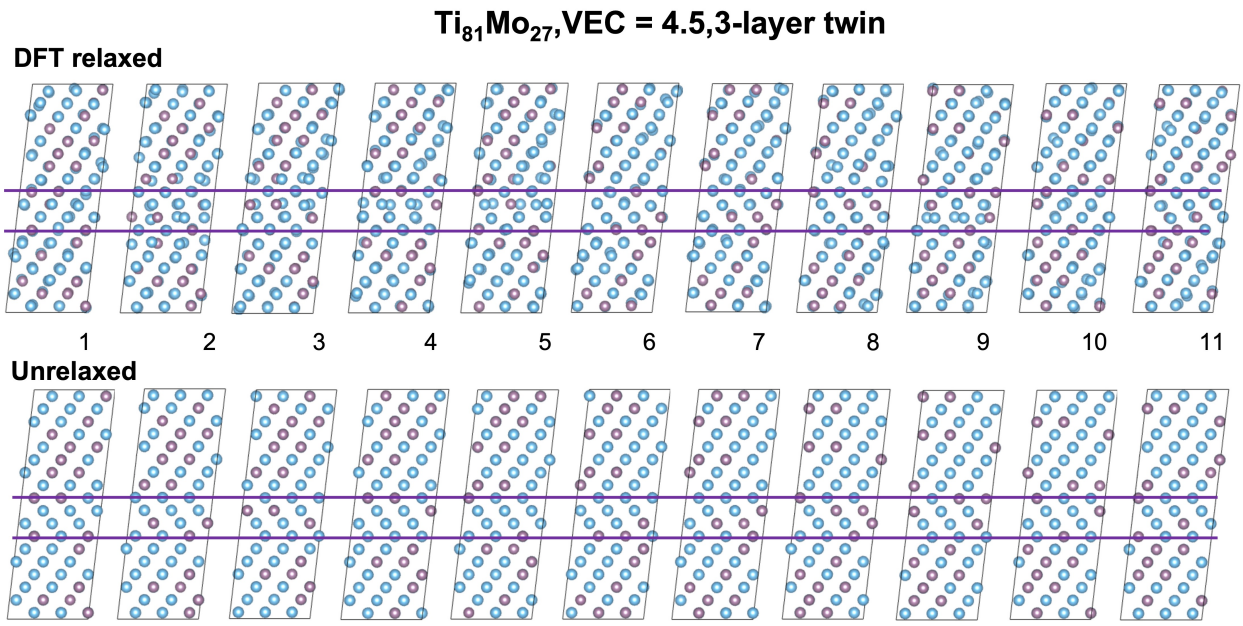


Figure B.7: Snapshots for unrelaxed and DFT fully relaxed atomic structures of 3-layer twin embryo in Ti_3Mo. Blue color is for Ti atoms, purple color is for Mo atoms and region between two dark purple lines indicated the initial location of twin boundaries.

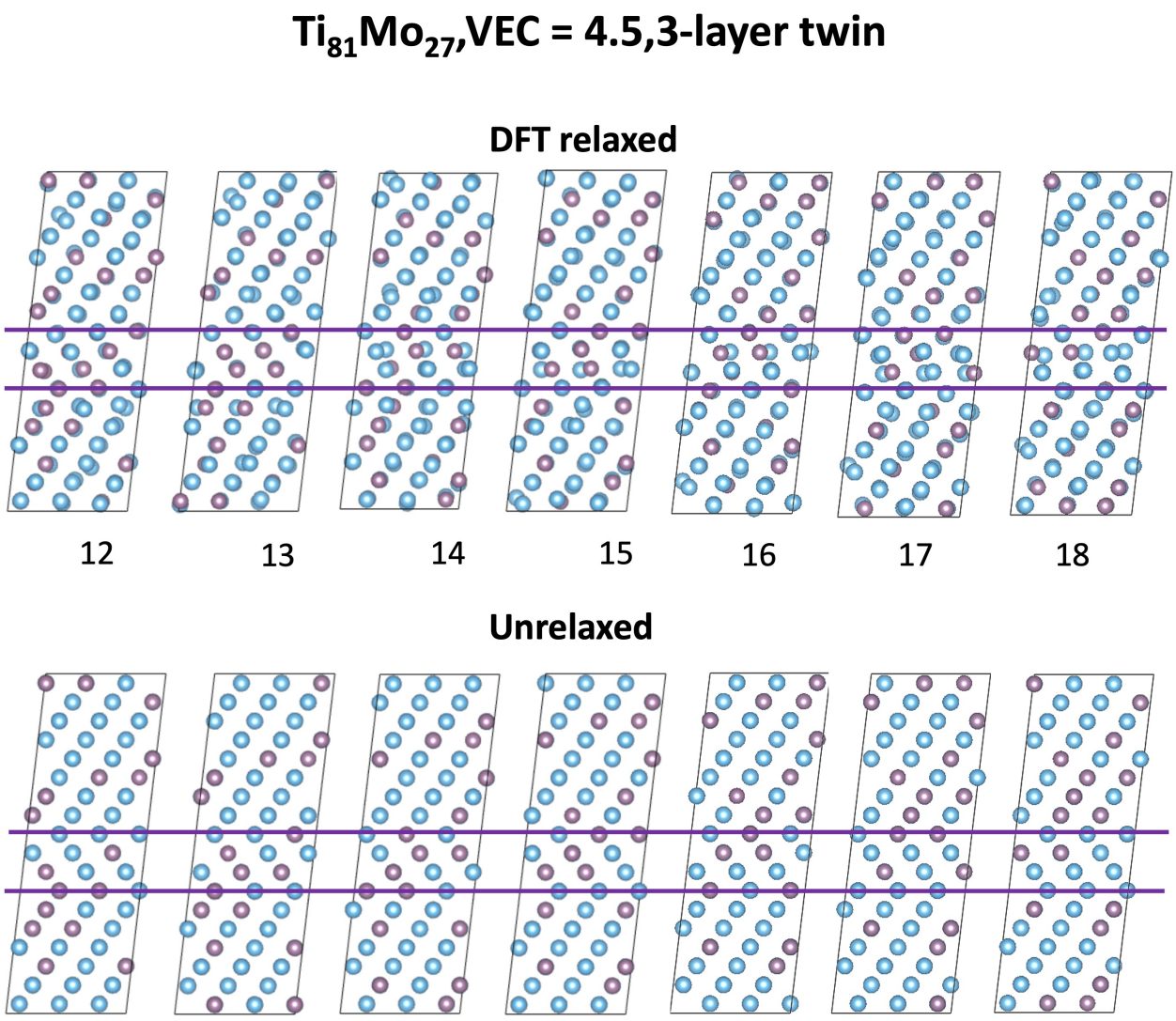


Figure B.8: Snapshots for unrelaxed and DFT fully relaxed atomic structures of 3-layer twin embryo in Ti_3Mo. Blue color is for Ti atoms, purple color is for Mo atoms and region between two dark purple lines indicated the initial location of twin boundaries.

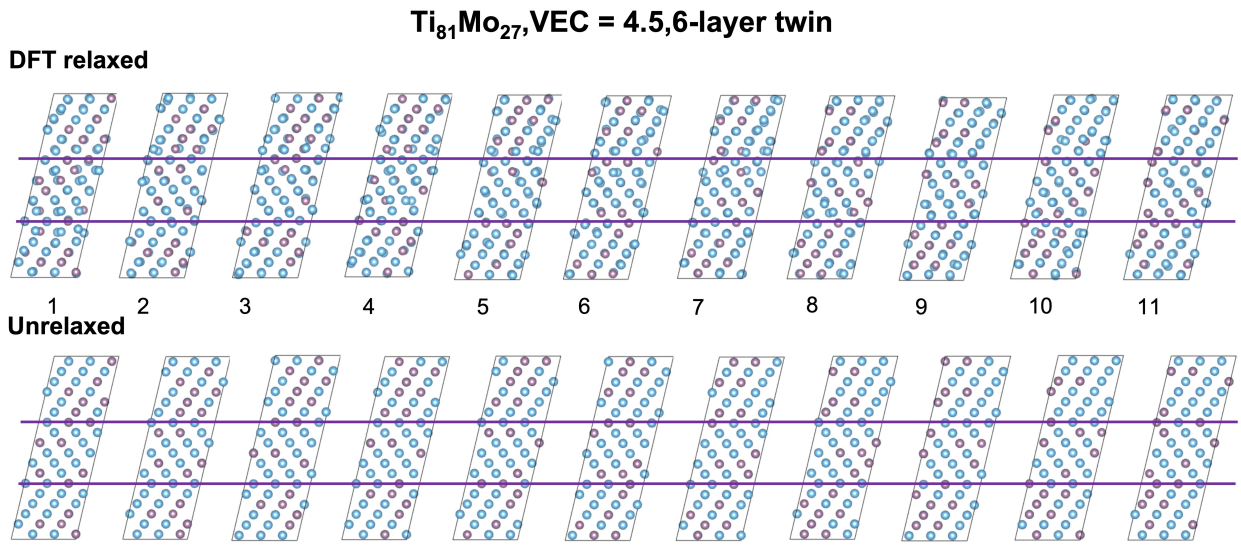


Figure B.9: Snapshots for unrelaxed and DFT fully relaxed atomic structures of 6-layer twin embryo in Ti_3Mo. Blue color is for Ti atoms, purple color is for Mo atoms and region between two dark purple lines indicated the initial location of twin boundaries.

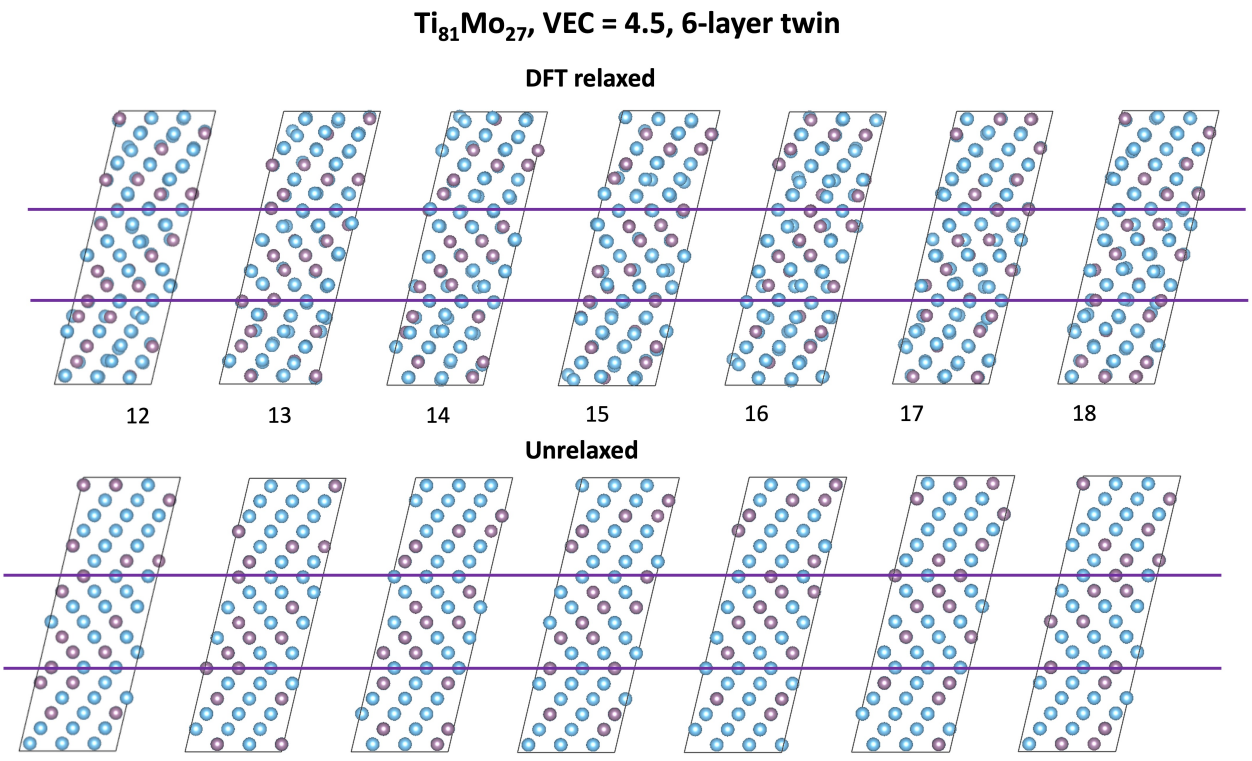


Figure B.10: Snapshots for unrelaxed and DFT fully relaxed atomic structures of 6-layer twin embryo in Ti_3Mo. Blue color is for Ti atoms, purple color is for Mo atoms and region between two dark purple lines indicated the initial location of twin boundaries.

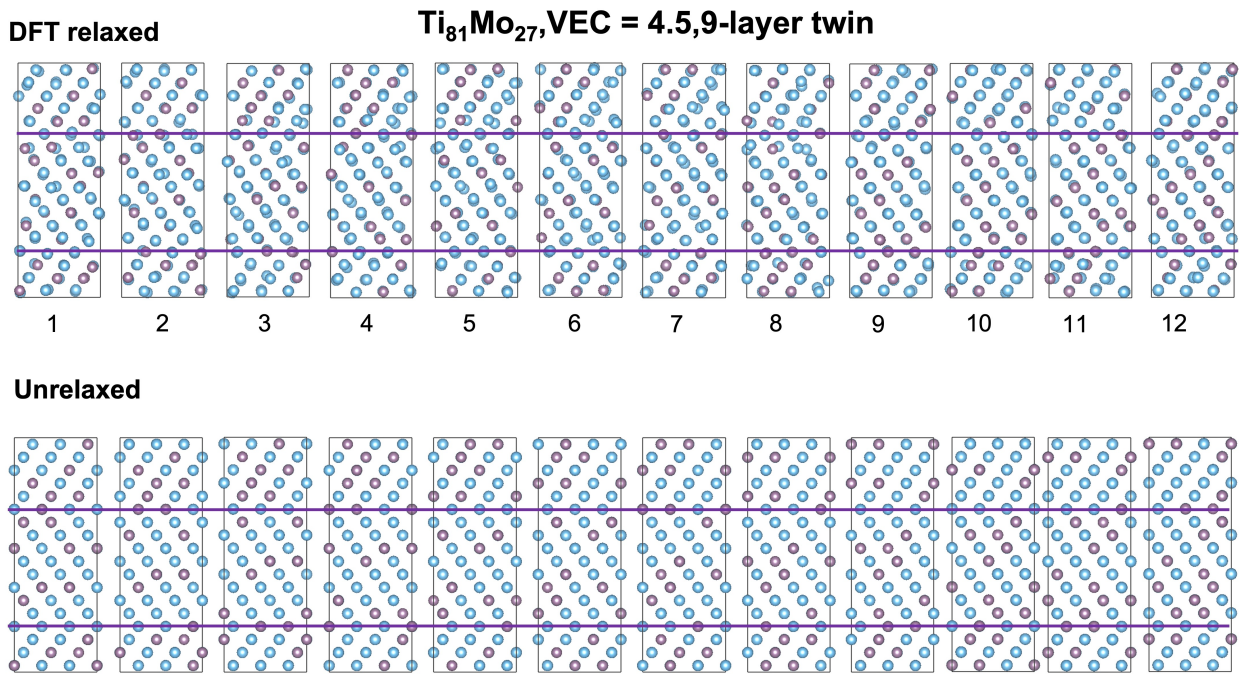


Figure B.11: Snapshots for unrelaxed and DFT fully relaxed atomic structures of 9-layer twin embryo in Ti_3Mo. Blue color is for Ti atoms, purple color is for Mo atoms and region between two dark purple lines indicated the initial location of twin boundaries.

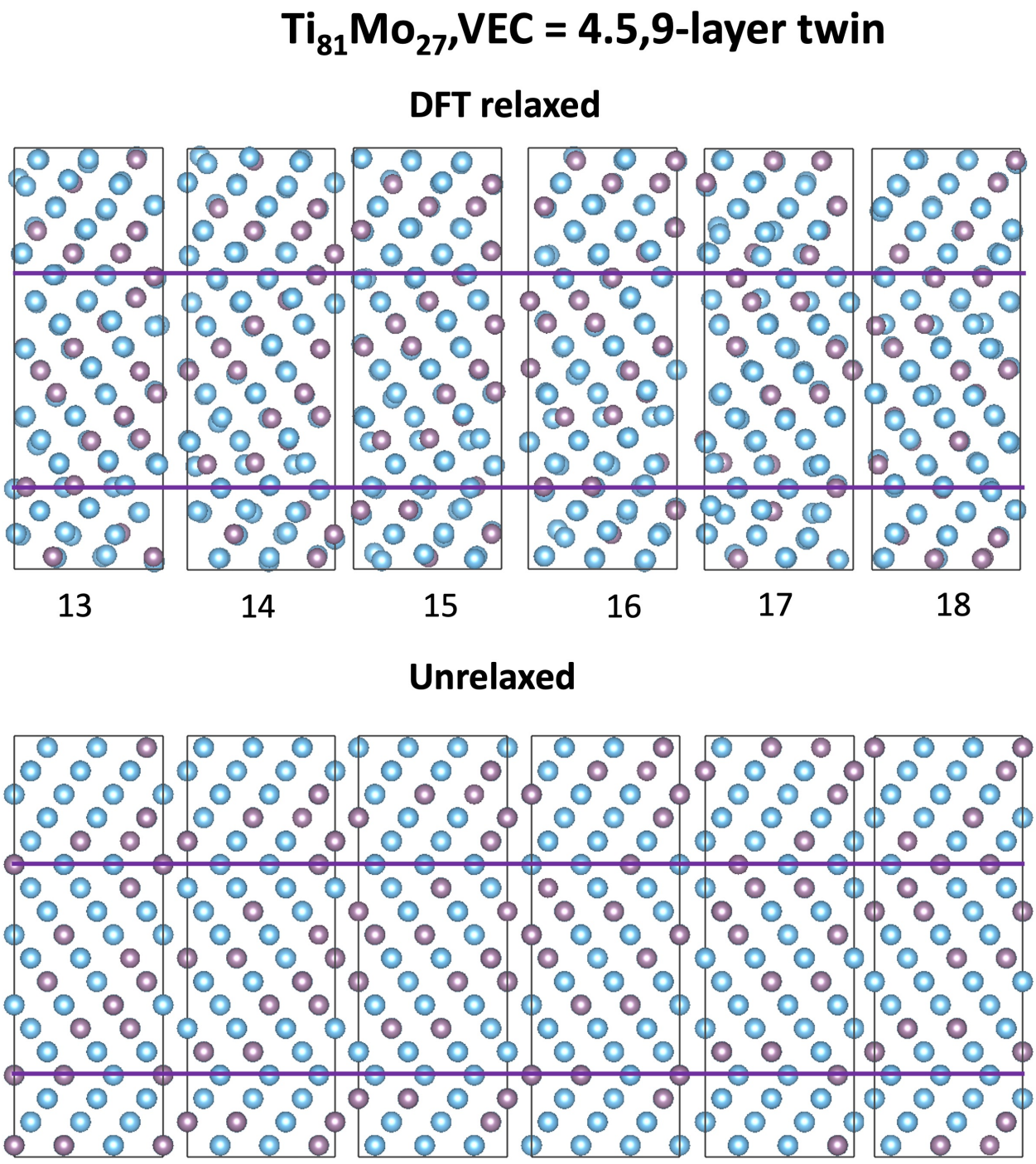


Figure B.12: Snapshots for unrelaxed and DFT fully relaxed atomic structures of 9-layer twin embryo in Ti_3Mo. Blue color is for Ti atoms, purple color is for Mo atoms and region between two dark purple lines indicated the initial location of twin boundaries.

B.2 $d_{[111]}$ Histogram for DFT Relaxed Supercells

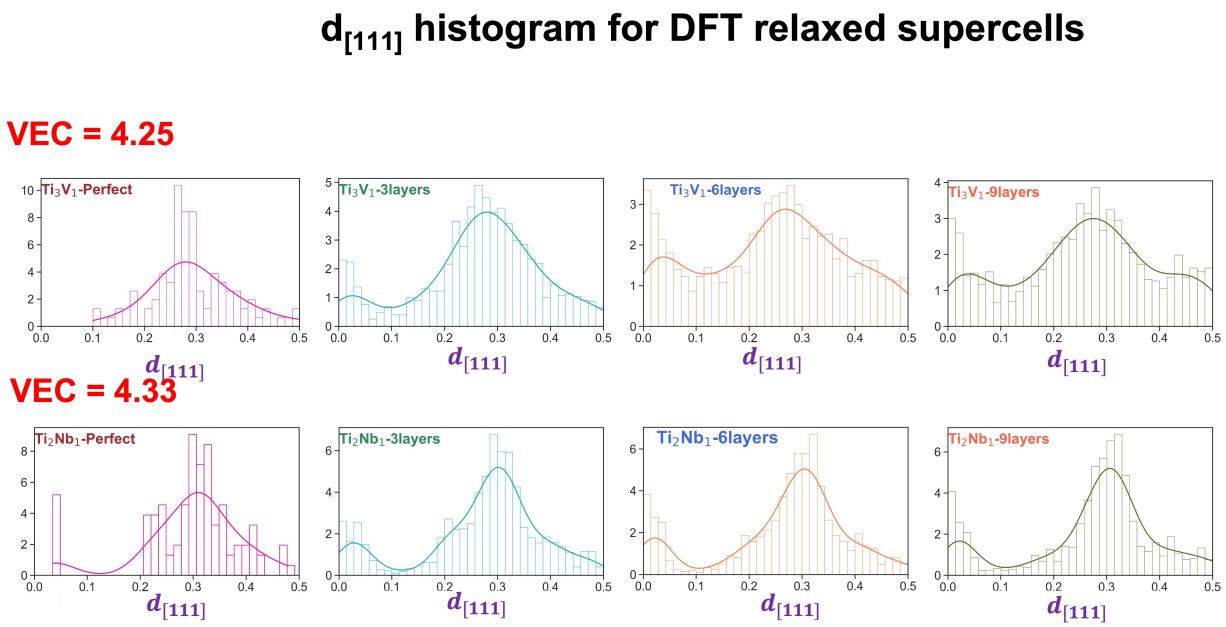


Figure B.13: Histograms of $d_{[111]}$ values (normalized in the unit of the length of $\frac{1}{2}[111]_\beta$) for DFT-relaxed supercells of different alloy compositions and twin embryo structures. From left to right the subfigures of upper row are for the perfect BCC matrix, 3-layer twin, 6-layer twin, and 9-layer twin embryo structure for Ti_3V (VEC=4.25), respectively. The subfigures at the lower row are histograms of $d_{[111]}$ values for corresponding twin embryo strictures for Ti_2Nb (VEC=4.33).

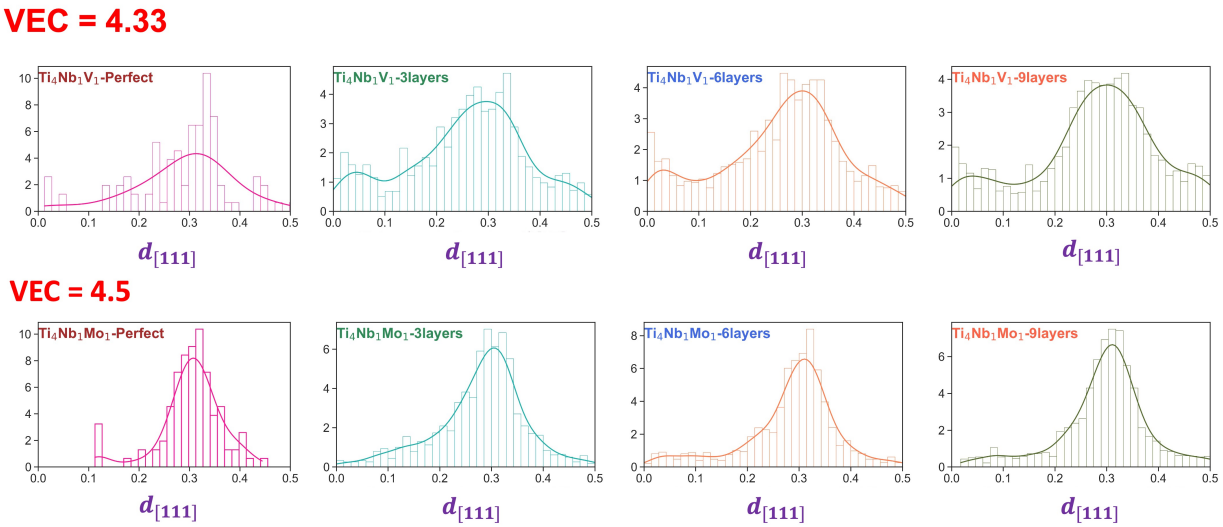


Figure B.14: Histograms of $d_{[111]}$ values (normalized in the unit of the length of $\frac{1}{2}[111]_\beta$) for DFT-relaxed supercells of different alloy compositions and twin embryo structures. From left to right the subfigures of upper row are for the perfect BCC matrix, 3-layer twin, 6-layer twin, and 9-layer twin embryo structure for Ti_4NbV (VEC=4.33), respectively. The subfigures at the lower row are histograms of $d_{[111]}$ values for corresponding twin embryo strictures for Ti_4NbMo (VEC=4.5).

B.3 Thickness Measurement

To illustrate the methods of measurement for local ω phases thickness at twin boundaries from experimental data of published papers, we take our experiment data as an example: There are 4 steps to evaluate the average thickness of ω phase the twin boundary:

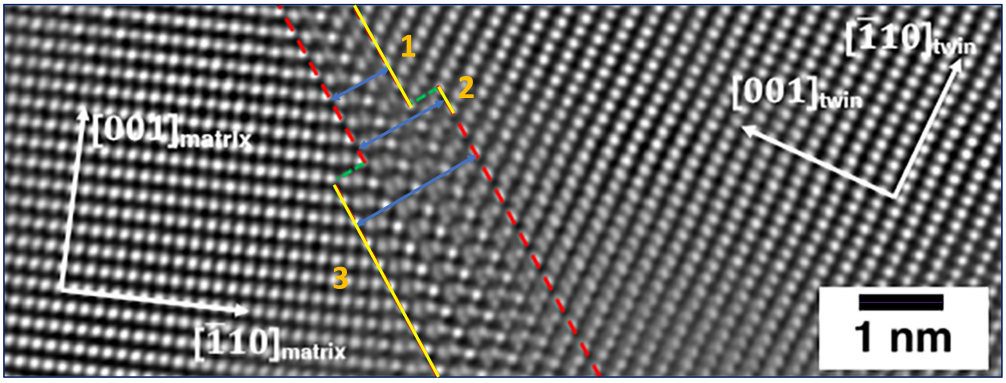


Figure B.15: Illustration of method to measure statistical results of ω phase thickness on {112} twin boundaries in β-Ti alloys. The aberration-corrected high-angle annular dark field scanning transmission electron microscopy (HAADF-STEM) imaging showing the hexagonal ω phase formed at {112} deformation twin boundary in the 20% cold-rolled Ti-24Nb-4Zr-8Sn alloy. This is also presented in the main text.

1. We need to void the measures of the frontier of twin embryos and only pick locations of ω phases at the middle of twin boundaries.

2. There are local ω phases (locally homogeneous and have constant thickness) parallel to twin boundaries, we need to pick out the representative cases with different lengths along the twin boundaries (Label 1, 2, and 3 in FIG. S. B.15).

3. We measure the length (yellow solid line along the twin boundaries) and thickness (blue arrow perpendicular to the twin boundaries) of local ω phases. The results in FIG. S. B.15 are summarized in the following Table:

Label	Thickness(nm)	Length(nm)
1	1.204819277	1.45158949
2	2.409638554	2.90317898
3	3.614457831	4.35476847

4. We calculate the average thickness of local ω phases weighted by the corresponding length. We also calculate the weighted standard deviation (sd_w) of weighted data points based on the Equation B.1:

$$sd_w = \sqrt{\frac{\sum_{i=1}^{N} w_i (x_i - \bar{x_w})^2}{\frac{(N'-1)\sum_{i=1}^{N} W_i}{N}}} \tag{B.1}$$

B.4 Shear Stress-Strain Curves for Twin Growth

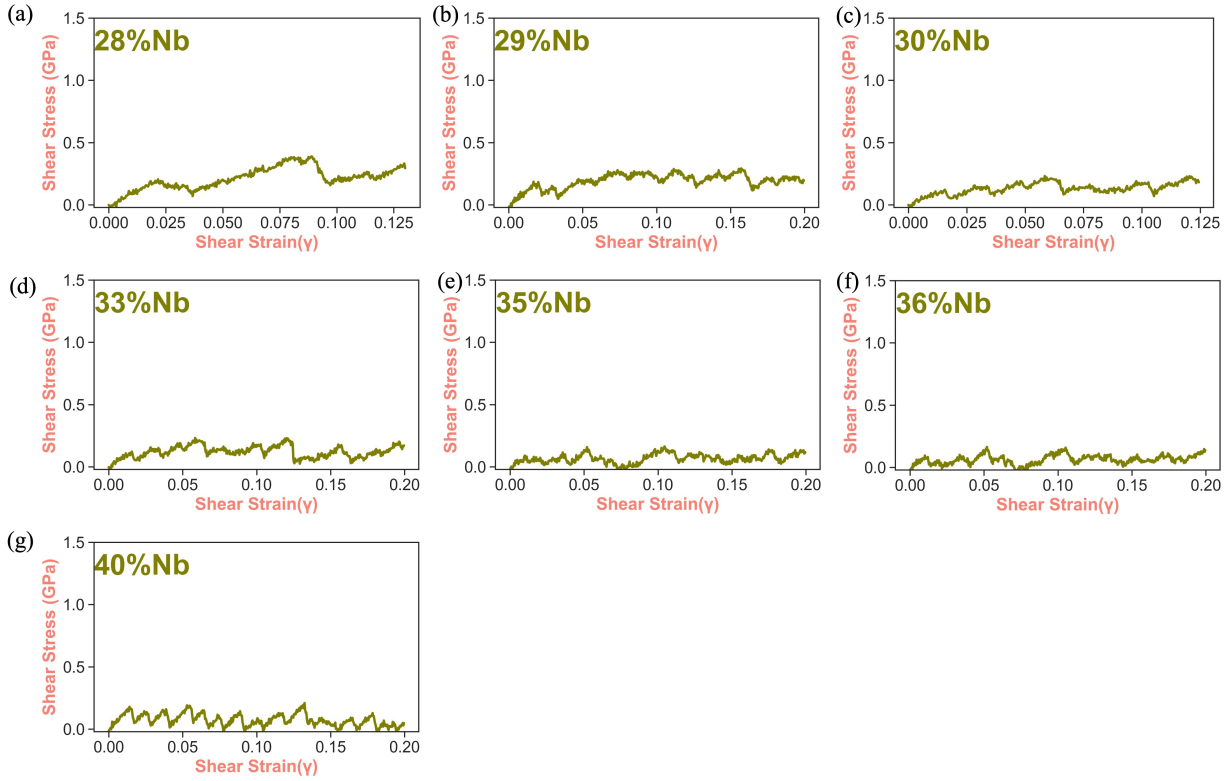


Figure B.16: Shear stress-strain curves for 9-layer twin embryo for different compositions. Engineering shear strain rate is 4 $\times 10^8$ s^{-1} along [111] direction on $(11\bar{2})$ planes at 300 K.

B.5 Twin Nucleation at Twist Grain Boundaries

In this section, we conduct {112} twin nucleation simulation at a stable twist grain boundary to investigate the role of ω phase in {112} twin nucleation. There is a long debate on origin of {112} twin. Ex-situ experiments always found thick ω phase around the {112} twin in metastable Ti alloys. Nevertheless, the sequence of formation of ω phase and {112} twin has not been verified. Based on following simulation results, we found ω phase nucleate spontaneously after {112} twin embryos forms. It will not form before the {112} twin nucleates. Instead, α" phase plays the role of intermediate step for twin nucleation. We provide comprehensive investigation on α" phase-mediated twin nucleation behaviors in Chapter 4.

B.5.1 Grain boundary Set Up

Here we construct Σ 9 $\langle 111 \rangle$ twist grain boundary to investigate the effect of grain boundaries on {112} twin nucleation. This type of twist grain boundary is already demonstrated to be common and stable in BCC alloys [62]. The schematic illustration is shown below. Meanwhile, we also construct a supercell that is in the perfect BCC lattice for comparison. The orientation is the same as BCC matrix defined in the manuscript.

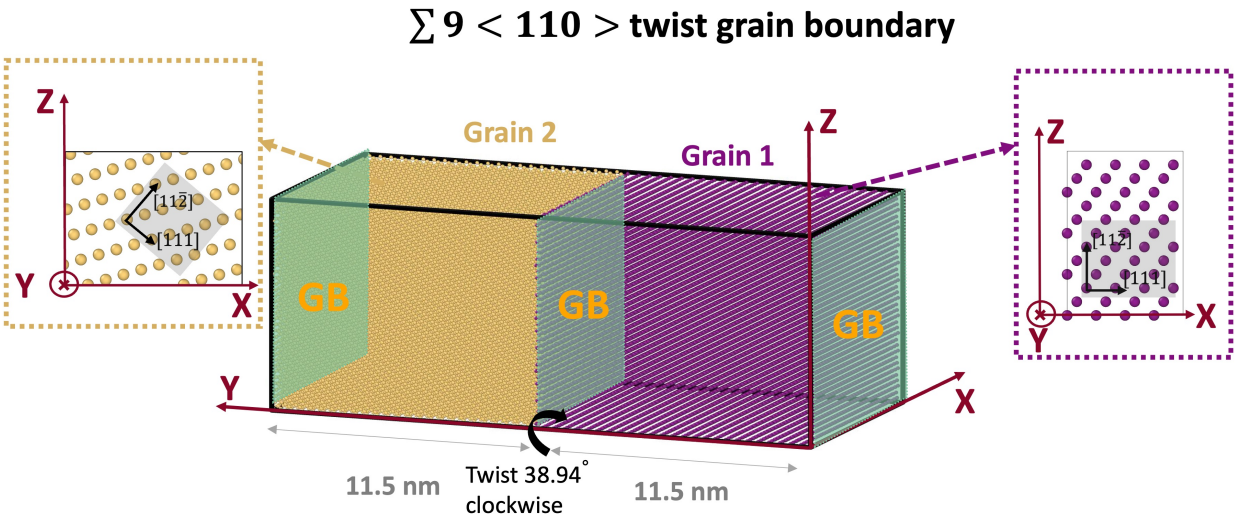


Figure B.17: Schematic draw of Σ 9 ⟨111⟩ twist grain boundary. Purple and yellow matrix indicate two grains in different orientations. Grain 2 is generated by clockwise rotating Grain 1 along $[1\bar{1}0]$ axis by 38.94°. The corresponding front views along $[1\bar{1}0]$ are shown in the dotted purple and yellow rectangles, respectively. Green planes indicate the location of grain boundaries, and the simulation box is periodic along shared $[1\bar{1}0]$ direction.

B.5.2 Shear Stress-Strain Curves for Twin Nucleation

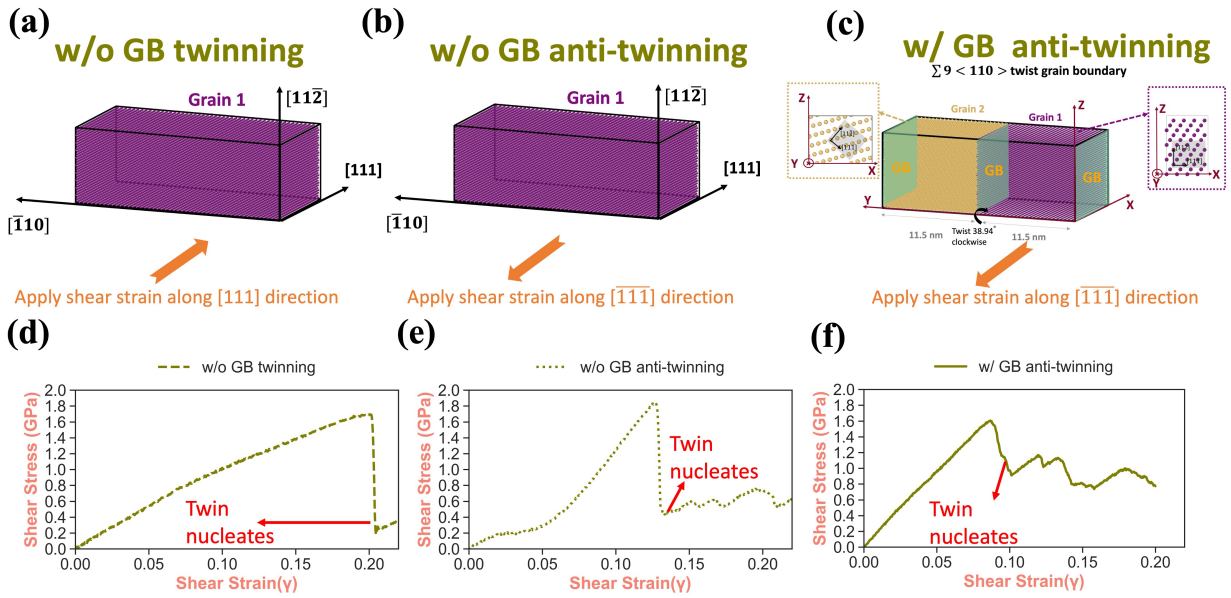


Figure B.18: Schematic illustration of shear deformation on different cases and the corresponding shear stress-strain curves. (a) and (b) is shear deformation setup for 120000-atoms supercells without grain boundaries, (c) is shear deformation setup for the 120000-atoms supercell containing grain boundaries. Orange arrows indicate the direction of shear stress applied. (d)-(f) shows the shear stress-strain curves for (a), (b) and (c), respectively. The engineering shear strain rate is 10^8/s and the deformation process is operated at constant 300K.

B.5.3 Twin Nucleation at Twist Grain Boundary

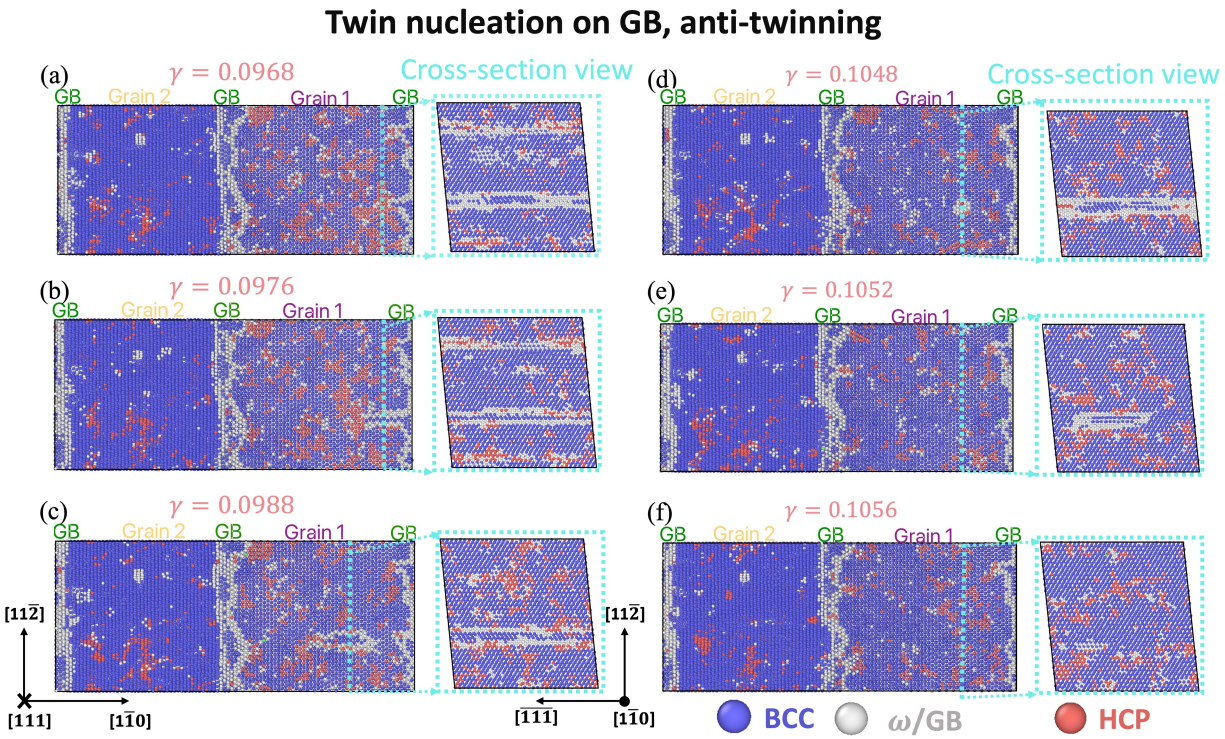


Figure B.19: Twin nucleation dynamics in Ti_3Nb (VEC=4.25) containing grain boundaries under uniform shear along anti-twinning direction. (a)-(f) are snapshots of both side views (along [111] direction) of some critical states and cross-section views of twin nucleic, corresponding shear strain γ is 0.0968, 0.0976, 0.0988, 0.1048, 0.1052 and 0.1056, respectively. Color coding for atoms in all subfigures are based on phases of atoms are in, which is identified by Common Neighbor Analysis (CNA)in OVITO [183, 91, 59]. Atoms in blue are in BCC phase, atoms in red are in HCP (α'/α" phase). Atoms in white color is unrecognized in CNA. Since atoms at grain boundaries can not identify the phase and CNA method can not identify ω phase and so those atoms are classfied as "Other" in CNA. Here we treat "Other" atoms as those at grain boundaries and in ω phase. Light blue dashed lines in (a)-(f) mark the location for cross-section cutting.

Appendix C

Energetic Model for Nucleation of Deformation Modes

C.1 Structural Analysis on Metastable Phases during Deformations

In this study, multiple metastable phases (ω phase, α"/α' phases) beside β phase in BCC-like phase will come out during deformation. As for ω phase, we use Common Neighbor Analysis (CNA) [91] methods to filter out ω phase from β phase and α"/α' phases. CNA method is good at distinguishing α"/α' phases and ω phase. In CNA methods, ω phase is classified as "Other" type. Since at finite temperature, lattice distortion is relative small compared to high temperature and no vacancies exist, the "Other" type phase is contributed from ω phase. Meanwhile, If $\{112\}$ twin nucleates, ω phase can form near the $\{112\}$ twin boundaries and atoms in "Other" type are in ω phase and possible located align $\{112\}$ twin boundaries. We label the atoms that have already be classified as "Other" and so the left are atoms either in β phase or in α"/α' phases. Once filter out "Other" phase, we use polyhedral template matching (PTM) methods to filter β phase (BCC-like) and α"/α' phases. Here the reference template of β phase (BCC-like) and α"/α' phases in PTM are perfect BCC and HCP lattice defined by corresponding symmetry operations. Here α" and α' phase are similar and both show a HCP-like structure relative to β(BCC) phase, so we do not distinguish α" with α' phase and classify them as α" phase. The reason we use a different methods to identify β phase (BCC-like) and α" phase is because PTM method can consistently output quaternions

and elastic deformation gradient matrix of β phase (BCC-like) and α"/α' phases. These two pieces of information is very helpful to further identify twin phase and calculate misfit strain along habit planes at deformed states. Therefore, we identify β phases, α" phases and ω phase via CNA and PTM methods. As for identification of deformation modes, we use Dislocation Analysis (DXA) methods in OVITO [184] to identify dislocation slip. Methods to identify deformation modes ($\{112\}$ twin and $\{332\}$ twin are in the next section.

C.2 Misorientation Calculation of β Phases During Deformations

To analyze the twinning modes nucleated during the shear loading, we need to quantify the misorientation between a reference (parent β variant) and a deformed β grain, we represent both orientations using unit quaternions. We use the polyhedral template matching (PTM) methods from OVITO [117, 183] to calculate quaternions. Let $\boldsymbol{q}_{\text{ref}}$ and $\boldsymbol{q}_{\text{def}}$ denote the quaternions corresponding to the reference (in the basis of X = $[3\,1\,1]$,Y = $[\overline{2}\,3\,3]$ and Z = $[0\,\overline{1}\,1]$) and deformed states, respectively. The β grains with different orientation is extracted from grain segmentation and polyhedral template matching (PTM) methods [117, 19]. The minimum size of grain is 100 atoms. The misorientation angle θ is calculated from the inner product of the two quaternions as:

$$\theta = 2\cos^{-1}\left(|\boldsymbol{q}_{\text{ref}} \cdot \boldsymbol{q}_{\text{def}}|\right) \tag{C.1}$$

Since both confined and non-confined simple shear we performed in this study is in X-Y plane and so the rotation is mainly along Z = $[0\,\overline{1}\,1]$. To ensure symmetry with respect to crystallographically equivalent misorientation, we also define:

$$\theta_{\text{sym}} = \min(\theta, 180^\circ - \theta) \tag{C.2}$$

Here the θ_{sym} is the final calculate misorientation angle. In theory, misorientation between $\{112\}$ twin relative to β parent phase along $[0\,\bar{1}\,1]$ is 70.53° [192] while $\{332\}$ twin relative to β parent phase along $[0\,\bar{1}\,1]$ is 50.5° [189].

C.3 Identifications on Barriers of β-α" Phase Transformations

Once we obtain the data of free energy landscape (FEL) from previous calculation, we then need to identify the location of all local minima and barrier between two local minima. We define local minima as grid points whose free energy values are lower than all neighboring points within a 3 by 3 window on the FEL grid. We use the function of "minimum filter" from SciPy package [196] to find out the local minima. The local minima belong to β phase and α" phase. To further calculate barrier between two local minima, we first need to find minimum energy path (MEP). We use discrete cost minimization algorithm using package called scikit-image [195] to find the path of minimum cumulative free energy between two local minima. Then we obtain absolute values of two barriers along the MEP (forward barrier $\Delta F^{\text{A}}_{\beta\leftarrow\alpha''}$and backward barrier $\Delta F^{\text{A}}_{\beta\rightarrow\alpha''}$). Finally we can obtain $\left|\Delta F^{\text{A}}_{\beta\leftrightarrow\alpha''}\right|$ in the **Equation 2** in the manuscript.

C.4 Calculations of Directional Elastic Moduli, Poisson's Ratio and Misfit Strain Energy Density

We here provide the general formulas of directional elastic moduli, and directional Poisson's ratio, which are derived from linear anisotropic elasticity [154]. As for directional Young's modulus $E(\boldsymbol{n})$, given a uniaxial stress σ along $\boldsymbol{n} = (l_1, l_2, l_3)$, the general form of the inverse Young's modulus in cubic system based on the elastic compliance tensor S_{ijkl} is:

$$\frac{1}{E(\boldsymbol{n})} = S_{11}\left(l_1^4 + l_2^4 + l_3^4\right) + 2S_{12}\left(l_1^2 l_2^2 + l_2^2 l_3^2 + l_3^2 l_1^2\right) + S_{44}\left(l_1^2 l_2^2 + l_2^2 l_3^2 + l_3^2 l_1^2\right). \tag{C.3}$$

As for directional shear modulus $G(\boldsymbol{n})$ along an arbitrary slip system in a cubic crystal, if shear direction $\mathbf{d} = (d_1, d_2, d_3)$ and the slip plane normal $\mathbf{n} = (n_1, n_2, n_3)$,the general form of the inverse shear modulus for cubic system based on the elastic compliance tensor S_{ijkl} can be expressed explicitly as:

$$\begin{aligned}\frac{1}{G(\boldsymbol{n})} = 4\Big\{S_{11}\left[(d_1n_1)^2 + (d_2n_2)^2 + (d_3n_3)^2\right] + 2S_{12}(d_1n_1d_2n_2 + d_1n_1d_3n_3 + d_2n_2d_3n_3)\Big\} \\ + S_{44}\left[(d_2n_3 + d_3n_2)^2 + (d_1n_3 + d_3n_1)^2 + (d_1n_2 + d_2n_1)^2\right]\end{aligned} \tag{C.4}$$

As for general form of directional Poisson's ratio $v_{p\to q}$, here we define two unit vector: $\mathbf{p} = (p_1, p_2, p_3)$ for longitudinal direction and $\mathbf{q} = (q_1, q_2, q_3)$ for transverse direction, and then it can be expressed explicitly in cubic system as:

$$v_{p\to q} = -\frac{\varepsilon_{qq}}{\varepsilon_{pp}} = -\frac{S_{12} + (S_{11} - S_{12} - \frac{1}{2}S_{44})(p_1^2q_1^2 + p_2^2q_2^2 + p_3^2q_3^2)}{S_{11} - 2(S_{11} - S_{12} - \frac{1}{2}S_{44})(p_1^2p_2^2 + p_2^2p_3^2 + p_3^2p_1^2)} \tag{C.5}$$

As for misfist strain energy density calculations, in this study, we only apply shear within [311]-[$\bar{2}$33] plane, and so there is little deformation in [0$\bar{1}$1] direction. Based on structural analysis, shear components of both β and nucleated α" phase along [0$\bar{1}$1] direction is at the scale of 0.01%. Also misfit strain along [0$\bar{1}$1] direction is at the scale of 0.01%. We provide

the shear components in Section S C.10.Therefore, the misfit strain energy density defined in **Equation 5** in the manuscript can be simplified in this study:

$$W_{\text{twin}}^{\text{misfit}} = \frac{1}{2}\left(\frac{E_1}{1-\nu_{12}\nu_{21}}\varepsilon_{11}^2\right)\Omega_\beta \tag{C.6}$$

C.5 Misfit Strain between β and α" Phase at Deformed State

Here we present a step-by-step procedure to calculate misfit strain between β parent phase and nucleated α" grains along specific orientations (ε_{11} in **Equation C.6**. **Step 1: Set the reference state for β phase and α" phase** As for β phase, we set the reference state (**State 1 of BCC**)in perfect BCC lattice with the coordination system that X = [100], Y =[011], Z = [0$\bar{1}$1].Then we use PTM methods in OVITO to calculate the elastic deformation gradient matrix of State 1 as $F^{\beta}_{\mathbf{ref}}$. Here ratio of unit length along X, Y and Z in ideal BCC phase is 1:$\sqrt{2}$:$\sqrt{2}$. As for α" phase, we set perfect HCP phase as reference state (**State 1 of** α") and the coordination system is: X=[11$\bar{2}$0], Y=[$\bar{1}$100], Z=[0001], corresponding elastic deformation gradient matrix is $F^{\alpha"}_{\mathbf{ref}}$. Here ratio of unit length along X, Y and Z in perfect HCP is 1:$\sqrt{3}$:$\sqrt{8/3}$. Here we want to point out that the choice of reference coordination system for β (BCC-like) and α" phase (HCP-like) is following the orientation relationships along Burgers path of BCC-HCP phase transformation. The next step is to define the deformed state of β matrix grain and α" phase grain.

Step 2: Set deformed state for β matrix and α" phase. In our study, simulation box before dynamic loading is in β phase and the coordination system is X=[311], Y=[$\bar{2}$33], Z=[01$\bar{1}$]. The orientation relationship between the simulation box in the initial state and the reference state defined in Step 1 corresponds to a clockwise rotation of approximately θ= 25.24° ($\theta = \arccos\left(\frac{[100]\cdot[311]}{\|[100]\|\,\|[311]\|}\right)$) about the $Z \parallel [0\bar{1}1]$ axis. Once shear loading (along XY direction) operations apply to the simulation box, β matrix undergoes shear in XY and rotation along Z direction. Meanwhile, α" martensites nucleate from β matrix, and then undergo shear and rotation under loading conditions. Elastic deformation gradient matrix obtained from OVITO via PTM method can record the deform state of β matrix and nucleated α" martensite. Since under applied loading condition, β twin phase is also possible to nucleate and so here we define the β matrix is the β grain whose volume fraction

is largest among all β grains and corresponding misorientation relative to reference β state is within 25.24°±5° (here 5° is theoretical rotation degree when 0.1 shear strain applied) . Then we record elastic deformation gradient matrix of deformed β matrix and deformed α" as $F^{\beta}_{\mathbf{deform}}$ and $F^{\alpha"}_{\mathbf{deform}}$, respectively.

Step 3: Calculation of stretch tensor from elastic deformation gradient matrix of deformed state relative to reference state. Once we obtain elastic deformation gradient matrix of reference state and deformed state, following frame-invariant nature, we can capture how shape deviation of deformed state relative to reference state directly:

$$\mathbf{F}_{\mathrm{rel}}^{\beta\ /\alpha"} = \mathbf{F}_{\mathrm{deform}}^{\beta\ /\alpha"}\,\mathbf{F}_{\mathrm{ref}}^{\beta\ /\alpha"-1} \tag{C.7}$$

We then can filter out rotation part and obtain the pure stretch tensor:

$$\mathbf{U}_{\mathrm{rel}}^{\beta\ /\alpha"} = \sqrt{\mathbf{F}_{\mathrm{rel}}^{\beta\ /\alpha"\,\mathbf{T}}\,\mathbf{F}_{\mathrm{rel}}^{\beta\ /\alpha"}} = \begin{bmatrix} \varepsilon_{xx} & \gamma_{xy} & \gamma_{xz} \\ \gamma_{yx} & \varepsilon_{yy} & \gamma_{yz} \\ \gamma_{zx} & \gamma_{zy} & \varepsilon_{zz} \end{bmatrix} \tag{C.8}$$

Here coordination system in stretch tensor $\mathbf{U}_{\mathrm{rel}}^{\beta\ /\alpha"}$ is based on reference state of β and HCP phase:

$$\begin{aligned} X &= [100]_{\beta} \leftrightarrow [11\bar{2}0]_{\mathrm{HCP}} \leftrightarrow [100]_{\alpha''} \\ Y &= [011]_{\beta} \leftrightarrow [\bar{1}100]_{\mathrm{HCP}} \leftrightarrow [010]_{\alpha''} \\ Z &= [01\bar{1}]_{\beta} \leftrightarrow [0001]_{\mathrm{HCP}} \leftrightarrow [001]_{\alpha''} \end{aligned} \tag{C.9}$$

Step 4: Calculation of misfit strain along different habit planes. To simply, based on the orthogonal coordination system defined in **Equation C.9**, here we define the reference lattice matrix $L_{\mathbf{ref}}$ as:

$$L_{\mathbf{ref}} = \begin{bmatrix} a & 0 & 0 \\ 0 & b & 0 \\ 0 & 0 & c \end{bmatrix} \tag{C.10}$$

Here,

$$\mathbf{a}_{\text{ref}} = \begin{bmatrix} a \\ 0 \\ 0 \end{bmatrix} \text{ is the unit vector of } [100]_{\beta} \text{ for } \beta \text{ } ([100]_{\alpha"} \text{ for } \alpha" \text{ phase})$$

$$\mathbf{b}_{\text{ref}} = \begin{bmatrix} 0 \\ b \\ 0 \end{bmatrix} \text{ is the unit vector of } [011]_{\beta} \text{ for } \beta \text{ } ([010]_{\alpha"} \text{ for } \alpha" \text{ phase}) \tag{C.11}$$

$$\mathbf{c}_{\text{ref}} = \begin{bmatrix} 0 \\ 0 \\ c \end{bmatrix} \text{ is the unit vector of } [01\overline{1}]_{\beta} \text{ for } \beta \text{ } ([001]_{\alpha"} \text{ for } \alpha" \text{ phase})$$

$\mathbf{a}$ is the unit length of $[100]_{\beta}$ for β ($[100]_{\alpha"}$ for $\alpha"$ phase); $\mathbf{b}$ is the unit length of $[011]_{\beta}$ for β ($[010]_{\alpha"}$ for $\alpha"$ phase) and $\mathbf{c}$ is the unit length of $[01\overline{1}]_{\beta}$ for β ($[001]_{\alpha"}$ for $\alpha"$ phase). Therefore,

$$\begin{aligned} d^{\beta}_{[111]_{\text{ref}}} = \left|\vec{a}^{\beta}_{\text{ref}} + \vec{b}^{\beta}_{\text{ref}}\right|, d^{\alpha"}_{[110]_{\text{ref}}} = \left|\vec{a}^{\alpha"}_{\text{ref}} + \vec{b}^{\alpha"}_{\text{ref}}\right| \\ d^{\beta}_{[311]_{\text{ref}}} = \left|3\vec{a}^{\beta}_{\text{ref}} + \vec{b}^{\beta}_{\text{ref}}\right|, d^{\alpha"}_{[310]_{\text{ref}}} = \left|3\vec{a}^{\alpha"}_{\text{ref}} + \vec{b}^{\alpha"}_{\text{ref}}\right| \end{aligned} \tag{C.12}$$

Once external loading conditions apply to the reference undeformed simulation box, the lattice will undergo the stretch deformation (rotation part has been filtered out in **Equation C.8)**, the lattice coordination system at deformed state, $L_{\mathbf{deform}}$, is given by:

$$L_{\mathbf{deform}} = \begin{bmatrix} \varepsilon_{xx} & \gamma_{xy} & \gamma_{xz} \\ \gamma_{yx} & \varepsilon_{yy} & \gamma_{yz} \\ \gamma_{zx} & \gamma_{zy} & \varepsilon_{zz} \end{bmatrix} \cdot \begin{bmatrix} a & 0 & 0 \\ 0 & b & 0 \\ 0 & 0 & c \end{bmatrix} = \begin{bmatrix} \varepsilon_{xx}a & \gamma_{xy}b & \gamma_{xz}c \\ \gamma_{yx}a & \varepsilon_{yy}b & \gamma_{yz}c \\ \gamma_{zx}a & \gamma_{zy}b & \varepsilon_{zz}c \end{bmatrix} \tag{C.13}$$

Since shear loading is along X-Y direction and so the stretch behaviors in principle mainly happen within the X-Y plane and rotation along Z direction. We also analyze the stretch tensor under different shear strain state and find that the z-related shear components (γ_{xz},γ_{zx},γ_{yz},γ_{zy}) in stretch tensor $\mathbf{U}^{\beta/\alpha"}_{\text{rel}}$ is quite small and at the scale of 0.01%, which

is reasonable to ignore them. Meanwhile, γ_{xy} and γ_{yx} is at the scale of 1%, which is not so small and so we keep them. Hence, we can further simplify $L_{\mathbf{deform}}$ as :

$$L_{\mathbf{deform}} = \begin{bmatrix} \varepsilon_{xx}a & \gamma_{xy}b & 0 \\ \gamma_{yx}a & \varepsilon_{yy}b & 0 \\ 0 & 0 & \varepsilon_{zz}c \end{bmatrix} \tag{C.14}$$

Therefore, the lattice vectors under loading condition become:

$$\mathbf{a}_{\text{deform}} = \begin{bmatrix} \varepsilon_{xx}a \\ \gamma_{yx}a \\ 0 \end{bmatrix}, \mathbf{b}_{\text{deform}} = \begin{bmatrix} \gamma_{xy}b \\ \varepsilon_{yy}b \\ 0 \end{bmatrix}, \text{ and } \mathbf{c}_{\text{deform}} = \begin{bmatrix} 0 \\ 0 \\ \varepsilon_{zz}c \end{bmatrix} \tag{C.15}$$

Meanwhile, the rotation is mainly along z axis and rotation in other dimensions are less than 0.1°. Therefore, we can directly calculate average unit length along z axis of deformed simulation box (denoted by, $c^{\beta}_{\mathbf{deform}}$) and treat it as $\varepsilon_{zz}c$, and then calculate all other terms in $\mathbf{a}_{\text{deform}}$ and $\mathbf{b}_{\text{deform}}$. Since at reference state, as shown in **Step1**:

$$\begin{aligned} a_{\beta} : b_{\beta} : c_{\beta} &= 1 : \sqrt{2} : \sqrt{2} \\ a_{\text{HCP}} : b_{\text{HCP}} : c_{\text{HCP}} &= 1 : \sqrt{3} : \sqrt{\frac{8}{3}} \end{aligned} \tag{C.16}$$

If we define average unit length along Z axis ($[01\bar{1}]_{\beta} \parallel [0001]_{\text{HCP}} \parallel [001]_{\alpha"}$) at deformed state of β and α" phase as $c^{\beta}_{\text{deform}}$ and $c^{\alpha"}_{\text{deform}}$,respectively, then input them it into **Equation C.15** and **C.16**, and we can obtain the absolute value of a_{deform} (which is $\varepsilon_{xx}a$ in **Equation C.15)**and b_{deform} (which is $\varepsilon_{yy}b$ in **Equation C.15)** in deformed β and α" phase:

$$\begin{aligned} a^{\beta}_{\text{deform}} = \varepsilon_{xx}a = \frac{c^{\beta}_{\text{deform}}}{\sqrt{2}}\frac{\varepsilon_{xx}}{\varepsilon_{zz}},\ b^{\beta}_{\text{deform}} = \varepsilon_{yy}b = c^{\beta}_{\text{deform}}\frac{\varepsilon_{yy}}{\varepsilon_{zz}} \\ a^{\alpha"}_{\text{deform}} = \varepsilon_{xx}a = \frac{c^{\alpha"}_{\text{deform}}}{\sqrt{\frac{8}{3}}}\frac{\varepsilon_{xx}}{\varepsilon_{zz}},\ b^{\alpha"}_{\text{deform}} = \varepsilon_{yy}b = \frac{c^{\alpha"}_{\text{deform}}}{\sqrt{\frac{8}{3}}}\frac{\sqrt{3}\varepsilon_{yy}}{\varepsilon_{zz}} \end{aligned} \tag{C.17}$$

And then **Equation C.18** can be rewrite as:

$$\mathbf{a}^{\beta}_{\text{deform}} = \begin{bmatrix} \frac{c^{\beta}_{\text{deform}}}{\sqrt{2}} \frac{\varepsilon_{xx}}{\varepsilon_{zz}} \\ \frac{c^{\beta}_{\text{deform}}}{\sqrt{2}} \frac{\gamma_{yx}}{\varepsilon_{zz}} \\ 0 \end{bmatrix}, \mathbf{b}^{\beta}_{\text{deform}} = \begin{bmatrix} c^{\beta}_{\text{deform}} \frac{\gamma_{xy}}{\varepsilon_{zz}} \\ c^{\beta}_{\text{deform}} \frac{\varepsilon_{yy}}{\varepsilon_{zz}} \\ 0 \end{bmatrix}, \text{ and } \mathbf{c}^{\beta}_{\text{deform}} = \begin{bmatrix} 0 \\ 0 \\ c^{\beta}_{\text{deform}} \end{bmatrix}$$
$$\mathbf{a}^{\alpha"}_{\text{deform}} = \begin{bmatrix} \frac{c^{\alpha"}_{\text{deform}}}{\sqrt{\frac{8}{3}}} \frac{\varepsilon_{xx}}{\varepsilon_{zz}} \\ \frac{c^{\alpha"}_{\text{deform}}}{\sqrt{\frac{8}{3}}} \frac{\gamma_{yx}}{\varepsilon_{zz}} \\ 0 \end{bmatrix}, \mathbf{b}^{\alpha"}_{\text{deform}} = \begin{bmatrix} \frac{c^{\alpha"}_{\text{deform}}}{\sqrt{\frac{8}{3}}} \frac{\sqrt{3}\gamma_{xy}}{\varepsilon_{zz}} \\ \frac{c^{\alpha"}_{\text{deform}}}{\sqrt{\frac{8}{3}}} \frac{\sqrt{3}\varepsilon_{yy}}{\varepsilon_{zz}} \\ 0 \end{bmatrix}, \text{ and } \mathbf{c}^{\alpha"}_{\text{deform}} = \begin{bmatrix} 0 \\ 0 \\ c^{\alpha"}_{\text{deform}} \end{bmatrix} \tag{C.18}$$

Finally, we can obtain the unit length along [111] in deformed β ([110] in α" phase) and unit length along [311] in deformed β ([310] in α" phase):

$$\begin{aligned} d^{\beta}_{[111]_{\text{deform}}} &= \sqrt{(\frac{c^{\beta}_{\text{deform}}}{\sqrt{2}} \frac{\varepsilon_{xx}}{\varepsilon_{zz}} + c^{\beta}_{\text{deform}} \frac{\gamma_{xy}}{\varepsilon_{zz}})^2 + (\frac{c^{\beta}_{\text{deform}}}{\sqrt{2}} \frac{\gamma_{yx}}{\varepsilon_{zz}} + c^{\beta}_{\text{deform}} \frac{\varepsilon_{yy}}{\varepsilon_{zz}})^2} \\ d^{\alpha"}_{[110]_{\text{deform}}} &= \sqrt{(\frac{c^{\alpha"}_{\text{deform}}}{\sqrt{\frac{8}{3}}} \frac{\varepsilon_{xx}}{\varepsilon_{zz}} + \frac{c^{\alpha"}_{\text{deform}}}{\sqrt{\frac{8}{3}}} \frac{\sqrt{3}\gamma_{xy}}{\varepsilon_{zz}})^2 + (\frac{c^{\alpha"}_{\text{deform}}}{\sqrt{\frac{8}{3}}} \frac{\gamma_{yx}}{\varepsilon_{zz}} + \frac{c^{\alpha"}_{\text{deform}}}{\sqrt{\frac{8}{3}}} \frac{\sqrt{3}\varepsilon_{yy}}{\varepsilon_{zz}})^2} \\ d^{\beta}_{[311]_{\text{deform}}} &= \sqrt{(3\frac{c^{\beta}_{\text{deform}}}{\sqrt{2}} \frac{\varepsilon_{xx}}{\varepsilon_{zz}} + c^{\beta}_{\text{deform}} \frac{\gamma_{xy}}{\varepsilon_{zz}})^2 + (3\frac{c^{\beta}_{\text{deform}}}{\sqrt{2}} \frac{\gamma_{yx}}{\varepsilon_{zz}} + c^{\beta}_{\text{deform}} \frac{\varepsilon_{yy}}{\varepsilon_{zz}})^2} \\ d^{\alpha"}_{[310]_{\text{deform}}} &= \sqrt{(3\frac{c^{\alpha"}_{\text{deform}}}{\sqrt{\frac{8}{3}}} \frac{\varepsilon_{xx}}{\varepsilon_{zz}} + \frac{c^{\alpha"}_{\text{deform}}}{\sqrt{\frac{8}{3}}} \frac{\sqrt{3}\gamma_{xy}}{\varepsilon_{zz}})^2 + (3\frac{c^{\alpha"}_{\text{deform}}}{\sqrt{\frac{8}{3}}} \frac{\gamma_{yx}}{\varepsilon_{zz}} + \frac{c^{\alpha"}_{\text{deform}}}{\sqrt{\frac{8}{3}}} \frac{\sqrt{3}\varepsilon_{yy}}{\varepsilon_{zz}})^2} \end{aligned} \tag{C.19}$$

Then we input **Equation C.19** into Table 4.2 and to obtain misfit strain along different interphase boundaries:

$$\begin{aligned} \varepsilon^{\{112\}\text{ twin}}_{11\text{deform}} &= \frac{\sqrt{(\frac{c^{\beta}_{\text{deform}}}{\sqrt{2}} \frac{\varepsilon_{xx}}{\varepsilon_{zz}} + c^{\beta}_{\text{deform}} \frac{\gamma_{xy}}{\varepsilon_{zz}})^2 + (\frac{c^{\beta}_{\text{deform}}}{\sqrt{2}} \frac{\gamma_{yx}}{\varepsilon_{zz}} + c^{\beta}_{\text{deform}} \frac{\varepsilon_{yy}}{\varepsilon_{zz}})^2} - \sqrt{(\frac{c^{\alpha"}_{\text{deform}}}{\sqrt{\frac{8}{3}}} \frac{\varepsilon_{xx}}{\varepsilon_{zz}} + \frac{c^{\alpha"}_{\text{deform}}}{\sqrt{\frac{8}{3}}} \frac{\sqrt{3}\gamma_{xy}}{\varepsilon_{zz}})^2 + (\frac{c^{\alpha"}_{\text{deform}}}{\sqrt{\frac{8}{3}}} \frac{\gamma_{yx}}{\varepsilon_{zz}} + \frac{c^{\alpha"}_{\text{deform}}}{\sqrt{\frac{8}{3}}} \frac{\sqrt{3}\varepsilon_{yy}}{\varepsilon_{zz}})^2}}{\sqrt{(\frac{c^{\beta}_{\text{deform}}}{\sqrt{2}} \frac{\varepsilon_{xx}}{\varepsilon_{zz}} + c^{\beta}_{\text{deform}} \frac{\gamma_{xy}}{\varepsilon_{zz}})^2 + (\frac{c^{\beta}_{\text{deform}}}{\sqrt{2}} \frac{\gamma_{yx}}{\varepsilon_{zz}} + c^{\beta}_{\text{deform}} \frac{\varepsilon_{yy}}{\varepsilon_{zz}})^2}} \\ \varepsilon^{\{332\}\text{ twin}}_{11\text{deform}} &= \frac{\sqrt{(\frac{c^{\alpha"}_{\text{deform}}}{\sqrt{\frac{8}{3}}} \frac{\varepsilon_{xx}}{\varepsilon_{zz}} + \frac{c^{\alpha"}_{\text{deform}}}{\sqrt{\frac{8}{3}}} \frac{\sqrt{3}\gamma_{xy}}{\varepsilon_{zz}})^2 + (\frac{c^{\alpha"}_{\text{deform}}}{\sqrt{\frac{8}{3}}} \frac{\gamma_{yx}}{\varepsilon_{zz}} + \frac{c^{\alpha"}_{\text{deform}}}{\sqrt{\frac{8}{3}}} \frac{\sqrt{3}\varepsilon_{yy}}{\varepsilon_{zz}})^2} - \sqrt{(3\frac{c^{\alpha"}_{\text{deform}}}{\sqrt{\frac{8}{3}}} \frac{\varepsilon_{xx}}{\varepsilon_{zz}} + \frac{c^{\alpha"}_{\text{deform}}}{\sqrt{\frac{8}{3}}} \frac{\sqrt{3}\gamma_{xy}}{\varepsilon_{zz}})^2 + (3\frac{c^{\alpha"}_{\text{deform}}}{\sqrt{\frac{8}{3}}} \frac{\gamma_{yx}}{\varepsilon_{zz}} + \frac{c^{\alpha"}_{\text{deform}}}{\sqrt{\frac{8}{3}}} \frac{\sqrt{3}\varepsilon_{yy}}{\varepsilon_{zz}})^2}}{\sqrt{(\frac{c^{\alpha"}_{\text{deform}}}{\sqrt{\frac{8}{3}}} \frac{\varepsilon_{xx}}{\varepsilon_{zz}} + \frac{c^{\alpha"}_{\text{deform}}}{\sqrt{\frac{8}{3}}} \frac{\sqrt{3}\gamma_{xy}}{\varepsilon_{zz}})^2 + (\frac{c^{\alpha"}_{\text{deform}}}{\sqrt{\frac{8}{3}}} \frac{\gamma_{yx}}{\varepsilon_{zz}} + \frac{c^{\alpha"}_{\text{deform}}}{\sqrt{\frac{8}{3}}} \frac{\sqrt{3}\varepsilon_{yy}}{\varepsilon_{zz}})^2}} \end{aligned} \tag{C.20}$$

Which then input misfit strain at deformed state.

C.6 Atomic Structure of {112} and {332} Twin Boundary.

Here we present the snapshots of the atomic structure of {112} and {332} twin boundary. Consistent with many experimental and computational study [215, 39, 74, 113], ω phase forms spontaneously around {112} twin boundary, while α" phase forms along {332} twin boundary.

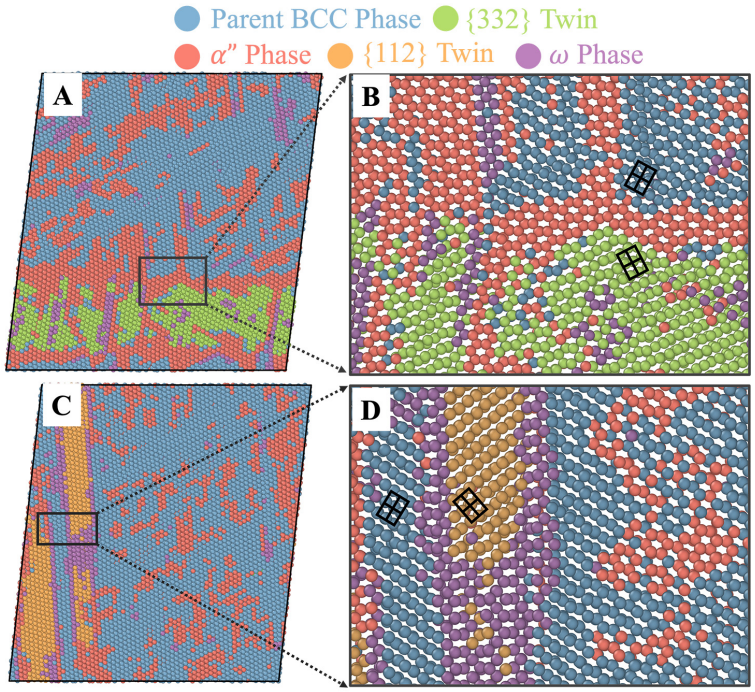


Figure C.1: **Atomic structure of {112} twin and {332} twin boundary**.**A** is snapshot of an example of {332} twin, which is Ti_5Nb at 77 K under "Confined Simple Shear" condition, and the current applied shear strain is 0.12. Shear direction is along [311] direction on $(\bar{2}33)$ planes. **B** is an enlarged figure showing atomic structure of {332} twin boundary. We can observe α" phase at the twin boundary. **C** is snapshot of an example of {112} twin, which is Ti_4Nb at 300 K under "Non-confined Simple Shear" condition, and the current applied shear strain is 0.12. Shear direction is along [311] direction on $(\bar{2}33)$ planes. **C** is an enlarged figure showing atomic structure of {112} twin boundary, more precisely, twin tip. We can observe ω phase surrounding the tip.

C.7 β Grains Misorientation Plots under Loading.

Here we present the misorientation of β grains(parent phase and new nucleated β phases in different variants along $[0\bar{1}1]$ directions under loading conditions. During loading conditions, there are several β grains in different variants are possible to nucleate. We here define the variant whose volume fraction is largest as the parent phase at deformed state. During loading, as for β grains which is in parent phase, we define the misorientation is relative to initial unrelaxed state. As for the other β grains in different orientations, we calculate the misorientation relative to deformed parent β phase. Consistent with the descriptions in Figure 2 in the manuscript, dominant deformation modes in Figure C.2 (A) is α" phase and only very small amount of new β variant nucleate, the misorientation close to $\{112\}$ twin in a larges distortion state (5° deviates from ideal misorientation angle. Dominant deformation modes in Figure C.2 (B) and (C) are $\{332\}$ twin and $\{112\}$ twin, respectively. Compared to theoretical misorientation of $\{332\}$ twin and $\{112\}$ twin relative to parent β phase, the corresponding misorientation of nucleated twin in MD is close and only $1^\circ - 3^\circ$ deviation, confirming the twin type in the simulation box. As for Figure C.2 (D), the phase transformation behaviors are very limited and almost no new β phase nucleates.

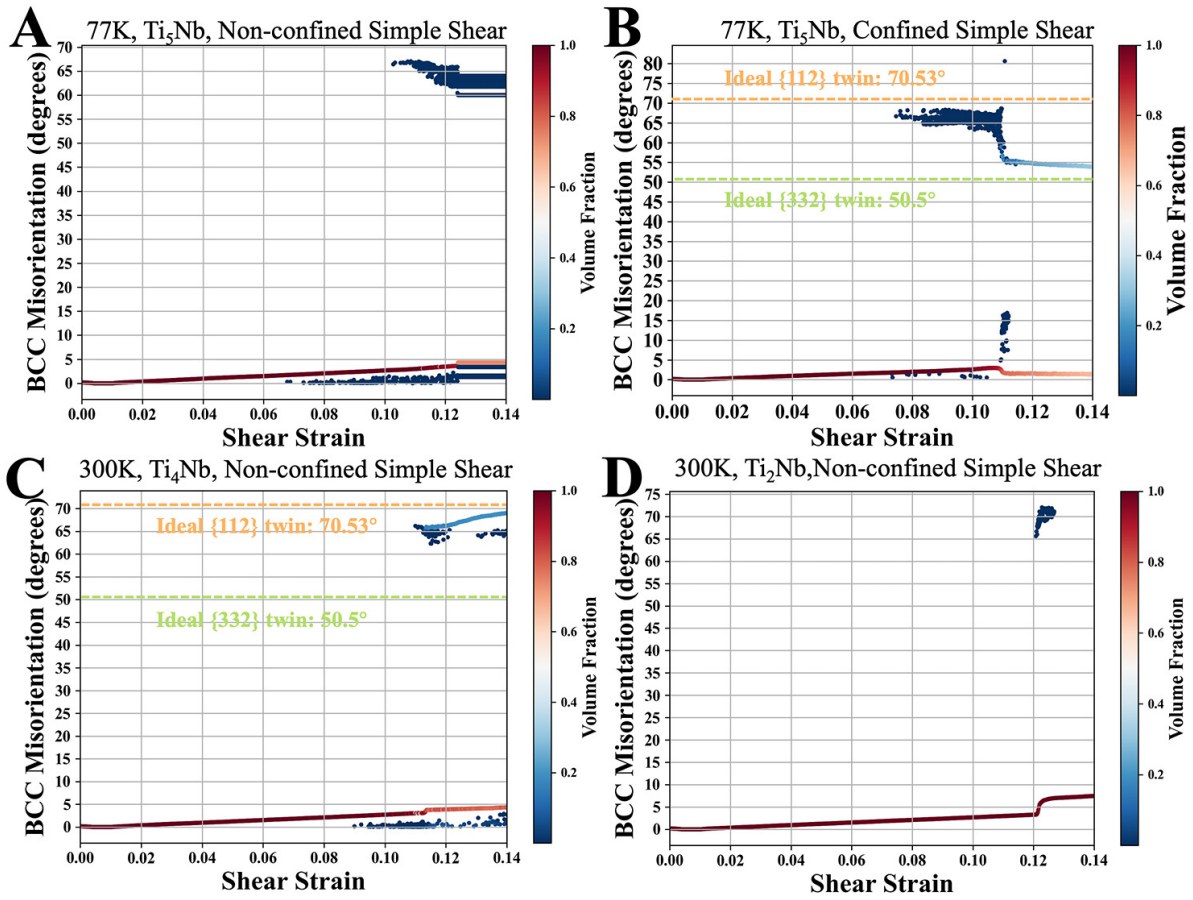


Figure C.2: **Misorientation of β grains along $[0\bar{1}1]$ directions under loading conditions.** Heatmap on data points is based on corresponding volume fraction of total β grains at the certatin strain state. **A** is Ti_5Nb at 77 K, under non-confined simple shear condition, dominant deformation mode is α" martensite with small amount of {112} twin; **B** is Ti_5Nb at 77 K, under confined simple shear condition, dominant deformation mode is {332} twin; **C** is Ti_4Nb at 300 K, under non-confined simple shear condition, dominant deformation mode is {112} twin; **D** is Ti_2Nb at 300 K, under non-confined simple shear condition, dominant deformation mode is dislocation slip.

C.8 Atomic Structure of Deformation Modes and Structural Evolution

Here we show the detailed information on the defects nucleation and structural evolution for different alloy system under different loading conditions, we also previously summarize the dominant deformation modes in Table 1 in the manuscript.

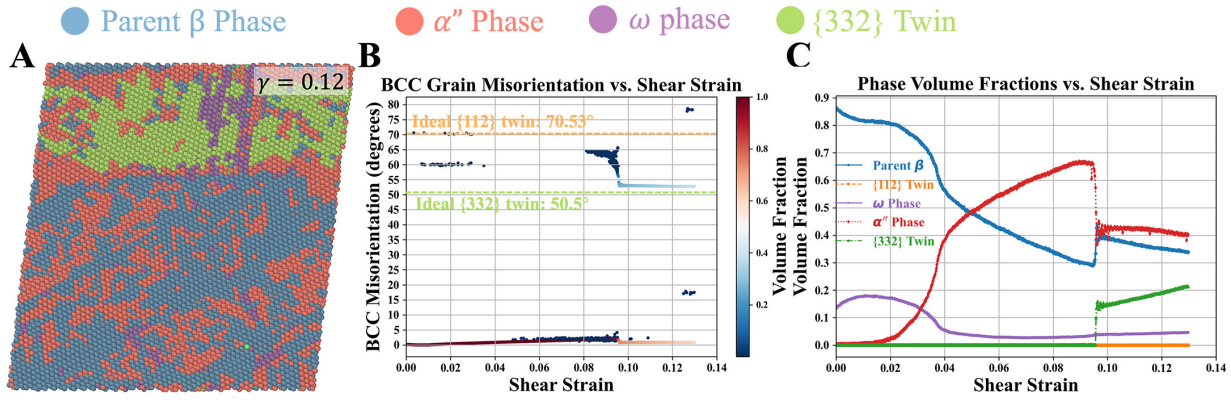


Figure C.3: **Atomistic structural evolution and deformation modes of Ti_5Nb alloys under 300 K and "Confined simple shear" loading condition by MD simulations. In all cases, the shear loading is along [311] direction on $(\bar{2}33)$ planes. (A)** are snapshots of atomistic structures when applied shear strain is 0.12 and dominant deformation mode is {332} twin; **(B)** illustrate how parent β phase evolve during deformation and how new β variants forms and confirm the twin relationship relative to parent phase; **(C)** illustrate nucleation of different metastable phases during shear loading and dynamic volume fraction change. Color interpretation of atoms in the MD snapshots locating at the top of the figure.

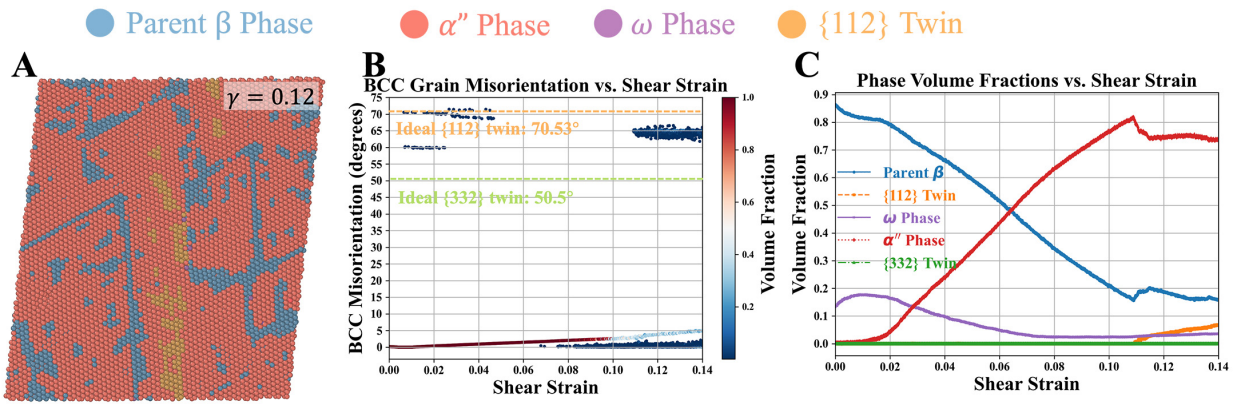


Figure C.4: **Atomistic structural evolution and deformation modes of Ti_5Nb alloys under 300 K and "Non-confined Simple Shear" loading condition by MD simulations. In all cases, the shear loading is along [311] direction on $(\bar{2}33)$ planes.** **(A)** are snapshots of atomistic structures when applied shear strain is 0.12 and dominant deformation mode is {112} twin and α" martensite; **(B)** illustrate how parent β phase evolve during deformation and how new β variants forms and confirm the twin relationship relative to parent phase; **(C)** illustrate nucleation of different metastable phases during shear loading and dynamic volume fraction change. Color interpretation of atoms in the MD snapshots locating at the top of the figure.

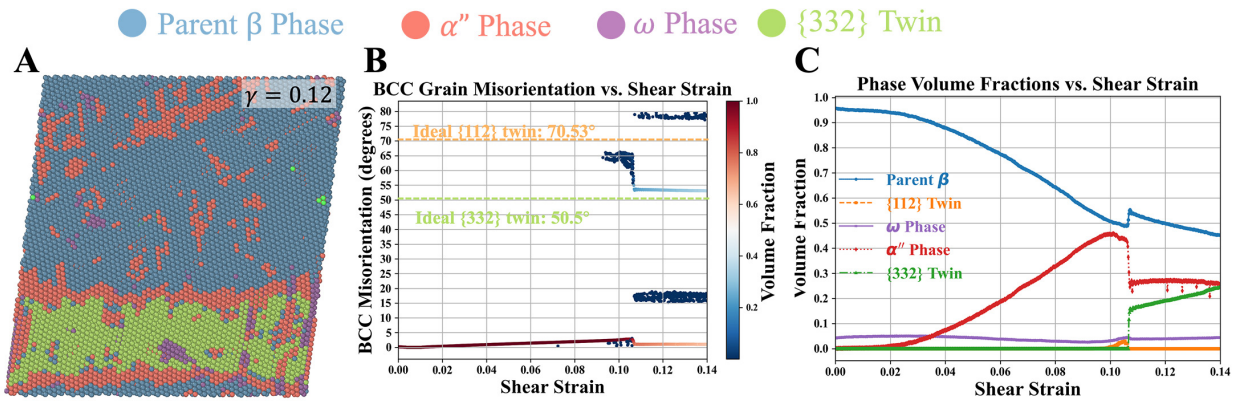


Figure C.5: **Atomistic structural evolution and deformation modes of Ti_4Nb alloys under 77 K and "Confined simple shear" loading condition by MD simulations. In all cases, the shear loading is along [311] direction on $(\bar{2}33)$ planes. (A)** are snapshots of atomistic structures when applied shear strain is 0.12 and dominant deformation mode is {332} twin; **(B)** illustrate how parent β phase evolve during deformation and how new β variants forms and confirm the twin relationship relative to parent phase; **(C)** illustrate nucleation of different metastable phases during shear loading and dynamic volume fraction change. Color interpretation of atoms in the MD snapshots locating at the top of the figure.

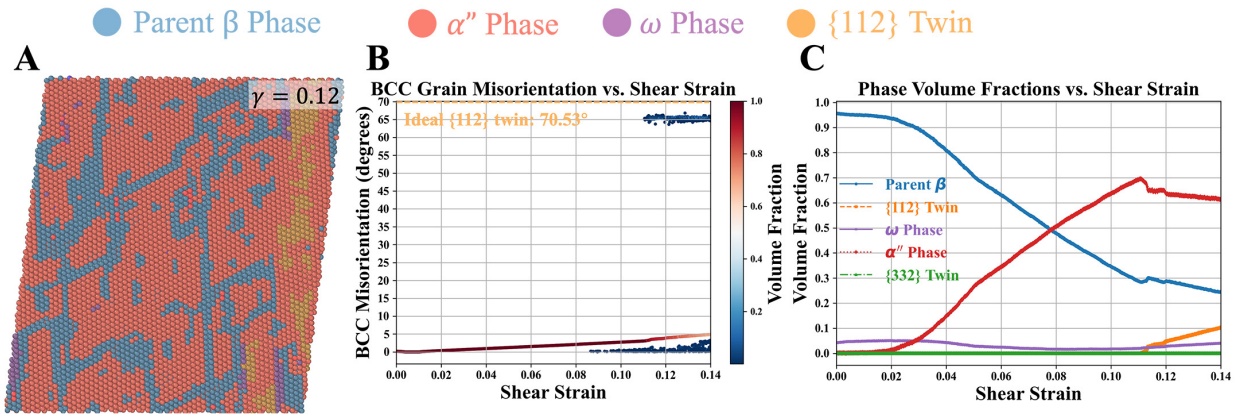


Figure C.6: **Atomistic structural evolution and deformation modes of Ti_4Nb alloys under 77 K and "Non-confined Simple Shear" loading condition by MD simulations. In all cases, the shear loading is along [311] direction on $(\bar{2}33)$ planes.** **(A)** are snapshots of atomistic structures when applied shear strain is 0.12 and dominant deformation mode is {112} twin and α" martensite; **(B)** illustrate how parent β phase evolve during deformation and how new β variants forms and confirm the twin relationship relative to parent phase; **(C)** illustrate nucleation of different metastable phases during shear loading and dynamic volume fraction change. Color interpretation of atoms in the MD snapshots locating at the top of the figure.

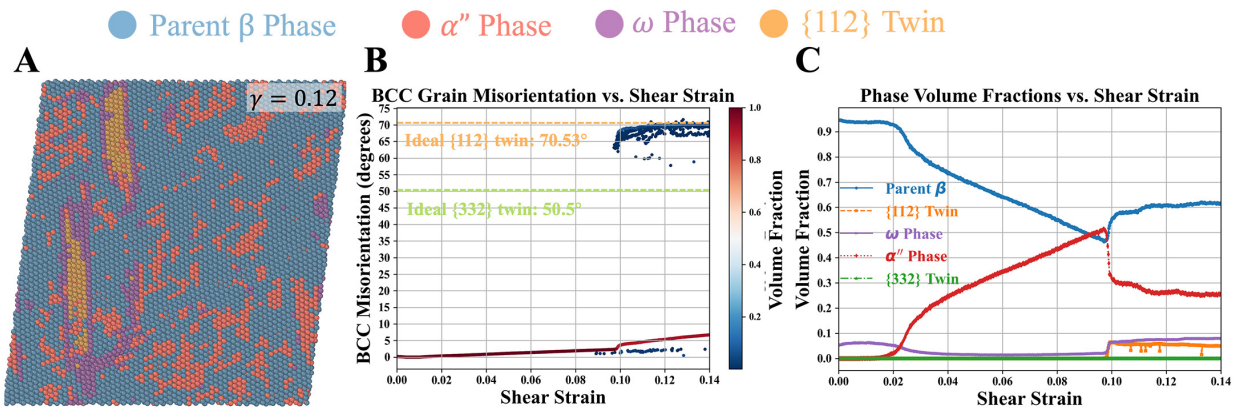


Figure C.7: **Atomistic structural evolution and deformation modes of Ti_4Nb alloys under 300 K and "Confined simple shear" loading condition by MD simulations. In all cases, the shear loading is along [311] direction on $(\bar{2}33)$ planes.** **(A)** are snapshots of atomistic structures when applied shear strain is 0.12 and dominant deformation mode is {112} twin; **(B)** illustrate how parent β phase evolve during deformation and how new β variants forms and confirm the twin relationship relative to parent phase; **(C)** illustrate nucleation of different metastable phases during shear loading and dynamic volume fraction change. Color interpretation of atoms in the MD snapshots locating at the top of the figure.

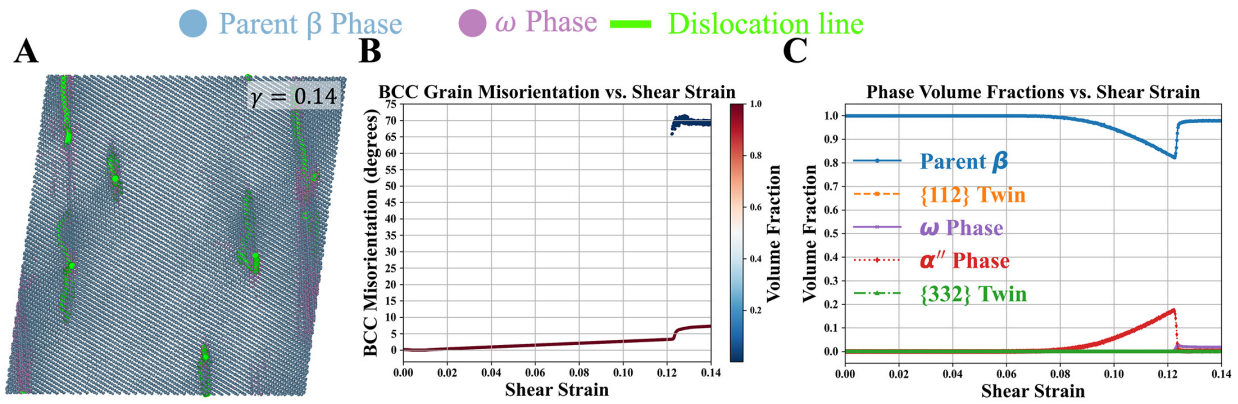


Figure C.8: **Atomistic structural evolution and deformation modes of Ti_2Nb alloys under 77 K and "Confined simple shear" loading condition by MD simulations. In all cases, the shear loading is along [311] direction on $(\bar{2}33)$ planes.** **(A)** are snapshots of atomistic structures when applied shear strain is 0.12 and dominant deformation mode is dislocation slip; **(B)** illustrate how parent β phase evolve during deformation and how new β variants forms and confirm the twin relationship relative to parent phase; **(C)** illustrate nucleation of different metastable phases during shear loading and dynamic volume fraction change. Color interpretation of atoms in the MD snapshots locating at the top of the figure.

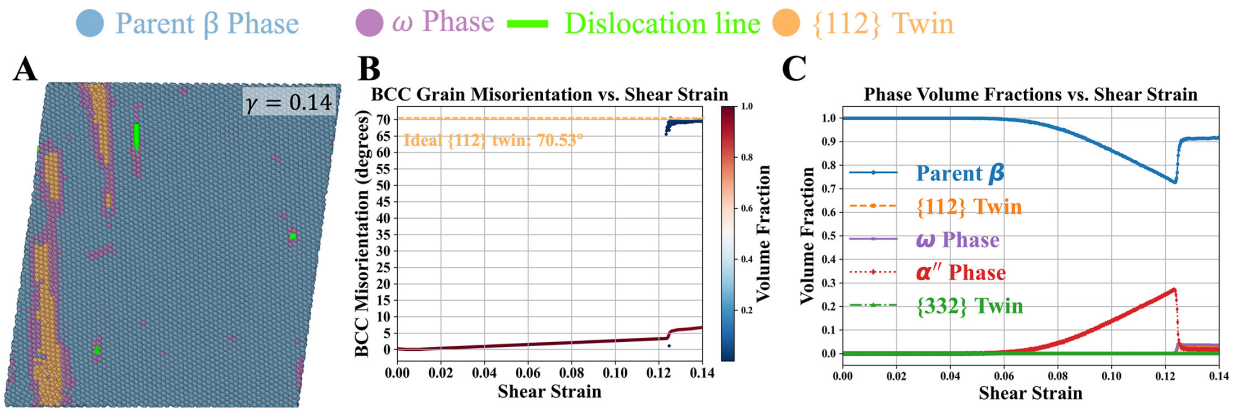


Figure C.9: **Atomistic structural evolution and deformation modes of Ti_2Nb alloys under 77 K and "Non-confined Simple Shear" loading condition by MD simulations. In all cases, the shear loading is along [311] direction on $(\bar{2}33)$ planes. (A)** are snapshots of atomistic structures when applied shear strain is 0.12 and dominant deformation mode is {112} twin and dislocation slip; **(B)** illustrate how parent β phase evolve during deformation and how new β variants forms and confirm the twin relationship relative to parent phase; **(C)** illustrate nucleation of different metastable phases during shear loading and dynamic volume fraction change. Color interpretation of atoms in the MD snapshots locating at the top of the figure.

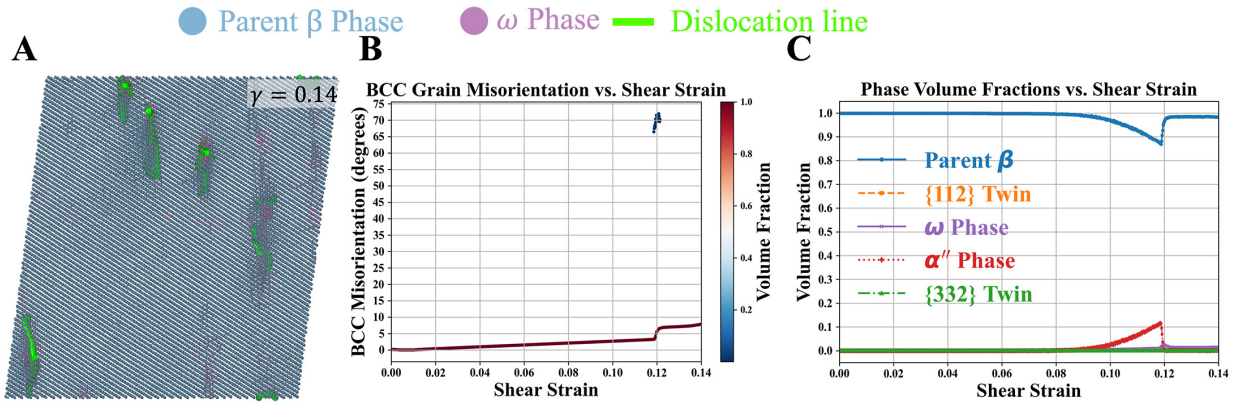


Figure C.10: **Atomistic structural evolution and deformation modes of Ti_2Nb alloys under 300 K and "Confined simple shear" loading condition by MD simulations. In all cases, the shear loading is along [311] direction on $(\bar{2}33)$ planes. (A)** are snapshots of atomistic structures when applied shear strain is 0.12 and dominant deformation mode is dislocation slip; **(B)** illustrate how parent β phase evolve during deformation and how new β variants forms and confirm the twin relationship relative to parent phase; **(C)** illustrate nucleation of different metastable phases during shear loading and dynamic volume fraction change. Color interpretation of atoms in the MD snapshots locating at the top of the figure.

C.9 Free Energy Landscape of Phase Space in Ti-Mo and Ti-Nb Systems

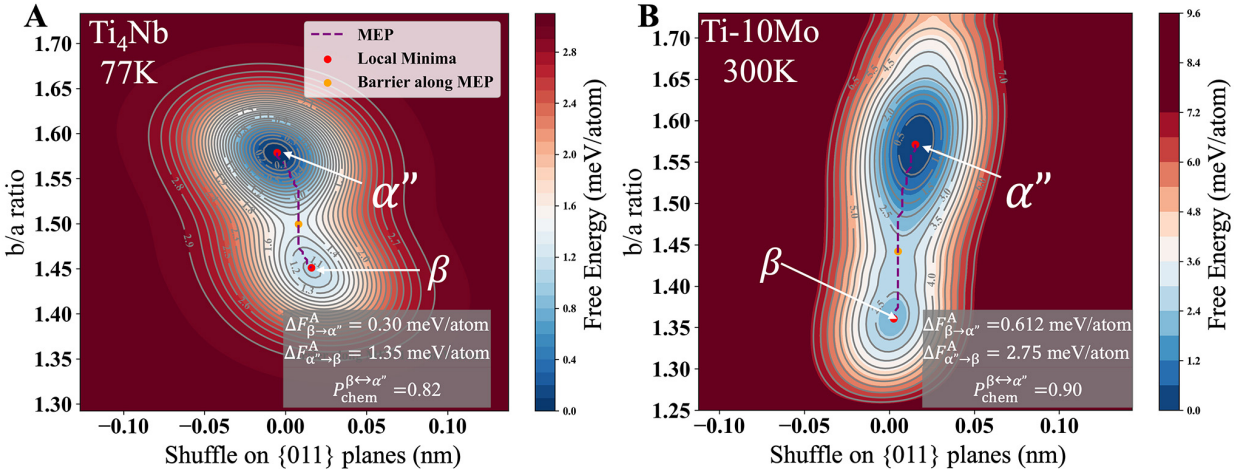


Figure C.11: β-α" **free energy landscape of varies Ti-Nb and Ti-Mo alloy systems at different temperatures. Here we choose two collective variables: shuffle magnitude between (011) planes along** $[0\bar{1}1]$ **directions and "b/a" ratios ("b" is the length of** $\langle 0\bar{1}1 \rangle$ **in** β **and "a" is the length of** $\langle 100 \rangle$ **in** β **phase). Positions of** β **and** α" **phase are marked in the figure. (A)** is Ti_4Nb at 77 K. **(B)** is Ti-10Mo (wt.%) at 300 K.

C.10 Shear Components of β and α" Grains during Shear Loading.

Here we present shear components of β and α" grains at high shear loading state that close to defects nucleation state. In all cases, X is along $[100]_\beta$, Y is along $[011]_\beta$ and Z is along $[0\bar{1}1]_\beta$. U_{xz} and U_{yz} in all cases are at the scale of 0.01% to 0.1%, therefore we not include them into the misfit strain calculation. U_{xy} is at the scale of 2% and so it is not negligible and we keep them into the misfit strain calculation.

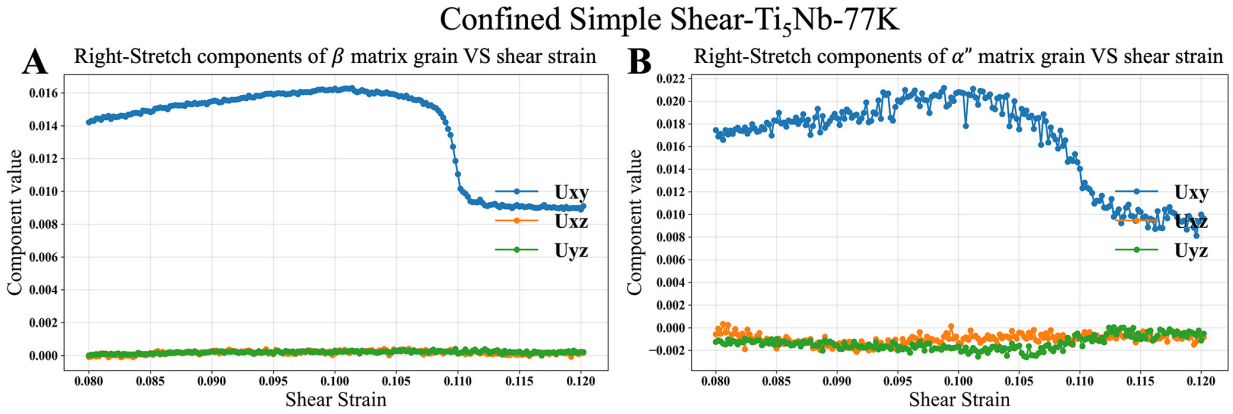


Figure C.12: **Shear components of β and α" grains at high shear loading state that close to defects nucleation state.** Here, X is along $[100]_\beta$, Y is along $[011]_\beta$ and Z is along $[0\bar{1}1]_\beta$. **(A)** is β grain in Ti_5Nb at 77 K, under "Confined simple shear" loading condition and **(B)** is α" phase in Ti_5Nb at 77 K, under "Confined simple shear" loading condition.

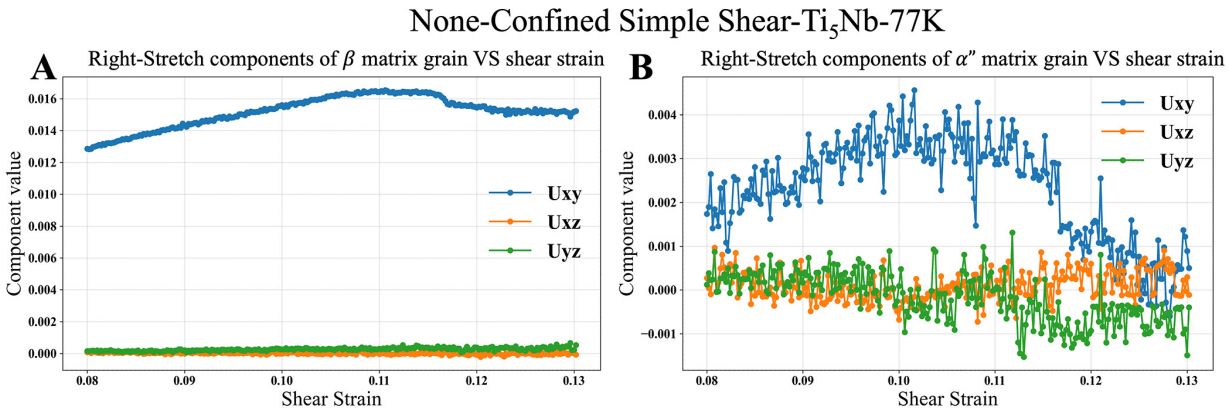


Figure C.13: **Shear components of β and α" grains at high shear loading state that close to defects nucleation state.** Here, X is along $[100]_\beta$, Y is along $[011]_\beta$ and Z is along $[0\bar{1}1]_\beta$. **(A)** is β grain in Ti_5Nb at 77 K, under "Non-confined Simple Shear" loading condition and **(B)** is α" phase in Ti_5Nb at 77 K, under "Non-confined Simple Shear" loading condition.

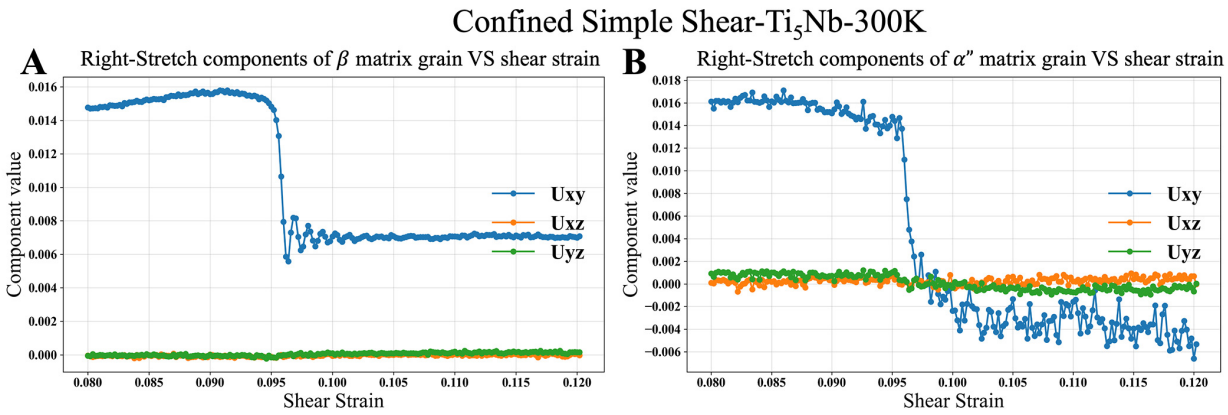


Figure C.14: **Shear components of β and α" grains at high shear loading state that close to defects nucleation state.** Here, X is along $[100]_\beta$, Y is along $[011]_\beta$ and Z is along $[0\bar{1}1]_\beta$. **(A)** is β grain in Ti_5Nb at 300 K, under "Confined simple shear" loading condition and **(B)** is α" phase in Ti_5Nb at 300 K, under "Confined simple shear" loading condition.

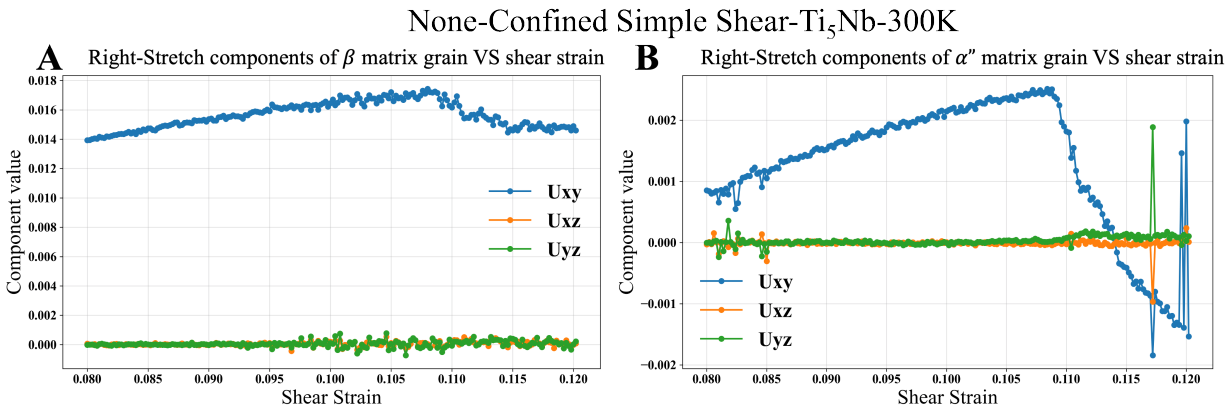


Figure C.15: **Shear components of β and α" grains at high shear loading state that close to defects nucleation state.** Here, X is along $[100]_\beta$, Y is along $[011]_\beta$ and Z is along $[0\bar{1}1]_\beta$. **(A)** is β grain in Ti_5Nb at 300 K, under "Non-confined Simple Shear" loading condition and **(B)** is α" phase in Ti_5Nb at 300 K, under "Non-confined Simple Shear" loading condition.

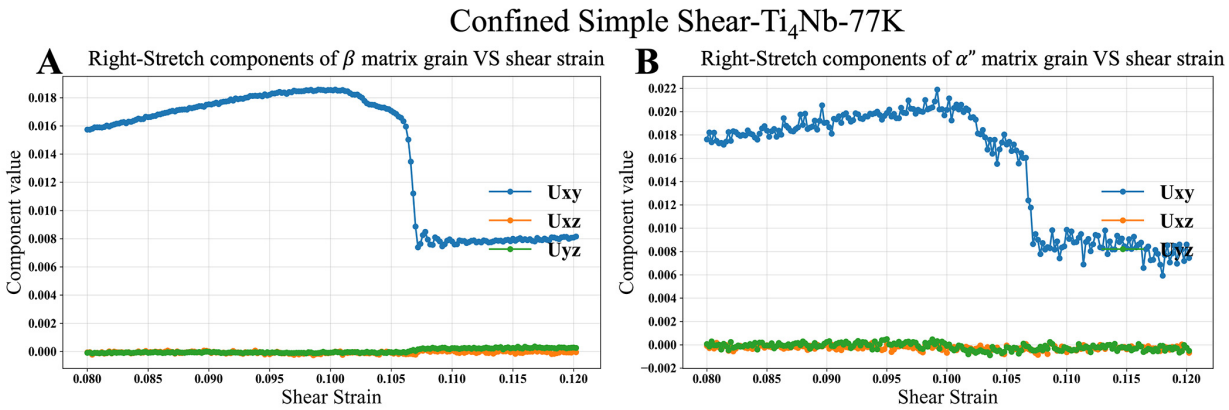


Figure C.16: **Shear components of β and α" grains at high shear loading state that close to defects nucleation state.** Here, X is along $[100]_\beta$, Y is along $[011]_\beta$ and Z is along $[0\bar{1}1]_\beta$. **(A)** is β grain in Ti_4Nb at 77 K, under "Confined simple shear" loading condition and **(B)** is α" phase in Ti_4Nb at 77 K, under "Confined simple shear" loading condition.

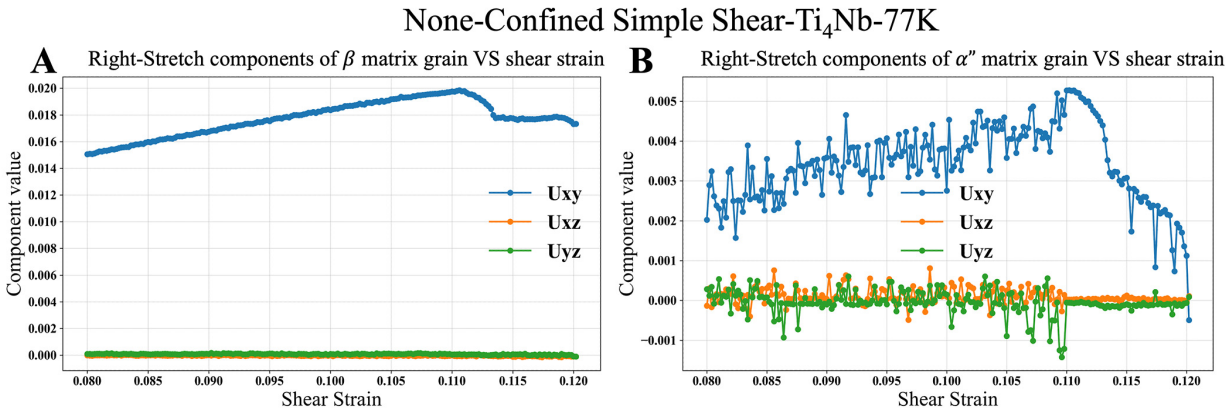


Figure C.17: **Shear components of β and α" grains at high shear loading state that close to defects nucleation state.** Here, X is along $[100]_\beta$, Y is along $[011]_\beta$ and Z is along $[0\bar{1}1]_\beta$. **(A)** is β grain in Ti_4Nb at 77 K, under "Non-confined Simple Shear" loading condition and **(B)** is α" phase in Ti_4Nb at 77 K, under "Non-confined Simple Shear" loading condition.

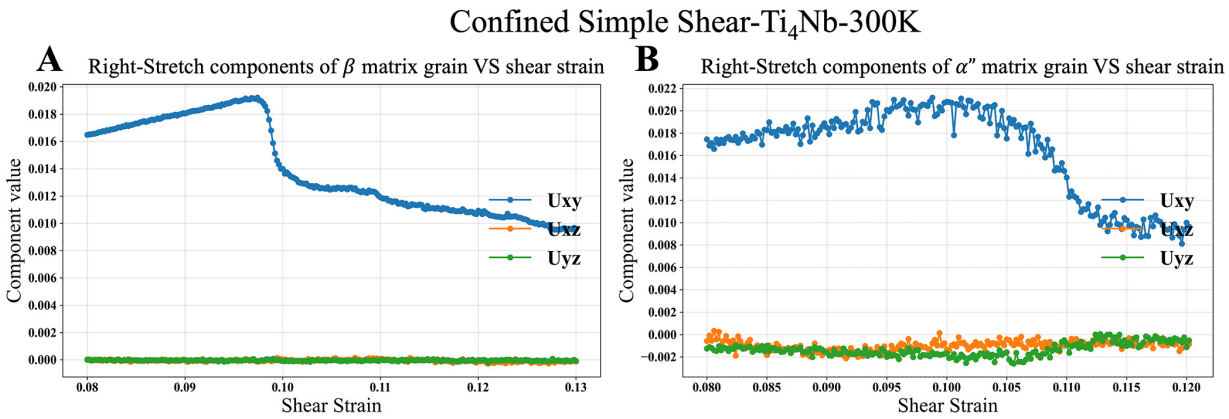


Figure C.18: **Shear components of β and α" grains at high shear loading state that close to defects nucleation state.** Here, X is along $[100]_\beta$, Y is along $[011]_\beta$ and Z is along $[0\bar{1}1]_\beta$. **(A)** is β grain in Ti_4Nb at 300 K, under "Confined simple shear" loading condition and **(B)** is α" phase in Ti_4Nb at 300 K, under "Confined simple shear" loading condition.

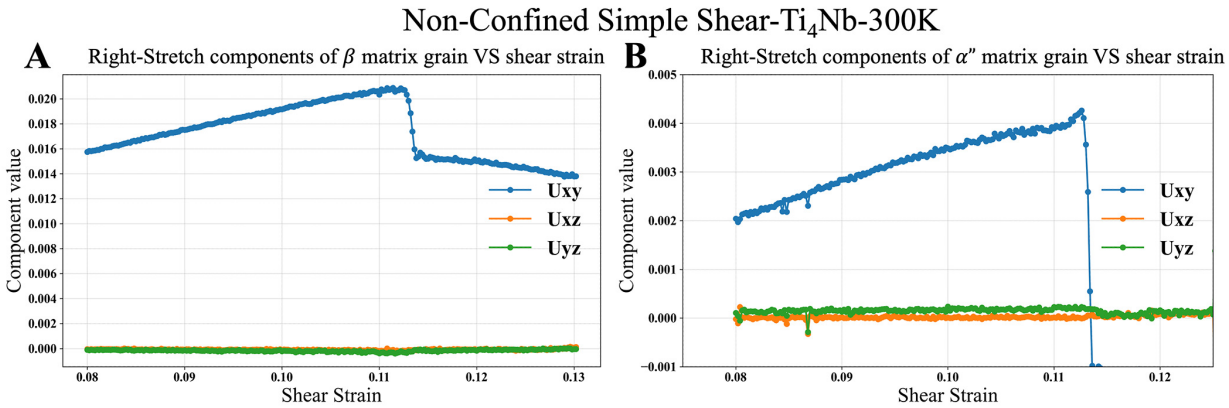


Figure C.19: **Shear components of β and α" grains at high shear loading state that close to defects nucleation state.** Here, X is along $[100]_\beta$, Y is along $[011]_\beta$ and Z is along $[0\bar{1}1]_\beta$. **(A)** is β grain in Ti_4Nb at 300 K, under "Non-confined Simple Shear" loading condition and **(B)** is α" phase in Ti_4Nb at 300 K, under "Non-confined Simple Shear" loading condition.

C.11 Elastic Constants and Elastic Moduli of Ti Alloys at 0 K.

To evaluate the direction-dependent elastic moduli, we employ anisotropic elasticity theory [154]. This calculation requires the crystallographic slip system information, and the elastic constants C_{11}, C_{12} and C_{44}. Figure C.20 presents Nb concentration dependent elastic constants (A) and elastic moduli (B). Here, the elastic constants in Figure C.20 (A) are under the condition of 0 K. Although the elastic constants are generally temperature dependent, Ti-Nb alloys often exhibits an Elinvar-like anomaly and so their elastic constants are very weakly dependent on temperature [76]. Therefore, to ensure efficient and robust estimation, in this study we here directly input 0 K elastic constants to calculate all energetic parameters. The plots of concentration-dependent elastic constants are consistent with the results in the Ti-Nb MEAM potential training data [57]. Figure C.20 (B) shows the curves of elastic moduli at the different Nb concentration. Especially, C' characterize tetragonal shear and shuffle resistance along $\{110\}\langle\bar{1}10\rangle$ slip system, which is linked to β to α" phase transformation. The general trends on the change of shear moduli with Nb concentration is consistent with first-principles DFT calculations [128]. In our study, Nb concentration is no less than 16%, where C' (or C_{11}-C_{12}) is larger than 0, indicating BCC phase can be (meta)stable.

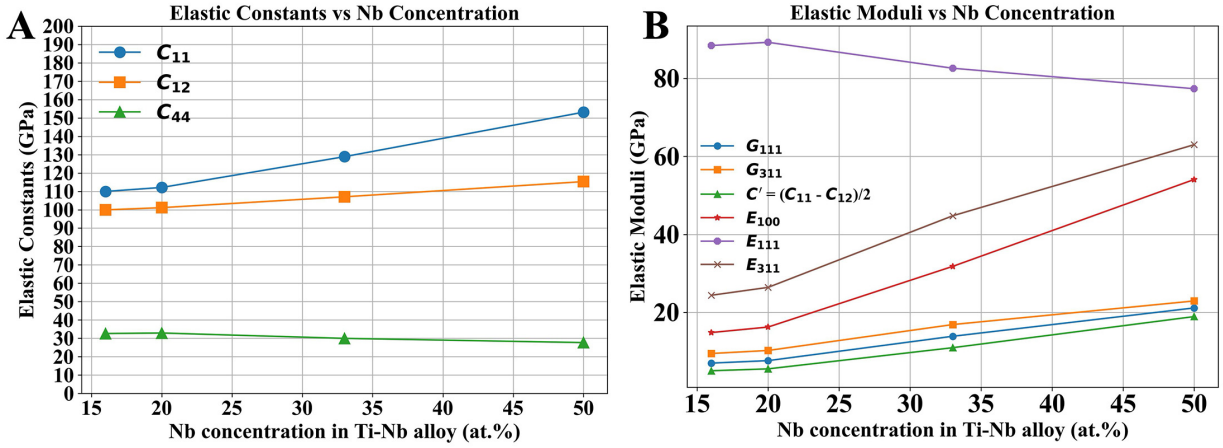


Figure C.20: **Nb concentration dependent elastic constants and shear modulus. A** shows elastic constants of parent β (BCC-like) phase: C_{11} is in blue color; C_{12} is in orange color and C_{44} is in green color. **B** presents directional elastic moduli of parent β phase: G_{111} is in blue color; G_{311} is in orange color, and C' is in green color, which characterize the shear modulus for β to α" phase transformations along Burgers path;E_{100} is in red color;E_{111} is in purple color and E_{311} is in brown color.

C.12 Competition of Δg_{twin} under Loading Conditions

Besides the cases in the manuscript, here we provides the other cases in Table 1 in the manuscript. When shear strain is around 0.1, the α" phase comes to saturation stage and the twin is about to nucleate. The preferred twinning type is whose effective nucleation barrier is smaller at critical stage (shear strain is 0.1). The MD observations on the deformation mode is consistent with trend on the change of Δg_{twin}.

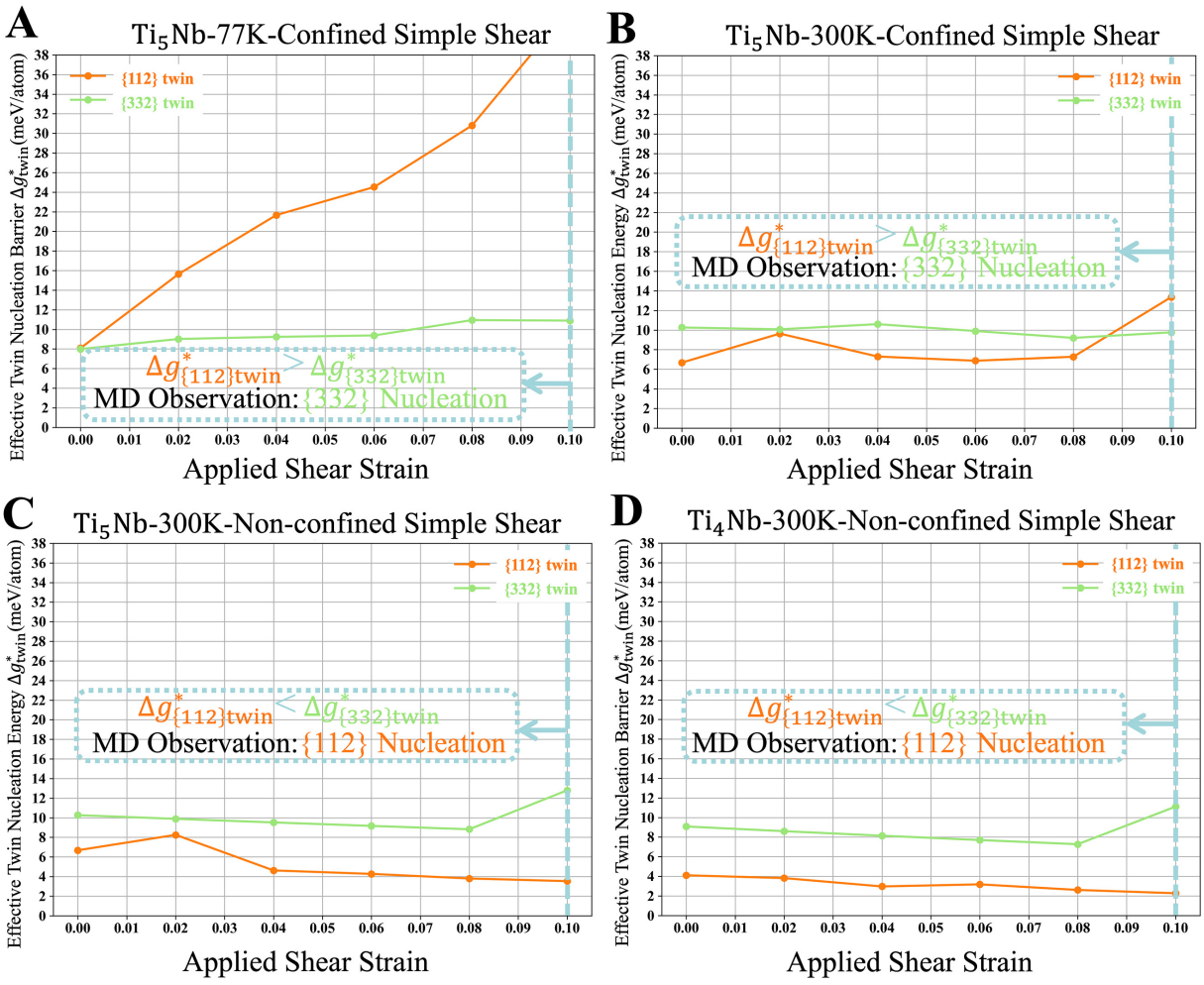


Figure C.21: **Dynamic change of effective twin nucleation metric, Δg_{twin} under loading conditions for different alloy systems.**

BIBLIOGRAPHY

[1] Y Al-Zain, HY Kim, H Hosoda, TH Nam, and S Miyazaki. Shape memory properties of ti–nb–mo biomedical alloys. Acta Materialia, 58(12):4212–4223, 2010.

[2] Michael P Allen and Dominic J Tildesley. Computer simulation of liquids. Oxford university press, 2017.

[3] Dylan M Anstine and Olexandr Isayev. Machine learning interatomic potentials and long-range physics. The Journal of Physical Chemistry A, 127(11):2417–2431, 2023.

[4] Stoichko Antonov, Zachary Kloenne, Yipeng Gao, Dong Wang, Qiang Feng, Yunzhi Wang, Hamish L Fraser, and Yufeng Zheng. Novel deformation twinning system in a cold rolled high-strength metastable-β ti-5al-5v-5mo-3cr-0.5 fe alloy. Materialia, 9:100614, 2020.

[5] Ali Argon. Strengthening mechanisms in crystal plasticity, volume 4. OUP Oxford, 2007.

[6] Edohamen Awannegbe, Yue Zhao, Zhijun Qiu, and Huijun Li. Influence of heat treatment on the tensile properties of ti–15mo additively manufactured by laser metal deposition. Materials Science and Engineering: A, 892:146062, 2024.

[7] JoAnn Ballor, Tong Li, Frédéric Prima, Carl J Boehlert, and Arun Devaraj. A review of the metastable omega phase in beta titanium alloys: The phase transformation mechanisms and its effect on mechanical properties. International Materials Reviews, 68(1):26–45, 2023.

[8] Dipankar Banerjee and JC Williams. Perspectives on titanium science and technology. Acta Materialia, 61(3):844–879, 2013.

[9] Paul J Bania. Beta titanium alloys and their role in the titanium industry. Jom, 46(7):16–19, 1994.

[10] Alessandro Barducci, Giovanni Bussi, and Michele Parrinello. Well-tempered metadynamics: a smoothly converging and tunable free-energy method. Physical review letters, 100(2):020603, 2008.

[11] Emmanuel Bertrand, Philippe Castany, Isabelle Péron, and Thierry Gloriant. Twinning system selection in a metastable β-titanium alloy by schmid factor analysis. Scripta materialia, 64(12):1110–1113, 2011.

[12] Emmanuel Bertrand, Philippe Castany, Yang Yang, Edern Menou, and Thierry Gloriant. Deformation twinning in the full-α" martensitic ti–25ta–20nb shape memory alloy. Acta Materialia, 105:94–103, 2016.

[13] Kaushik Bhattacharya. Microstructure of martensite: why it forms and how it gives rise to the shape-memory effect, volume 2. Oxford University Press, 2003.

[14] Bruce Alexander Bilby and AG Crocker. The theory of the crystallography of deformation twinning. Proceedings of the Royal Society of London. Series A. Mathematical and physical sciences, 288(1413):240–255, 1965.

[15] Erik Bitzek, Pekka Koskinen, Franz Gähler, Michael Moseler, and Peter Gumbsch. Structural relaxation made simple. Physical review letters, 97(17):170201, 2006.

[16] Martin J Blackburn and John A Feeney. Stress-induced transformations in ti-mo alloys. Technical report, BOEING CO RENTON WA COMMERCIAL AIRPLANE GROUP, 1970.

[17] MJ Blackburn. Stress-induced transformations in ti–mo alloys. J. Inst. Metals, 99:132, 1971.

[18] Peter E Blöchl. Projector augmented-wave method. Physical review B, 50(24):17953, 1994.

[19] Thomas Bonald, Bertrand Charpentier, Alexis Galland, and Alexandre Hollocou. Hierarchical graph clustering using node pair sampling. arXiv preprint arXiv:1806.01664, 2018.

[20] Massimiliano Bonomi, Davide Branduardi, Giovanni Bussi, Carlo Camilloni, Davide Provasi, Paolo Raiteri, Davide Donadio, Fabrizio Marinelli, Fabio Pietrucci, Ricardo A Broglia, et al. Plumed: A portable plugin for free-energy calculations with molecular dynamics. Computer Physics Communications, 180(10):1961–1972, 2009.

[21] M Born and R Oppenheimer. Ann. phys. Ann. Phys, 84:457, 1927.

[22] Max Born and Werner Heisenberg. Zur quantentheorie der molekeln. In Original Scientific Papers Wissenschaftliche Originalarbeiten, pages 216–246. Springer, 1985.

[23] Carolina Catanio Bortolan, Leonardo Contri Campanelli, Carlo Paternoster, Nicolas Giguere, Nicolas Brodusch, Claudemiro Bolfarini, Raynald Gauvin, Paolo Mengucci, Gianni Barucca, and Diego Mantovani. Effect of oxygen content on the mechanical properties and plastic deformation mechanisms in the twip/trip ti–12mo alloy. Materials Science and Engineering: A, 817:141346, 2021.

[24] O Bouaziz and NJMS Guelton. Modelling of twip effect on work-hardening. Materials Science and Engineering: A, 319:246–249, 2001.

[25] Olivier Bouaziz, S Allain, CP Scott, P Cugy, and Damien Barbier. High manganese austenitic twinning induced plasticity steels: A review of the microstructure properties relationships. Current opinion in solid state and materials science, 15(4):141–168, 2011.

[26] Renee R Boyer. An overview on the use of titanium in the aerospace industry. Materials Science and Engineering: A, 213(1-2):103–114, 1996.

[27] RR Boyer and RD Briggs. The use of β titanium alloys in the aerospace industry. Journal of Materials Engineering and Performance, 14:681–685, 2005.

[28] PD Bristowe and AG Crocker. A computer simulation study of the structures of twin boundaries in body-centred cubic crystals. The Philosophical Magazine: A Journal of Theoretical Experimental and Applied Physics, 31(3):503–517, 1975.

[29] PD Bristowe, AG Crocker, and MJ Norgett. The structure of twin boundaries in body centred cubic metals. Journal of Physics F: Metal Physics, 4(11):1859, 1974.

[30] C. Brozek, F. Sun, P. Vermaut, Y. Millet, A. Lenain, D. Embury, P.J. Jacques, and F. Prima. A β-titanium alloy with extra high strain-hardening rate: Design and mechanical properties. Scripta Materialia, 114:60–64, 2016.

[31] C Brozek, F Sun, P Vermaut, Y Millet, Astrid Lenain, D Embury, PJ Jacques, and F Prima. A β-titanium alloy with extra high strain-hardening rate: design and mechanical properties. Scripta Materialia, 114:60–64, 2016.

[32] WG Burgers. On the process of transition of the cubic-body-centered modification into the hexagonal-close-packed modification of zirconium. Physica, 1(7-12):561–586, 1934.

[33] Giovanni Bussi, Davide Donadio, and Michele Parrinello. Canonical sampling through velocity rescaling. The Journal of chemical physics, 126(1), 2007.

[34] John W Cahn. Nucleation on dislocations. Acta Metallurgica, 5(3):169–172, 1957.

[35] MZ Cao and BB He. A review on deformation mechanisms of metastable β titanium alloys. Journal of Materials Science, 59(32):14981–15016, 2024.

[36] P Castany, Y Yang, E Bertrand, and T Gloriant. Reversion of a parent $\{130\}\langle 310\rangle$ α" martensitic twinning system at the origin of {332}langle 113rangle β twins observed in metastable β titanium alloys. Physical review letters, 117(24):245501, 2016.

[37] Bin Chen and Wei Sun. Omega transitional structure associated with $\{112\}$ $\langle 111\rangle$ deformation twinning in a metastable beta ti-nb alloy, revealed by atomic resolution high-angle annular dark-field scanning transmission electron microscopy. Journal of Alloys and Compounds, 766:123–130, 2018.

[38] Bin Chen and Wei Sun. Transitional structure of $\{332\}\langle 113\rangle\beta$ twin boundary in a deformed metastable β-type ti-nb-based alloy, revealed by atomic resolution electron microscopy. Scripta Materialia, 150:115–119, 2018.

[39] Ganlin Chen, Dian Li, Yufeng Zheng, and Liang Qi. Stability and growth kinetics of $\{112\}$ twin embryos in β-ti alloys. Acta Materialia, 263:119520, 2024.

[40] Long-Qing Chen. Phase-field models for microstructure evolution. Annual review of materials research, 32(1):113–140, 2002.

[41] Ken Cho, Ryota Morioka, Stefanus Harjo, Takuro Kawasaki, and Hiroyuki Y Yasuda. Study on formation mechanism of $\{332\}\langle 113\rangle$ deformation twinning in metastable β-type ti alloy focusing on stress-induced α" martensite phase. Scripta Materialia, 177:106–111, 2020.

[42] Kathleen Chou, Nan Li, and Emmanuelle A Marquis. Enhanced work hardening from oxygen-stabilized ω precipitates in an aged metastable β ti-nb alloy. Acta Materialia, 220:117302, 2021.

[43] Kathleen Chou and Emmanuelle A Marquis. Oxygen effects on ω and α phase transformations in a metastable β ti–nb alloy. Acta Materialia, 181:367–376, 2019.

[44] Kathleen Chou and Emmanuelle A Marquis. Role of oxygen on the precipitation and deformation behavior of an aged β ti-15mo alloy. Journal of Alloys and Compounds, 891:161811, 2022.

[45] John Wyrill Christian. The theory of transformations in metals and alloys. i. Equilibrium and general kinetic theory., 1975.

[46] John Wyrill Christian and Subhash Mahajan. Deformation twinning. Progress in materials science, 39(1-2):1–157, 1995.

[47] JW Christian, GB Olson, and M Cohen. Classification of displacive transformations: What is a martensitic transformation? Le Journal de Physique IV, 5(C8):C8–3, 1995.

[48] Marion Coffigniez, P-P De Breuck, Laurine Choisez, Matthieu Marteleur, MJ van Setten, Guido Petretto, G-M Rignanese, and PJ Jacques. Combination of ab initio descriptors and machine learning approach for the prediction of the plasticity mechanisms in β-metastable ti alloys. Materials & Design, 239:112801, 2024.

[49] The PLUMED consortium. Promoting transparency and reproducibility in enhanced molecular simulations. Nature methods, 16(8):670–673, 2019.

[50] AH Cottrell and BA Bilby. Lx. a mechanism for the growth of deformation twins in crystals. The London, Edinburgh, and Dublin Philosophical Magazine and Journal of Science, 42(329):573–581, 1951.

[51] AG Crocker. Twinned martensite. Acta Metallurgica, 10(2):113–122, 1962.

[52] CY Cui and DH Ping. Microstructural evolution and ductility improvement of a ti–30nb alloy with pd addition. Journal of alloys and compounds, 471(1-2):248–252, 2009.

[53] Alexandru Dan, Elisabeta Mirela Cojocaru, Doina Raducanu, Anna Nocivin, Ion Cinca, and Vasile Danut Cojocaru. $\{332\}\langle 113\rangle$ and $\{112\}\langle 111\rangle$ twin variant activation during cold-rolling of a ti-nb-zr-ta-sn-fe alloy. Materials, 15(19):6932, 2022.

[54] Murray S Daw and Michael I Baskes. Embedded-atom method: Derivation and application to impurities, surfaces, and other defects in metals. Physical review B, 29(12):6443, 1984.

[55] Bruno C De Cooman, Yuri Estrin, and Sung Kyu Kim. Twinning-induced plasticity (twip) steels. Acta Materialia, 142:283–362, 2018.

[56] Hui-ping Duan, Hong-xia Xu, Wen-huang Su, Yu-bin Ke, Zeng-qian Liu, and Hong-hai Song. Effect of oxygen on the microstructure and mechanical properties of ti-23nb-0.7 ta-2zr alloy. International Journal of Minerals, Metallurgy, and Materials, 19:1128–1133, 2012.

[57] Robert C Ehemann and John W Wilkins. Force-matched empirical potential for martensitic transitions and plastic deformation in ti-nb alloys. Physical Review B, 96(18):184105, 2017.

[58] John Douglas Eshelby. The elastic field outside an ellipsoidal inclusion. Proceedings of the royal society of London. Series A. Mathematical and physical sciences, 252(1271):561–569, 1959.

[59] Daniel Faken and Hannes Jónsson. Systematic analysis of local atomic structure combined with 3d computer graphics. Computational Materials Science, 2(2):279–286, 1994.

[60] Benhu Fan, Xiaoguang Mei, Kuan Sun, and Jianyong Ouyang. Conducting polymer/carbon nanotube composite as counter electrode of dye-sensitized solar cells. Applied Physics Letters, 93(14), 2008.

[61] Eilon Faran and Doron Shilo. Twin motion faster than the speed of sound. Physical review letters, 104(15):155501, 2010.

[62] Ya-Xin Feng, Jia-Xiang Shang, Zeng-Hui Liu, and Guang-Hong Lu. The energy and structure of (1 1 0) twist grain boundary in tungsten. Applied Surface Science, 357:262–267, 2015.

[63] FD Fischer, QP Sun, and K Tanaka. Transformation-induced plasticity (trip). Applied Mechanics Reviews, 49(6):317, 1996.

[64] Franz-Dieter Fischer, G Reisner, E Werner, K_ Tanaka, Georges Cailletaud, and T Antretter. A new view on transformation induced plasticity (trip). International Journal of Plasticity, 16(7-8):723–748, 2000.

[65] Søren L Frederiksen and Karsten W Jacobsen. Density functional theory studies of screw dislocation core structures in bcc metals. Philosophical magazine, 83(3):365–375, 2003.

[66] Rodrigo Freitas and Yifan Cao. Machine-learning potentials for crystal defects. MRS Communications, 12(5):510–520, 2022.

[67] Yu Fu, Yue Gao, Wentao Jiang, Wenlong Xiao, Xinqing Zhao, and Chaoli Ma. A review of deformation mechanisms, compositional design, and development of titanium alloys with transformation-induced plasticity and twinning-induced plasticity effects. Metals, 14(1):97, 2024.

[68] Brent Fultz. Phase transitions in materials. Cambridge University Press, 2020.

[69] Tadahiko Furuta, Shigeru Kuramoto, Chen Rong, Junghwang Hwang, Kazuaki Nishino, Takashi Saito, and Masahiko Ikeda. Effect of oxygen on phase stability and elastic deformation behavior in gum metal. Journal of the Japan Institute of Metals, 70(7):579–585, 2006.

[70] SB Gabriel, JVP Panaino, ID Santos, LS Araujo, PR Mei, LH De Almeida, and CA Nunes. Characterization of a new beta titanium alloy, ti–12mo–3nb, for biomedical applications. Journal of Alloys and Compounds, 536:S208–S210, 2012.

[71] Junheng Gao, Yuhe Huang, Dikai Guan, Alexander J Knowles, Le Ma, David Dye, and W Mark Rainforth. Deformation mechanisms in a metastable beta titanium twinning induced plasticity alloy with high yield strength and high strain hardening rate. Acta Materialia, 152:301–314, 2018.

[72] Yipeng Gao, Jia-Hong Ke, Bo Mao, Yiliang Liao, Yufeng Zheng, and Larry K Aagesen. Twinning path determined by broken symmetry: A revisit to deformation twinning in hexagonal close-packed titanium and zirconium. Physical Review Materials, 4(7):070601, 2020.

[73] Yipeng Gao, Rongpei Shi, Jian-Feng Nie, Suliman A Dregia, and Yunzhi Wang. Group theory description of transformation pathway degeneracy in structural phase transformations. Acta Materialia, 109:353–363, 2016.

[74] Yipeng Gao, Yufeng Zheng, Hamish Fraser, and Yunzhi Wang. Intrinsic coupling between twinning plasticity and transformation plasticity in metastable β ti-alloys: a symmetry and pathway analysis. Acta Materialia, 196:488–504, 2020.

[75] Yue Gao, Wenlong Xiao, Damon Kent, Junshuai Wang, Wentao Jiang, Fanqiang Meng, Ziling Peng, Yu Fu, and Chaoli Ma. Manipulating twip/trip via oxygen-doping to synergistically enhance strength and ductility of metastable beta titanium alloys. Journal of Materials Science & Technology, 215:58–70, 2025.

[76] DL Gong, HL Wang, SH Hao, Peng Liu, X Yang, YN Jiang, WJ Wang, Kun Lin, Bing Li, Kui Du, et al. Ordering-induced elinvar effect over a wide temperature range in a spinodal decomposition titanium alloy. Journal of Materials Science & Technology, 150:245–255, 2023.

[77] DM Gordin, F Sun, D Laillé, F Prima, and T Gloriant. How a new strain transformable titanium-based biomedical alloy can be designed for balloon expendable stents. Materialia, 10:100638, 2020.

[78] Roman Gröger, Jakub Holzer, and Tomáš Kruml. Twinning and antitwinning in body-centered cubic metals. Computational Materials Science, 216:111874, 2023.

[79] Ivan Gutierrez-Urrutia, Cheng Lin Li, Xin Ji, Satoshi Emura, and Koichi Tsuchiya. Twinning and detwinning mechanisms in beta-ti alloys. In Materials Science Forum, volume 941, pages 821–826. Trans Tech Publ, 2019.

[80] S Hanada and O Izumi. Transmission electron microscopic observations of mechanical twinning in metastable beta titanium alloys. Metallurgical Transactions A, 17:1409–1420, 1986.

[81] S Hanada and O Izumi. Correlation of tensile properties, deformation modes, and phase stability in commercial β-phase titanium alloys. Metallurgical and Materials Transactions A, 18:265–271, 1987.

[82] S Hanada, M Ozeki, and O Izumi. Deformation characteristics in β phase ti-nb alloys. Metallurgical transactions A, 16:789–795, 1985.

[83] S Hanada, T Yoshio, and O Izumi. Effect of plastic deformation modes on tensile properties of beta titanium alloys. Transactions of the Japan institute of metals, 27(7):496–503, 1986.

[84] YL Hao, SJ Li, SY Sun, and R Yang. Effect of zr and sn on young's modulus and superelasticity of ti–nb-based alloys. Materials Science and Engineering: A, 441(1-2):112–118, 2006.

[85] YL Hao, SJ Li, SY Sun, CY Zheng, QM Hu, and Rui Yang. Super-elastic titanium alloy with unstable plastic deformation. Applied Physics Letters, 87(9), 2005.

[86] YL Hao, SJ Li, SY Sun, CY Zheng, and Rui Yang. Elastic deformation behaviour of ti–24nb–4zr–7.9 sn for biomedical applications. Acta biomaterialia, 3(2):277–286, 2007.

[87] YL Hao, HL Wang, T Li, JM Cairney, AV Ceguerra, YD Wang, Y Wang, D Wang, EG Obbard, SJ Li, et al. Superelasticity and tunable thermal expansion across a wide temperature range. Journal of Materials Science & Technology, 32(8):705–709, 2016.

[88] OBM Hardouin Duparc. A review of some elements for the history of mechanical twinning centred on its german origins until otto mügge's k 1 and k 2 invariant plane notation. Journal of materials science, 52(8):4182–4196, 2017.

[89] M Hida, Eiichi Sukedai, C Henmi, K Sakaue, and H Terauchi. Stress induced products and ductility due to lattice instability of β phase single crystal of ti-mo alloys. Acta Metallurgica, 30(8):1471–1479, 1982.

[90] Pierre Hohenberg and Walter Kohn. Inhomogeneous electron gas. Physical review, 136(3B):B864, 1964.

[91] J Dana Honeycutt and Hans C Andersen. Molecular dynamics study of melting and freezing of small lennard-jones clusters. Journal of Physical Chemistry, 91(19):4950–4963, 1987.

[92] William G Hoover. Canonical dynamics: Equilibrium phase-space distributions. Physical review A, 31(3):1695, 1985.

[93] TY Hsu. Martensitic transformation under stress. Materials Science and Engineering: A, 438:64–68, 2006.

[94] Hailong Huang, Yuan Wu, Junyang He, Hui Wang, Xiongjun Liu, Ke An, Wei Wu, and Zhaoping Lu. Phase-transformation ductilization of brittle high-entropy alloys via metastability engineering. Advanced Materials, 29(30):1701678, 2017.

[95] Yuji Ikeda, Konstantin Gubaev, Jörg Neugebauer, Blazej Grabowski, and Fritz Körmann. Chemically induced local lattice distortions versus structural phase transformations in compositionally complex alloys. npj Computational Materials, 7(1):34, 2021.

[96] Robert M Jones. Mechanics of composite materials. CRC press, 2018.

[97] Larry Kaufman and Morris Cohen. Thermodynamics and kinetics of martensitic transformations. Progress in metal physics, 7:165–246, 1958.

[98] Ken Kelton and Alan Lindsay Greer. Nucleation in condensed matter: applications in materials and biology, volume 15. Elsevier, 2010.

[99] Armen G Khachaturyan. Theory of structural transformations in solids. Courier Corporation, 2013.

[100] Hee Young Kim, Jie Fu, Hirobumi Tobe, Jae Il Kim, and Shuichi Miyazaki. Crystal structure, transformation strain, and superelastic property of ti–nb–zr and ti–nb–ta alloys. Shape memory and Superelasticity, 1(2):107–116, 2015.

[101] Hee Young Kim, Satoru Hashimoto, Jae Il Kim, Hideki Hosoda, and Shuichi Miyazaki. Mechanical properties and shape memory behavior of ti-nb alloys. materials Transactions, 45(7):2443–2448, 2004.

[102] Hee Young Kim and Shuichi Miyazaki. Martensitic transformation and superelastic properties of ti-nb base alloys. Materials Transactions, 56(5):625–634, 2015.

[103] HY Kim, Y Ikehara, J Il Kim, H Hosoda, and Shuichi Miyazaki. Martensitic transformation, shape memory effect and superelasticity of ti–nb binary alloys. Acta materialia, 54(9):2419–2429, 2006.

[104] Walter Kohn and Lu Jeu Sham. Self-consistent equations including exchange and correlation effects. Physical review, 140(4A):A1133, 1965.

[105] R Prakash Kolli and Arun Devaraj. A review of metastable beta titanium alloys. Metals, 8(7):506, 2018.

[106] Georg Kresse and Jürgen Furthmüller. Efficiency of ab-initio total energy calculations for metals and semiconductors using a plane-wave basis set. Computational materials science, 6(1):15–50, 1996.

[107] Georg Kresse and Jürgen Hafner. Ab initio molecular dynamics for liquid metals. Physical review B, 47(1):558, 1993.

[108] Georg Kresse and Daniel Joubert. From ultrasoft pseudopotentials to the projector augmented-wave method. Physical review b, 59(3):1758, 1999.

[109] Sebastian A Kube and Jan Schroers. Metastability in high entropy alloys. Scripta Materialia, 186:392–400, 2020.

[110] P Kwasniak, F Sun, S Mantri, R Banerjee, and F Prima. Polymorphic nature of {332}¡ 113¿ twinning mode in bcc alloys. Materials Research Letters, 10(5):334–342, 2022.

[111] MJ Lai, Tong Li, and Dierk Raabe. ω phase acts as a switch between dislocation channeling and joint twinning-and transformation-induced plasticity in a metastable β titanium alloy. Acta Materialia, 151:67–77, 2018.

[112] MJ Lai, Cemal Cem Tasan, and Dierk Raabe. Deformation mechanism of ω-enriched ti–nb-based gum metal: Dislocation channeling and deformation induced ω–β transformation. Acta Materialia, 100:290–300, 2015.

[113] MJ Lai, Cemal Cem Tasan, and Dierk Raabe. On the mechanism of {332} twinning in metastable β titanium alloys. Acta Materialia, 111:173–186, 2016.

[114] MJ Lai, Cemal Cem Tasan, Jian Zhang, Blazej Grabowski, LF Huang, and Dierk Raabe. Origin of shear induced β to ω transition in ti–nb-based alloys. Acta Materialia, 92:55–63, 2015.

[115] Alessandro Laio and Michele Parrinello. Escaping free-energy minima. Proceedings of the national academy of sciences, 99(20):12562–12566, 2002.

[116] Lev Davidovich Landau et al. On the theory of phase transitions. Zh. eksp. teor. Fiz, 7(19-32):926, 1937.

[117] Peter Mahler Larsen, Søren Schmidt, and Jakob Schiøtz. Robust structural identification via polyhedral template matching. Modelling and Simulation in Materials Science and Engineering, 24(5):055007, 2016.

[118] Hassel Ledbetter and Martin L Dunn. Habit planes, inclusion theory, and twins. Materials Science and Engineering: A, 273:222–225, 1999.

[119] JK Lee and MH Yoo. Elastic strain energy of deformation twinning in tetragonal crystals. Metallurgical Transactions A, 21(9):2521–2530, 1990.

[120] Christoph Leyens and Manfred Peters. Titanium and titanium alloys: fundamentals and applications. Wiley Online Library, 2006.

[121] Mingjia Li and Xiaohua Min. Origin of ω-phase formation in metastable β-type ti-mo alloys: cluster structure and stacking fault. Scientific Reports, 10(1):1–15, 2020.

[122] Peiyou Li, Xindi Ma, Ting Tong, and Yongshan Wang. Microstructural and mechanical properties of β-type ti–mo–nb biomedical alloys with low elastic modulus. Journal of Alloys and Compounds, 815:152412, 2020.

[123] Xiyao Li, Ze Zhang, and Jiangwei Wang. Deformation twinning in body-centered cubic metals and alloys. Progress in Materials Science, 139:101160, 2023.

[124] Xiyao Li, Qingkun Zhao, Yanzhong Tian, Qiannan Wang, Jitang Fan, Kexing Song, Haofei Zhou, and Jiangwei Wang. Phase transformation induced transitional twin boundary in body-centered cubic metals. Acta Materialia, page 118815, 2023.

[125] Qianglong Liang, Zachary Kloenne, Yufeng Zheng, Dong Wang, Stoichko Antonov, Yipeng Gao, Yulin Hao, Rui Yang, Yunzhi Wang, and Hamish L Fraser. The role of nano-scaled structural non-uniformities on deformation twinning and stress-induced transformation in a cold rolled multifunctional β-titanium alloy. Scripta Materialia, 177:181–185, 2020.

[126] Lola Lilensten, Jean-Philippe Couzinié, Julie Bourgon, Loïc Perrière, Guy Dirras, Frédéric Prima, and Ivan Guillot. Design and tensile properties of a bcc ti-rich high-entropy alloy with transformation-induced plasticity. Materials Research Letters, 5(2):110–116, 2017.

[127] Hong Liu, Fengxiang Lin, Nele Moelans, Liming Peng, Jian-Feng Nie, and Irene J Beyerlein. Three-dimensional shape and stress field of a deformation twin in magnesium. Acta Materialia, 250:118845, 2023.

[128] Mingyuan Lv, Xiaohua Min, and Fengjin Liu. A novel approach to control the thermal/stress-induced products of body-centered cubic titanium alloys in terms of specific orientation moduli. Acta Materialia, 284:120594, 2025.

[129] R Maddin. A history of martensite: some thoughts on the early hardening of iron. ASM International, Martensite(USA), 1992,, pages 11–19, 1992.

[130] S Mahajan. Accommodation at deformation twins in bcc crystals. Metallurgical Transactions A, 12:379–386, 1981.

[131] Srinivas Aditya Mantri, F Sun, Deep Choudhuri, Talukder Alam, Bharat Gwalani, Frederic Prima, and Rajarshi Banerjee. Deformation induced hierarchical twinning coupled with omega transformation in a metastable β-ti alloy. Scientific reports, 9(1):1334, 2019.

[132] Matthieu Marteleur, Hosni Idrissi, Behnam Amin-Ahmadi, Frédéric Prima, Dominique Schryvers, and PJ Jacques. On the nucleation mechanism of {112}¡ 111¿ mechanical twins in as-quenched β metastable ti-12 wt.% mo alloy. Materialia, 7:100418, 2019.

[133] Matthieu Marteleur, Fan Sun, Thierry Gloriant, Philippe Vermaut, Pascal J Jacques, and Frédéric Prima. On the design of new β-metastable titanium alloys with improved work hardening rate thanks to simultaneous trip and twip effects. Scripta Materialia, 66(10):749–752, 2012.

[134] Matthieu Marteleur, Fan Sun, Thierry Gloriant, Philippe Vermaut, Pascal J. Jacques, and Frédéric Prima. On the design of new β-metastable titanium alloys with improved

work hardening rate thanks to simultaneous trip and twip effects. Scripta Materialia, 66(10):749–752, 2012.

[135] Simone Melchionna, Giovanni Ciccotti, and Brad Lee Holian. Hoover npt dynamics for systems varying in shape and size. Molecular Physics, 78(3):533–544, 1993.

[136] MPAT Methfessel and AT Paxton. High-precision sampling for brillouin-zone integration in metals. Physical Review B, 40(6):3616, 1989.

[137] XH Min, S Emura, K Tsuchiya, T Nishimura, and K Tsuzaki. Transition of multi-deformation modes in ti–10mo alloy with oxygen addition. Materials Science and Engineering: A, 590:88–96, 2014.

[138] XH Min, K Tsuzaki, S Emura, and K Tsuchiya. Enhancement of uniform elongation in high strength ti–mo based alloys by combination of deformation modes. Materials Science and Engineering: A, 528(13-14):4569–4578, 2011.

[139] XH Min, K Tsuzaki, S Emura, and K Tsuchiya. Heterogeneous twin formation and its effect on tensile properties in ti–mo based β titanium alloys. Materials Science and Engineering: A, 554:53–60, 2012.

[140] Xiaohua Min, Pengfei Bai, Satoshi Emura, Congqian Cheng, Beibei Jiang, Koichi Tsuchiya, et al. Effect of oxygen content on deformation mode and corrosion behavior in β-type ti-mo alloy. Materials Science and Engineering: A, 684:534–541, 2017.

[141] Xiaohua Min, Xuejiao Chen, Satoshi Emura, and Koichi Tsuchiya. Mechanism of twinning-induced plasticity in β-type ti–15mo alloy. Scripta Materialia, 69(5):393–396, 2013.

[142] Xiaohua Min, Satoshi Emura, Ling Zhang, Kaneaki Tsuzaki, and Koichi Tsuchiya. Improvement of strength–ductility tradeoff in β titanium alloy through pre-strain induced twins combined with brittle ω phase. Materials Science and Engineering: A, 646:279–287, 2015.

[143] DB Miracle, ON Senkov, Carolina Frey, S Rao, and TM Pollock. Strength vs temperature for refractory complex concentrated alloys (rccas): A critical comparison with refractory bcc elements and dilute alloys. Acta Materialia, 266:119692, 2024.

[144] Y Mishin. Machine-learning interatomic potentials for materials science. Acta Materialia, 214:116980, 2021.

[145] Uichiro Mizutani. The hume-rothery rules for structurally complex alloy phases. In Surface properties and engineering of complex intermetallics, pages 323–399. World Scientific, 2010.

[146] M Morinaga. The molecular orbital approach and its application to biomedical titanium alloy design. In Titanium in medical and dental applications, pages 39–64. Elsevier, 2018.

[147] MASAHIKO Morinaga, N Yukawa, T Maya, K Sone, and H Adachi. Theoretical design of titanium alloys. In Sixth world conference on titanium. III, pages 1601–1606, 1988.

[148] Bohayra Mortazavi, Xiaoying Zhuang, Timon Rabczuk, and Alexander V Shapeev. Atomistic modeling of the mechanical properties: the rise of machine learning interatomic potentials. Materials horizons, 10(6):1956–1968, 2023.

[149] MA Murzinova, SV Zherebtsov, DN Klimenko, and SL Semiatin. The effect of β stabilizers on the structure and energy of α/β interfaces in titanium alloys. Metallurgical and Materials Transactions A, 52(5):1689–1698, 2021.

[150] Masaaki Nakai, Mitsuo Niinomi, Toshikazu Akahori, Harumi Tsutsumi, and Michiharu Ogawa. Effect of oxygen content on microstructure and mechanical properties of biomedical ti-29nb-13ta-4.6 zr alloy under solutionized and aged conditions. Materials transactions, 50(12):2716–2720, 2009.

[151] Mitsuo Niinomi. Mechanical biocompatibilities of titanium alloys for biomedical applications. Journal of the mechanical behavior of biomedical materials, 1(1):30–42, 2008.

[152] Mitsuo Niinomi and Carl J Boehlert. Titanium alloys for biomedical applications. Advances in metallic biomaterials: tissues, materials and biological reactions, pages 179–213, 2015.

[153] Zenji Nishiyama. Martensitic transformation. Elsevier, 2012.

[154] John Frederick Nye. Physical properties of crystals: their representation by tensors and matrices. Oxford university press, 1985.

[155] EG Obbard, YL Hao, RJ Talling, SJ Li, YW Zhang, David Dye, and R Yang. The effect of oxygen on α" martensite and superelasticity in ti–24nb–4zr–8sn. Acta Materialia, 59(1):112–125, 2011.

[156] Shigenobu Ogata, Ju Li, and Sidney Yip. Energy landscape of deformation twinning in bcc and fcc metals. Physical Review B, 71(22):224102, 2005.

[157] Avinesh Ojha and Huseyin Sehitoglu. Twinning stress prediction in bcc metals and alloys. Philosophical magazine letters, 94(10):647–657, 2014.

[158] M Oka and Y Taniguchi. Stress-induced products in metastable beta ti–mo and ti–v alloys. Journal of the Japan Institute of Metals, 42(8):814–820, 1978.

[159] M Oka and Y Taniguchi. {332} deformation twins in a ti-15.5 pct v alloy. Metallurgical Transactions A, 10:651–653, 1979.

[160] Nilson TC Oliveira, Giorgia Aleixo, Rubens Caram, and Antonio C Guastaldi. Development of ti–mo alloys for biomedical applications: Microstructure and electrochemical characterization. Materials Science and Engineering: A, 452:727–731, 2007.

[161] GB Olson and WS Owen. Martensite, asm international. Materials Park, OH, 1992.

[162] Gregory B Olson and M Azrin. Transformation behavior of trip steels. Metallurgical Transactions A, 9:713–721, 1978.

[163] Sertan Ozan, Jixing Lin, Yuncang Li, Yaowu Zhang, Khurram Munir, Hongwei Jiang, and Cuie Wen. Deformation mechanism and mechanical properties of a thermomechanically processed β ti–28nb–35.4 zr alloy. Journal of the mechanical behavior of biomedical materials, 78:224–234, 2018.

[164] Junyun Pan, Renhai Shi, Zhihao Zhang, Hongtao Zhang, Yuhong Zhao, Weidong Li, Huadong Fu, and Jianxin Xie. Composition-deformation mechanism-property machine learning model for strength-ductility improvement of β-type titanium alloys. International Journal of Plasticity, page 104461, 2025.

[165] Michele Parrinello and Aneesur Rahman. Polymorphic transitions in single crystals: A new molecular dynamics method. Journal of Applied physics, 52(12):7182–7190, 1981.

[166] Anthony Paxton. Theoretical strength, twinning, antitwinning and pseudotwinning-a quantum-mechanical approach. In Symposium on Twinning in Advanced Materials, as part of the 1993 Materials Week, pages 27–41. MINERALS, METALS & MATERIALS SOC, 1994.

[167] John P Perdew, Kieron Burke, and Matthias Ernzerhof. Generalized gradient approximation made simple. Physical review letters, 77(18):3865, 1996.

[168] Pralhad Pesode and Shivprakash Barve. A review—metastable β titanium alloy for biomedical applications. Journal of Engineering and Applied Science, 70(1):25, 2023.

[169] Dehai Ping. Review on ω phase in body-centered cubic metals and alloys. Acta Metallurgica Sinica (English Letters), 27:1–11, 2014.

[170] Steve Plimpton. Fast parallel algorithms for short-range molecular dynamics. 117(1):1–19.

[171] Dierk Raabe, Zhiming Li, and Dirk Ponge. Metastability alloy design. MRS Bulletin, 44(4):266–272, 2019.

[172] John R Ray and Aneesur Rahman. Statistical ensembles and molecular dynamics studies of anisotropic solids. The Journal of chemical physics, 80(9):4423–4428, 1984.

[173] Kenneth C Russell. Nucleation in solids: the induction and steady state effects. Advances in Colloid and Interface Science, 13(3-4):205–318, 1980.

[174] Takashi Saito, Tadahiko Furuta, Jung-Hwan Hwang, Shigeru Kuramoto, Kazuaki Nishino, Nobuaki Suzuki, Rong Chen, Akira Yamada, Kazuhiko Ito, Yoshiki Seno, et al. Multifunctional alloys obtained via a dislocation-free plastic deformation mechanism. Science, 300(5618):464–467, 2003.

[175] R Shi, N Ma, and Y Wang. Predicting equilibrium shape of precipitates as function of coherency state. Acta Materialia, 60(10):4172–4184, 2012.

[176] Zhe Shi and Chandra Veer Singh. Competing twinning mechanisms in body-centered cubic metallic nanowires. Scripta Materialia, 113:214–217, 2016.

[177] Sumin Shin, Cheng Zhang, and Kenneth S Vecchio. Phase stability dependence of deformation mode correlated mechanical properties and elastic properties in ti-nb gum metal. Materials Science and Engineering: A, 702:173–183, 2017.

[178] Wataru Shinoda, Motoyuki Shiga, and Masuhiro Mikami. Rapid estimation of elastic constants by molecular dynamics simulation under constant stress. Physical Review B, 69(13):134103, 2004.

[179] Paramjit Singh, Harish Pungotra, and Nirmal S Kalsi. On the characteristics of titanium alloys for the aircraft applications. Materials today: proceedings, 4(8):8971–8982, 2017.

[180] AW Sleeswyk. 1/2¡ 111¿ screw dislocations and the nucleation of {112}¡ 111¿ twins in the bcc lattice. Philosophical Magazine, 8(93):1467–1486, 1963.

[181] Raymond Edward Smallman. Modern physical metallurgy. Elsevier, 2016.

[182] Cyril Stanley Smith. A history of martensite: early ideas on the structure of steel. ASM International, Martensite(USA), 1992,, pages 21–39, 1992.

[183] Alexander Stukowski. Visualization and analysis of atomistic simulation data with ovito–the open visualization tool. Modelling and simulation in materials science and engineering, 18(1):015012, 2009.

[184] Alexander Stukowski, Vasily V Bulatov, and Athanasios Arsenlis. Automated identification and indexing of dislocations in crystal interfaces. Modelling and Simulation in Materials Science and Engineering, 20(8):085007, 2012.

[185] F Sun, JY Zhang, Matthieu Marteleur, Thierry Gloriant, P Vermaut, Denis Laillé, Philippe Castany, C Curfs, PJ Jacques, and FJAM Prima. Investigation of early stage deformation mechanisms in a metastable β titanium alloy showing combined twinning-induced plasticity and transformation-induced plasticity effects. Acta Materialia, 61(17):6406–6417, 2013.

[186] Masaki Tahara, Tomonari Inamura, Hee Young Kim, Shuichi Miyazaki, and Hideki Hosoda. Role of oxygen atoms in α" martensite of ti-20 at.% nb alloy. Scripta Materialia, 112:15–18, 2016.

[187] Y Takemoto, M Hida, and A Sakakibara. Structural relaxation of interface of $\{332\}\langle 113\rangle$ twin in βti alloy. Nippon Kinzoku Gakkaishi (1952), 57(12):1471–1472, 1993.

[188] Aidan P. Thompson, H. Metin Aktulga, Richard Berger, Dan S. Bolintineanu, W. Michael Brown, Paul S. Crozier, Pieter J. in 't Veld, Axel Kohlmeyer, Stan G. Moore, Trung Dac Nguyen, Ray Shan, Mark J. Stevens, Julien Tranchida, Christian Trott, and Steven J. Plimpton. LAMMPS - a flexible simulation tool for particle-based materials modeling at the atomic, meso, and continuum scales. 271:108171.

[189] Hirobumi Tobe, Hee Young Kim, Tomonari Inamura, Hideki Hosoda, and Shuichi Miyazaki. Origin of {3 3 2} twinning in metastable β-ti alloys. Acta materialia, 64:345–355, 2014.

[190] ND Tomashov, RM Altovsky, and GP Chernova. Passivity and corrosion resistance of titanium and its alloys. Journal of the Electrochemical Society, 108(2):113–119, 1961.

[191] Gareth A Tribello, Massimiliano Bonomi, Davide Branduardi, Carlo Camilloni, and Giovanni Bussi. Plumed 2: New feathers for an old bird. Computer physics communications, 185(2):604–613, 2014.

[192] Mark A Tschopp, KN Solanki, Fei Gao, Xin Sun, Mohammad A Khaleel, and MF Horstemeyer. Probing grain boundary sink strength at the nanoscale: Energetics and length scales of vacancy and interstitial absorption by grain boundaries in α-fe. Physical Review B—Condensed Matter and Materials Physics, 85(6):064108, 2012.

[193] David Turnbull. Metastable structures in metallurgy. Metallurgical Transactions B, 12(2):217–230, 1981.

[194] A Van de Walle, P Tiwary, M De Jong, DL Olmsted, M Asta, A Dick, D Shin, Yi Wang, L-Q Chen, and Z-K Liu. Efficient stochastic generation of special quasirandom structures. Calphad, 42:13–18, 2013.

[195] Stefan Van der Walt, Johannes L Schönberger, Juan Nunez-Iglesias, François Boulogne, Joshua D Warner, Neil Yager, Emmanuelle Gouillart, and Tony Yu. scikit-image: image processing in python. PeerJ, 2:e453, 2014.

[196] Pauli Virtanen, Ralf Gommers, Travis E. Oliphant, Matt Haberland, Tyler Reddy, David Cournapeau, Evgeni Burovski, Pearu Peterson, Warren Weckesser, Jonathan Bright, Stéfan J. van der Walt, Matthew Brett, Joshua Wilson, K. Jarrod Millman, Nikolay Mayorov, Andrew R. J. Nelson, Eric Jones, Robert Kern, Eric Larson, C J Carey, İlhan Polat, Yu Feng, Eric W. Moore, Jake VanderPlas, Denis Laxalde, Josef Perktold, Robert Cimrman, Ian Henriksen, E. A. Quintero, Charles R. Harris, Anne M. Archibald, Antônio H. Ribeiro, Fabian Pedregosa, Paul van Mulbregt, and SciPy 1.0 Contributors. SciPy 1.0: Fundamental Algorithms for Scientific Computing in Python. Nature Methods, 17:261–272, 2020.

[197] V. Vítek. Intrinsic stacking faults in body-centred cubic crystals. Philosophical Magazine, 18(154):773–786, 1968.

[198] V Vitek. Multilayer stacking faults and twins on {211} planes in bcc metals. Scripta Metallurgica, 4(9):725–732, 1970.

[199] Vaclav Vitek. Intrinsic stacking faults in body-centred cubic crystals. Philosophical Magazine, 18(154):773–786, 1968.

[200] J Wang and H Sehitoglu. Twinning stress in shape memory alloys: theory and experiments. Acta materialia, 61(18):6790–6801, 2013.

[201] Jiangwei Wang, Zhi Zeng, Christopher R Weinberger, Ze Zhang, Ting Zhu, and Scott X Mao. In situ atomic-scale observation of twinning-dominated deformation in nanoscale body-centred cubic tungsten. Nature materials, 14(6):594–600, 2015.

[202] Junshuai Wang, Wenlong Xiao, Lei Ren, Yu Fu, and Chaoli Ma. The roles of oxygen content on microstructural transformation, mechanical properties and corrosion resistance of ti-nb-based biomedical alloys with different β stabilities. Materials Characterization, 176:111122, 2021.

[203] Lu Wang, Chao Fu, Yidong Wu, Qinjia Wang, Xidong Hui, and Yandong Wang. Formation and toughening of metastable phases in tizrhfalnb medium entropy alloys. Materials Science and Engineering: A, 748:441–452, 2019.

[204] Shubin Wang, Da Shu, Peiying Shi, Xianbing Zhang, Bo Mao, Donghong Wang, Peter K Liaw, and Baode Sun. Tizrhfnb refractory high-entropy alloys with twinning-induced plasticity. Journal of Materials Science & Technology, 187:72–85, 2024.

[205] Shubin Wang, Mingxu Wu, Da Shu, Guoliang Zhu, Donghong Wang, and Baode Sun. Mechanical instability and tensile properties of tizrhfnbta high entropy alloy at cryogenic temperatures. Acta Materialia, 201:517–527, 2020.

[206] Siqi Wang, Tongqi Wen, Jian Han, and David J Srolovitz. Coherent and semicoherent α/β interfaces in titanium: structure, thermodynamics, migration. npj Computational Materials, 9(1):216, 2023.

[207] XL Wang, L Li, H Xing, P Ou, and J Sun. Role of oxygen in stress-induced ω phase transformation and {3 3 2}¡ 1 1 3¿ mechanical twinning in βti–20v alloy. Scripta Materialia, 96:37–40, 2015.

[208] Xuanli Wang, Shungui Zuo, Gaishi Wang, Jun Cao, Yuqi Zhang, and Mingjiang Jin. Influence of nb content on mechanical behavior and microstructure of ti–nb alloys. International Journal of Materials Research, 113(3):205–213, 2022.

[209] Yi Wang, L-Q Chen, Z-K Liu, and SN Mathaudhu. First-principles calculations of twin-boundary and stacking-fault energies in magnesium. Scripta Materialia, 62(9):646–649, 2010.

[210] Yue Wang, Fengkai Yan, Minjie Lai, and Xiuyan Li. Formation of nanocrystalline and nanolaminate structures in a twinning induced plasticity ti-12mo alloy: The role played by {332}¡ 113¿ twinning. Acta Materialia, 276:120078, 2024.

[211] Michael L. Waskom. seaborn: statistical data visualization. Journal of Open Source Software, 6(60):3021, 2021.

[212] Shaolou Wei, Feng He, and Cemal Cem Tasan. Metastability in high-entropy alloys: A review. Journal of Materials Research, 33(19):2924–2937, 2018.

[213] Wikipedia contributors. Kosmos 482, 2025. Accessed: 2026-05-01.

[214] JC Williams, BS Hickman, and DH Leslie. The effect of ternary additions on the decompositon of metastable beta-phase titanium alloys. Metallurgical Transactions, 2:477–484, 1971.

[215] SQ Wu, DH Ping, Y Yamabe-Mitarai, WL Xiao, Y Yang, QM Hu, GP Li, and R Yang. $\{112\}\langle 111\rangle$ twinning during ω to body-centered cubic transition. Acta materialia, 62:122–128, 2014.

[216] H Xing and J Sun. Mechanical twinning and omega transition by¡ 111¿{112} shear in a metastable β titanium alloy. Applied Physics Letters, 93(3):031908, 2008.

[217] LJ Xu, YY Chen, Zh G Liu, and FT Kong. The microstructure and properties of ti–mo–nb alloys for biomedical application. Journal of Alloys and Compounds, 453(1-2):320–324, 2008.

[218] Y Yang, P Castany, E Bertrand, M Cornen, JX Lin, and T Gloriant. Stress release-induced interfacial twin boundary ω phase formation in a β type ti-based single crystal displaying stress-induced α" martensitic transformation. Acta Materialia, 149:97–107, 2018.

[219] Y Yang, Philippe Castany, YL Hao, and T Gloriant. Plastic deformation via hierarchical nano-sized martensitic twinning in the metastable β ti-24nb-4zr-8sn alloy. Acta Materialia, 194:27–39, 2020.

[220] Y Yang, SQ Wu, GP Li, YL Li, YF Lu, K Yang, and P Ge. Evolution of deformation mechanisms of ti–22.4 nb–0.73 ta–2zr–1.34 o alloy during straining. Acta Materialia, 58(7):2778–2787, 2010.

[221] Yi Yang, Bohua Zhang, Zhichao Meng, Lei Qu, Hao Wang, Sheng Cao, Jianan Hu, Hao Chen, Songquan Wu, Dehai Ping, et al. $\{332\}\langle 113\rangle$ twinning transfer behavior and its effect on the twin shape in a beta-type ti-23.1 nb-2.0 zr-1.0 o alloy. Journal of Materials Science & Technology, 91:58–66, 2021.

[222] Ming Yin, Hengjun Luo, Hao Deng, Longqing Chen, and Wenbin Qiu. Thermomechanical processing of near-β ti–5al–5mo–5v–1cr–1fe alloys: Effect of deformation reduction on microstructures and mechanical properties. Materials Science and Engineering: A, 853:143786, 2022.

[223] MH Yoo and JK Lee. Deformation twinning in hcp metals and alloys. Philosophical Magazine A, 63(5):987–1000, 1991.

[224] MC Zang, HZ Niu, HR Zhang, H Tan, and DL Zhang. Cryogenic tensile properties and deformation behavior of a superhigh strength metastable beta titanium alloy ti–15mo–2al. Materials Science and Engineering: A, 817:141344, 2021.

[225] Clarence Zener. Contributions to the theory of beta-phase alloys. Physical Review, 71(12):846, 1947.

[226] Hongyi Zhan, Gui Wang, Damon Kent, and Matthew Dargusch. The dynamic response of a metastable β ti–nb alloy to high strain rates at room and elevated temperatures. Acta Materialia, 105:104–113, 2016.

[227] Hongyi Zhan, Weidong Zeng, Gui Wang, Damon Kent, and Matthew Dargusch. On the deformation mechanisms and strain rate sensitivity of a metastable β ti–nb alloy. Scripta Materialia, 107:34–37, 2015.

[228] Jinyong Zhang, Yangyang Fu, Yijin Wu, Bingnan Qian, Zheng Chen, Akihisa Inoue, Yuan Wu, Yang Yang, Fan Sun, Ju Li, et al. Hierarchical $\{332\}\langle 113\rangle$ twinning in a metastable β ti-alloy showing tolerance to strain localization. Materials Research Letters, 8(7):247–253, 2020.

[229] Jinyong Zhang, Fan Sun, Zheng Chen, Yang Yang, Baolong Shen, Ju Li, and Frédéric Prima. Strong and ductile beta ti–18zr–13mo alloy with multimodal twinning. Materials research letters, 7(6):251–257, 2019.

[230] Long Zhang, Huameng Fu, Shaofan Ge, Zhengwang Zhu, Hong Li, Hongwei Zhang, Aiming Wang, and Haifeng Zhang. Phase transformations in body-centered cubic nbxhfzrti high-entropy alloys. Materials Characterization, 142:443–448, 2018.

[231] Wei-dong Zhang, Zhenggang Wu, Yong Liu, Hongbin Bei, Bin Liu, and Jingwen Qiu. Plastic deformation mechanism of ti–nb–ta–zr–o alloy at cryogenic temperatures. Materials Science and Engineering: A, 765:138293, 2019.

[232] Wen-Zheng Zhang, Xin-Fu Gu, and Fu-Zhi Dai. Faceted interfaces: a key feature to quantitative understanding of transformation morphology. npj Computational Materials, 2(1):1–14, 2016.

[233] Xianbing Zhang, Shubin Wang, Jie Wang, Xinyu Xu, Song Lu, and Binbin He. Unique transitions in uniform elongation and deformation mechanisms of a refractory medium-entropy alloy at cryogenic temperatures. International Journal of Plasticity, 186:104245, 2025.

[234] Guohua Zhao, Xiaoqing Li, and Nik Petrinic. Materials information and mechanical response of trip/twip ti alloys. npj Computational Materials, 7(1):91, 2021.

[235] Yubao Zhen and Chengbiao Chu. A deformation–fluctuation hybrid method for fast evaluation of elastic constants with many-body potentials. Computer Physics Communications, 183(2):261–265, 2012.

[236] Hui Zheng, Lauren TW Fey, Xiang-Guo Li, Yong-Jie Hu, Liang Qi, Chi Chen, Shuozhi Xu, Irene J Beyerlein, and Shyue Ping Ong. Multi-scale investigation of short-range order and dislocation glide in monbti and tanbti multi-principal element alloys. npj Computational Materials, 9(1):89, 2023.

[237] Yufeng Zheng, Robert EA Williams, Soumya Nag, Rajarshi Banerjee, Hamish L Fraser, and Dipankar Banerjee. The effect of alloy composition on instabilities in the β phase of titanium alloys. Scripta Materialia, 116:49–52, 2016.

[238] YT Zhu, XZ Liao, and XL Wu. Deformation twinning in nanocrystalline materials. Progress in Materials Science, 57(1):1–62, 2012.

[239] Yuman Zhu, Suming Zhu, and Jian-Feng Nie. Atomic-scale study of {1 1 2} twin boundary structure in a β-ti alloy. Philosophical Magazine Letters, 96(7):280–285, 2016.

[240] Alex Zunger, S-H Wei, LG Ferreira, and James E Bernard. Special quasirandom structures. Physical review letters, 65(3):353, 1990.